Image/Model Fusion for the Quantification of Mitral Regurgitation Severity

Alexandre This

Image/Model Fusion for the Quantification of Mitral Regurgitation Severity

THÈSE DE DOCTORAT

Présentée par

Alexandre This

pour obtenir le grade de

DOCTEUR DE
L' UNIVERSITÉ PIERRE ET MARIE CURIE - Paris VI

Spécialité : Mathématiques Appliquées

Soutenue publiquement le 28 mai 2019 devant le jury composé de :

Frédéric Hecht	Président
Christian Vergara	Rapporteur
Franck Nicoud	Rapporteur
Stéphanie Salmon	Examinatrice
Marcela Szopos	Examinatrice
Jean-Frédéric Gerbeau	Directeur de thèse
Odile Bonnefous	Encadrante industrielle

Co-directeur de thèse : Miguel A. Fernández
Co-encadrant industriel : Hernán Morales

Thèse préparée avec le soutien de l'équipe-projet REO
Laboratoire Jacques-Louis Lions
Université Pierre et Marie Curie - Paris 6
et **Centre de Recherche Inria de Paris**
2 rue Simone Iff
75589 Paris Cedex 12

Remerciements

À ma fiancée,

Il est rare d'avoir l'occasion de remercier, sincèrement, celles et ceux qui nous aident à grandir, à avancer, et à nous dépasser. Alors si c'est sans doute une erreur de ne pas le faire plus souvent, plus spontanément, je vais saisir l'opportunité qui m'est offerte ici pour réparer cette erreur !

> *Certes, je ne m'attendais pas à prendre la plume, mais le triste privilège de ma réputation ne me permet pas de résister à la tentation dont je suis animé, car il est dans la vie des hommes comme dans celles des doctorants des heures heureuses [...]*

J'interromps quelques secondes ce discours entièrement improvisé, qui saura occuper quelques instants ceux de mes proches qui comprendront la référence, pendant que je dédie toute mon attention à celles et ceux qui auront été les plus impliqués dans le suivi de mon travail de doctorant. En effet, je souhaite exprimer toute ma reconnaissance aux quatre personnes qui m'ont encadré pendant ces trois années. Jean-Frédéric, Miguel, Odile et Hernán, je tiens à vous remercie pour l'intérêt permanent que vous su manifester pour mes travaux, pour votre encadrement parfaitement dosé, à mon goût, pour vos conseils et pour le formidable environnement de travail que vous avez pu me fournir. On lit, parfois, que la thèse est une période difficile. Pour moi, cela aura été tout l'inverse. Grâce à vous. Alors, merci.

Bien entendu, je suis très reconnaissant envers Prof. C. Vergara et Prof. F. Nicoud, pour avoir accepté de rapporter ma thèse et pour leur lecture détaillée de ce manuscrit. Je remercie également les autres membres du jury: Prof. F. Hecht, pour avoir accepté de le présider, Prof. S. Salmon et Prof. M. Szopos, pour avoir bien voulu y participer, en qualité d'examinatrices.

> *[...] où l'individu quelque intelligent qu'il soit et quelque bien intentionné qu'il puisse être, n'en est pas moins astreint à des considérations morales, politiques, religieuses ou philosophiques [...]*

En espérant avoir diverti l'attention de certains, quelques instants encore, je voudrais remercier maintenant mes très nombreux collègues, maintenant amis. Ainsi, et par ordre chronologique, je pense tout particulièrement à Vincent B., qui a été déterminant dans mon parcours. C'est en grande partie grâce à toi que j'ai intégré le Master MVA, et ces quelques mots sont sans aucun doute bien insuffisants pour exprimer toute ma gratitude. J'y ai passé la meilleure année *scolaire* de ma vie, en compagnie de Nicolas P., camarade de tous les instants et de tous les projets.

J'adresse ensuite mes remerciements aux membres, nombreux, des deux équipes que j'aurais eu la chance de côtoyer pendant ces trois années de thèse. Du côté de l'INRIA, j'ai une pensée particulière pour Damiano, Céline, Marina, Irène, Miguel et Jean-Frédéric d'abord, ces personnes qui impressionnent par leurs compétences, mais auprès desquels on apprend tant, en douceur et dans la bonne humeur. Chloé, Eliott, Fabien, Florian, Matteo, Nicolas, Noémie, Sanjay,

ensuite, pour avoir guidé mes premiers pas de doctorant, et pour tous ces instants passés en votre compagnie. Fannie, Felipe et Daniele, j'ai été très heureux de vous voir arriver dans l'équipe et je suis certain que votre bonne humeur donnera tout son sens au nouveau nom de REO. Enfin, bien sûr, Ludovic. Parce que tu m'auras fait rigoler à invectiver sans vergogne. Parce que le ton direct fait parfois du bien. Parce que celui auquel j'aurais le plus parlé par messagerie pendant ces trois ans, c'est sans doute toi. Parce que finalement on se sera quand même bien amusé. Mes chers collègues de l'équipe Medisys, de Philips, ensuite. Si vous êtes trop nombreux pour que je cite chacun, individuellement, vous savez à quel point j'ai aimé faire partie, à vos côtés, du petit village gaulois. Parce que c'est ce que vous êtes : un village hétéroclite, dans lequel le vendeur de poisson pas frais (ou devrais-je dire de Deep Learning) côtoie le valeureux forgeron et ses outils magnifiques (ou devrais-je dire la simulation numérique), dans lequel on aime bien se chamailler, faire du bruit et festoyer. Mais également un village dans lequel chacun a sa petite maison, et dans lequel on peut toujours compter sur ses voisins lorsque cela devient nécessaire. Ce n'est pas pour rien qu'après avoir été en location pendant un peu plus de trois années, j'y vis maintenant dans une charmante maisonnette. Je termine enfin par les deux personnes qui, dans ces équipes respectives, rendent notre travail plus simple et nos vies plus agréables : Maryse et Nathalie. Merci. Merci infiniment.

[. . .] de sorte qu'en disant ces mots, je ne craindrais pas d'être taxé d'avarice sentimentale. Et c'est pourquoi, mes très chers amis, je propose à tous, mais aussi à chacun, fort d'une conviction interne puissante, de lever notre verre à la fin de cette fabuleuse étape de vie, et au commencement de la prochaine.

Le voici enfin, en entier, ce discours dont vous n'aurez souvent entendu que les premiers mots dans ma bouche, trop pressé sans doute d'en accomplir les derniers. J'espère que vous aurez attendu jusqu'ici, mes très chers amis, pour que je puisse vous exprimer toute ma reconnaissance d'avoir été présent à mes côtés depuis si longtemps: la *team mokay*: Adrien, Alexandre, Ivain, Karl et Romain, ces amis de la première heure que l'on conserve à vie, peu importe où ils s'exportent. Alexandre et Julen, ensuite, parce que si le cinéma permet de garder une proximité certaine, il s'agit en fait de bien plus que cela. Antonin, Ilan, Isabelle, Guillaume, parce que finalement, un jeu vidéo ou une soirée est le prétexte pour rencontrer et faire rencontrer des gens qui resteront proches pendant des années. Et qui deviennent, le temps aidant, des amis de plus en plus importants. La *team ECE*, enfin : Benjamin, Cédric, Emmanuel, Jessica, Thomas, qui savent très bien à quel point je suis heureux de les compter parmi mes plus proches amis. Que ceux que je n'ai pas mentionnés (les conjoints, la *team poulailler*,. . .) ne s'en offusquent pas: je pense bien évidemment à vous, mais il était difficile de faire tenir autant de belles personnes en si peu de page. . . .

Mes derniers mots vont à la *KFZ*. Papa, Maman, Wolfgang, merci. On ne choisit pas sa famille, moi j'aime la mienne, et j'en suis fier. Et puis en réalité, si, on peut en choisir une partie. . . Celle que j'ai choisie a débuté ces remerciements ; elle en marquera également la conclusion. À toi, Marie-Sophie, aujourd'hui ma fiancée, demain ma femme, et après-demain sans doute plus encore (PS : après-demain, on sera jeudi, je crois bien).

Fusion Image/Modèles numériques pour la quantification de la sévérité de la Régurgitation Mitrale

Résumé :

Afin d'assurer le bon fonctionnement des organes du corps humain, un apport régulier en nutriment et en oxygène est nécessaire. Cet apport est assuré par la contraction régulière du cœur, organe majeur du système cardiovasculaire. De manière périodique, le cœur – partitionné en quatre cavités – se remplit de sang puis se contracte pour l'éjecter vers les différents organes du corps. L'oreillette droite et le ventricule droit permettent l'envoi le sang désoxygéné aux poumons, alors que l'oreillette gauche et le ventricule gauche envoient le sang oxygéné au reste du corps.

Quatre valves passives permettent de prévenir les reflux de sang entre les différentes cavités cardiaques. En conséquence de certaines pathologies cardiaques, il arrive que ces valves ne fonctionnent pas correctement, pouvant entraîner un flux rétrograde de sang. Dans le cas de la valve mitrale, située entre le ventricule gauche et l'oreillette gauche, on parle de régurgitation mitrale. La prise en charge de cette maladie est complexe et peut nécessiter des traitements lourds tels que le remplacement de la valve. Il est donc nécessaire de quantifier au mieux la sévérité de la régurgitation mitrale pour proposer un traitement adapté.

Diverses techniques ont été mises au point afin de quantifier la sévérité de la régurgitation mitrale. Par exemple, la méthode PISA (Proximal Isovelocity Surface Area), fondée sur des hypothèses simplificatrices, permet d'estimer la taille de l'orifice régurgitant ainsi que le volume de sang régurgité lors d'un battement cardiaque à partir d'images échocardiographiques Doppler. Malgré sa popularité, cette méthode souffre d'un certain nombre de défauts portant sur la précision de l'estimation et sur sa reproductibilité.

Les développements récents en imagerie échographique permettent l'acquisition de données pertinentes en ce qui concerne l'hémodynamique cardiaque et la dynamique ventriculaire. D'autre part, la maturité de la modélisation numérique cardiaque permet de simuler les écoulements sanguins de manière satisfaisante. Dans ce contexte, il est fait l'hypothèse que combiner des images échocardiographique avec des modèles numériques pourrait aider à améliorer la quantification de la régurgitation mitrale et par conséquent la qualité de prise en charge des patients.

Dans la première partie de cette thèse, un modèle numérique 3D de l'hémodynamique cardiaque est présenté. On s'attache notamment à y intégrer un modèle de régurgitation mitrale à la fois versatile et simple de mise en oeuvre. Des exemples numériques permettent d'apprécier les avantages et les inconvénients du modèle proposé. On en profitera également pour proposer un modèle permettant la modélisation des phases isovolumétriques du cœur. Un modèle relativement précis de l'hémodynamique cardiaque, mais de complexité numérique raisonnable, est ainsi obtenu à l'issue de cette première partie.

La seconde partie de cette thèse décrit la stratégie adoptée pour permettre la fusion de données provenant des images médicales avec des modèle numériques. Dans un premier temps, une méthode automatique permettant la personnalisation du modèle numérique développé dans la

première partie du manuscrit, à partir d'images médicales, est présentée. Une base de donnée d'images échocardiographique est utilisée pour tester la robustesse de la méthode. Cette variabilité de cas est également utilisée pour la simulation de régurgitations synthétiques, permettant ainsi une évaluation systématique la méthode PISA. Une seconde étape consiste à évaluer à quel point l'absence de composante tangentielle du mouvement des parois, une composante du mouvement difficile à obtenir en échocardiographie, peut impacter l'hémodynamique cardiaque. Enfin, comme les méthodes présentées sont encore trop complexes d'un point de vue numérique, on termine la thèse avec la présentation d'une méthode de reconstruction du flux sanguin combinant des images Doppler Couleur à des contraintes physiques liées à l'incompressibilité du sang. Une évaluation quantitative de la qualité de cette reconstruction est permise par l'utilisation des simulations numériques produites tout au long de cette thèse.

Mots clés : Échographie, Modélisation, Hémodynamique, Personnalisation de modèle, Quantification, Régurgitation Mitrale

Image/Model Fusion for the Quantification of Mitral Regurgitation Severity

Abstract:

In order to ensure the proper functioning of the organs of the human body, a regular supply of nutrients and oxygen is necessary. This is ensured by the regular contraction of the heart, a major organ of the cardiovascular system. Periodically, the heart – divided into four cavities – fills with blood and then contracts to eject it toward the various organs of the body. The right atrium and right ventricle send the deoxygenated blood to the lungs while the left atrium and left ventricle send the oxygenated blood toward the rest of the body.

Four passive valves prevent backward blood flow between the different heart cavities. As a result of certain cardiac diseases, these valves may not function properly, which can lead to a retrograde flow of blood. In the case of the mitral valve, located between the left ventricle and the left atrium, it is referred to as mitral regurgitation. The management of this disease is complex and may require extensive treatment such as valve replacement. It is therefore necessary to quantify the severity of mitral regurgitation in order to propose an appropriate treatment.

A number of techniques have been developed to quantify the severity of mitral regurgitation. One example is the PISA (Proximal Isovelocity Surface Area) method; based on simplifying assumptions, this method estimates the size of the regurgitant orifice as well as the volume of regurgitated blood during a heartbeat from Color Doppler echocardiographic images. Despite its popularity, this method suffers from a number of shortcomings in terms of estimation accuracy and reproducibility.

Recent developments in ultrasound imaging allow the acquisition of relevant data regarding cardiac hemodynamics and ventricular dynamics. On the other hand, the maturity of cardiac mathematical modeling makes it possible to simulate blood flow in a satisfactory way. In this context, it is assumed that combining echocardiographic images with digital models could help to improve the quantification of mitral regurgitation and therefore the quality of patient care.

In the first part of this document, a 3D mathematical model of cardiac hemodynamics is developed. Particular attention is being paid to integrating a mitral regurgitation model that is both versatile and simple to use. Numerical examples are provided to assess the advantages and disadvantages of the proposed model. We will also take the opportunity to model the isovolumetric phases of the heart. A relatively accurate model of cardiac hemodynamics, but nevertheless reasonable in term of numerical complexity, is thus obtained at the end of this first part.

The second part of this document describes the strategy adopted to allow the fusion of medical images with the numerical simulations. First, an automatic method allowing the personalization of the mathematical model developed in the first part of the manuscript, based on medical images, is presented. An echocardiographic image database is used to test the robustness of the method. The variability of this database is also used for the simulation of synthetic regurgitation, thus allowing a systematic evaluation of the PISA method. A second step is to evaluate how much the absence of a tangential component of wall movement, a component of

movement difficult to obtain in echocardiography, can impact cardiac hemodynamics. Finally, as the methods presented are still too expensive from a numerical point of view, we conclude with the presentation of a blood flow reconstruction method combining Color Doppler images with physical constraints related to blood incompressibility. A quantitative assessment of the quality of this reconstruction is made possible by the use of the numerical simulations produced throughout this thesis.

Keywords: Echocardiography, Modeling, Hemodynamics, Model personalization, Quantification, Mitral regurgitation

Contents

List of Figures

List of Tables

Chapter 1
Thesis introduction

In this first chapter, we propose to put the presented research work into context. To that end, the clinical background is first described in Section 1.1. The motivations and objectives are then exposed in Section 1.2. Finally, Section 1.3 describes how this manuscript is organized as well as the main contributions.

1.1 Clinical context

This first section is devoted to the clinical context. It is proposed to slowly progress from generalities regarding the cardiovascular system to specifics regarding the mitral valve and its pathologies. Those elements will both help understand the objectives of this manuscript and form the basis for the modeling work presented in the rest of this thesis.

1.1.1 Physiology and hemodynamics of the healthy left ventricle

The different organs of the human body need to be supplied by nutrients and oxygen to function properly. This regular intake is achieved by the circulation of blood in the cardiovascular system. The blood, acting as a provider and as a waste disposal, is moving thanks to the work of an organic pump made of muscles: the heart. We first describe the general organization of this organ. This description is supplemented with a schematic representation (Figure 1.1).

While the average heart beat rate is around one beat per second, the variability among the population is important. This variability is also expressed in the heart size and weight (ranging from 230 to 350 g for adults) even though the heart is generally described as a "*somewhat conical*" organ that "*measures about* 12 cm *in length and* 8-9 cm *in breadth at the broadest part*" [1].

Despite the inter-subject variability, the main anatomical features of the heart are similar between patients: the presence of two circulatory systems in the human body (the pulmonary and the systemic circulation) leads the heart to be separated into two – left and right – part by a membrane called septum. Each part is further divided into two chambers, called atrium and ventricle. The atria serve as filling chambers, while the ventricles act as ejecting chambers. Valves are located at the inlet and at the outlet of the ventricles preventing blood from flowing backward.

The right and left atria inlets are respectively connected to the *venae cavae* and the *pulmonary veins* (PV) and the valves located between those atria and the ventricles are respectively called the *tricuspid* and *mitral valve*. On the outlet side, the right and left ventricles are respectively connected to the *pulmonary artery* by the *pulmonary semilunar valve* and to the *aorta* by the *aortic valve*.

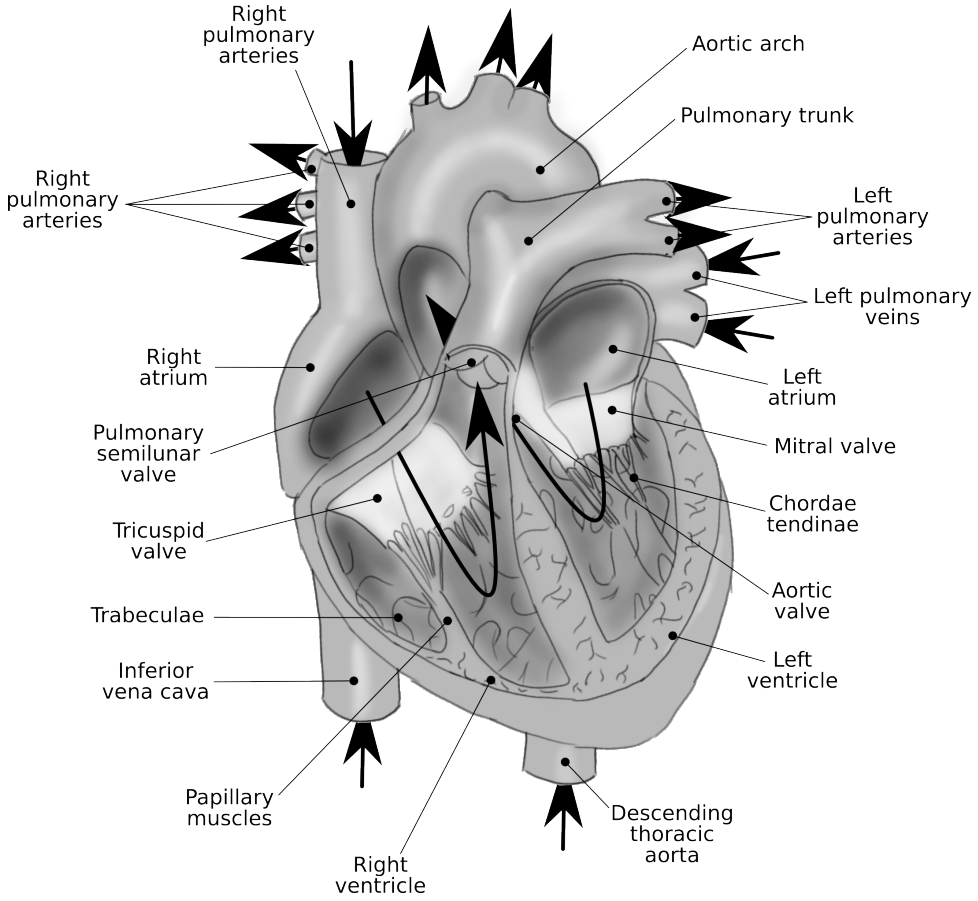

Figure 1.1 – Human heart anatomy. The four cavities are cut by an imaginary plane to allow the observation of interior features. The black arrows represent the path of the blood flow inside the heart.

Left ventricle anatomy

The left ventricular (LV) anatomy is now detailed. The LV shape is generally described as conical [1]. It is divided into three portions that are not clearly delimited by any anatomical borders: the inlet of the ventricle contains the mitral apparatus, while the outlet portion of the ventricle contains the aortic valve. Between this inlet and this outlet is an apical portion that contains fine trabeculations, described as a "criss-crossing meshwork of thin muscle bundles" [2]. The LV walls also contain papillary muscles; separated in two groups positioned in the antero-lateral and the postero-medial locations of the LV, those muscles helps hold the mitral valve during the systolic (*i.e.* contraction) phase.

The bulk of the LV is made of contractile tubular fibers, called myocites, that are interconnected as a complex three-dimensional network. This network is anisotrope, *i.e.* the main orientation of the myocites is not uniform throughout the LV (Figure 1.2). While the network is mainly oriented obliquely at the superficial section of the myocardium, it gradually switches to a circumferential orientation in a middle layer to a longitudinal orientation in the endocardium (the innermost layer of tissue of the LV) [2].

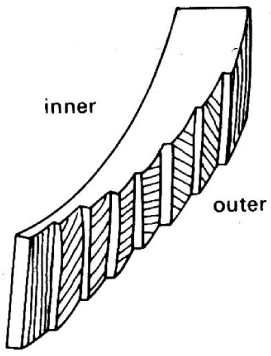

Figure 1.2 – Muscle fiber orientation in the LV wall [3]. The fibers are oriented obliquely on the *outer* side and progressively switches to a circumferential orientation in the middle layer and then to a longitudinal orientation in the *inner* side.

Left heart physiology

While the cardiac cycle is driven by a complex combination of phenomena, this section focuses on the physiology of the left ventricle and the hemodynamic consequences. As mentioned previously, the heart is beating at a rate of approximately 60 beats per minute. As the heart behavior is periodic, a description focusing on only one heart beat will be provided. The description is supplemented with the Wiggers diagram (Figure 1.3) in which the pink-colored region represents a full cardiac cycle.

In this pink-colored region, the period begins from the heart relaxation from a previous cardiac cycle. As a result of this relaxation, the LV volume starts to increase. The pressure of the ventricle is lower than the atrium pressure and this pressure difference causes the blood to flow from the atrium to the ventricle through the mitral valve. The aortic valve, on the other hand, is closed because of the aortic pressure which is greater, thus preventing backflow. This phase is called *passive filling*, or *E-wave*, and corresponds to the two sections denoted *rapid inflow* and *diastasis* in Figure 1.3.

An electrical impulse is generated by the sinoatrial node and propagates through the myocardial tissue, triggering myocites contraction. This contraction first reaches the atrium, pushing more blood into the ventricle this phase is called *atrial systole*, or *A-wave*.

The electrical impulse then reaches the ventricle resulting in the contraction of the LV myocites. This phase is called the *ventricular systole*. As a result, the pressure gradient that existed between the atrium and the ventricle is inverted and results in a blood flow reversal which drives the mitral valve closure. The chordae tendinae, attached to the papillary muscles, help prevent the mitral leaflet from being pushed back too far in the atrium. Literature also describes various other conjoint effects that may be part of the mitral valve closure (*e.g.,* the action of a pre-existing blood flow pattern) but the relative importance of those effects are difficult to quantify in a precise manner and might depend on the specificity of the patient [4].

A very short part of the systole (the *isovolumetric contraction*) corresponds to the time where the ventricle starts to contract while the two valves are closed. As no blood can be pushed out, the

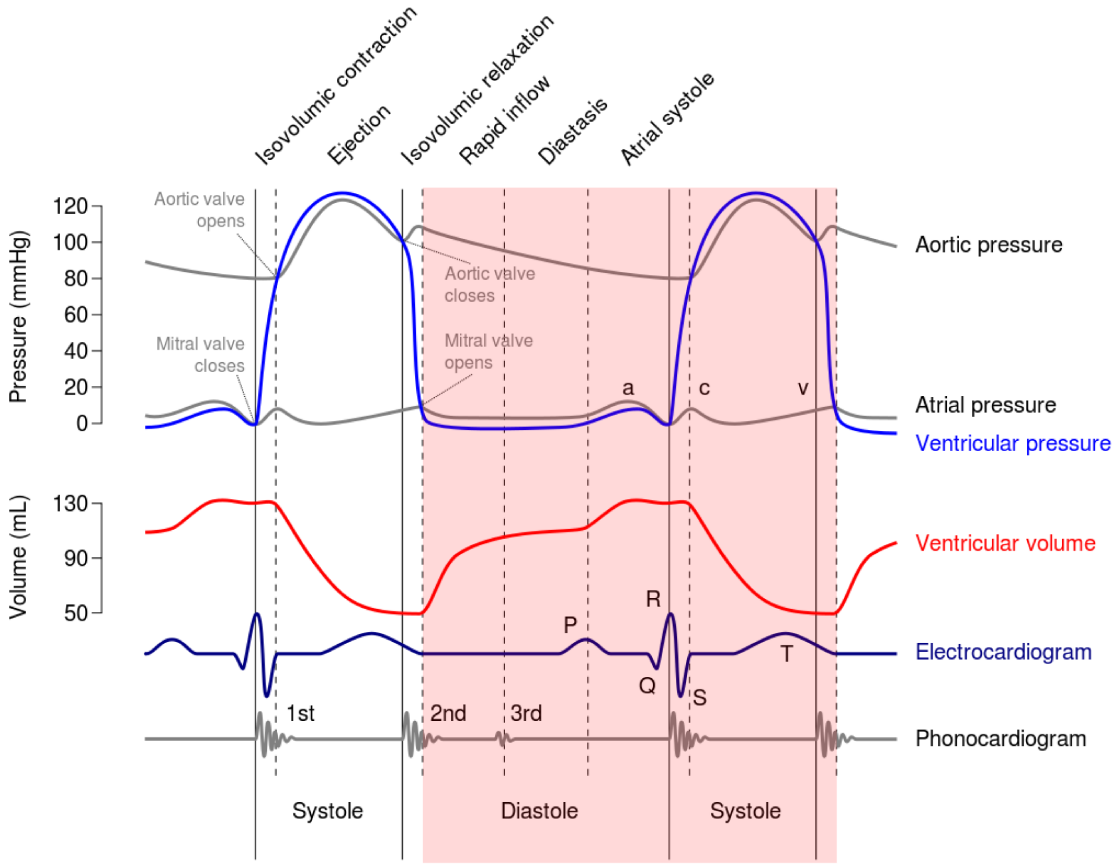

Figure 1.3 – Wiggers diagram [5]. This diagram superimposes several quantitative measurement related to the heart functions in order to help understanding cardiac physiology

volume of the ventricle does not change and the pressure inside the ventricle increases sharply. Once the ventricular pressure exceeds the aortic pressure, the aortic valve opens and blood is ejected from the ventricles towards the aorta. The orientation of the myocites in the LV wall has a strong influence the LV contraction: while the circumferential and longitudinal strands shorten the ventricle in those respective directions, the oblique strand of myocites impose a twist to the LV. This twist has been reported to increase the amount of blood ejected from the ventricle. If there was no twisting motion, the ventricle would not be able to reach a physiological ejection fraction (EF) as the myocites only shorten by 15-20 % at most [6].

Once the myocardial cells stop contracting, the pressure drops below the aortic pressure and the aortic valve closes. Again, a short phase called *isovolumetric relaxation* corresponds to the myocardial cell relaxation while the two valves are still closed. As a result of this relaxation, the pressure in the ventricle drops sharply and, once the pressure reduces below the atrial pressure, blood can enter the ventricle again through the mitral valve, thus completing the cardiac cycle.

Left heart hemodynamics

The left ventricle complex anatomy, geometry and motion described in the previous section determine the flow of blood.

During the diastole, the blood enters the left ventricle in two phases (the E and A wave). The blood flows through the mitral valve at a mean peak velocity of approximately 0.8 m/s [7].

At the peak of the E-wave, a vortex ring is observed and detaches from the tip of the mitral leaflet. A second vortex may appear due by atrial contraction (A-wave). Because of the asymmetric positioning and geometry of the mitral valve, the part of the vortex ring that is close to the posterior leaflet diminishes rapidly while the anteroseptal part is still present and enlarges. This phenomenon has been revealed both in experimental and numerical studies [8, 9, 10, 11] and it is believed that this vortical structure facilitates the ejection of blood during the systole [12].

During the systole, as the ventricle contracts, the blood is ejected through the aortic valve at a mean peak velocity of approximately 1 m/s [7, 13].

1.1.2 Anatomy and pathophysiology of the mitral complex

As aforementioned, the mitral valve is located between the LV and the left atrium (LA). It serves as a barrier to blood coming back in the left atrium when the ventricle contracts during the systolic phase. This valve is part of a mitral complex composed of a mitral annulus, two mitral leaflets, chordae tendinae and papillary muscles (Figure 1.4).

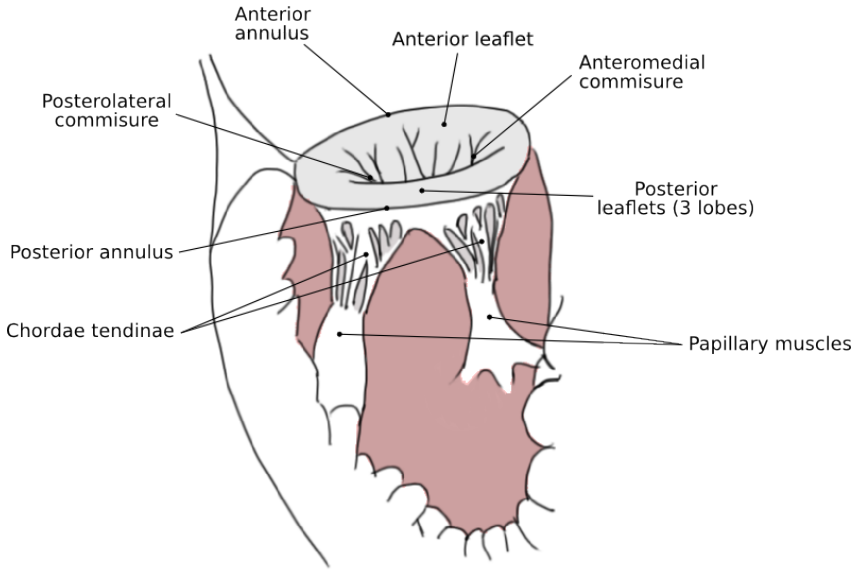

Figure 1.4 – Mitral complex. The mitral complex is composed of a mitral annulus, located at the base of the LV, on which is attached the MV. Chordae tendinae link the extremity of the anterior and posterior leaflets of the MV to papillary muscles.

The mitral annulus is a relatively fixed framework, shaped as a letter D, made of collagenous tissue that serves as an anchor for the anterior and for the posterior leaflets of the mitral valve.

While the base of those leaflets are attached to the annulus, the distal part is linked to the chordae tendinae, a network of strong cords supporting the leaflets when blood is expelled of the LV cavity during ventricular systole. Those chordae tendinae are themselves attached to the papillary muscles of the ventricle [4] (Figure 1.4 and Figure 1.5).

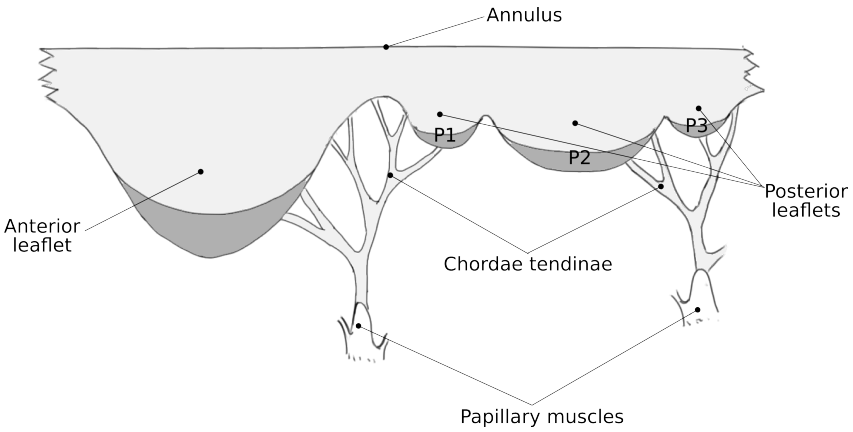

Figure 1.5 – Schematics of an exised mitral valve leaflet with attached chordae tendinae. The posterior leaflet divides into three scallops.

The morphology of the mitral valve has been studied extensively in the past [14, 15, 16, 17, 18]. In particular, a study of fifty normal mitral valves has been conducted to quantify the size of the mitral leaflets [15]. It has been shown that the mitral valve is composed of an anterior and a posterior leaflet which are separated by the anteromedial and the posterolateral commissures (Figure 1.5). The anterior and posterior leaflet differs in size and, more notably, the posterior leaflet further divides into three scallops (posteromedial commissural scallop, middle scallop and anterolateral commissural scallop). It has been noted that some patients had an even greater number of scallops dividing the posterior leaflet.

Pathologies of the mitral complex

Pathologies of the heart, either structural (*e.g.,* a deformation of the geometry) or physiological (*e.g.,* a defect of the electrical conductivity of the myocardium) can lead to a modification of the blood flow behavior [9, 19, 20]. In this work, a specific focus is made on the pathologies of the mitral complex. Following is a short list of such pathologies based on the literature [4], alongside potential causes and consequences:

- Several diseases can affect the mitral annulus like abscesses, inflammation, or calcifications. Change of shapes of the mitral annulus can also happen when the left ventricle is subject to large deformation (*e.g.,* ventricular hypertrophy)
- Changes in the mobility of the leaflets can happen due to various pathologies. Thickening, stiffening and calcification of the leaflets can change their behavior due to several diseases (*e.g.,* syphilis, poliomyelitis). Congenital diseases like Marphan Syndrome can also affect the valve dynamics.

- Acting as a network evening out the forces due to ventricular systole, the chordae tendinae are links between the papillary muscles and the valve leaflets. Those links can, in pathological cases, be shortened, elongated, fused or even break.
- Papillary muscles can be affected by fibrosis, which weakens the muscle support and could trigger a valve prolapse. Moreover, the muscles can also be subject to changes in position due to ventricular hypertrophy. This pathology changes the configuration of the heart and the position of the papillary muscle. As a result, the chordae tendineae might be pulling the mitral leaflets sideways.

1.1.3 Mitral regurgitation: description and severity assessment

The pathologies affecting the mitral valve complex can result in blood leaking through the mitral valve [4]. During ventricular systole, blood is pushed through the leakage and can reach high velocities (up to several meters per seconds) [21]. This phenomenon is called mitral valve regurgitation (MVR or more commonly MR).

Mitral regurgitation is one of the most prevalent valvular heart disease [22, 23]. Moreover, ageing is associated with a large increase in prevalence (Figure 1.6).

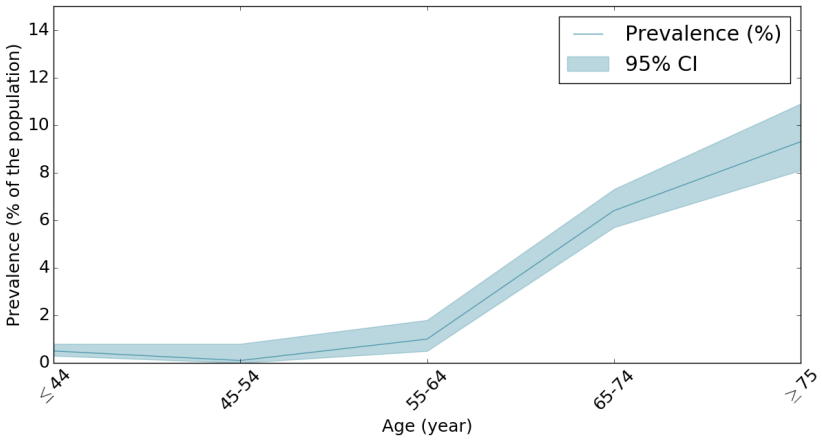

Figure 1.6 – Moderate/Severe MR prevalence by age in the US population, based on [22]

Depending on the pathology, mitral regurgitation can be classified in two groups: (1) primary mitral regurgitation and (2) secondary mitral regurgitation. Primary mitral regurgitation is caused when components of the mitral apparatus are directly affected (*e.g.,* prolapse caused by a chordae rupture), whereas secondary mitral regurgitation is a result of a distant pathology affecting a structurally healthy mitral apparatus (*e.g.,* MR caused by an alteration of the LV geometry) [24]. MR is classified using the Carpentier classification in Type 1 (normal leaflets motion), Type 2 (excessive leaflet motion) and Type 3 (restrictive leaflet motion) [25]. Figure 1.7 depicts several pathologies leading to MR and classified using the Carpentier classification.

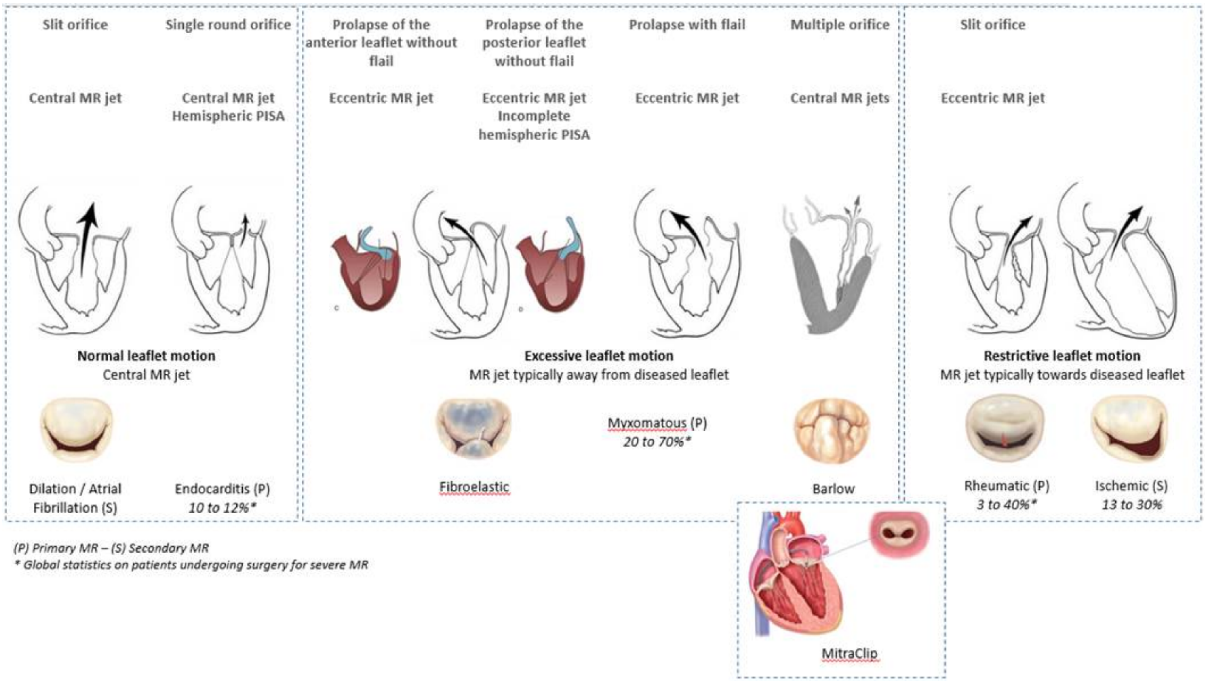

Figure 1.7 – MR classification, image courtesy of Helene Langet (based on [26]). The three main boxes represent, from left to right, Type 1, Type 2 and Type 3 MR.

Physicians evaluate the severity of the regurgitation to adapt their medical response. This evaluation can lead to mitral valve surgery, even for asymptomatic patients as reported in the clinical guidelines [27, 28, 24]. Figure 1.8 depicts how the current clinical guidelines recommend managing MR [27].

As the evaluation of the MR should be as accurate, reproducible and reliable as possible, the current clinical guidelines recommend integrating specific, supportive and quantitative features to provide the best MR severity assessment [29, 30, 31]. Those features are mainly extracted from medical images including 2D and 3D echocardiography (2DE and 3DE), computed tomography (CT) and cardiac magnetic resonance imaging (CMR) images. In the clinical setting, echocardiography (2D or 3D) plays a significant role [31] from which the following quantitative measurement can be estimated:

- Effective Regurgitant Orifice Area (EROA): the effective regurgitant orifice area is the area that is subject to regurgitation on the mitral valve. An EROA of less than $0.20\,\mathrm{cm}^2$ is classified as mild MR, an EROA between $0.20\,\mathrm{cm}^2$ and $0.39\,\mathrm{cm}^2$ is a sign of a moderate MR, and finally an EROA of more than $0.40\,\mathrm{cm}^2$ is associated with a severe MR [29].
- Vena contracta (VC): the vena contracta is the narrowest portion of the regurgitant jet in the atrium. It is located near the orifice. Vena contracta width (VCW), derived from 2D images, and vena contracta area (VCA), derived from 3D images, are correlated with MR severity. The VCA is claimed to be more accurate than VCW [32].
- Regurgitant volume (RV) and regurgitant fraction (RF): the regurgitant volume is the amount (volume) of blood that is ejected back to the atrium during the ventricular systole. The regurgitant fraction is the ratio between the RV and the total volume ejected from the LV

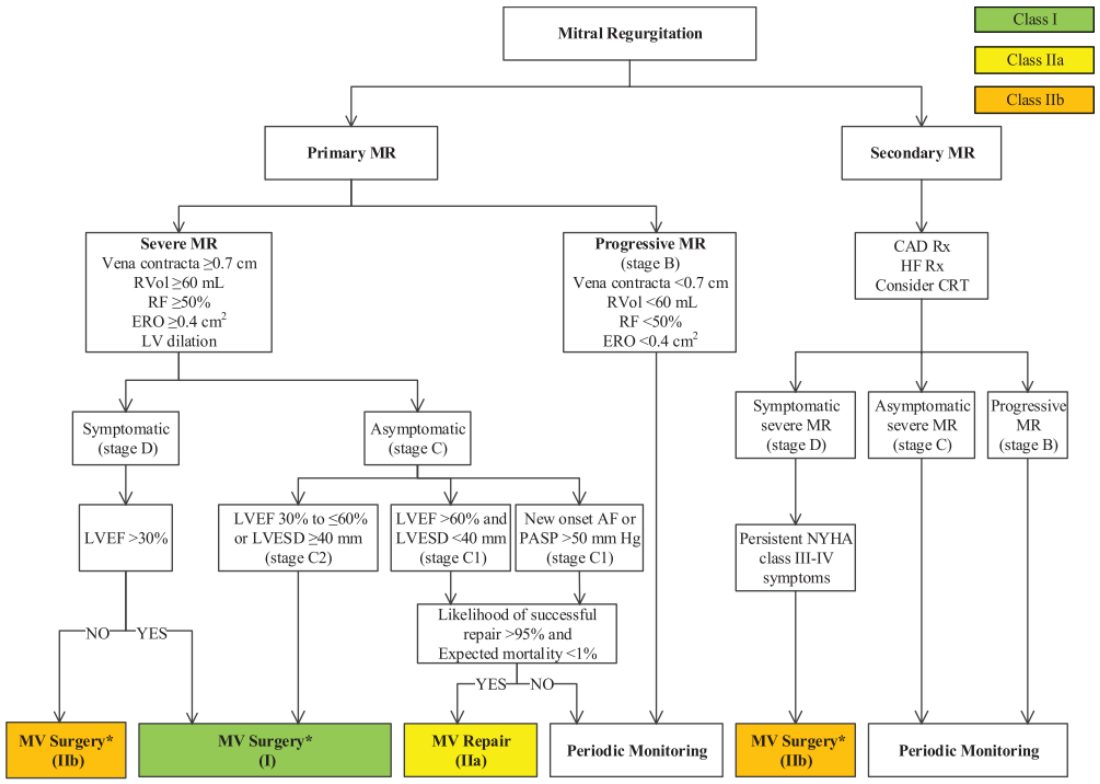

Figure 4. Indications for Surgery for MR. *Mitral valve repair is preferred over MVR when possible. AF indicates atrial fibrillation; CAD, coronary artery disease; CRT, cardiac resynchronization therapy; ERO, effective regurgitant orifice; HF, heart failure; LV, left ventricular; LVEF, left ventricular ejection fraction; LVESD, left ventricular end-systolic dimension; MR, mitral regurgitation, MV, mitral valve; MVR, mitral valve replacement; NYHA, New York Heart Association; PASP, pulmonary artery systolic pressure; RF, regurgitant fraction; RVol, regurgitant volume; and Rx, therapy.

Figure 1.8 – Indication for Surgery for MR [27]

during systole. Several methods can be used to quantify the EROA, the RV and the RF. The main one is referred to as the Proximal Isovelocity Surface Area (PISA) method [33].

Some context on Color Doppler echocardiography

To describe the PISA technique, some additional detail on Color Doppler (CD) imaging are provided first. Color Doppler imaging refers to a specific image acquisition technique that uses ultrasound waves to produce an image on which a gray-scale image of the solid tissue and a color-coded image of fluid velocities are superimposed.

The tissue is imaged using standard B-mode acquisition, consisting of sending beams of ultrasonic signals and recording to the echoes. By sweeping the beam lines across the domain, an image of the internal tissue can be reconstructed. On the other hand, a velocity color-coded image is created leveraging the Doppler effect. Short ultrasonic pulses of a specific frequency are sent. When a pulse gets reflected by a red blood cell, the frequency of the echo is shifted: if the blood cell is moving towards the probe, the received frequency is increased, while it is decreased if the pulse is reflected by a red blood cell moving away from the probe. As the frequency shift is proportional to the velocity component which is aligned with the ultrasound beam, a velocity

value can be associated with a frequency shift. By sending several pulses and sweeping the scan lines across the domain, an image of the blood velocity can be obtained. Color doppler images are obtained by superimposing the B-mode image and the color-coded velocity image [34, 35].

There are several limitations associated with echography and more specifically Color Doppler images. Among those, it must be noted that a single representative number is assigned to each pixel of the image while the actual data recorded by the probes contains a range of different frequency shifts. Additionally, as the sweeping of the scan lines can take a certain amount of time, it might be the case that the B-mode image and that the velocity fields are not acquired exactly at the same time [34].

Moreover, Color Doppler is not an exact representation of the fluid velocity: this imaging technique can only represent the velocity component which is aligned with the ultrasonic beam. This results in a partial signal misrepresenting the actual velocity field and clinical guidelines therefore recommend being careful with respect to the probe location in order to alleviate this limitation [34].

Finally, if the fluid velocity is very high, the frequency shift of the emitted signal might be greater than the Nyquist frequency of the probe. As a result, the signal gets aliased and the velocity estimation *wraps around*, meaning that the blood flow is depicted as if it was in the opposite direction [34].

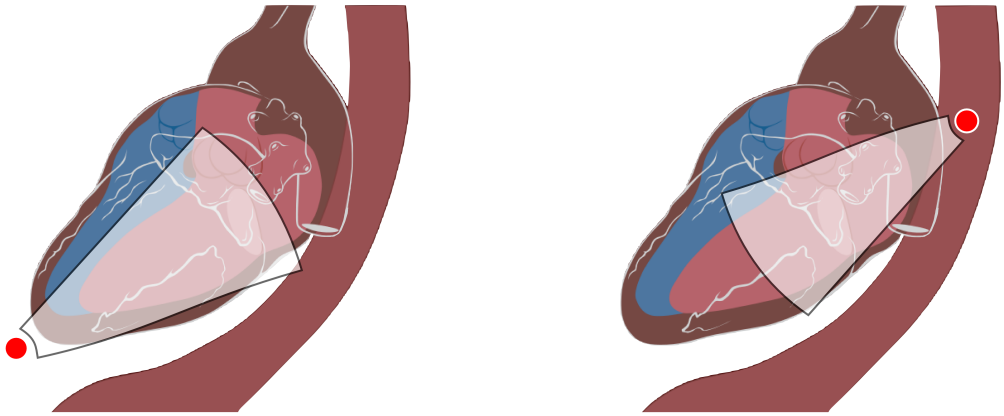

(a) (b)

Figure 1.9 – Schematic representation of probe positioning and field of view for (a) TTE and (b) TEE. The blue region represents the right heart while the red region the left heart. The probe is depicted by the red dot and the field of view is represented by the grayed area. The apex of the LV is located at the bottom left of the image.

In order to image the heart, and more specifically the flow around the mitral valve, two different techniques can be used. The most common technique is the trans-thoracic echocardiography (TTE), where the probe placed on the thorax of the patient and oriented properly to image the heart cavities (Figure 1.9a). In particular, the apical 3-Chamber view gives a very good representation of the flow field as it images the LA, the LV and the aorta with both MV and aortic valve (AV) visible.

On the other hand, the transesophageal echocardiography (TEE) is a more invasive procedure

as specifically designed probe, smaller than the TTE probe, is inserted down the throat and into the esophagus (Figure 1.9b). While it is a more invasive procedure, it also allows to get a better image resolution. In this case, the cavities are seen from the LA as opposed to apical TTE.

Both TTE and TEE can produce 2D, 2D+t, 3D and 3D+t Color Doppler sequences with reasonable spatio-temporal resolution. Probe position and variability in heart size and shape also result in tissue image that might not be complete, with sections of the heart outside of the imaging domain.

The PISA technique

The PISA technique is now detailed. As mentioned previously, this technique aims to quantify the EROA and can further be used to compute RV and RF. This technique is based on the conservation of mass and the continuity equation in hydrodynamics. Under several assumptions described below, the flow isovelocities form hemispheric concentric shells of increasing velocity and decreasing area converging to the orifice. Figure 1.10a depicts a schematic representation while Figure 1.10b shows an actual Color Doppler image of the flow convergence region.

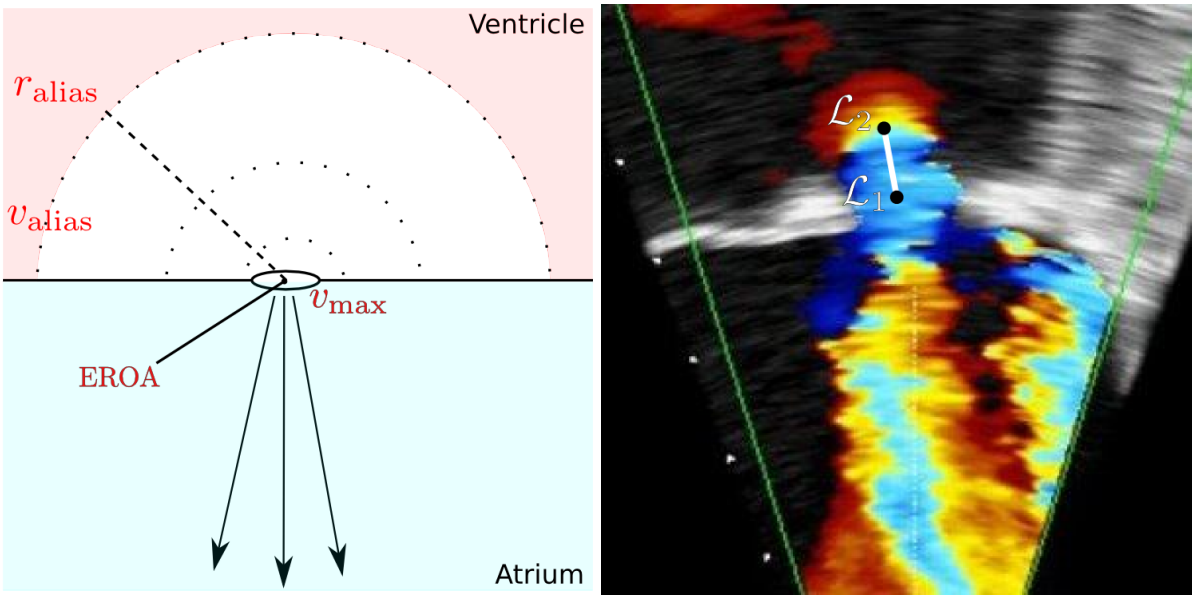

(a) (b)

Figure 1.10 – Flow convergence region depicting the hemispheric isovelocity shells caused by a circular hole in the MV: (a) Schematic representation and (b) in-vivo TTE Color-Doppler image.

The considered assumptions of the PISA method are:

- The orifice is small compared to its surroundings
- The orifice shape is circular
- The orifice lies on a planar surface
- The fluid is inviscid

As the blood is incompressible, the PISA technique relies on the fact that the blood flow rate passing through the hemispheric shells is equal to the blood flow rate passing through the MV. By knowing the surface area of an isovelocity hemispheric shell, its associated velocity and the velocity at the regurgitation level, one can easily compute the area at the MV level by cross multiplication.

Now that the basic principle is known, the full procedure is described in more detail. Using Color Doppler echocardiography, the physician choses a frame during systole in which the MR is visible and fully developed. He selects a first landmark $\mathcal{L}_1$ at the MR center and then chooses an aliasing velocity, denoted v_{alias}, usually ranging from 20 to 60 cm/s [21, 29, 36, 37]. Under the PISA assumptions, blood is converging towards the regurgitation and the isovalues of this aliasing velocity are hemispherically distributed around the MR center in the convergence region. The physician chooses a second landmark $\mathcal{L}_2$ located on this isovelocity surface and the distance r_{alias} between the two selected landmarks is computed (see Figure 1.10b for an example of where $\mathcal{L}_1$ and $\mathcal{L}_2$ are located on an actual Color Doppler image). The physician computes the area of an hemisphere of radius r_{alias} and multiplies it with the velocity v_{alias} to obtain the flow rate at the isovelocity surface level. By dividing this flow rate by the maximal velocity of the regurgitation v_{max}, the physician obtains the EROA:

$$\text{EROA} = \frac{2\pi \cdot \mathrm{r}_{\text{alias}}^2 \cdot \mathrm{v}_{\text{alias}}}{\mathrm{v}_{\text{max}}}. \tag{1.1}$$

Using the velocity time integral (VTI), the integral of the velocity magnitude at the valve level with respect to time during the MR, the total regurgitant volume can also be estimated:

$$R_{\text{vol,PISA}} = \text{VTI} \cdot \text{EROA} = \text{VTI} \cdot \frac{2\pi \cdot \mathrm{r}_{\text{alias}}^2 \cdot \mathrm{v}_{\text{alias}}}{\mathrm{v}_{\text{max}}}. \tag{1.2}$$

Even though the PISA method is widely used, it suffers from an important number of limitations [38, 30, 29]. First, echocardiography is an imaging technique that is highly physician-dependent. The way the ultrasound (US) probe is placed, and the way the US probe is oriented can highly affect the results. In the Color-Doppler case, for example, it is only possible to record velocities along the US beams. Therefore, if the blood is flowing orthogonally with respect to the beam, the recorded velocity will be zero. To alleviate this limitation, guidelines states that the US probe should be placed in alignment with the MR jet [31]. The PISA technique also relies on the physician to select landmarks and that operator choice might lead to additional error. For example, an error of 1 mm when the true PISA radius is 1 cm leads to approximately 20 % error in the measurement as pointed out by P.A. Grayburn [29].

Another limitation is related to the constant motion of the heart muscle and valves. While the mitral orifice is dynamic, the traditional PISA method is typically a single frame measurement that is known to potentially overestimate MR severity in mitral prolapse with only late systolic MR [29, 31].

Finally, the traditional PISA technique also suffers from several drawbacks due to chosen simplifying assumptions: The mitral valve is not really planar, and the hole in the mitral valve depends on the patient pathology, on the dynamic of the valve and other factors. Multiple regurgitation can also occur at the same time on a given valve, leading to several jets and complex isovelocity surfaces [21, 29, 31].

1.2 Motivations and objectives

Modern echocardiography allows to visualize cardiac structures and blood flow in three dimensions and in real-time. In particular, 3D transoesophagial probes allow to visualize in detail the morphology of the heart valves and the blood flowing through them. 3D transthoracic probes allow for bigger field of view acquisitions of the heart allowing the simultaneous acquisition of the four cardiac cavities from which morphology and dynamics can be extracted.

As 3D echocardiography is richer in information than traditional 2D ultrasound sequences, it is believed that analysis of the 3D blood flow could help to better assess mitral regurgitation by overcoming some of the 2D PISA limitations. Several novel 3D methods have therefore been proposed [39, 37, 40, 41, 42, 43, 44]. Nevertheless, several limitations are still associated with those techniques including computational complexity [41, 43], difficulty to handle eccentric MR [37, 44] or trouble to account for the Doppler signal limitations [42, 40, 44]. Some methods have been proposed to quantify RV using CMR [45, 46, 47, 48]. However, while using CMR images has been reported to be slightly more reproducible than the PISA method [46], acquiring CMR images is much more cumbersome than an echocardiography exam.

Based on those observations, we propose to combine numerical simulations with ultrasound imaging techniques in order to improve the current MR quantification tools. We also propose to keep in mind the constraints associated with the clinical setting, in particular by carefully balancing the accuracy of the models with the computational costs. The following objectives are therefore considered:

A. Develop physiological simulations of the heart hemodynamics starting from [49], including the following objectives:
    1. Improve the geometrical aspects of the model in the context of MR modeling (*e.g.,* include the left atrium and improve the mitral valve geometry.)
    2. Propose an improvement of the current model to allow the simulation of mitral regurgitation.
    3. Derive a methodology to include US image data into the model, in particular cardiac motion and/or hemodynamic boundary conditions (BC).

B. In order to propose a better MR quantification:
    1. Evaluate the current quantification tools and propose new hemodynamic features to quantify MR.
    2. Develop a simplified mathematical model of the blood flow, based on US images and biophysical principles, which accounts for the constraints of the clinical setting.
    3. Evaluate the simplified model with respect to the complex 3D model and other potentially available data.

C. Improve current understanding of cardiac hemodynamics

1.3 Thesis organization and contributions

In order to achieve the aforementioned objectives, the research work was separated in the two parts that compose this manuscript.

Following an introductory chapter aimed at describing the global context with regard to modeling of the intracardiac hemodynamics and to the modeling of healthy and pathological mitral valves, Chapter 2 describes a mathematical model of the cardiac hemodynamics. A novel model of the mitral regurgitation is also introduced. Numerical examples are conducted in order to assess the benefits and limitations of the chosen approach. As the modeling choices prevent the proper modeling of isovolumetric phases, a common issue in the cardiac modeling community, we present in Chapter 3 an improvement of the valve model which allows the modeling of the isovolumetric phases given an external intraventricular pressure curve.

The objective of Part II is to use the tools presented in Part I in combination with ultrasound images in order to improve the MR severity quantification methods. The additional challenges which arise from the personalization of numerical simulations with medical images are introduced in the introductory chapter. In particular, we highlight the fact that the data pre-processing is still time-consuming and that the potential misrepresentation of the reality can be introduced due to imaging limitations. The need for simplified models is also highlighted. In Chapter 4, we present a novel fully automatic pipeline which uses real-time 3D echocardiography (RT3DE) images to personalize numerical simulations with a specific focus on reducing the amount of pre-processing time. This pipeline is applied on a database of RT3DE images to produce a database of healthy and pathological cases. By investigating the hemodynamics of the pathological simulations, the PISA methods is evaluated to highlight its potential limitations. In Chapter 5, we investigate how a misrepresentation of the LV wall torsion in the ultrasound images might affect the intracardiac hemodynamics. Finally, we describe, in Chapter 6, an algorithm which aims at reconstructing 2D intracardiac velocity field based on CD images. This 2D optimization problem – similar to a pre-existing work – is applied to the specific case of MR and generalized to the 3D case. The database generated in Chapter 4 is used as ground truth to quantify the reconstruction potential of the method, and in particular to assess how the reconstruction of pathological blood flow could be beneficial for MR severity quantification.

Chapter 7 finally concludes this manuscript by summarizing the main results and by presenting some general perspectives with respect to the presented work.

1.4 List of publications and oral presentations

First author publications

(Submitted): A. This, L. Boilevin-Kayl, M. A. Fernández, and J.-F. Gerbeau, "Augmented Resistive Immersed Surfaces valve model for the simulation of cardiac hemodynamics with isovolumetric phases." 2018

(In preparation): A. This, H. G. Morales, O. Bonnefous, M. A. Fernández, and J.-F. Gerbeau, "Synthetic Mitral Valve Regurgitation modeling using 3D echocardiography : Assessment of the PISA technique."

Conference proceedings

A. This, L. Boilevin-Kayl, H. G. Morales, O. Bonnefous, P. Allain, M. A. Fernández, and J.-F. Gerbeau, "One Mesh to Rule Them All: Registration-Based Personalized Cardiac Flow Simulations," in *International Conference on Functional Imaging and Modeling of the Heart*, pp. 441–449, Springer, Cham, 2017

A. This, H. G. Morales, and O. Bonnefous, "PROXIMAL ISOVELOCITY SURFACE FOR DIFFERENT MITRAL VALVE HOLE GEOMETRIES," in *Proceedings of the VII European Congress on Computational Methods in Applied Sciences and Engineering (ECCOMAS Congress 2016)*, vol. 94, (Athens), pp. 155–163, Institute of Structural Analysis and Antiseismic Research School of Civil Engineering National Technical University of Athens (NTUA) Greece, 2016

Coauthored conference proceedings

L. Boilevin-Kayl, A. This, M. A. Fernández, and J.-f. Gerbeau, "An efficient valve model based on resistive immersed surfaces enhanced with physiological data," in *5th International Conference on Computational & Mathematical Biomedical Engineering*, 2017

È. Lluch, R. Doste, S. Giffard-Roisin, A. This, M. Sermesant, O. Camara, M. De Craene, and H. Morales, "Smoothed particle hydrodynamics for electrophysiological modeling: An alternative to finite element methods," in *International Conference on Functional Imaging and Modeling of the Heart*, pp. 333–343, 2017

Seminar and workshops

- Oral presentation at the 8^{th} "World Congress of Biomechanics" (WCB), July 8-12 2018, Dublin, Ireland
- Oral presentation in the "Mathematical and Numerical Modeling of the Cardiovascular System" workshop, April 16-19 2018, Istituto Nazionale di Alta Matematica (INdAM), Roma, Italy
- Oral presentation at the Living Heart Project (LHP) annual meeting, April 4-5 2018, Dassault, Velizy, France
- Poster presentation at the 9^{th} international conference on "Functional Imaging and Modeling of the Heart" (FIMH), June 11-13 2017, Toronto, Canada
- Oral presentation at the 7^{th} European Congress on Computational Modelign in Applied Sciences and Engineering (ECCOMAS), June 5-10 2016, Crete, Greece

Part I

Mathematical modeling of the heart hemodynamics in healthy and pathological situations

Introduction

In this short introduction, we present the global context in which the modeling work presented in Part I fits. We first present the modeling difficulties which arise from modeling a complex system of coupled physical phenomena. To satisfy the specific constraints of the industrial and clinical environments, we propose to consider some model simplifications. In a second step, we briefly recall the state of the art of the modeling of healthy and pathological mitral valve (MV). We finally describe the different chapters that compose Part I.

Multiphysics modeling

In this manuscript, the task of modeling the cardiac hemodynamics is considered. As this system depends of several identified biochemical and biophysical phenomena, it is proposed to first describe roughly the chain of events which leads to a single heart contraction.

Known as the heart's natural pacemaker, the sino-atrial node periodically triggers the propagation of an electrical wave across the heart. This electrical wave is propagated both through the His bundle and by ionic exchanges at the membrane level of myocites. Due to a depolarization of the myocites, intracellular calcium ions are released; this triggers chemical reactions that generate mechanical forces within the sarcomeres (the basic contractile units of the cardiac muscle cells). Calcium ions are therefore the coupling units between the electrical and mechanical component of the heart. The resulting muscle stress is transmitted through the endocardium to the enclosed fluid allowing the blood to flow through the cavities and the heart valves to open and close in a careful sequence [56, 57].

Modeling all the phenomena involved in the intracardiac hemodynamics therefore requires expertise of various different fields. Moreover, modeling those sub-systems with the most state-of-the art description of the observed phenomena might result in very complex models. Industrial and clinical environments, however, imposes some constraints with respect to complexity of the models. To satisfy those constraints, we propose to consider some model simplifications.

For example, instead of modeling the fluid-structure interactions (FSI) between the solid surfaces and the enclosed fluid, several models have been proposed in the literature to reduce the difficulties arising from the coupling of those different physical problems [49, 58, 59, 60]. The fundamental idea consists in uncoupling the kinematics of the cardiac hemodynamics and electromechanics (*i.e.* displacement fields, coming either from measurements or from simulations, are imposed on the boundaries of the fluid cavities). These simplifications come, however, at a price: since the kinematic uncoupling ignores the dynamic balance between cardiac hemodynamics and electromechanics, the fluid pressure within the ventricle is not well defined during the isovolumetric phases (*i.e.* when all the valves are closed). This explains why this portion of the cardiac cycle is always neglected in the above-mentioned uncoupled approaches. Though short-lasting, the isovolumetric phases play a major role in the preservation of a correct unidi-

rectional blood flow within the heart. A recent review of the status of cardiac hemodynamics modeling can be found in [61].

Another example relates to the modeling of the blood outside of the cardiac chambers. Instead of considering a 3D representation of the full vasculature system, 0D models (*i.e.* models without spatial dependency) have been derived, such as the Windkessel model for example, to provide somewhat realistic boundary conditions [62, 63, 49]. This choice allows to circumvent the need of complex 3D simulations of fluid flows in locations that are not the primary focus of the studies. A thorough review of the lumped parameter models applied in a cardiovascular setting was presented by Shi et al. [64].

Healthy and pathological valve modeling

The modeling of cardiac valves is one of the main bottleneck of the intracardiac hemodynamics modeling. Indeed, the cardiac valves are thin structures immersed in the fluid which exhibit important deformation during the cardiac cycle [26]. We propose a short review of the models of cardiac valves both in an healthy and a pathological point of view.

Complex simulations have been performed to study the FSI between the blood and the heart valves. Su et al. [65] modeled the FSI of the blood inside the left ventricle with mechanical valves. This model allowed to study LV hemodynamics under valve gradual opening and closure and to observe the regurgitation which physiologically happens in healthy individuals during the closure of the valve. Recently, FSI models which included the LV mechanics, the MV mechanics as well as the fluid inside the LV have also been presented [66]. As modeling the FSI of realistic valves inside a physiological heart is complex, FSI simulations of physiological mitral valve, including chordae, were also be performed in reduced 3D domains localized around the valve [67, 68]. In those models, MR was obtained by altering the physical parameters of the valve and the chordae. A review of the literature discussing the history of FSI models in the context of heart valves can be found in Einstein et al. [69].

In order to limit the complexity of models including heart valve, numerical simulations of the blood flow in reduced geometrical domain have been proposed. As early as 1992, this technique was used to evaluate the PISA model assumption in a 2D configuration with a geometrical domain localized around a fixed mitral valve [70]. This technique has also been used to study alternative MR quantification methods, either in 2D [42] or in 3D [43].

In [39, 71, 53, 72], 3D CFD models with idealized LV geometries have been designed. In these models, mitral valve regurgitation was modeled as a tiny channel linking two fluid chambers. While the models were involving unrealistic geometries, relevant knowledge about MR could be acquired.

Lumped parameter models have also been proposed to model healthy and pathological mitral valves. C. Philips [73] proposed a fully lumped parameter model of the cardiovascular system in which an ideal diode model was used as a surrogate of the healthy mitral behavior. MR was introduced by modifying this ideal diode model to allow some backflow. Lassila et al. [74] coupled a similar lumped parameter model with a 3D CFD model of the left ventricle. The coupled MV lumped model was used as a boundary condition at the inlet of the LV. Using a porous model formulation, Astorino et al. [49] modeled the valve as a thin immersed surface

embedded in the fluid domain. Using a lumped model to control opening and closing the valve, the immersed surface allowed to model the valve as an integral part of the 3D CFD model in a simple manner. This work has further been extended to incorporate valve dynamics [75].

To date, there is no simplified model combining mitral regurgitation with 3D representation of the mitral valve including valve opening and closing.

Structure of Part I

The objective of the Part I is to describe a 3D mathematical model of the cardiac hemodynamics with a specific focus on modeling MR. We now describe its organization and provide a short summary of the different chapters.

In Chapter 2, a 3D model of the blood flow inside the left heart is presented. The geometry of the fluid domain is extracted from a detailed human heart geometry and manually processed to obtain a geometric domain fitted for numerical simulation. Based on the Arbitrary Lagrangian-Eulerian method, a 3D model of the blood flow in a moving domain is detailed. The heart valves are included by considering a simplified model based on a porous media analogy. Finally, this model is supplemented with initial and boundary conditions. Using prescribed LV wall displacements originating from an electro-mechanical simulation, the model is used to simulate the cardiac hemodynamics allowing for a detailed description of the blood flow structures. By slightly modifying the simplified valve model, a mitral regurgitation model is proposed and a numerical experiment is conducted to illustrate its capability.

It will be shown that the model proposed in Chapter 2 provides realistic cardiac hemodynamics. However, a proper description of the isovolumetric phases cannot be obtained, partly due to the choice of not modeling the complete FSI of the fluid with the surrounding tissues. As this issue is quite common with *one-way* coupling [76, 77, 78, 79], a new approach is proposed in Chapter 3 to tackle this difficulty. Starting from the initial valve model, an analysis of the intraventricular pressure is provided to highlight the model flaws with respect to the isovolumetric phases. Based on this analysis, an extension to the valve model, enhanced with an external reference data is proposed. Two numerical examples – a toy problem and a realistic physiological heart – are presented to test this new formulation and assess its benefits and limitations.

The generation of a reliable generic mathematical model of cardiac hemodynamics allows to elaborate personalized models using image data. The generation and study of those personalized models will be covered in Part II

Chapter 2
Mathematical modeling of the left heart hemodynamics

In this chapter, a mathematical model of the left heart hemodynamics is described. In Section 2.1, the considered geometrical domain including the left ventricle, the left atrium, a portion of the aorta and immersed valves is detailed. Section 2.2 describes the numerical methods and discretization options used to approximate the intracardiac hemodynamics. In Section 2.3, a numerical experiment was conducted to illustrate the performances of the proposed approach. The intracardiac hemodynamics resulting of the numerical simulation are described and compared to the usual physiological description allowing to discuss the advantages and disadvantages of the proposed model. Finally, Section 2.4 describes a slight modification of the mitral valve model, associated with a region marking strategy, which allows the modeling of mitral regurgitation. A numerical example illustrates the modeling of the blood flow in a heart exhibiting a severe Type 1 mitral regurgitation.

2.1 Geometrical description

The computational domain has been created based on the *Zygote 3D Human Heart Model*[1]. This heart geometrical model was developed using computed tomography and magnetic resonance imaging of a healthy, middle-aged, Caucasian male. Manual segmentation and post-processing were performed by *Zygote Media Group, Inc* to clean the surfaces, remove artifacts and produce the heart model shown on Figure 2.1 [80]. We modified this initial geometry to fit our simulation requirements (*e.g.,* the fact that we only want to model the blood in the left heart cavities). Those modifications are therefore detailed in the rest of this section.

2.1.1 Fluid domain

From the *Zygote 3D Human Heart Model*, the inner layer of cardiac tissue, the layer in contact with blood, was extracted. The two right cavities were discarded and the left ventricle and left atrium inner surfaces were used as a basis of the proposed realistic heart model. As the *Zygote 3D Human Heart Model* did not include atrial septum, manual edition of the surface mesh, using the software *Materialise 3-Matic V11.0*[2] , was necessary. Surface smoothing was performed to ensure that the surface was free of artifacts. A portion of the ascending aorta was also included in the fluid domain in order to model a short section of blood after the aortic valve location. The resulting fluid domain is shown on Figure 2.2a.

[1] Zygote Media Group, Inc. (UT, USA), https://www.zygote.com/cad-models (last accessed 03 Dec 2018)
[2] https://www.materialise.com/fr/software/3-matic (last accessed 03 Dec 2018)

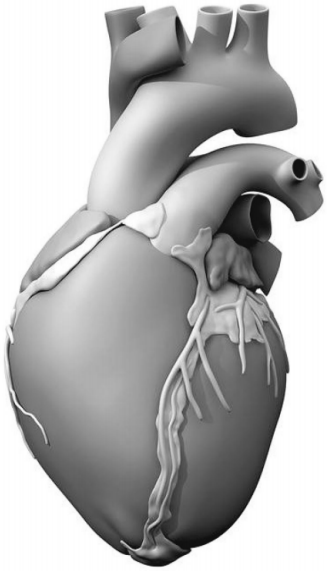

Figure 2.1 – Zygote 3D Human Heart Model [80].

2.1.2 Valve geometry

The mathematical model of the valve, which will be described in Section 2.2.2, requires inclusion of the valve geometrical surfaces in open and/or closed configuration. The mitral valve was designed, both in open and closed configuration, using the computer aided design (CAD) software *SALOME V7.7.1*[3]. Table A.1 (Appendix A) reports all the dimensions used and the associated references. Figure A.1 (Appendix A), shows the resulting mitral valve surface in open configuration. On the other hand, the closed aortic valve could be taken directly from the *Zygote 3D Human Heart Model* and the aortic valve in open-configuration was not included. The valves were inserted in the full geometrical domain, as represented on Figure 2.2b.

2.1.3 Full simulation domain

The surface was cleaned and meshed using *Materialise 3-Matic V11.0*[4] and *Gmsh*[5] and a volumetric mesh was then generated using *Ghs3D V3.0*[6] and *Mmg3D V5.1.4*[7] (Figure 2.2c).

[3] `https://www.salome-platform.org/` (last accessed 03 Dec 2018)
[4] `https://www.materialise.com/fr/software/3-matic` (last accessed 03 Dec 2018)
[5] `http://gmsh.info/` (last accessed 03 Dec 2018)
[6] `https://team.inria.fr/gamma3/gamma-software/ghs3d/` (last accessed 03 Dec 2018)
[7] `https://www.mmgtools.org/` (last accessed 03 Dec 2018)

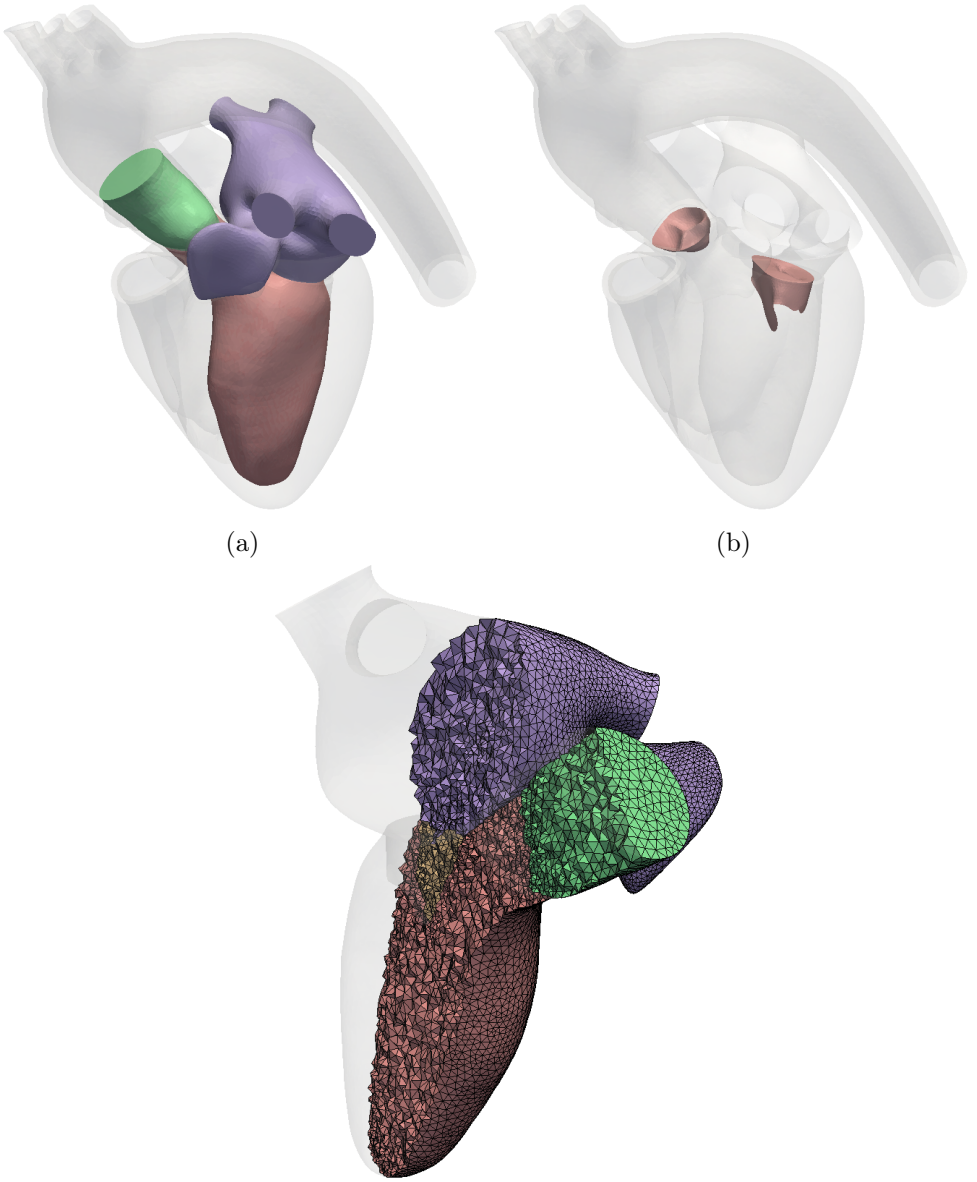

(a) (b)

(c)

Figure 2.2 – Geometrical domain: (a) Fluid domain (b) Immersed valve surfaces (c) Resulting tetrahedral mesh.

2.2 Numerical methods

In this section, we now describe the numerical methods and discretization choices used to model the intracardiac hemodynamics in a moving domain which includes cardiac valves.

Consider the domain $\Omega \subset \mathbb{R}^3$ in which the fluid is described. The solid layer of tissue surrounding the fluid is denoted by $\partial\Omega_s$. This boundary can be decomposed into the atrium endocardium

$\partial\Omega_{\text{s,at}}$, the ventricular endocardium $\partial\Omega_{\text{s,v}}$, and the aorta walls $\partial\Omega_{\text{s,ao}}$: $\partial\Omega_{\text{s}} = \partial\Omega_{\text{s,at}} \cup \partial\Omega_{\text{s,v}} \cup \partial\Omega_{\text{s,ao}}$. The valve surfaces are denoted by $\Sigma_{\text{ao,c}}$ (aortic valve in closed configuration), $\Sigma_{\text{mv,o}}$ (mitral valve in open configuration) and $\Sigma_{\text{mv,c}}$ (mitral valve in closed configuration). The fluid inlets, cross-section of the four pulmonary veins, are denoted $\partial\Omega_{\text{pv}}$. Finally, the fluid outlet, cross-section of the aorta, is denoted $\partial\Omega_{\text{ao}}$.

2.2.1 Basic governing equations

Blood is composed of different constituents: plasma ($\approx 54\,\%$), red blood cells ($\approx 45\,\%$) and white blood cells ($\approx 1\,\%$). This composite material exhibits non-Newtonian behavior [81]. Nevertheless, in large vessels and cavities, it is reported that it is a reasonable assumption to model blood as a homogeneous, incompressible, single-phase Newtonian fluid [82, 83, 84]. Such fluid can be modeled by the Navier-Stokes (N-S) equations.

The fluid is described by its velocity $\boldsymbol{u}$ and its pressure p. The Cauchy stress tensor $\boldsymbol{\sigma}(\boldsymbol{u},p) = -p\boldsymbol{I} + 2\mu\varepsilon(\boldsymbol{u})$ is defined to characterize the modeled fluid. In this Cauchy stress tensor, μ is the fluid viscosity, $\boldsymbol{I}$ is the identity tensor and $\varepsilon(\boldsymbol{u}) = \frac{1}{2}\left(\boldsymbol{\nabla u} + \boldsymbol{\nabla u}^T\right)$ is the symmetric strain rate tensor. Modeling the blood amounts to solving the incompressible N-S equations:

Fluid problem in the Eulerian formulation

Find the velocity $\boldsymbol{u} : \Omega \times \mathbb{R}^+ \to \mathbb{R}^3$ and the pressure $p : \Omega \times \mathbb{R}^+ \to \mathbb{R}$ such that, under a certain set of initial and boundary conditions:

$$\rho\left(\frac{\partial \boldsymbol{u}}{\partial t} + \boldsymbol{u}\cdot\boldsymbol{\nabla u}\right) - \boldsymbol{\nabla}\cdot\boldsymbol{\sigma}(\boldsymbol{u},p) = \boldsymbol{f} \quad \text{in} \quad \Omega \tag{2.1}$$

$$\boldsymbol{\nabla}\cdot\boldsymbol{u} = 0 \quad \text{in} \quad \Omega \tag{2.2}$$

The description of motion, in continuum mechanics, can be categorized into two families. The Eulerian description, where the observers (*i.e.* the computational nodes) are fixed and *watch* the fluid flowing around, and the Lagrangian description, where the observers *follow* individual parcel of fluid. Problem (2.1)-(2.2) is written in the Eulerian setting. While the Eulerian description is the most classical choice when modeling fluid dynamics in fixed geometries, difficulties can arise when deformations of the domain occur.

To alleviate those difficulties, the ALE formulation was developed in attempt to combine the advantages of both Eulerian and Lagrangian descriptions [85]. In the ALE description of motion, the observer is chosen to *move arbitrarily while watching* the flow around it. Unlike unfitted mesh methods, the ALE formulation relies on the use of a fitting discretization at the interface between the solid and the fluid. This facilitates the imposition of boundary conditions. Moreover, the ALE method also facilitates the time-discretization of the model in the case of a moving domain.

In the ALE formulation, an arbitrary mapping $\mathcal{A}$ is defined to map the *reference* domain Ω into the *current* spatial domain $\Omega(t)$ at each time instant.

$$\begin{aligned} \mathcal{A} : \Omega \times \mathbb{R}^+ &\to \Omega(t) \\ (\boldsymbol{\chi},t) &\to \boldsymbol{x} \end{aligned}$$

Defining $\boldsymbol{w}$ as the fluid domain velocity, the ALE time derivative of a given scalar or tensorial field f is expressed as:

$$\left.\frac{\partial f}{\partial t}\right|_{\mathcal{A}} = \frac{\partial f}{\partial t} + \boldsymbol{w} \cdot \boldsymbol{\nabla} f \tag{2.3}$$

By applying 2.3 on the fluid velocity, one obtains:

$$\frac{\partial \boldsymbol{u}}{\partial t} = \left.\frac{\partial \boldsymbol{u}}{\partial t}\right|_{\mathcal{A}} - \boldsymbol{w} \cdot \boldsymbol{\nabla} \boldsymbol{u} \tag{2.4}$$

Provided a boundary displacement $\boldsymbol{d}(\boldsymbol{x},t)$ on $\Gamma \subset \partial\Omega_{\mathrm{s}}$, one can recast problem (2.1)-(2.2) using 2.4 to obtain problem:

Fluid problem in the ALE formulation

Find $\boldsymbol{w} : \Omega \times \mathbb{R}^+ \to \mathbb{R}^3$ such that, given an arbitrary chosen lifting operator $\mathcal{L}$, a boundary displacement $\boldsymbol{d}(\boldsymbol{x},t)$ on $\Gamma \subset \partial\Omega_{\mathrm{s}}$ and some possible additional boundary conditions:

$$\begin{cases} \boldsymbol{d} = \mathcal{L}\left(\boldsymbol{d}|_{\Gamma \subset \partial\Omega_{\mathrm{s}}}\right) \\ \boldsymbol{w} = \dfrac{\partial \boldsymbol{d}}{\partial t} \end{cases} \quad \text{in} \quad \Omega \tag{2.5}$$

Find the velocity $\boldsymbol{u} : \Omega \times \mathbb{R}^+ \to \mathbb{R}^3$ and the pressure $p : \Omega \times \mathbb{R}^+ \to \mathbb{R}$ such that, under a certain set of initial and boundary conditions:

$$\rho\left(\left.\frac{\partial \boldsymbol{u}}{\partial t}\right|_{\mathcal{A}} + (\boldsymbol{u} - \boldsymbol{w}) \cdot \boldsymbol{\nabla} \boldsymbol{u}\right) - \boldsymbol{\nabla} \cdot \boldsymbol{\sigma}(\boldsymbol{u},p) = \boldsymbol{f} \quad \text{in} \quad \Omega(t) \tag{2.6}$$

$$\boldsymbol{\nabla} \cdot \boldsymbol{u} = 0 \quad \text{in} \quad \Omega(t) \tag{2.7}$$

In problem (2.5)-(2.7), the lifting operator $\mathcal{L}$ can be chosen arbitrarily. One of the main difficulties of the ALE method is to handle very large deformation of the domain. In that regard, we use the strategy described by Landajuela et al. [86]: the lifted displacements are computed by solving a linear elasticity problem incrementally to enhance the robustness with respect to large deformations. Additionally, the Lamé parameters are defined element-wise in such a way that small elements are stiffer than large elements [87].

Initial conditions: The fluid is considered initially at rest:

$$\boldsymbol{u}|_{t=0} = \boldsymbol{0} \quad \text{in} \quad \Omega(0). \tag{2.8}$$

Solid surfaces: As the fluid is viscous, it is assumed that the fluid has zero velocity relative to the solid boundary $\partial\Omega_{\mathrm{s}}$. This boundary condition is called the *no-slip* boundary condition:

$$\boldsymbol{u}|_{\partial\Omega_{\mathrm{s}}} = \boldsymbol{w} \quad \text{on} \quad \partial\Omega_{\mathrm{s}}(t). \tag{2.9}$$

Pulmonary veins inlet: A normal stress is applied at the inlet (Eq 2.10) to impose a constant static pressure P_{pv}:

$$\boldsymbol{\sigma}(\boldsymbol{u},p)\cdot\boldsymbol{n} = -P_{\text{pv}}\boldsymbol{n} \quad \text{on} \quad \partial\Omega_{\text{pv}}(t). \tag{2.10}$$

Aortic outlet: A normal stress was also applied at the outlet of the domain. As it was shown that proper choice of outlet boundary condition is critical to obtain realistic physiological behavior [63], a Windkessel RCR lumped parameter model was therefore chosen to represent the afterload of the heart related to the arterial system. The boundary conditions is therefore expressed by:

$$\boldsymbol{\sigma}(\boldsymbol{u},p)\cdot\boldsymbol{n} = -P_{\text{ao}}(t)\boldsymbol{n}, \quad \text{on } \partial\Omega_{\text{ao}}(t), \tag{2.11}$$

$$P_{\text{ao}}(t) + R_d C\frac{dP_{\text{ao}}(t)}{dt} = (R_p + R_d)\,Q(t) + R_p R_d C\frac{dQ(t)}{dt} + P_d + R_d C\frac{dP_d(t)}{dt}. \tag{2.12}$$

In (2.12), the proximal resistance R_p, distal resistance R_d, capacitance C and distal pressure $P_d(t)$ are parameters of the model that must be chosen appropriately.

A backflow stabilization based on a local regularization of the fluid velocity is applied at the aortic outlet [88], eventually modifying (2.11).

2.2.2 Valve model

The valves were modeled using the Resistive Immersed Surface (RIS) model originally proposed to model flow through a porous interface [89] and further extended to model the heart valves [49]. The RIS model consists of introducing dissipative surface terms in the N-S momentum equation at the leaflet locations. This model is chosen to allow a 3D representation of the heart valve while keeping the numerical complexity of the model reasonable compared to FSI. In Eq 2.13, δ_{Σ_i} is the Dirac measure on the immersed surface Σ_i and $R_{\Sigma_i}(t)$ is the associated resistance. In the limit $R_{\Sigma_i} \to \infty$, this model is equivalent to imposing no-slip boundary condition on the immersed surface. By including the RIS model into (2.6)-(2.7), the fluid model reads:

Fluid problem with RIS model

Find the velocity $\boldsymbol{u} : \Omega \times \mathbb{R}^+ \to \mathbb{R}^3$ and the pressure $p : \Omega \times \mathbb{R}^+ \to \mathbb{R}$ such that, under a certain set of IC and BC:

$$\rho\left(\left.\frac{\partial \boldsymbol{u}}{\partial t}\right|_{\mathcal{A}} + (\boldsymbol{u}-\boldsymbol{w})\cdot\boldsymbol{\nabla}\boldsymbol{u}\right) - \boldsymbol{\nabla}\cdot\boldsymbol{\sigma}(\boldsymbol{u},p) + \sum_i \delta_{\Sigma_i} R_{\Sigma_i}(t)\,(\boldsymbol{u}-\boldsymbol{w}) = \boldsymbol{f} \quad \text{in} \quad \Omega(t) \tag{2.13}$$

$$\boldsymbol{\nabla}\cdot\boldsymbol{u} = 0 \quad \text{in} \quad \Omega(t) \tag{2.14}$$

The evolution law of the closed-valve resistances $R_{\Sigma_{\text{i,c}}}$ is the same as the one proposed by Astorino et al. [49] and is based on physiological considerations (Figure 2.3). A valve opens ($R_{\Sigma_{\text{i,c}}} = 0$) when a positive pressure difference across the valve is computed. On the other hand, a valve is closed ($R_{\Sigma_{\text{i,c}}} = R_{\max}$) when backflow occurs ($Q < Q_{\text{backflow}}$). This evolution law is only computed on the valve closed configuration. The open configuration of the mitral valve is considered as the dual of its closed configuration (*i.e.* if $R_{\Sigma_{mv,c}} = 0$ then $R_{\Sigma_{mv,o}} \neq 0$, and if $R_{\Sigma_{mv,c}} \neq 0$ then $R_{\Sigma_{mv,o}} = 0$).

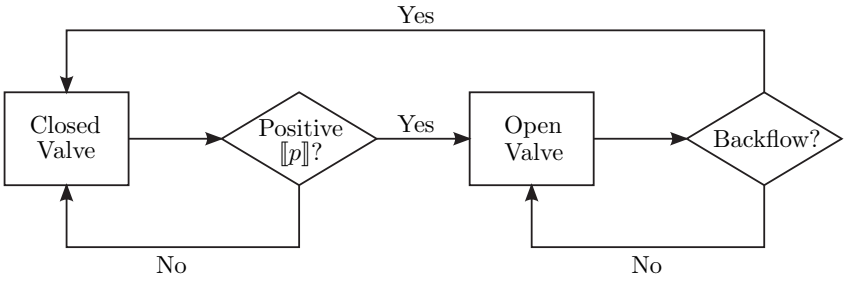

Figure 2.3 – Valve evolution law schematics

2.2.3 Time and space discretization

In what follows, we denote by τ the time-step length. The time discretization (2.13)-(2.14) is performed via a semi-implicit backward Euler scheme. As regards the discretization in space, a stabilized finite element method is considered. To this purpose, we consider a family of triangulations $\{\mathcal{T}_h\}_{0<h<1}$ of the reference fluid domain Ω which are fitted to the (reference) valve surfaces Σ_i. The discrete space for the velocity $\boldsymbol{V}_h \subset [H^1(\Omega)]^3$ is the standard Lagrange finite element space of continuous piece-wise affine functions. The pressure space $Q_h \subset L^2(\Omega)$ is also made of piece-wise affine functions which are globally continuous except across Σ_i. The resulting fully discrete method is detailed in (2.15).

Fully discrete approximation of (2.13)-(2.14)

Find $\left(\widehat{\boldsymbol{u}}_h^n, \widehat{p}_h^n\right) \in \boldsymbol{V}_h \times Q_h$ with $\widehat{\boldsymbol{u}}_h^n|_{\partial\Omega_s} = \boldsymbol{w}_h^n$, such that

$$\begin{aligned}\frac{\rho}{\tau}\left[\int_{\Omega^n} \boldsymbol{u}_h^n \cdot \boldsymbol{v}_h - \int_{\Omega^{n-1}} \boldsymbol{u}_h^{n-1} \cdot \boldsymbol{v}_h\right] + a^{\mathrm{f}}_{\Omega^n,h}\left(\boldsymbol{u}_h^{n-1} - \boldsymbol{w}_h^n; (\boldsymbol{u}_h^n, p_h^n), (\boldsymbol{v}_h, q_h)\right) \\ - \rho \int_{\Omega^n} (\boldsymbol{\nabla} \cdot \boldsymbol{w}_h^n) \boldsymbol{u}_h^n \cdot \boldsymbol{v}_h + \sum_i R^n_{\Sigma_i} \int_{\Sigma_i^n} (\boldsymbol{u}_h^n - \boldsymbol{w}_h^n) \cdot \boldsymbol{v}_h \\ = \int_{\Omega^n} \boldsymbol{f}^n \cdot \boldsymbol{v}_h - \int_{\partial\Omega^n_{\mathrm{pv}}} P^n_{\mathrm{pv}} \boldsymbol{n} \cdot \boldsymbol{v}_h - \int_{\partial\Omega^n_{\mathrm{ao}}} P^n_{\mathrm{ao}} \boldsymbol{n} \cdot \boldsymbol{v}_h \end{aligned} \tag{2.15}$$

for all $(\widehat{\boldsymbol{v}}_h, \widehat{q}_h) \in \boldsymbol{V}_h \times Q_h$ with $\widehat{\boldsymbol{v}}_h|_{\partial\Omega_s} = \boldsymbol{0}$.

In (2.15), we have considered the discrete Navier-Stokes tri-linear form

$$\begin{aligned} a^{\mathrm{f}}_{\Omega^n,h}\left(\boldsymbol{z}_h; (\boldsymbol{u}_h, p_h), (\boldsymbol{v}_h, q_h)\right) =& \rho \int_{\Omega^n} \boldsymbol{z}_h \cdot \boldsymbol{\nabla} \boldsymbol{u}_h \cdot \boldsymbol{v}_h + \frac{\rho}{2} \int_{\Omega^n} (\boldsymbol{\nabla} \cdot \boldsymbol{z}_h) \boldsymbol{u}_h \cdot \boldsymbol{v}_h \\ &+ \int_{\Omega^n} \boldsymbol{\sigma}(\boldsymbol{u}_h, p_h) : \boldsymbol{\nabla} \boldsymbol{v}_h + \int_{\Omega^n} q_h \boldsymbol{\nabla} \cdot \boldsymbol{u}_h \\ &+ \sum_{K \in \mathcal{T}_h^n} \int_K \delta_h \left(\rho \left(\boldsymbol{z}_h \cdot \boldsymbol{\nabla}\right) \boldsymbol{u}_h + \boldsymbol{\nabla} p_h\right) \cdot \left(\rho \left(\boldsymbol{z}_h \cdot \nabla\right) \boldsymbol{v}_h + \boldsymbol{\nabla} q_h\right), \end{aligned}$$

where the last term stands for the SUPG/PSPG stabilization (see, e.g., [90]).

Remark: In (2.15), the fluid integrals in the deformed configurations has to be evaluated by composition with the corresponding discrete ALE map. For example, for the the second term

we have

$$\int_{\Omega^n} \boldsymbol{u}_h^{n-1} \cdot \boldsymbol{v}_h = \int_{\Omega^n} \widehat{\boldsymbol{u}}_h^{n-1} \circ (\boldsymbol{\mathcal{A}}_h^n)^{-1} \cdot \widehat{\boldsymbol{v}}_h \circ (\boldsymbol{\mathcal{A}}_h^n)^{-1}.$$

2.2.4 Complete model

Combining the previously described elements, the complete numerical algorithm reads:

Complete model

For $n \geq 1$, let $\boldsymbol{d}^n$ on $\Gamma \subset \partial\Omega_\mathrm{s}$ and iterate over the following steps:

[1] Update the computational domain and compute the numerical domain velocity $\boldsymbol{w}^n$ using the discretized version of the problem (2.5)

[2] Given $\{\boldsymbol{u}^{n-1}, p^{n-1}\}$, compute the valves resistance values R_Σ^n using the valve evolution law.

[3] Given $\{\boldsymbol{u}^{n-1}, p^{n-1}\}$, compute the value of P_ao solving the discretized version of the Windkessel ordinary differential equation (2.12)

[4] Given $\boldsymbol{w}^n$, P_ao and R_Σ^n , solve the discretized version of the fluid problem (2.13)-(2.14) under the chosen initial conditions (2.8) and boundary conditions (2.9)-(2.11)

This model was implemented using the finite element library FELiScE[8].

2.3 Numerical experiment: Simulation of the hemodynamics in a healthy left heart

In this section, the geometrical domain presented in Section 2.1 is used in combination with the mathematical model presented in Section 2.2 to simulate the intracardiac hemodynamics of a healthy left heart. The model parameters are presented and the blood flow resulting from the simulation are then described in detail.

2.3.1 Model setup

An electro-mechanical simulation of the heart was performed by the INRIA team *M3DISIM* [91]. Based on a multi-scale physiological description of the heart muscle, this simulation included fiber orientation and complex behavior of the heart sarcomeres. Moreover, the fluid inside the heart cavities was described using 0D models. This simulation was performed on a geometry that was also extracted from the *Zygote 3D Human Heart Model* and it was ensured that a common interface was shared on the endocardium. As a result, the displacements of the ventricular endocardium can be extracted providing the LV displacements $\boldsymbol{d}^n$ with $\Gamma = \partial\Omega_{\mathrm{s,v}}$ necessary for (2.5). A zero-traction boundary condition was applied on all the other external surfaces

[8] https://gforge.inria.fr/projects/felisce/ (last accessed 03 Dec 2018)

(in particular, we note that the atrium displacements is ad-hoc, as no information about its displacement can be obtained).

Model parameters

Table 2.1 lists the parameters that were used for this numerical experiment.

Type	Parameter	Value
Blood parameters	ρ	$1.06\,\mathrm{g/cm^3}$
	μ	$0.04\,\mathrm{g/cm/s}$
	$\boldsymbol{f}$	$\mathbf{0}$
	P_{pv}	$1.5 \times 10^4\,\mathrm{dyn/cm^2}$ ($\approx 11\,\mathrm{mmHg}$)
Windkessel parameters	$P_{ao}\vert_{t=0}$	$9 \times 10^4\,\mathrm{dyn/cm^2}$ ($\approx 68\,\mathrm{mmHg}$)
	R_p	$150\,\mathrm{dyn \cdot s/cm^5}$
	R_d	$2300\,\mathrm{dyn \cdot s/cm^5}$
	C	$0.9\,\mathrm{cm^5/dyn}$
	P_d	$0\,\mathrm{dyn/cm^2}$
Valve parameters	R_{max}	$10^6\,\mathrm{g/cm^2/s}$
	Q_{backflow}	$2\,\mathrm{cm^3/s}$
Time discretization	τ	$10^{-3}\,\mathrm{s}$

Table 2.1 – Model parameters (CGS units)

2.3.2 Simulation and results

In this section, the results from the numerical simulation are described.

The simulation was carried out over a full cardiac cycle, lasting 0.85 s (corresponding to a frequency of 71 beats per minutes). The left ventricle was initially in a mid-diastolic configuration (during the plateau phase between the E and A wave), as prescribed by the BC extracted from the electro-mechanical simulation. The initial ventricular volume was approximately 87 mL.

As the active filling occurs, the prescribed ventricular surface displacements results in an increase in volume of the left ventricle. A negative pressure difference between the aortic pressure and ventricular pressure causes a small blood backflow which closes the aortic valve. On the other hand, due to the dilatation of the left ventricle, the intraventricular pressure also drops below the atrial pressure, resulting in an opened mitral valve. This pressure difference also causes blood to enter from the four pulmonary veins inside the atrium. The four pulmonary veins inflow jet collides inside the atrium and are directed towards the mitral valve. (Figure 2.4). Note that, in the figure, streamlines were used to show the blood flow structure. A limitation inherent to this representation is that it only gives information at a certain time-instant, unlike pathlines for example. Nevertheless, it helps appreciate some global structures. The same remark applies for all subsequent images.

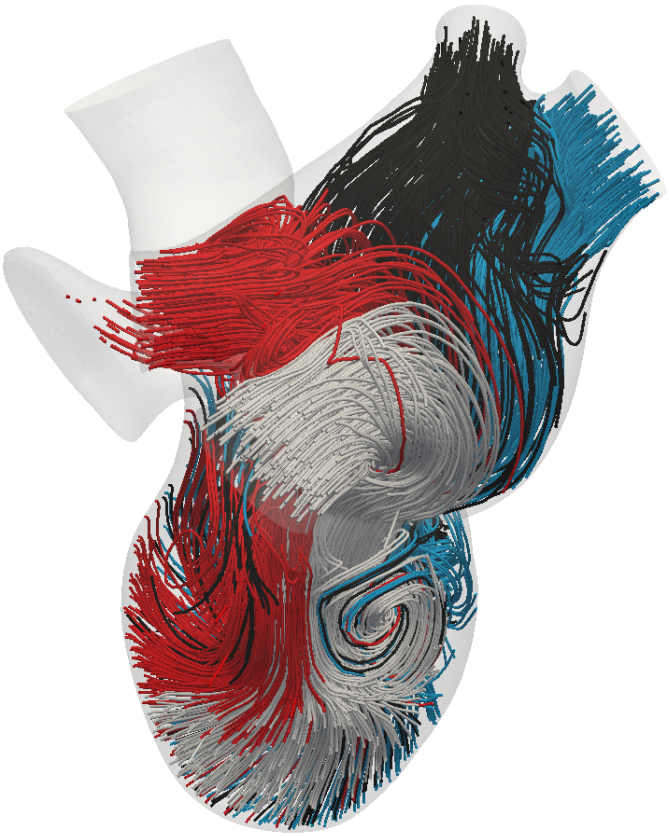

Figure 2.4 – Streamlines generated from the four pulmonary veins at $t/T \approx 0.05$. Each color represents streamlines of one pulmonary veins. The four PV inflow, at the top of the image, collide in the atrium and are directed towards the mitral valve.

As the blood converges towards the mitral annulus and passes through the mitral valve, it accelerates strongly, with a peak velocity of approximately 2.5 m/s. This blood inflow then reaches the tip of the MV leaflets. Due to the viscosity of the blood and the difference of blood velocity between the mitral inflow and the left ventricular blood velocity, a vortex ring appears at the tip of the leaflets (Figure 2.5). Due to the asymmetry of the valve leaflets and their opening angle, the blood entering the LV is directed towards the posterior wall of the ventricle. The vortical structure propagates within the ventricle and, as the blood reaches the posterior wall, the part of the vortex ring that is on the posterior side of the left ventricle gets squished whereas the most anterior side of the ring can fully develop.

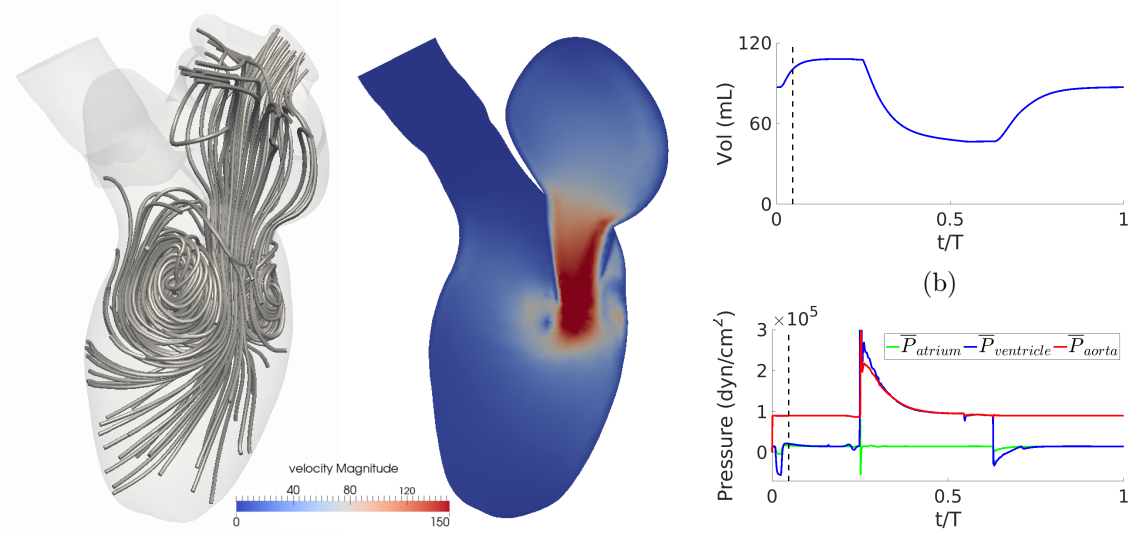

Figure 2.5 – Intracardiac hemodynamics: (a) Streamlines and blood velocity magnitude, (b) ventricular volume and (c) average pressure in the three volumic cavities at $t/T \approx 0.05$. A vortical structure appears at the tip of the mitral valve.

As the diastole comes to an end, the left ventricular reaches its maximum volume. This results in a reduction of the global left ventricular blood velocities. It is interesting to note that the blood swirl, caused by the vortex ring, is still visible (Figure 2.6). During the entire duration of the A-wave, the volume rose from 87 mL to 108 mL, resulting in a net volume increase of 21 mL.

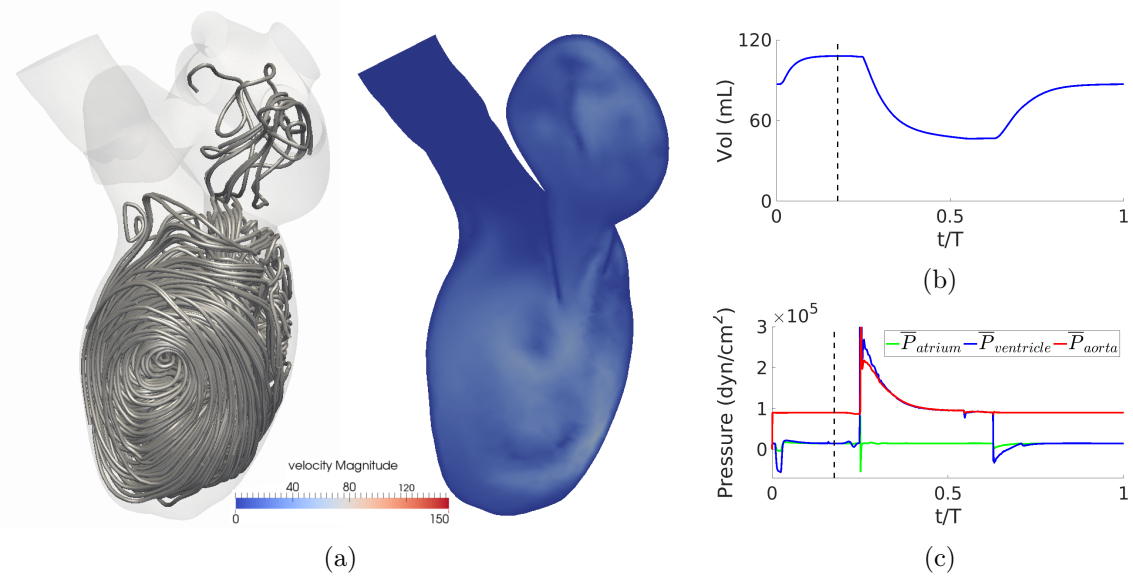

Figure 2.6 – Intracardiac hemodynamics: (a) Streamlines and blood velocity magnitude, (b) ventricular volume and (c) average pressure in the three volumic cavities at $t/T \approx 0.18$. The anterior side of the vortex now fills the entire LV.

After a small plateau phase, a strong contraction of the left ventricle results in a very steep rise in intraventricular pressure. This results in a backflow that closes the MV and in a pressure difference which opens the AV. Pushed by the LV endocardial surface, the blood converges towards the aortic tract and results in a high volume of ejected blood (62 mL) through the aorta (Figure 2.7). The reduction in cross-section from the LV cavity to the aortic cross section results in a very high velocity of the blood (peaking at 3.7 m/s). The sudden acceleration of the blood results in a reorganization of the hemodynamical structure. The vortical structure visible during diastole entirely disappears and is replaced by a very organized flow structure in which the blood is directed towards the aorta. The blood flow then slows down and disorganizes as the ventricle finishes contracting.

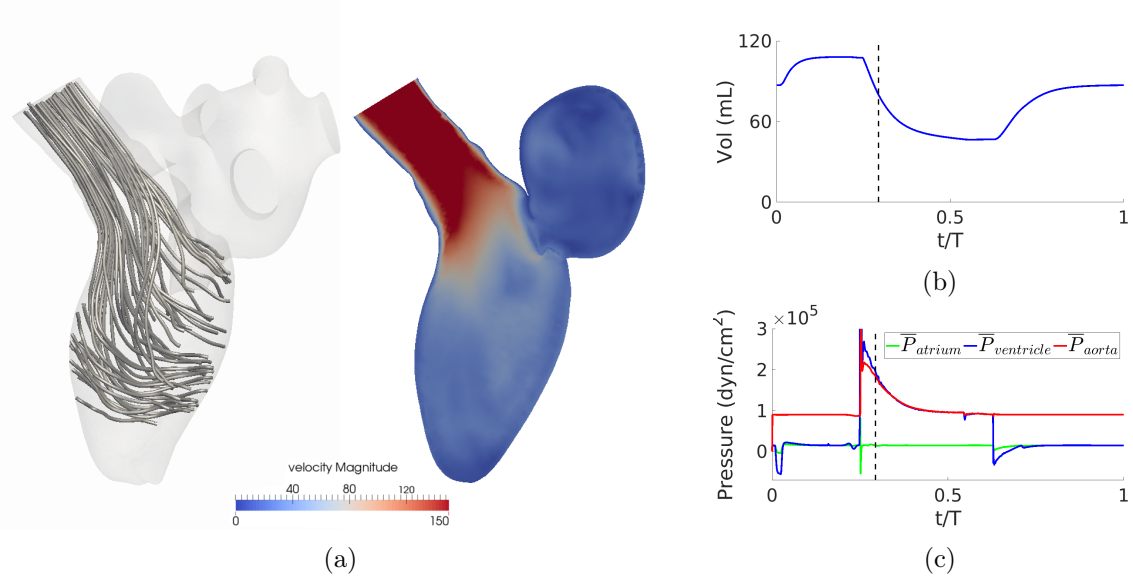

Figure 2.7 – Intracardiac hemodynamics: (a) Streamlines and blood velocity magnitude, (b) ventricular volume and (c) average pressure in the three volumic cavities at $t/T \approx 0.3$. The blood is ejected through the aorta. Streamlines reveal a very organized blood flow.

The ventricle then relaxes, starting the E-wave of the diastolic phase. In a similar manner as depicted for the A-wave, the dilatation of the ventricle results in a lower pressure in the LV compared to the atrium. As a consequence, the aortic valve closes, the mitral valve opens, and blood flows in from the pulmonary veins to the left ventricle at a maximum velocity magnitude of approximately 2.35 m/s. The vortical structure described previously appears once again and fills the left ventricle (Figure 2.8). During the entire duration of this E-wave, the ventricular volume increases from 46 mL to 87 mL, resulting in a net volume increase of 41 mL.

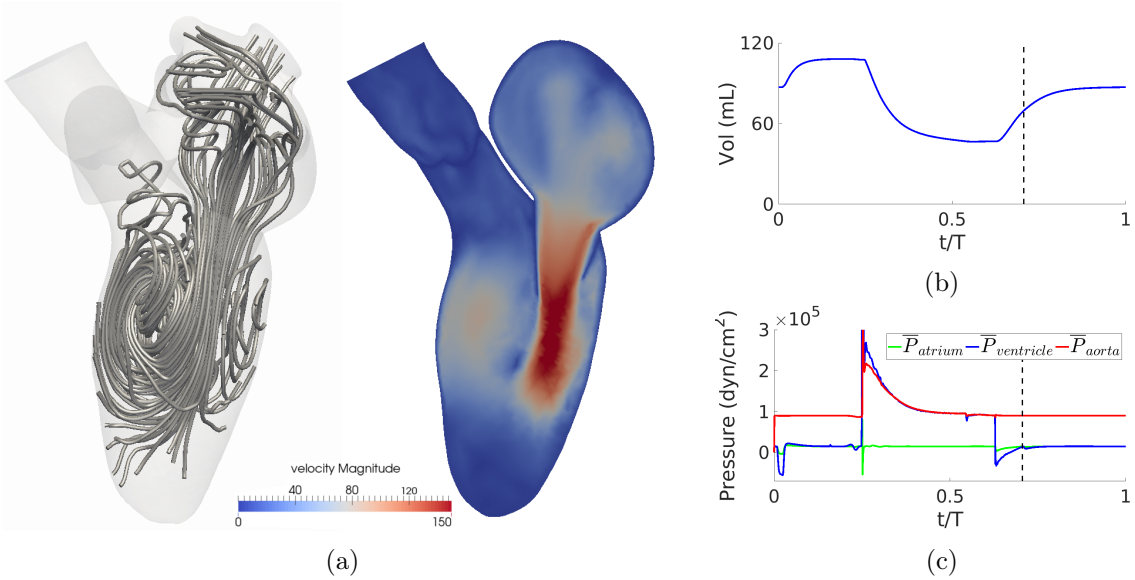

Figure 2.8 – Intracardiac hemodynamics: (a) Streamlines and blood velocity magnitude, (b) ventricular volume and (c) average pressure in the three volumic cavities at $t/T \approx 0.64$. The vortex ring observed earlier appears again as the ventricle starts to dilate.

A small discussion about those results is provided in Section 2.6.1.

2.4 Mitral regurgitation modeling

In this section, we describe an extension of the valve model to model mitral regurgitation and illustrate its use with a simple numerical example. We start from the N-S momentum equation 2.13 described in Section 2.2.2: This standard RIS model consisted of adding a resistive term $R_{\Sigma_i}(t)$ on solid surfaces Σ_i, immersed in the fluid domain. An evolution law for the resistance term $R_{\Sigma_i}(t)$ was also introduced to allow opening and closing of the valve..

In order to model mitral valve regurgitation, it is proposed to modify the spatial value of the resistance term $R_{\Sigma_i}(t)$ to allow a local control on the valve mesh porosity. Three closed mitral valve geometry are introduced in order to allow the modeling of Type 1, Type 2 and Type 3 MR.

Mathematical model of the regurgitation

We first describe how the mathematical model of the valve is modified to allow mitral regurgitation.

The scalar resistance term $R_{\Sigma_i}(t)$ is redefined as a scalar field $R_{\Sigma_i}(\boldsymbol{x},t)$ in order to locally control the porous behavior of the valve and allow blood to pass through at specific locations.

The momentum equations including the modified resistance term therefore reads:

$$\rho\left(\left.\frac{\partial \boldsymbol{u}}{\partial t}\right|_{\mathcal{A}} + (\boldsymbol{u}-\boldsymbol{w})\cdot\boldsymbol{\nabla}\boldsymbol{u}\right) - \boldsymbol{\nabla}\cdot\boldsymbol{\sigma}(\boldsymbol{u},p) + \sum_i \delta_{\Sigma_i} R_{\Sigma_i}(\boldsymbol{x},t)\,(\boldsymbol{u}-\boldsymbol{w}) = \boldsymbol{f} \tag{2.16}$$

A geometric sub-region of the valve surface is chosen *a priori* and the valve resistance term is modified accordingly to reflect that choice. The local definition of the regurgitation region is prescribed by a MR region marking method inspired from constructive solid geometry. This technique allows to construct complex geometries as a combination of simple geometrical objects. In the presented work, we use combination of spheres to define the regurgitant region: a first indicator function is defined on the valve surface such that it represents the region enclosed in a ball B:

$$\mathbb{1}_{B,\Sigma_i}(\boldsymbol{x},t) = \begin{cases} 1 & \forall \boldsymbol{x} \in \Sigma_i : \boldsymbol{x} \in B \\ 0 & \forall \boldsymbol{x} \in \Sigma_i : \boldsymbol{x} \notin B \end{cases}$$

By considering the union of n balls $\{B_j\}_{j=1,\cdots,n}$ to define the indicator function, this idea is therefore naturally extended to define more complex MR region:

$$\mathbb{1}_{\{B_j\},\Sigma_i}(\boldsymbol{x},t) = \begin{cases} 1 & \forall \boldsymbol{x} \in \Sigma_i : \boldsymbol{x} \in \bigcup\{B_j\} \\ 0 & \forall \boldsymbol{x} \in \Sigma_i : \boldsymbol{x} \notin \bigcup\{B_j\} \end{cases}$$

Figure 2.9 depicts examples of MR region marking using both strategies.

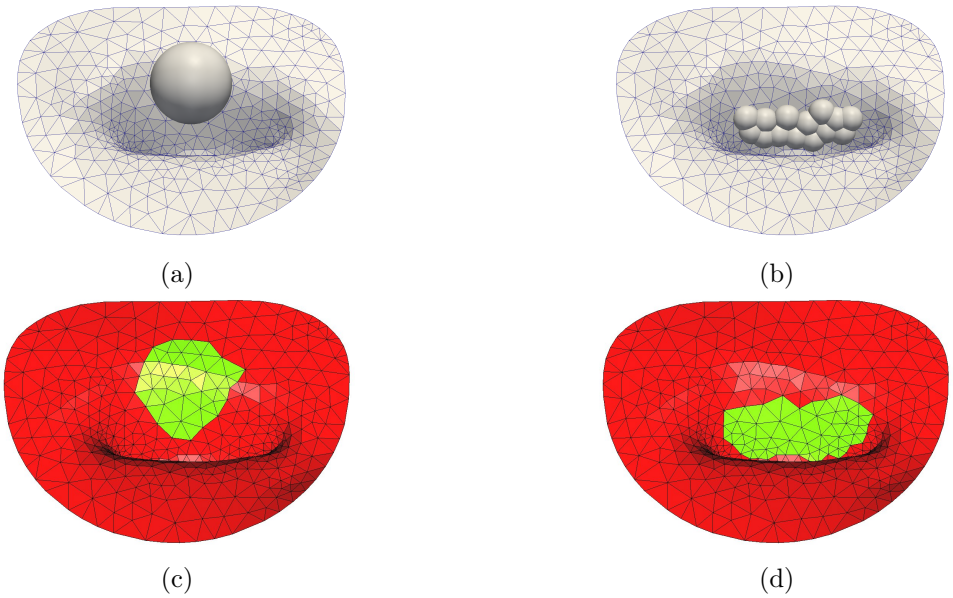

Figure 2.9 – Example of the region marking strategy. Figures (c) and (d) depict respectively the marked region resulting the use of(a) a single sphere and (b) a union of spheres. The green triangles represent the region on which the indicator function is active.

The indicator functions defined previously are used to modify the original resistance term locally and produce the scalar field $R_{\Sigma_i}(\boldsymbol{x},t)$, as defined by (2.17). When the indicator function is

inactive, the normal valve behavior occurs without any modification. On the contrary, in the location where the indicator function is active, the resistance term is set equal to zero, therefore disabling the porosity locally and allowing fluid to pass through the valve.

Remark: No changes were made to the valve evolution law of the valve, in particular no changes were made neither to the valve opening nor to the valve closing criterions.

$$R_{\Sigma_i}(\boldsymbol{x},t) = R_{\Sigma_i}(t) \cdot (1 - \mathbb{1}_{\cdot,\Sigma_i}(\boldsymbol{x})) \tag{2.17}$$

Due to the original formulation of the RIS model, the valves are inherently either in open or closed state and no valve dynamics are included. This modeling choice imposes an *a priori* geometrical modeling of the valve geometry which might be a strong simplification of reality, in particular for highly dynamic MVR such as MVR due to flail leaflet [92].

Moreover, as the valve is geometrically defined *a priori*, the valve also undergoes the meshing procedure before any specification of the mitral regurgitation. The discretization of the surface might lead to a delimitation of the MR boundaries that is imposed by the mesh discretization. Figure 2.10 illustrates this behavior: a mitral valve mesh is gradually refined and a ball of fixed radius is used to mark the regurgitant region in each case. For illustration purpose, the triangles of the surface were colored if at least one of their vertices is within the ball radius. One can appreciate how the marked region becomes closer and closer to a circular hole as the mesh is refined. The counterpart of this limitation is that the MR design is very quickly set-up before the numerical simulation making this model very versatile.

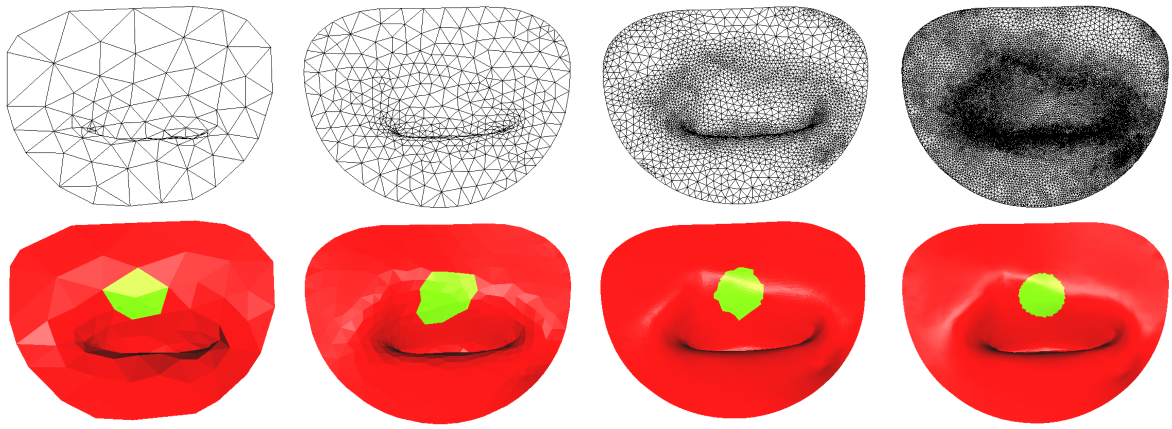

Figure 2.10 – Dependence of the MR region marking strategy on the underlying mesh. Using the same sphere to mark the MV, progressive refinement of the MV mesh (top row) results in a marked region more and more circular.

Geometrical description of the mitral valve

Figure 1.7 in Chapter 1 summarizes in a comprehensive way the different pathologies leading to MR and depicts the geometry of the mitral valve in different pathologies. The objective is to design MV geometries that can reproduce this broad range of possible MR.

Carpentier's functional classification of MV diseases [25] was used to design three different MV

closed-state geometries (Figure 2.11). While the closed-state surface described in Section 2.1 can be used to model slit orifice or single round orifice (Type 1, or T1, MR), two additional MV closed-state geometries were designed to allow the modeling of mitral prolapse (Type 2, or T2, MR), as well as restrictive valve regurgitation (Type 3, or T3, MR)

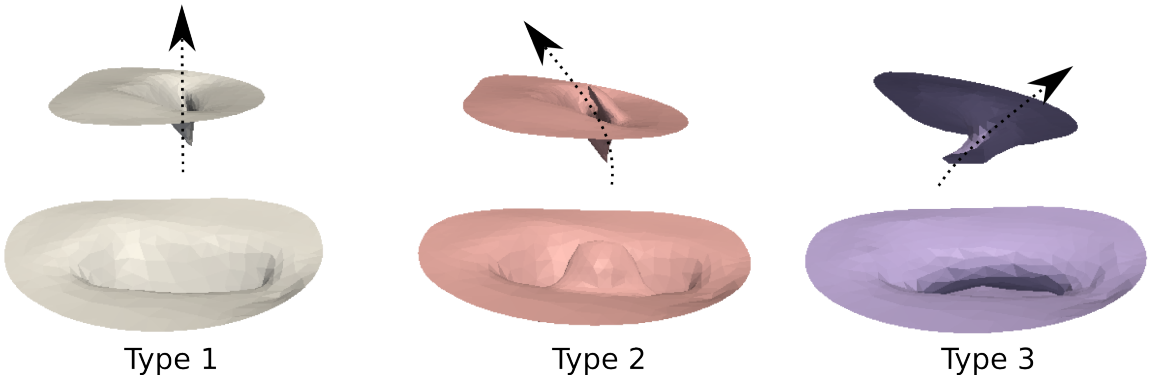

Figure 2.11 – Mitral valve closed-state geometry for Type 1, Type 2 and Type 3 MR. Top and bottom rows of the figures represent different views of the same surface and the black arrows represent potential blood flow resulting the different valve geometries.

2.5 Numerical experiment: Simulation of the hemodynamics in a left heart suffering from mitral regurgitation

In this section, the simulation of intracardiac hemodynamics in a left heart suffering from MR is considered by combining the geometrical domain presented in Section 2.1, the mathematical model of the blood flow presented in Section 2.2 with the MR model described in Section 2.4. The setup of the model is first described and the the blood flow resulting from the simulation is described.

2.5.1 Model setup

In this numerical experiment, the LV boundary displacements were prescribed using the same electromechanical simulation previously described in Section 2.3. Similarly, the parameters described in Table 2.1 were used. The simulation was carried out over a full cardiac cycle, lasting 0.85 s.

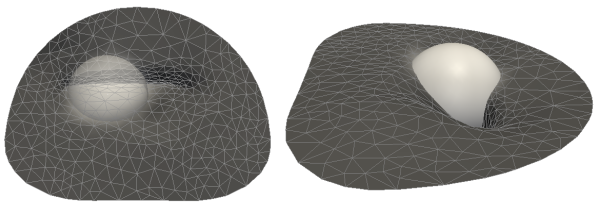

Figure 2.12 – The valve in black is marked with a ball of radius 0.4 cm to produce a severe T1 MR.

To assess the MR modeling methodology, a simple circular MR was designed. A ball of radius 0.4 cm was used to mark the regurgitant region on the flat MV geometry, as depicted by Figure 2.12. This resulted in a hole corresponding to a T1 MR with an EROA of 0.5 cm^2. This regurgitation is categorized as "severe".

2.5.2 Description of the hemodynamics

As before, the simulation started from the mid-diastole, between the E and A-wave. The hemodynamics of the diastolic phase is the same as the one described in detail in the Section 2.3.2, due to the use of the same IC, BC and model parameters. For this reason the diastole will not be detailed. The hemodynamics of the systole, on the contrary, is strongly modified by the presence of the synthetic MR.

As the systole begins ($t/T \approx 0.25$, Figure 2.13a), a region of high blood velocity appears at the MV level, corresponding to blood converging and accelerating towards the MV hole. One can observe nearly semicircular isovelocity levels (depicted by the black lines on the figure). This is coherent with the fact that the modeled hole is circular and with the PISA model. At $t/T \approx 0.27$, (Figure 2.13b), one can see that the blood progresses through the atrium as a coherent jet of very high velocity, at a velocity of approximately 5 m/s at the vena contracta. While some blood passes through the MV, part of the blood is still ejected through the AV towards the aorta.

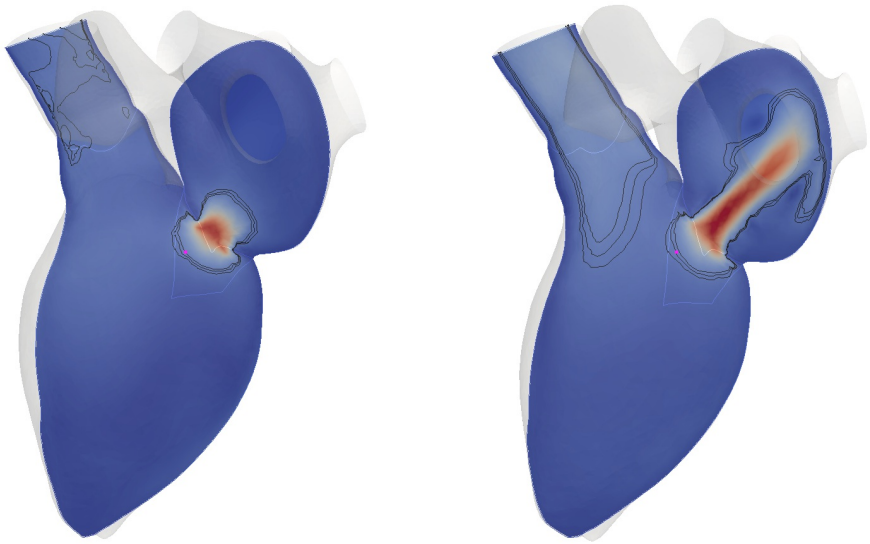

(a) (b)

Figure 2.13 – Blood velocity magnitude of the MR case at (a) $t/T \approx 0.25$ and (b) $t/T \approx 0.27$. The blood strongly accelerates toward the mitral valve and form hemispheric isovelocity surface. As the systole continues, the blood penetrate the LA in a jet of high velocities.

As the systole continues ($t/T \approx 0.31$, Figure 2.14a), the blood jet reaches the posterior wall of

the atrium. Due to the angle the jet hits the wall at, the jet then follows the wall curvature in a rotating motion. Finally, as the systole ends ($t/T \approx 0.41$, Figure 2.14b), the blood velocity magnitude throughout the entire domain decreases.

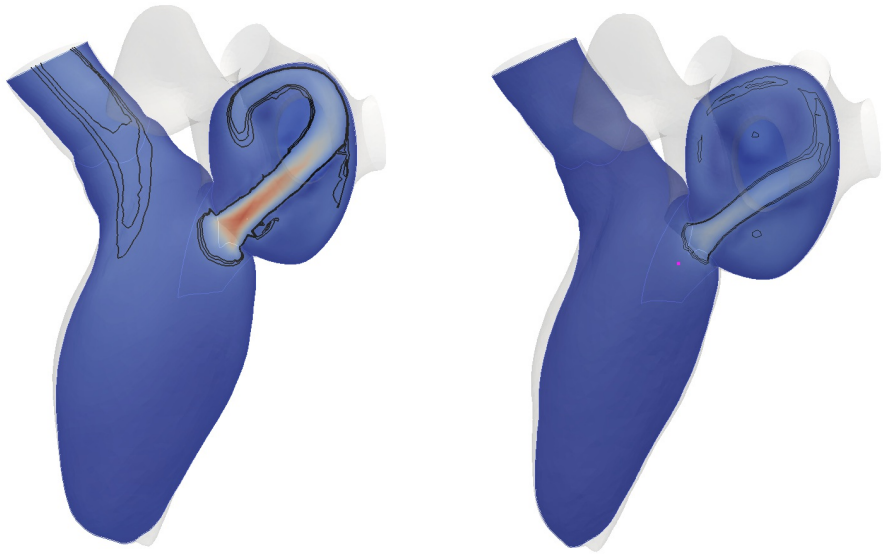

(a) (b)

Figure 2.14 – Blood velocity magnitude of the MR case at (a) $t/T \approx 0.31$ and (b) $t/T \approx 0.41$. The blood jet in the LA hits the wall and follows the wall curvature. Finally, at the end of the systole, the blood slows down.

A small discussion about those results is provided in Section 2.6.2.

2.6 Conclusion, discussion and perspectives

In this final section, we first provide some conclusion, discussion and perspectives with respect to the modeling of healthy blood flow. In a second time, conclusion, discussion and perspectives with respect to mitral regurgitation modeling will be presented.

2.6.1 Healthy blood flow modeling

In this chapter, a mathematical model of the left heart hemodynamics was described. A fluid domain including the LA, LV and a portion of the ascending aorta was constructed, based on the *Zygote 3D Human Heart Model*. Closed aortic and mitral valves were also extracted from the *Zygote 3D Human Heart Model*, while the mitral valve in open configuration was designed using physiological description from the literature. The models and discretization choices were then presented alongside the considered boundary conditions.

Using an external electro-mechanical simulation to provide the displacements of the LV wall, it was possible to obtain intracardiac hemodynamics which were coherent with the usual literature description of the structure of the blood flow. Indeed, the provided LV surface boundary condition imposed a change in ventricular volume similar to the human physiology. The ejection fraction, computed as $EF = (EDV - ESV)/EDV$ using the end-diastolic volume (EDV) and the end-systolic volume (ESV), was approximately 57 %, a physiological value with respect to the European Society of Cardiology Guidelines [93]. During the diastole, vortex rings located at the tip of the mitral valve leaflets appeared during the E and A-wave due to the inflow of viscous blood through the MV. The side of the vortex ring located near the LV posterior wall got squished while the opposite side could develop and fill the LV cavity. This behavior has been reported numerous times in clinical studies [94, 11, 9, 95] as well as in-silico studies [96, 19, 97, 98]. During systole, the intraventricular flow structures reorganized to form a nearly laminar blood flow directed towards the aorta. This relaminarization process was also previously described [99].

Looking at specific hemodynamic quantities revealed differences with the standard physiology. In particular, it was observed that the blood inflow through the mitral valve during diastole was approximately 2.35 m/s and 2.5 m/s, respectively for the E and A-wave, higher than physiological values of approximately 0.8 m/s [7, 100]. Similar remark can be made about the peak velocity during systolic ejection (3.7 m/s compared to the physiological 1.0 m/s) [7, 13].

The modeling choices resulted in a geometry that does not include the internal LV features such as the papillary muscles, trabeculae or chordae tendinae. The absence of such features could affect the flow fields locally. Therefore, while analyzing the flow fields, one needs to be careful interpreting locally the hemodynamics.

Moreover, it must be noted that the isovolumetric phases could not be obtained, due to the choice of not modeling the full interactions of the fluid with surrounding tissue. This indicates that the model could be improved in that regard. In Chapter 3, we aim to build on that remark and provide a solution to properly recover the isovolumetric phases.

While the general hemodynamic behavior obtained was physiologically coherent, the synthetic displacements imposed as boundary conditions of the LV wall had a strong influence on the intracardiac hemodynamics. In particular, it resulted, in the presented numerical example, in velocities that are too high compared to the usual adult physiology. In this regard, two strategies can be envisioned. On the first hand, the electro-mechanical simulation could be enhanced further to provide a better description of the LV wall dynamics. On a second hand, it might be beneficial to impose patient-specific boundary conditions to obtain more physiological hemodynamic quantities. Chapter 4 will describe a pipeline to bridge the gap between the numerical simulations presented in this chapter and patient data obtained using medical imaging techniques.

2.6.2 Mitral regurgitation modeling

A modification of the RIS model was also introduced in order to allow the modeling of mitral regurgitation. By introducing local variation in the resistive parameter of the valve model, the blood was allowed to flow freely through the valve at the prescribed location. A simple region marking strategy was presented in order to allow the modeling of different MR types and three different closed MV geometry were introduced to allow the modeling of the various different MR

including Type 1, Type 2 and Type 3.

A numerical example was proposed to illustrate the modeling of a simple Type 1 MR: a circular hole was prescribed and the numerical simulation of the blood flow during one cardiac cycle was performed. While the diastolic part of the hemodynamics was similar to the healthy case, the systole presented a very different outlook. Inspection of the velocity field revealed that a strong regurgitation could be obtained with blood converging rapidly toward the valvular hole. It has to be noted that the inclusion of the left atrium in the geometrical model was beneficial for the hemodynamics description as it allowed to describe the MR jet in detail.

The presented strategy offers an alternative to the main MR modeling strategies described in the literature. While several studies designed a tiny channel during the meshing stage to model MR ([39, 71, 53, 72]), the strategy proposed in our work does not require such tedious work. As a result, modeling new MR cases is very straightforward. Moreover, we think that, as a direct consequence of the absence of remeshing, time-evolving regurgitant region (*e.g.,* based on Color-Doppler images) can be prescribed easily by incorporating a time dependency in the indicator function used to define the regurgitant region. This is left for research

In the proposed model, gradual opening and closing of the valve cannot be achieved. Some recent work introduced a reduced model that combines the RIS model with immersed implicit surfaces [101]. A possible extension the presented model could be to combine this progressive opening and closing of the valve with MR modeling. Nevertheless, even in this case, the opening and closing of the valve are not physiologically represented. One should carefully evaluate if FSI models are not the best answers if one wants to model the valve dynamics.

Moreover, as the PV are considered fluid outlets, in the case of MR, another possible extension of the model would be to impose Windkessel models for the PV pressures. Indeed, the blood regurgitated depends both on the aortic and PV pressures. For this reason, accounting for a better upstream pressure model could allow a better representation of the hemodynamics.

While only a single Type 1 MR was presented in this chapter, the versatility of the presented MR modeling technique will be showcased in Chapter 4 in which various other regurgitation are considered.

Chapter 3
Augmented Resistive Immersed Surfaces method for the simulations of cardiac valves with isovolumetric phases

The model proposed in Chapter 2 provides realistic blood flow during systole and diastole. However, it is observed that the modeling of the isovolumetric phases cannot be obtained, partly due to the choice of not modeling the complete fluid-structure interaction of the fluid with the surrounding tissues. In this chapter, we propose a new simplified modeling approach which fixes this issue.

Starting from the resistive immersed surfaces (RIS) model for valve dynamics [89, 49], we introduce an additional interface term which controls the ventricle pressure when both valves are closed. This term involves ventricle pressure data coming either from measurements or from external electromechanical simulations, hence the terminology *augmented* RIS model. The fundamental idea of the proposed approach is that, under some basic assumptions and for moderate values of the resistive parameters, the simulated fluid pressure within the ventricle can be regulated in terms of the external pressures, the volume variation and the provided pressure data. Two three-dimensional numerical examples are proposed to test the new model and to assess the validity of its related assumptions.

The chapter is organized as follows: Section 3.1 briefly recalls the original RIS model and introduces the new augmented RIS model. In Section 3.2, two three-dimensional numerical examples are presented. Finally, a summary of the main results and some glimpses of future research are given in Section 3.3.

3.1 Problem setting and mathematical formulations

In this section, we first recall the original RIS model [89, 49] and detail the application of this model to a moving cavity enclosed by multiple immersed surfaces. Note that while this description might be redundant with the description of Chapter 2, it is purposefully described again in this chapter as the numerical method is the core of the proposed analysis. An estimate of the intracavity pressure is provided in a setting where all the valves are closed. This analysis allows to derive the Augmented Resistive Immersed Surfaces (ARIS) model whose goal is to properly control intracavity pressure.

3.1.1 Original RIS model

We consider the flow of a fluid within a moving domain $\Omega(t) \subset \mathbb{R}^3$ with n immersed valves. The closed configuration of the valves is given in terms of the surfaces $\Sigma_i(t) \subset \Omega$, $i = 1, \ldots, n$. Each surface is assumed to be oriented by a normal $\boldsymbol{n}$. We then define a negative and a positive side via the normal $\boldsymbol{n}^- \overset{\text{def}}{=} \boldsymbol{n}$ and $\boldsymbol{n}^+ \overset{\text{def}}{=} -\boldsymbol{n}^-$. For a given continuous scalar or tensorial field f defined in $\Omega(t)$ (possibly discontinuous across the immersed surface $\Sigma_i(t)$), we define its positive and negative sided restrictions to $\Sigma_i(t)$, denoted respectively by f^+ and f^-, as $f^+(\boldsymbol{x}) \overset{\text{def}}{=} \lim_{\xi \to 0^+} f(\boldsymbol{x} - \xi \boldsymbol{n}^+)$ and $f^-(\boldsymbol{x}) \overset{\text{def}}{=} \lim_{\xi \to 0^+} f(\boldsymbol{x} - \xi \boldsymbol{n}^-)$, for all $\boldsymbol{x} \in \Sigma_i(t)$.

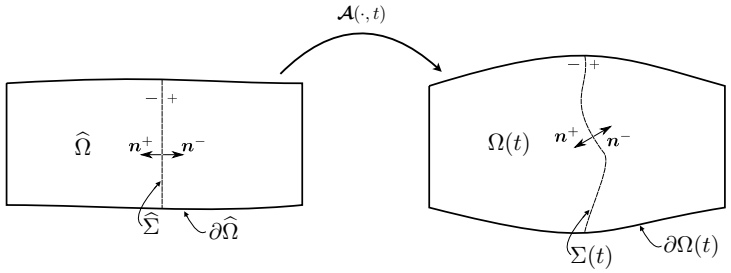

Figure 3.1 – Geometric description with a single valve and a moving domain. The ALE mapping transform the domain $\widehat{\Omega}$ into the domain $\Omega(t)$.

The current configuration, in time, is parametrized as $\Omega(t) = \boldsymbol{\mathcal{A}}(\widehat{\Omega},t)$, where $\widehat{\Omega}$ is the reference configuration and $\boldsymbol{\mathcal{A}} : \widehat{\Omega} \times \mathbb{R}^+ \to \mathbb{R}^3$ is the Arbitrary Lagrangian-Eulerian (ALE) one–to–one mapping (see Figure 3.1). Similarly, we have the parametrizations $\partial\Omega(t) \overset{\text{def}}{=} \boldsymbol{\mathcal{A}}(\partial\widehat{\Omega}, t)$ and $\Sigma(t) \overset{\text{def}}{=} \boldsymbol{\mathcal{A}}(\widehat{\Sigma}, t)$. This mapping is given in terms of the fluid domain displacement $\boldsymbol{d} : \widehat{\Omega} \times \mathbb{R}^+ \to \mathbb{R}^3$ with the expression: $\boldsymbol{\mathcal{A}} \overset{\text{def}}{=} \boldsymbol{I}_{\widehat{\Omega}} + \boldsymbol{d}$. The displacement field $\boldsymbol{d}$ is given in terms of an arbitrary lifting of the exterior boundary displacement $\boldsymbol{d}|_{\partial\widehat{\Omega}}$ through the relation $\boldsymbol{d} = \boldsymbol{\mathcal{L}}\left(\boldsymbol{d}|_{\partial\widehat{\Omega}}\right)$, where $\boldsymbol{\mathcal{L}}$ is a well chosen lifting operator from $\partial\widehat{\Omega}$ to $\widehat{\Omega}$. The fluid domain velocity $\boldsymbol{w} : \widehat{\Omega} \times \mathbb{R}^+ \to \mathbb{R}^3$ is then simply defined as $\boldsymbol{w} \overset{\text{def}}{=} \dfrac{\partial \boldsymbol{d}}{\partial t}$. We shall also use the notation $\left.\dfrac{\partial}{\partial t}\right|_{\boldsymbol{\mathcal{A}}}$ for the ALE time derivative.

The fluid is assumed to be homogeneous, incompressible, viscous and Newtonian. It is described by the incompressible Navier-Stokes equations in ALE formulation. The opening and closing dynamics of the valve can be described in a simplified manner by neglecting the mechanics of the leaflets via the RIS model proposed by Astorino et al. [49]. The idea consists in introducing a resistive surface term $R\delta_\Sigma(\boldsymbol{u} - \boldsymbol{w})$ in the fluid momentum equation, where δ_Σ denotes the Dirac measure on the immersed surface Σ and $R = R(t)$ is a time-dependent function which is null when the valve is open and large when the valve is closed. The resulting problem reads as follows: find the velocity $\boldsymbol{u} = \boldsymbol{u}(\boldsymbol{x},t) : \Omega \times \mathbb{R}^+ \to \mathbb{R}^3$ and the pressure $p = p(\boldsymbol{x},t) : \Omega \times \mathbb{R}^+ \to \mathbb{R}$, such that

$$\begin{cases} \rho\left(\left.\dfrac{\partial \boldsymbol{u}}{\partial t}\right|_{\boldsymbol{\mathcal{A}}} + (\boldsymbol{u} - \boldsymbol{w}) \cdot \boldsymbol{\nabla}\boldsymbol{u}\right) - \boldsymbol{\nabla} \cdot \boldsymbol{\sigma}(\boldsymbol{u},p) + \displaystyle\sum_{i=\{1\ldots n\}} R_i \delta_{\Sigma_i}(\boldsymbol{u} - \boldsymbol{w}) = \boldsymbol{f} \quad \text{in} \quad \Omega(t), \\ \boldsymbol{\nabla} \cdot \boldsymbol{u} = 0 \quad \text{in} \quad \Omega(t), \end{cases} \tag{3.1}$$

where the fluid Cauchy stress tensor is given by

$$\boldsymbol{\sigma}(\boldsymbol{u},p) \overset{\text{def}}{=} 2\mu\boldsymbol{\varepsilon}(\boldsymbol{u}) - p\boldsymbol{I}, \quad \boldsymbol{\varepsilon}(\boldsymbol{u}) \overset{\text{def}}{=} \frac{1}{2}(\boldsymbol{\nabla u} + \boldsymbol{\nabla u}^{\mathrm{T}}),$$

and where ρ and μ denote, respectively, the fluid density and the fluid dynamic viscosity and $\boldsymbol{I}$ the identity tensor. The above system has to be complemented with appropriate initial and boundary conditions. For the sake of notation, in the rest of the chapter, Ω will refer to $\Omega(t)$, $\partial\Omega$ to $\partial\Omega(t)$ and Σ to $\Sigma(t)$.

As pointed out in the original model [49], if one defines the stress jump:

$$[\![\boldsymbol{\sigma}(\boldsymbol{u},p)\boldsymbol{n}]\!] \overset{\text{def}}{=} \boldsymbol{\sigma}(\boldsymbol{u}^-,p^-)\boldsymbol{n}^- + \boldsymbol{\sigma}(\boldsymbol{u}^+,p^+)\boldsymbol{n}^+,$$

the system (3.1) enforces the interface conditions

$$[\![\boldsymbol{\sigma}(\boldsymbol{u},p)\boldsymbol{n}]\!] = -R_i\,(\boldsymbol{u} - \boldsymbol{w}) \quad \text{on} \quad \Sigma_i, \tag{3.2}$$

for $i = \{1,\dots,n\}$. Two asymptotic behaviors are then deduced: when R_i is large, $\boldsymbol{u} = \boldsymbol{w}$ is enforced on the moving surface Σ_i, whereas when R_i is close to 0, the flow does not 'see' Σ_i anymore and there is no pressure drop across it. When R_i is between these two extremes, Σ_i acts as a porous surface [89, 102] via the interface Robin condition (3.2).

3.1.2 Estimate of the pressure within an enclosed cavity

Based on the original RIS model (3.1), let Ω denote a moving domain, composed of three fluid sub-domains $\Omega \overset{\text{def}}{=} \Omega_1 \cup \Omega_2 \cup \Omega_3$, as depicted in Figure 3.2. We assume that Ω_1 shares an interface with Ω_2, denoted as Σ_{12}, and that Ω_2 also shares another interface with Ω_3, denoted as Σ_{23}. The domains Ω_1 and Ω_3 do not share any interface. The opening and closing dynamics of Σ_{12} and Σ_{23} are described using the RIS model.

The exterior boundary of Ω is divided into non-overlapping subsets $\partial\Omega_{\cdot,\mathrm{D}}$ and $\partial\Omega_{\cdot,\mathrm{N}}$ as depicted in Figure 3.2. No-slip Dirichlet boundary conditions are imposed on $\partial\Omega_{\cdot,\mathrm{D}} = \partial\Omega_{1,\mathrm{D}} \cup \partial\Omega_{2,\mathrm{D}} \cup \partial\Omega_{3,\mathrm{D}}$ and Neumann normal boundary conditions are imposed on $\partial\Omega_{\cdot,\mathrm{N}} = \partial\Omega_{1,\mathrm{N}} \cup \partial\Omega_{3,\mathrm{N}}$. The body force $\boldsymbol{f}$ is assumed to be equal to $\boldsymbol{0}$.

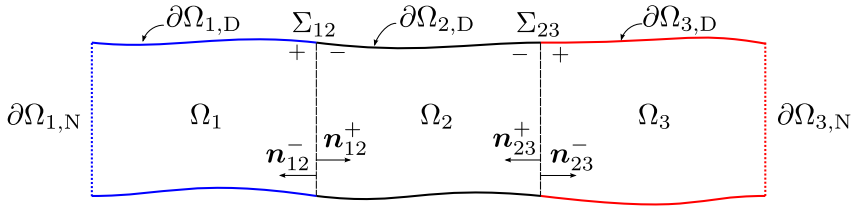

Figure 3.2 – Geometrical domain Ω considered for the problems (3.3) and (3.9).

The following problem is therefore considered: find the velocity $\boldsymbol{u} = \boldsymbol{u}(\boldsymbol{x},t) : \Omega \times \mathbb{R}^+ \to \mathbb{R}^3$ and

the pressure $p = p(\boldsymbol{x},t) : \Omega \times \mathbb{R}^+ \to \mathbb{R}$, such that

$$\begin{cases} \rho\left(\dfrac{\partial \boldsymbol{u}}{\partial t}\Big|_{\boldsymbol{\mathcal{A}}} + (\boldsymbol{u}-\boldsymbol{w})\cdot\boldsymbol{\nabla}\boldsymbol{u}\right) - \boldsymbol{\nabla}\cdot\boldsymbol{\sigma}(\boldsymbol{u},p) + \displaystyle\sum_{i=\{12,23\}} R_i\delta_{\Sigma_i}(\boldsymbol{u}-\boldsymbol{w}) = \boldsymbol{0} \quad \text{in} \quad \Omega, \\ \boldsymbol{\nabla}\cdot\boldsymbol{u} = 0 \quad \text{in} \quad \Omega, \\ \boldsymbol{u} = \boldsymbol{w} \quad \text{on} \quad (\partial\Omega_{1,\mathrm{D}} \cup \partial\Omega_{2,\mathrm{D}} \cup \partial\Omega_{3,\mathrm{D}}) \times (0,T), \\ \boldsymbol{\sigma}(\boldsymbol{u},p)\boldsymbol{n} = \boldsymbol{g_1} \quad \text{on} \quad \partial\Omega_{1,\mathrm{N}} \times (0,T), \\ \boldsymbol{\sigma}(\boldsymbol{u},p)\boldsymbol{n} = \boldsymbol{g_3} \quad \text{on} \quad \partial\Omega_{3,\mathrm{N}} \times (0,T). \end{cases} \tag{3.3}$$

The above system has to be complemented with appropriate initial conditions. The main difficulty which arises in the description of the isovolumetric phases using a uncoupling approach is that the ventricular pressure is defined up to a constant, since the fluid velocity is prescribed on the boundary of the enclosed cavity. This issue is circumvented in the original RIS model (3.1) thanks to the interface Robin condition (3.2), for moderate values of R_i. However, as we shall discuss below, this results in an arbitrarily fixed internal pressure.

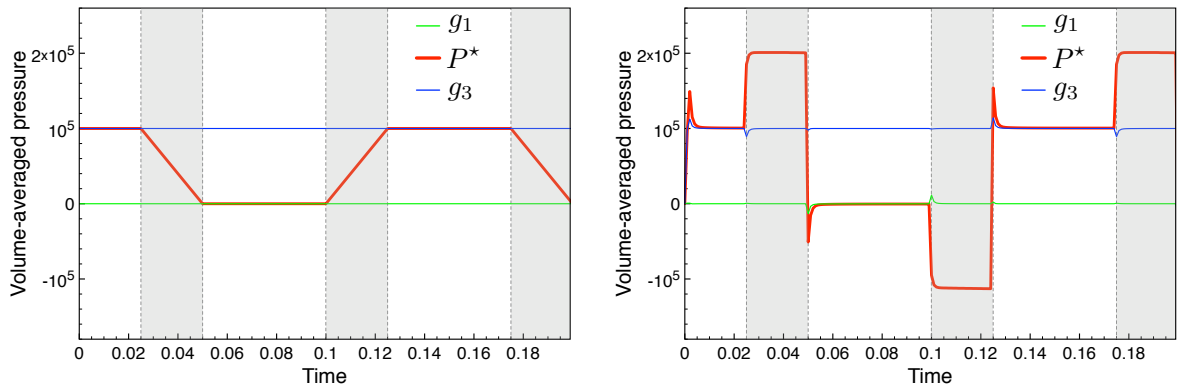

(a) Expected results.

(b) Typical obtained results.

Figure 3.3 – Time history of the pressures, in CGS unit, of the Toy-Problem. The gray areas delimit the isovolumetric phases. In the expected results, the red curve (*i.e.* the middle subdomain average pressure) transitions linearly between the average pressures from the side subdomains, whereas in the typically obtained results, an arbitrary internal pressure is obtained during the isovolumetric phases.

Figure 3.3a–3.3b depict, respectively, the expected pressures and the typical computed ones of a simple toy problem. This toy problem is aimed at reproducing basic heart behavior, is based on the domain depicted in Figure 3.2 and is described later in Section 3.2.1. Results portrayed on Figure 3.3b have been obtained by using the setting (3.3). Outside the chosen isovolumetric phases delimited by the gray areas, the computed pressures match the reference ones depicted on Figure 3.3a. On the other hand, when the middle cavity Ω_2 is closed, its inner computed volume-averaged pressure $\overline{P_{\Omega_2}}$ is clearly different from the expected one. It can be noted that, during these isovolumetric phases, $\overline{P_{\Omega_2}}$ reaches an arbitrary value, outside of the interval $\left[\overline{P_{\Omega_1}}, \overline{P_{\Omega_3}}\right]$.

In the following analysis, we provide an estimate of the resulting pressure inside Ω_2 in the situation where both R_{12} and R_{23} belong to $]0, +\infty[$. We consider two simplifying assumptions:

(H1) the viscous contribution to the normal stress is considered negligible on the valves;

(H2) the pressure inside the cavities are considered approximately constant in space when the valves are closed, namely:

$$p(\boldsymbol{x},t) \simeq P_{\Omega_i}(t) \quad \forall \boldsymbol{x} \in \Omega_i, \forall i \in \{1,2,3\}.$$

Proposition: Under assumptions (H1) and (H2), the pressure inside the cavity Ω_2 can be estimated as

$$P_{\Omega_2} \simeq \frac{\varepsilon_{12}|\Sigma_{12}|}{K} P_{\Omega_1} + \frac{\varepsilon_{23}|\Sigma_{23}|}{K} P_{\Omega_3} - \frac{1}{K} \int_{\partial\Omega_2} \boldsymbol{w} \cdot \boldsymbol{n}, \tag{3.4}$$

where $\varepsilon_i \overset{\text{def}}{=} \dfrac{1}{R_i}$, $K \overset{\text{def}}{=} (\varepsilon_{12}|\Sigma_{12}| + \varepsilon_{23}|\Sigma_{23}|)$ and $|\Sigma_i|$ stands for the measure of the surface Σ_i.

Proof. We consider the interface condition on Σ_i:

$$[\![\boldsymbol{\sigma}(\boldsymbol{u},p)\boldsymbol{n}]\!] = -R_i\,(\boldsymbol{u} - \boldsymbol{w}) \quad \text{on} \quad \Sigma_i.$$

Using assumption (H1) and rearranging the terms, we obtain

$$\boldsymbol{u} \simeq \boldsymbol{w} + \frac{1}{R_i}\left(p^-\boldsymbol{n}^- + p^+\boldsymbol{n}^+\right) \quad \text{on} \quad \Sigma_i.$$

Multiplying by $\boldsymbol{n}^-$ and integrating over Σ_i:

$$\int_{\Sigma_i} \boldsymbol{u} \cdot \boldsymbol{n}^- \simeq \int_{\Sigma_i} \boldsymbol{w} \cdot \boldsymbol{n}^- + \frac{1}{R_i} \int_{\Sigma_i} \left(p^- - p^+\right).$$

Using assumption (H2), we finally obtain

$$\int_{\Sigma_i} \boldsymbol{u} \cdot \boldsymbol{n}^- \simeq \int_{\Sigma_i} \boldsymbol{w} \cdot \boldsymbol{n}^- + \frac{1}{R_i}\left(p^- - p^+\right)|\Sigma_i|.$$

In particular, for Σ_{12} and Σ_{23}, we get

$$\int_{\Sigma_{12}} \boldsymbol{u} \cdot \boldsymbol{n}^- \simeq \int_{\Sigma_{12}} \boldsymbol{w} \cdot \boldsymbol{n}^- + \frac{1}{R_{12}}\left(P_{\Omega_2} - P_{\Omega_1}\right)|\Sigma_{12}|, \tag{3.5}$$

$$\int_{\Sigma_{23}} \boldsymbol{u} \cdot \boldsymbol{n}^- \simeq \int_{\Sigma_{23}} \boldsymbol{w} \cdot \boldsymbol{n}^- + \frac{1}{R_{23}}\left(P_{\Omega_2} - P_{\Omega_3}\right)|\Sigma_{23}|. \tag{3.6}$$

Applying the divergence theorem on $(3.3)_2$, we have

$$\int_{\Omega_2} \boldsymbol{\nabla} \cdot \boldsymbol{u} \; = 0 \quad \Leftrightarrow \quad \int_{\partial\Omega_{2,\mathrm{D}}} \boldsymbol{u} \cdot \boldsymbol{n}^- + \int_{\Sigma_{12}} \boldsymbol{u} \cdot \boldsymbol{n}^- + \int_{\Sigma_{23}} \boldsymbol{u} \cdot \boldsymbol{n}^- = 0. \tag{3.7}$$

Substituting by (3.5), (3.6) and $(3.3)_3$ into (3.7):

$$\int_{\partial\Omega_2} \boldsymbol{w} \cdot \boldsymbol{n}^- \; + \frac{1}{R_{12}}\left(P_{\Omega_2} - P_{\Omega_1}\right)|\Sigma_{12}| + \frac{1}{R_{23}}\left(P_{\Omega_2} - P_{\Omega_3}\right)|\Sigma_{23}| \simeq 0.$$

Rearranging the equation, we get the estimation (3.4).

This completes the proof. □

It is worth noting that, when the cavity is closed, and if the assumptions hold, the pressure P_{Ω_2} is regulated both by the exterior pressures (*i.e.*, with P_{Ω_1} and P_{Ω_3}) and by the change of the volume of Ω_2. In the case of a perfectly incompressible cavity (*i.e.*, when $\int_{\partial\Omega_2} \boldsymbol{w} \cdot \boldsymbol{n} = 0$), a balance of the exterior pressures is reached and is regulated both by the surface area of the immersed surfaces – $|\Sigma_{12}|$ and $|\Sigma_{23}|$ – and by the value of their corresponding resistive parameters R_i.

If the volume of the closed cavity is undergoing change (*i.e.*, $\int_{\partial\Omega_2} \boldsymbol{w} \cdot \boldsymbol{n} \neq 0$), its pressure will also evolve. Noting that $\boldsymbol{n}$ is the outgoing normal, the dilatation of the cavity (*i.e.*, $\int_{\partial\Omega_2} \boldsymbol{w} \cdot \boldsymbol{n} > 0$) would induce a negative pressure contribution. On the opposite, a contracting cavity (*i.e.*, $\int_{\partial\Omega_2} \boldsymbol{w} \cdot \boldsymbol{n} < 0$) would result in a positive pressure contribution. Moreover, this pressure change is proportional to R_i and inversely proportional to the surface area of the immersed surfaces – $|\Sigma_{12}|$ and $|\Sigma_{23}|$. This behavior is coherent with the fact that the original RIS formulation has been designed to model porous media. In the case of an increasing porous surface area, more fluid would pass through, resulting in a lower pressure jump across the surface. On the other hand, in the case of a decreasing porosity, less fluid would pass through, resulting in a higher pressure jump.

While the intracavity pressure has been estimated in a situation where both R_{12} and R_{23} are different from 0, it has to be noted that this estimation becomes singular when both R_{12} and R_{23} converge to $+\infty$. In this asymptotic case, the fact that the velocity is prescribed on the whole cavity boundary leaves the pressure undetermined and might not be compatible with the incompressibility constraint.

3.1.3 Augmented Resistive Immersed Surface model

As shown in Section 3.1.2, an estimation of the pressure P_{Ω_2} has been proposed. This expression involves the distal pressures, the wall velocity, the surface area of the immersed surfaces as well as the value of their resistive parameters. In this section, given a reference time dependent pressure $P^\star = P^\star(t)$, the objective is to modify the RIS model in order to enforce $P_{\Omega_2} \simeq P^\star$.

The proposed approach consists in considering an additional normal stress term on each of the immersed surfaces so that the corresponding interface condition becomes:

$$[\![\boldsymbol{\sigma}(\boldsymbol{u},p)\boldsymbol{n}]\!]_{\Sigma_i} = -R_i\,(\boldsymbol{u} - \boldsymbol{w}) + g_{\Sigma_i}\boldsymbol{n}. \tag{3.8}$$

The proposed approach will be referred to as the augmented resistive immersed surface model. Assuming the same setting as the one in Section 3.1.2 and applying this model on the immersed surfaces Σ_{12} and Σ_{23}, we consider the following problem: find the velocity $\boldsymbol{u} = \boldsymbol{u}(\boldsymbol{x},t) : \Omega \times \mathbb{R}^+ \to \mathbb{R}^3$ and the pressure $p = p(\boldsymbol{x},t) : \Omega \times \mathbb{R}^+ \to \mathbb{R}$, such that:

$$\begin{cases} \rho\left(\dfrac{\partial \boldsymbol{u}}{\partial t}\Big|_{\boldsymbol{\mathcal{A}}} + (\boldsymbol{u}-\boldsymbol{w})\cdot\boldsymbol{\nabla}\boldsymbol{u}\right) - \boldsymbol{\nabla}\cdot\boldsymbol{\sigma}(\boldsymbol{u},p) + \displaystyle\sum_{i=\{12,23\}} R_i\delta_{\Sigma_i}(\boldsymbol{u}-\boldsymbol{w}) = \sum_{i=\{12,23\}} g_i\delta_{\Sigma_i}\boldsymbol{n} \quad \text{in} \quad \Omega, \\ \boldsymbol{\nabla}\cdot\boldsymbol{u} = 0 \quad \text{in} \quad \Omega, \\ \boldsymbol{u} = \boldsymbol{w} \quad \text{on} \quad \partial\Omega_{1,\mathrm{D}} \cup \partial\Omega_{2,\mathrm{D}} \cup \partial\Omega_{3,\mathrm{D}}, \\ \boldsymbol{\sigma}(\boldsymbol{u},p)\boldsymbol{n} = \boldsymbol{g_1} \quad \text{on} \quad \partial\Omega_{1,\mathrm{N}}, \\ \boldsymbol{\sigma}(\boldsymbol{u},p)\boldsymbol{n} = \boldsymbol{g_3} \quad \text{on} \quad \partial\Omega_{3,\mathrm{N}}. \end{cases} \tag{3.9}$$

The above system has to be complemented with an appropriate initial condition. The following interface conditions are then satisfied on Σ_i:

$$[\![\boldsymbol{u}]\!]_{\Sigma_i} = \boldsymbol{0}, \quad [\![\boldsymbol{\sigma}(\boldsymbol{u},p)\boldsymbol{n}]\!]_{\Sigma_i} = -R_i(\boldsymbol{u}-\boldsymbol{w}) + g_{\Sigma_i}\boldsymbol{n}.$$

Proposition: Let $P^\star = P^\star(t)$ be a given time-depend function. Using the ARIS model with the stress terms $g_{\Sigma_{12}}$ and $g_{\Sigma_{23}}$ defined as

$$g_{12} = P_{\Omega_1} - P^\star - \frac{1}{K}\int_{\partial\Omega_2} \boldsymbol{w}\cdot\boldsymbol{n}, \quad g_{23} = P_{\Omega_3} - P^\star - \frac{1}{K}\int_{\partial\Omega_2} \boldsymbol{w}\cdot\boldsymbol{n}, \tag{3.10}$$

we have the following estimation of the pressure inside the cavity Ω_2:

$$P_{\Omega_2} \simeq P^\star. \tag{3.11}$$

Proof. By reproducing the proof of Section 3.1.2 using the interface condition resulting of the proposed ARIS model as a starting point, the pressure estimate P_{Ω_2} obtained is

$$P_{\Omega_2} \simeq \frac{\varepsilon_{12}|\Sigma_{12}|}{K}(P_{\Omega_1} - g_{\Sigma_{12}}) + \frac{\varepsilon_{23}|\Sigma_{23}|}{K}(P_{\Omega_3} - g_{\Sigma_{23}}) - \frac{1}{K}\int_{\partial\Omega_2} \boldsymbol{w}\cdot\boldsymbol{n}. \tag{3.12}$$

Substituting (3.10) into (3.12), one readily obtains (3.12). This completes the proof. □

Remark: Looking at the pressure estimate (3.12), it is clear that one can find an infinite number of pairs $\{g_{\Sigma_{12}}, g_{\Sigma_{23}}\}$ for which $P_{\Omega_2} \simeq P^\star$. The proposed pair (3.10) is nevertheless intuitive as each corrective term counteracts the contribution of the exterior pressure related to the immersed surface on which this term is applied. Moreover, the term related to the cavity volume change is counteracted by both $g_{\Sigma_{12}}$ and $g_{\Sigma_{23}}$ at the same time.

3.2 Numerical experiments

In this section, we illustrate and discuss the benefits brought by the pressure correction described in Section 3.1.3 in two numerical examples. Problem (3.9) is discretized in space using $\mathbb{P}_1/\mathbb{P}_1$ stabilized finite elements for the velocity and the pressure unknowns. The velocity approximations are globally continuous in space while the discrete pressure is allowed to be discontinuous across the immersed surface Σ_{12} and Σ_{23}. This allows to correctly capture the pressure jumps when the valves are closed [49].

As the core motivation of the present work is the simulation of the isovolumetric phases in the ventricle of the left heart, two three-dimensional examples mimicking the behavior of such system are considered. To assess the efficiency of the ARIS model, prescribed reference pressure will be compared with the simulated one in different formulations of the pressure corrective term (3.10). Finally, the choice of the resistive parameter R_i is crucial and requires a specific care. The determination of its value will be discussed, for each numerical example, in the next paragraphs. Note that throughout this section, all the reported units are given in the *CGS* unit system.

3.2.1 Toy problem

A simple academic problem is designed to reproduce the setting and the problematic described in Section 3.1. The simplified geometry of the fluid domain is given by Ω, which has the shape of a cylinder, as depicted in Figure 3.4a. The domain is divided into 3 parts, successively denoted as Ω_1, Ω_2 and Ω_3, as depicted in Figure 3.4b. Their dimensions are respectively given by $\{r_{\Omega_1} = 1, l_{\Omega_1} = 2\}$, $\{r_{\Omega_2} = 1, l_{\Omega_2} = 6\}$ and $\{r_{\Omega_3} = 1, l_{\Omega_3} = 2\}$, where r and l stand for, respectively, the radius and the length of the cylindric subdomain. Two identical plane surfaces are immersed inside the domain: Σ_{12} is the interface between Ω_1 and Ω_2 whereas Σ_{23} is the interface between Ω_2 and Ω_3, as shown in Figure 3.4b.

The physical parameters for the fluid are $\rho = 1.06$ and $\mu = 0.04$. The simulations are carried out for a total time of $t = 0.2$ with a time step of $\tau = 10^{-3}$. The fluid is initially at rest. The whole computational domain Ω is made of 7 375 tetrahedron. Both immersed surface, Σ_{12} and Σ_{23}, are made of 95 triangular elements.

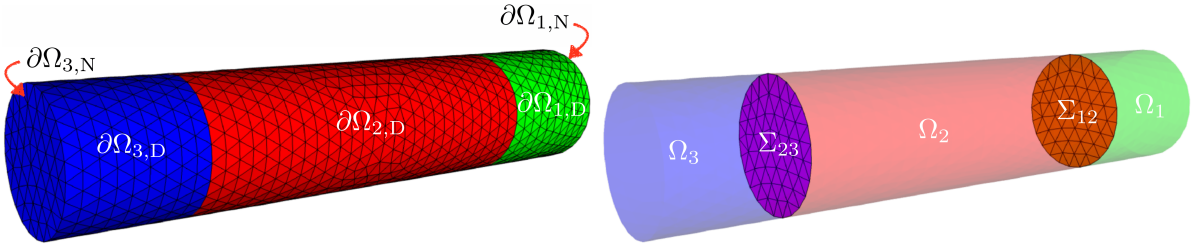

(a) Exterior of the fluid domain.

(b) Interior of the fluid domain.

Figure 3.4 – Computational domain used for the toy problem model.

A no-slip boundary condition is enforced on the solid wall of the large cylinder $\partial\Omega_{1,\mathrm{D}} \cup \partial\Omega_{2,\mathrm{D}} \cup \partial\Omega_{3,\mathrm{D}}$. The following Neumann conditions are prescribed on the inlet and outlet boundaries:

$$\begin{aligned} \boldsymbol{\sigma}(\boldsymbol{u},p)\boldsymbol{n} &= \mathbf{0} \quad &\text{on} \quad \partial\Omega_1, \\ \boldsymbol{\sigma}(\boldsymbol{u},p)\boldsymbol{n} &= -10^5\boldsymbol{n} \quad &\text{on} \quad \partial\Omega_3. \end{aligned}$$

Moreover, a reference pressure $P^\star$, which should be obtained for P_{Ω_2}, is used in the pressure corrective term (3.10). All these pressures have been analytically generated to imitate the main simplified characteristics of a human left heart [103] and are depicted on Figure 3.5.

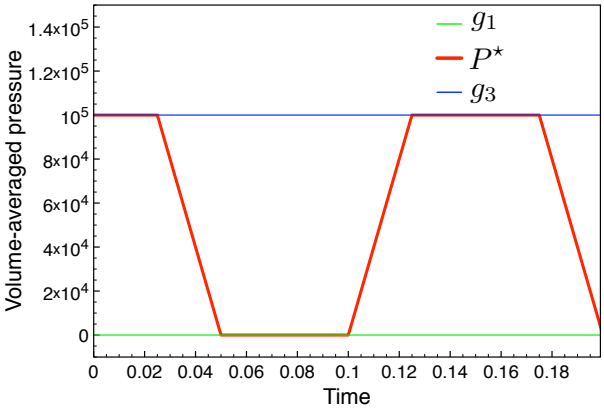

Figure 3.5 – Time history of the reference pressures, in CGS unit, used for each cavity of the toy problem model. The pressure $P^\star$, depicted by the red curve, is imposed to transitions linearly from the two other pressure curves during the isovolumetric phases.

The surface of the middle cavity $\partial\Omega_{2,\mathrm{D}}$ is displaced to mimic the typical behavior of a left ventricle during a heartbeat. In order to address different situations where the incompressibility constraint is broken or not, three different surface velocities, denoted $\boldsymbol{w}_0$, $\boldsymbol{w}_{\text{iso}}$ and $\boldsymbol{w}_{\text{not-iso}}$, evolving with time, are considered. The corresponding displacement field is then obtained thanks to a simple backward Euler method. The motion of the full domain is computed by extending the imposed surface displacements within the domain Ω using an appropriate non-linear lifting operator [104] (denoted $\boldsymbol{\mathcal{L}}$ in Section 3.1.1). The surface velocities are given by the following expressions for all $\boldsymbol{x} \in \partial\Omega_{2,\mathrm{D}}$:

$$\boldsymbol{w}_0(\boldsymbol{x},t) = \quad \mathbf{0} \qquad \forall t \in \mathbb{R}^+. \tag{3.13}$$

$$\boldsymbol{w}_{\text{iso}}(\boldsymbol{x},t) = \begin{cases} \mathbf{0} & \forall t \in \mathbb{R}^+ \mid (R_{12}(t) \neq 0 \text{ and } R_{23}(t) \neq 0)\,, \\ \boldsymbol{r}(\boldsymbol{x},t) & \forall t \in \mathbb{R}^+ \mid (R_{12}(t) = 0 \text{ or } R_{23}(t) = 0)\,. \end{cases} \tag{3.14}$$

$$\boldsymbol{w}_{\text{not-iso}}(\boldsymbol{x},t) = \begin{cases} \boldsymbol{r}(\boldsymbol{x},t)/10 & \forall t \in \mathbb{R}^+ \mid (R_{12}(t) \neq 0 \text{ and } R_{23}(t) \neq 0)\,, \\ \boldsymbol{r}(\boldsymbol{x},t) & \forall t \in \mathbb{R}^+ \mid (R_{12}(t) = 0 \text{ or } R_{23}(t) = 0)\,. \end{cases} \tag{3.15}$$

where $\boldsymbol{r}$ is a periodic function of period $T = 0.15\,\mathrm{s}$, mimicking contraction and dilatation of a pumping heart. This function $\boldsymbol{r}$ is tailored to produce a radial displacement. To obtain a negligible shift of the vertices at the immersed surface level, a Gaussian profile is prescribed to get a greater displacement at the center of Ω_2 compared with its extremities.

Figures 3.6a–3.6c present some typical snapshots of the displacement field obtained with $\boldsymbol{w}_{\text{iso}}$ and applied to the computational domain, respectively, at $t = 0$ (initial state), $t = 0.04$ (maximum contraction state) and $t = 0.115$ (maximum dilatation state).

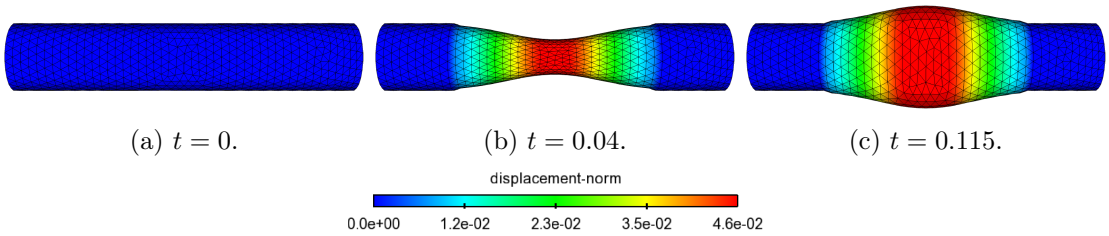

(a) $t = 0$. (b) $t = 0.04$. (c) $t = 0.115$.

Figure 3.6 – Snapshots of the displacement magnitude of the computational domain obtained with $\boldsymbol{w}_{\text{iso}}$ for the toy problem model. The amplitude of the deformation field has been amplified by 10 to increase its visibility.

In this toy problem model, the values of R_{12} and R_{23} are arbitrarily prescribed. Figure 3.7a depicts the evolution of the status of the valves and Figure 3.7b relates it to the evolution of the volume of the cavity Ω_2. Long contraction and dilatation phases are interspersed with three short isovolumetric phases (respectively defined by the time intervals $[t = 0.025, t = 0.05]$, $[t = 0.1, t = 0.125]$ and $[t = 0.175, t = 0.2]$). During the contraction and dilatation phases, at least one of the two valves is open, while both valves are closed during isovolumetric phases.

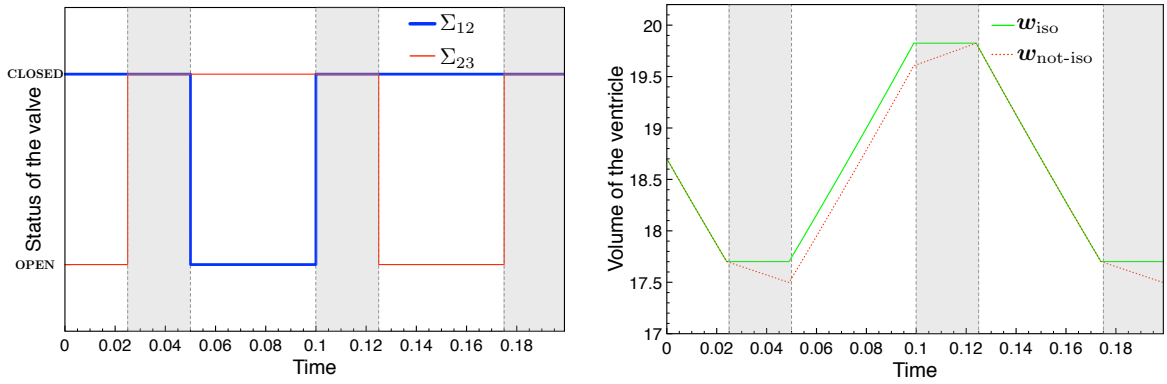

(a) Time history of the status of the valves.

(b) Time history of the volume of the cavity Ω_2.

Figure 3.7 – Description of the isovolumetric phases considered for the toy problem model. The gray areas delimit the isovolumetric phases. During the isovolumetric phases, both valves are closed as depicted in (a). In (b), one can observe that – during the phases where both valves are closed – $\boldsymbol{w}_{\text{iso}}$ results in a volume which stays constant. On the contrary, $\boldsymbol{w}_{\text{not-iso}}$ results in a volume that undergoes small changes.

The representation of the volume curves corresponding to $\boldsymbol{w}_{\text{iso}}$ and $\boldsymbol{w}_{\text{not-iso}}$ is given on Figure 3.7b. $\boldsymbol{w}_0$ represents the simple case where the computational domain is not moving. On the other hand, $\boldsymbol{w}_{\text{iso}}$ represents a case with perfect isovolumetric phases while $\boldsymbol{w}_{\text{not-iso}}$ reflects non-perfect isovolumetric phases where a slight residual is introduced when both valves are closed – between $t = 0.025$ and $t = 0.05$ and between $t = 0.1$ and $t = 0.125$ – hence inducing a violation of the incompressibility constraint.

The pressure correction is tested using successively the two following terms:

- $g_{\Sigma_i,\text{pc}} \overset{\text{def}}{=} p^+ - P^\star$ on Σ_i: the partial corrective term which only accounts for the contribution

of the distal pressures.

- $g_{\Sigma_i,\mathrm{c}} \overset{\text{def}}{=} g_{\Sigma_i,\mathrm{pc}} - \dfrac{1}{K}\int_{\partial\Omega_2} \boldsymbol{w}\cdot\boldsymbol{n}$ on Σ_i: the full corrective term, defined by (3.10), which accounts for both the distal pressures contribution and the residual volume change of the cavity.

An investigation is first provided to evaluate the influence of the resistive term R_i on the efficiency of the pressure correction. For this purpose, a case with no cavity motion (*i.e.*, when $\boldsymbol{w}(t)|_{\partial\Omega_{2,\mathrm{D}}} = \boldsymbol{w_0}(\boldsymbol{x},t)$) is considered and the term $g_{\Sigma_i,\mathrm{pc}}$ is used to correct the intracavity pressure. The set of values used for the resistive parameter R_i are

$$R_i = \{10^i,\, i = 0 \dots 10\}.$$

Defining $Q(t)$ as the inlet flow rate and $Q_0(t)$ as the inlet flow rate of a reference case in which no valve model is used, we define the logarithmic scaled residual flow rate Q_{res} as:

$$Q_{res}(t) = \log_{10}\left(\frac{Q(t)}{Q_0(t)}\right). \tag{3.16}$$

Its value is reported to assess the actual flow reduction provided by the resistive immersed surfaces. For each value of R_i, the average pressure inside the cavity Ω_2, denoted $\overline{P_{\Omega_2}}$, is compared with the reference pressure $P^\star$ to evaluate how good the intracavity pressure is corrected.

Following this first investigation, the best value of R_i is then empirically fixed and used for all cases described in the following Table 3.1:

Case	$\boldsymbol{w}\|_{\partial\Omega_{2,\mathrm{D}}}$	$g_{\Sigma_{12}}$	$g_{\Sigma_{23}}$
$T_{1,\mathrm{NC}}$	$\boldsymbol{w_0}(\boldsymbol{x},t)$	0	0
$T_{1,\mathrm{C}}$	$\boldsymbol{w_0}(\boldsymbol{x},t)$	$g_{\Sigma_{12},pc}$	$g_{\Sigma_{23},pc}$
$T_{2,\mathrm{NC}}$	$\boldsymbol{w}_{\mathrm{iso}}(\boldsymbol{x},t)$	0	0
$T_{2,\mathrm{C}}$	$\boldsymbol{w}_{\mathrm{iso}}(\boldsymbol{x},t)$	$g_{\Sigma_{12},pc}$	$g_{\Sigma_{23},pc}$
$T_{3,\mathrm{NC}}$	$\boldsymbol{w}_{\text{not-iso}}(\boldsymbol{x},t)$	0	0
$T_{3,\mathrm{PC}}$	$\boldsymbol{w}_{\text{not-iso}}(\boldsymbol{x},t)$	$g_{\Sigma_{12},pc}$	$g_{\Sigma_{23},pc}$
$T_{3,\mathrm{C}}$	$\boldsymbol{w}_{\text{not-iso}}(\boldsymbol{x},t)$	$g_{\Sigma_{12},c}$	$g_{\Sigma_{23},c}$

Table 3.1 – Cases of pressure correction considered for the toy problem model.

Cases T_1 are designed in order to test the pressure correction in a simple, non-moving domain. Cases T_2 are designed to test the pressure correction in a more complex setting involving domain motion. Cases T_3 are designed to test the pressure correction in an even more challenging setting involving domain motion and breaking of the incompressibility constraint. The subscripts NC, PC and C denote, respectively, "**N**o **C**orrection", "**P**artial **C**orrection", and "**C**orrection". Note that for the cases T_1 and T_2, there is no distinction between partial correction and correction as the cavity is not undergoing volume change during the isovolumetric phases (*i.e.*, when $\int_{\partial\Omega_2} \boldsymbol{w}\cdot\boldsymbol{n} = 0$). The average pressure $\overline{P_{\Omega_2}}$ inside the cavity Ω_2 is systematically computed in these different cases and compared with the prescribed pressure $P^\star$ to quantify the effectiveness of the pressure correction.

3.2.1.1 Results

Sensitivity analysis of the resistance parameter Figure 3.8 depicts the evolution of $Q_{\text{res}}(t)|_{t=0.17}$ with respect to the resistance value R_i. The time instant $t = 0.17$ has been chosen to allow the flow rate Q_0 to be fully developed in the open channel. Moreover, it represents a time instant where only one valve of the toy problem model is closed, hence allowing to properly quantify the flow reduction of Q compared to Q_0. It is noted that, as the resistance increases, the flow rate through the valves decreases, as expected from the standard RIS model. This result tends to justify the choice of a high value for the resistance R_i.

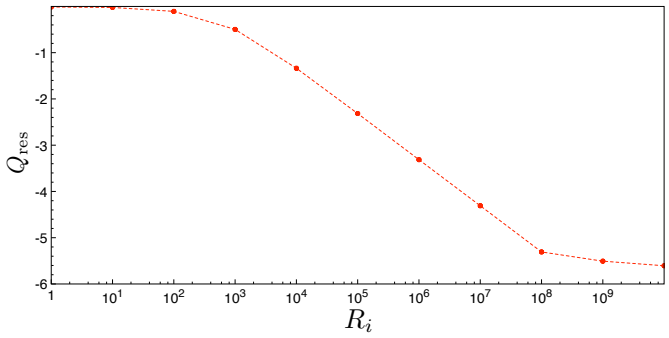

Figure 3.8 – Log relative flow rate through the valves with respect to R_i for the toy problem model.

On Figure 3.9, the pressures $\overline{P_{\Omega_2}}$ and $P^\star$ are compared, with respect to the time, using several values of R_i. From $R_i = 10^0$ to $R_i = 10^6$, the prescribed pressure $P^\star$ and computed pressure $\overline{P_{\Omega_2}}$ match properly during the isovolumetric phases depicting a successful behavior of the pressure correction. One can also notice that for $R_i = \left[10^5,10^6\right]$, the RIS model is impermeable enough to also ensure proper pressure values outside the isovolumetric phases. For higher values of R_i, the pressure corrective term cannot ensure a good fit anymore. At $R_i = 10^7$, a transition phase can be observed where $\overline{P_{\Omega_2}}$ is close to $P^\star$ but small steps are observed. At $R_i = 10^8$ and beyond, the pressure correction is completely inefficient. This highlights the preference of a small value for the resistance R_i.

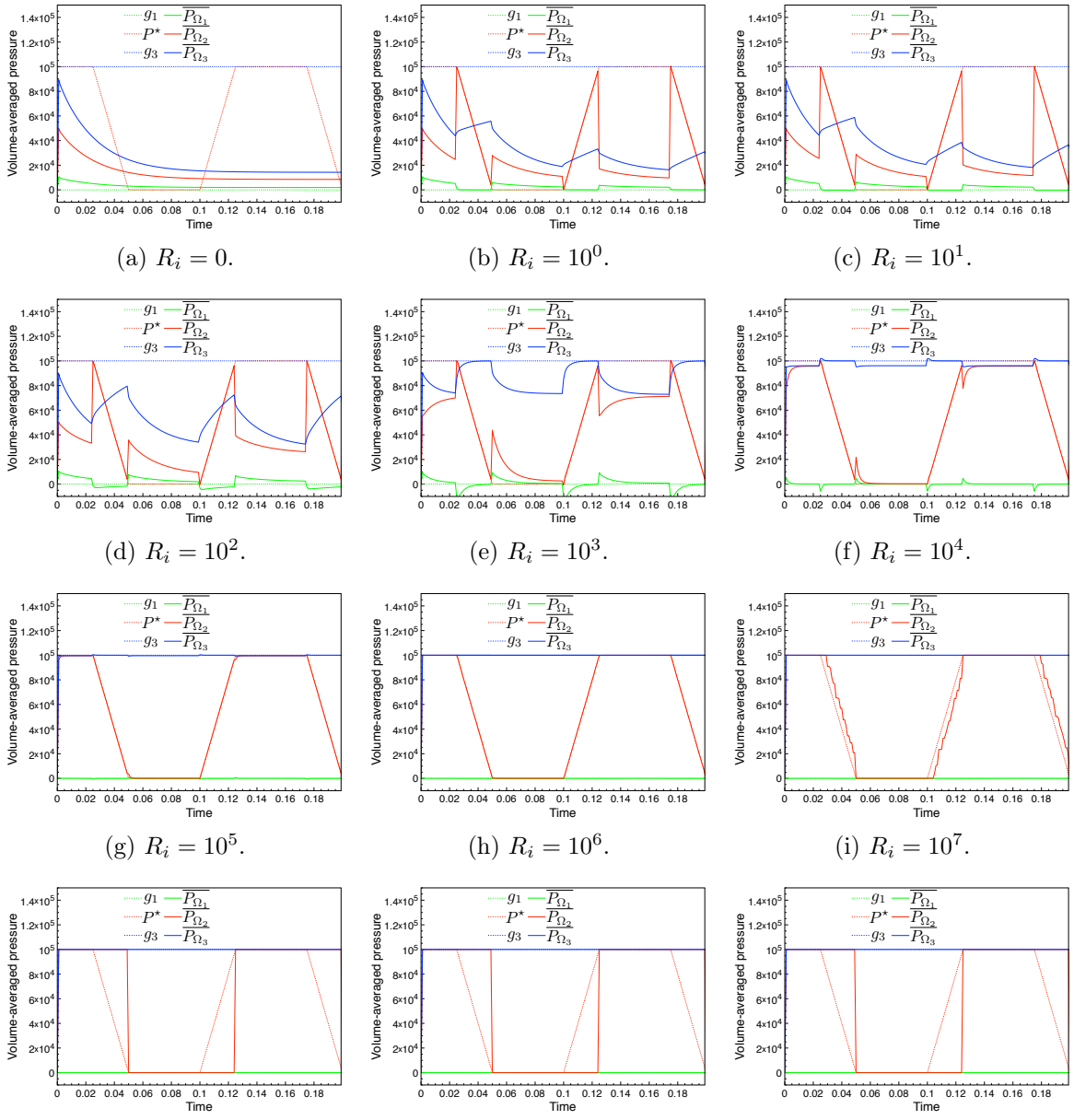

(a) $R_i = 0$. (b) $R_i = 10^0$. (c) $R_i = 10^1$.

(d) $R_i = 10^2$. (e) $R_i = 10^3$. (f) $R_i = 10^4$.

(g) $R_i = 10^5$. (h) $R_i = 10^6$. (i) $R_i = 10^7$.

(j) $R_i = 10^8$. (k) $R_i = 10^9$. (l) $R_i = 10^{10}$.

Figure 3.9 – Time history of the computed pressures, in CGS unit, obtained with pressure correction for different values of R_i for the toy problem model.

In conclusion, it is shown that a trade-off has to be made to ensure that the intracavity pressure is well corrected by the ARIS model while ensuring a good impermeability of the valve. In this specific setting, using $R_i = [10^5,10^6]$ satisfies both conditions: the pressure inside Ω_2 is properly corrected while ensuring a small residual flow rate compared with the open channel flow rate (*i.e.*, Q lower than 1% of Q_0). Based on this study, in the following, the value of the resistance R_i is set to 10^5.

Evaluation of the pressure correction for cases T_1, T_2 and T_3 Figures 3.10a–3.10b depict the results coming from, respectively, the cases $T_{1,\mathrm{NC}}$ and $T_{1,\mathrm{C}}$, for which no motion of the domain is imposed. In the case $T_{1,\mathrm{NC}}$, no pressure correction is applied. During the phases where both valves are closed, it is observed that the average pressure $\overline{P_{\Omega_2}}$ is approximately equal to 5×10^4. This result is coherent with the pressure estimation described by (3.4). Indeed, as $R_{12} = R_{23}$ and $|\Sigma_{12}| = |\Sigma_{23}|$, (3.4) can be rewritten as $P_{\Omega_2} = \frac{1}{2}P_{\Omega_1} + \frac{1}{2}P_{\Omega_3} \simeq 5 \times 10^4$, given that $P_{\Omega_1} \simeq 0$ and $P_{\Omega_3} \simeq 1 \times 10^5$ due to the considered applied Neumann normal boundary conditions. For the corrected case $T_{1,\mathrm{C}}$ (*i.e.*, when we are using the corrective term $g_{\Sigma_i,\mathrm{pc}}$), the intracavity pressure is now perfectly corrected during the isovolumetric phases.

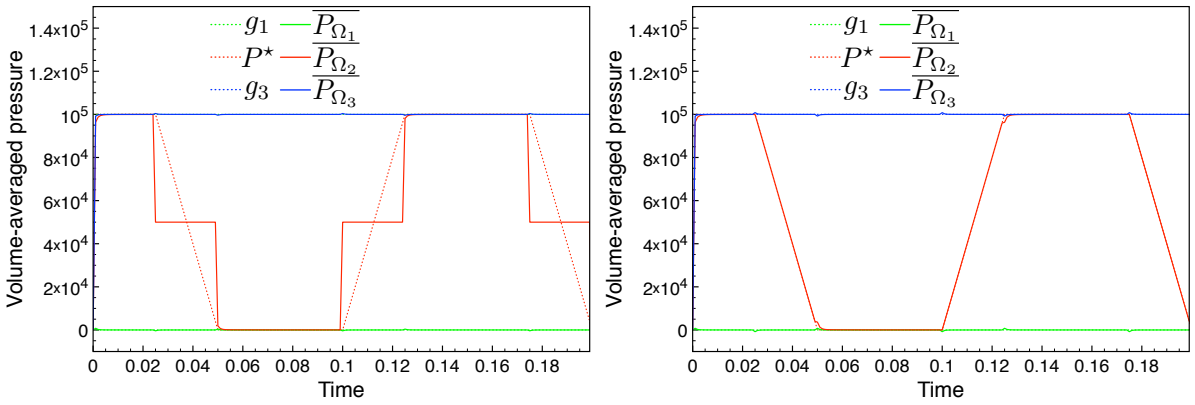

(a) Without correction.

(b) With partial correction.

Figure 3.10 – Time history of the computed pressures, in CGS unit, obtained for the cases T_1.

Figures 3.11a–3.11b depict the results coming from, respectively, the cases $T_{2,\mathrm{NC}}$ and $T_{2,\mathrm{C}}$. In those cases, a domain motion keeping the intracavity volume constant during the isovolumetric phases is imposed. Small peaks in the pressure are noticed during each transition between phases (*e.g.*, $t = 0.025$ or $t = 0.05$) but these pressure peaks decay quickly toward stable values. Similar to the cases T_1, the average intracavity pressure is properly predicted by the theoretical analysis (3.4) in case $T_{2,\mathrm{NC}}$. For the case $T_{2,\mathrm{C}}$, using the corrective term $g_{\Sigma_i,\mathrm{pc}}$ allows to get the expected intracavity pressure during the isovolumetric phases.

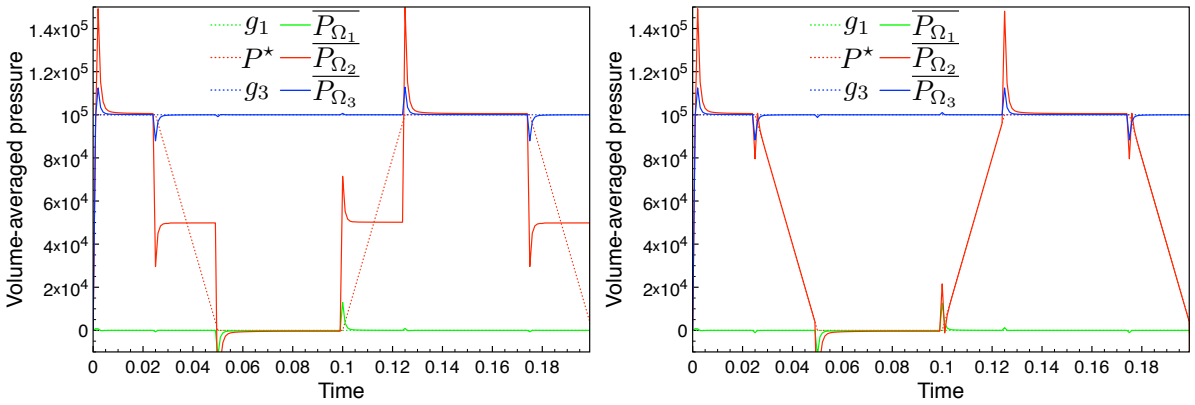

(a) Without correction. (b) With partial correction.

Figure 3.11 – Time history of the computed pressures, in CGS unit, obtained for the cases T_2.

Finally, Figures 3.12a–3.12c depict the results coming from, respectively, the cases $T_{3,\mathrm{NC}}$, $T_{3,\mathrm{PC}}$ and $T_{3,\mathrm{C}}$. In these cases, an additional difficulty is addressed by considering a residual motion imposed during the isovolumetric phases. Compared to previously, a major difference is observed for the intracavity pressure for the non-corrected case $T_{3,\mathrm{NC}}$. Indeed, the pressure is strongly offset during the non-perfect isovolumetric phases: positively when the residual motion induces a contraction of the cavity and negatively when it induces a dilatation. This behavior has been predicted by the analysis provided in the discussion of Section 3.1.2. In the partially corrected case $T_{3,\mathrm{PC}}$, it may also be noted that the corrective term $g_{\Sigma_i,\mathrm{pc}}$ is not enough to correct the intracavity pressure as the residual motion of the cavity is not taken into account into the correction. On the opposite, using the complete corrective term $g_{\Sigma_i,\mathrm{c}}$, the intracavity pressure is corrected much more efficiently. In this case, it is observed that both the overall behavior of the intracavity pressure and its value match the prescribed pressure $P^\star$. Nevertheless, a small gap between the two pressure curves is observed, probably caused by the non-perfect validity of the simplifying assumptions (H1) and (H2).

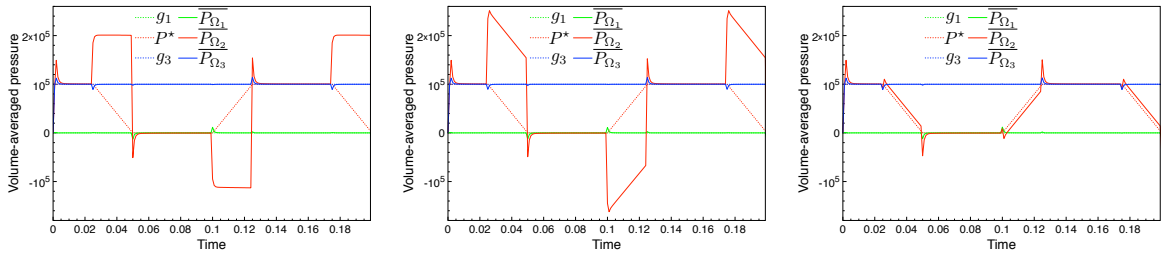

(a) Without correction. (b) With partial correction. (c) With correction.

Figure 3.12 – Time history of the computed pressures, in CGS unit, obtained for the cases T_3.

3.2.2 Realistic physiological model

Since the pressure correction introduced in Section 3.1 has proved its benefits in correcting the intraventricular pressure of the toy problem model in several settings, we would like to apply it on a more physiological case. As the value of the intraventricular pressure is used to decide the

status – active or inactive – of the resistive immersed surfaces [49], its good evaluation is crucial to get the correct behavior of the valves. This is the main focus of the following numerical experiment on a physiological human heart geometry.

We consider, for the fluid domain Ω, a realistic portion of the human left heart, as depicted in Figure 3.13a. For simplicity, we will use the physiological terminology of the cardiology to designate the different parts of the considered computational domain. Based on the previous notations of Section 3.1, the computational domains Ω_1, Ω_2, Ω_3 correspond, respectively, to the portion of the atrium, to the full ventricle and to the portion of the aorta, as shown in Figure 3.13b. The typical dimensions of these computational domains are based on the physiological ones. All the units are given in the CGS units system. The different geometries come from a CT scan realized by the Zygote company. The immersed resistive valves, Σ_{12} and Σ_{23}, correspond, respectively, to the mitral valve (see Figure 3.13c) and to the aortic valve (see Figure 3.13d). The former has been designed with the software 3-matic from physiological *in vivo* data [15, 105, 106, 17, 107] whereas the latter is already included in the Zygote human heart model we use.

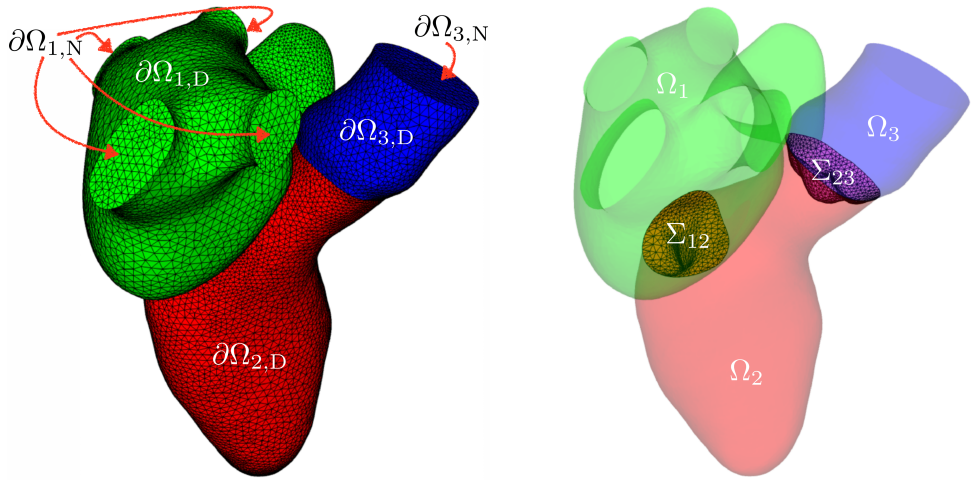

(a) Exterior of the fluid domain.

(b) Interior of the fluid domain.

(c) Immersed surface Σ_{12}.

(d) Immersed surface Σ_{23}.

Figure 3.13 – Computational domains used for the realistic model.

The physical parameters for the fluid are $\rho = 1.06$ and $\mu = 0.04$. The simulations are carried out for a total time of $t = 0.85$, based on averaged physiological values for the heartbeat of a young adult [108], with a time step $\tau = 10^{-3}$. The fluid is initially at rest. The whole computational domain Ω is made of 326 090 tetrahedron. The immersed surfaces, Σ_{12} and Σ_{23} are made of, respectively, 816 and 1 474 triangular elements.

As regards the boundary conditions, a no-slip boundary condition is enforced on $\partial\Omega_{1,\mathrm{D}} \cup \partial\Omega_{2,\mathrm{D}} \cup$

$\partial\Omega_{3,\mathrm{D}}$. The surface velocity $\boldsymbol{w}|_{\partial\Omega_{2,\mathrm{D}}}$ is obtained from an electromechanical simulation [91] in order to enhance the physiological validity of the considered numerical example. The pressure is prescribed on the inlet $\partial\Omega_{1,\mathrm{N}}$ – corresponding to the cut ends of the pulmonary veins – as well as on the outlet $\partial\Omega_{3,\mathrm{N}}$ – corresponding to the lower cut section of the aorta – using Neumann normal boundary conditions:

$$\begin{aligned}\boldsymbol{\sigma}(\boldsymbol{u},p)\boldsymbol{n} &= -g_1\boldsymbol{n} \quad \text{on} \quad \partial\Omega_1,\\ \boldsymbol{\sigma}(\boldsymbol{u},p)\boldsymbol{n} &= -g_3\boldsymbol{n} \quad \text{on} \quad \partial\Omega_3.\end{aligned}$$

The amplitude of these pressures, respectively denoted g_1 and g_3, is given by time-dependent functions coming from the above-mentioned electromechanical model. Their values are depicted on Figure 3.14. In addition, the physiological ventricular pressure $P^\star$, also depicted in Figure 3.14, used in the corrective term (3.10), comes from the same electromechanical simulation. Finally, a backflow stabilization based on a local regularization of the fluid velocity along the tangential directions on the Neumann boundaries [88] is applied on $\partial\Omega_{1,\mathrm{N}}$ and on $\partial\Omega_{3,\mathrm{N}}$.

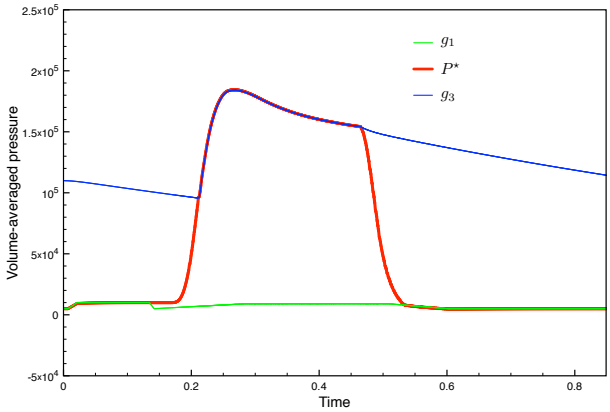

Figure 3.14 – Time history of the reference pressures, in CGS unit, used for each cavity of the realistic model.

The surface displacement prescribed on $\partial\Omega_{2,\mathrm{D}}$ is extended to the rest of the domain using an appropriate non-linear lifting operator [104] (denoted $\boldsymbol{\mathcal{L}}$ in Section 3.1.1). Figures 3.15a–3.15c present some typical snapshots of the resulting displacement field, applied to the computational domain, respectively, at $t = 0$ (initial state), $t = 0.2$ (maximum contraction state) and $t = 0.5$ (maximum dilatation state).

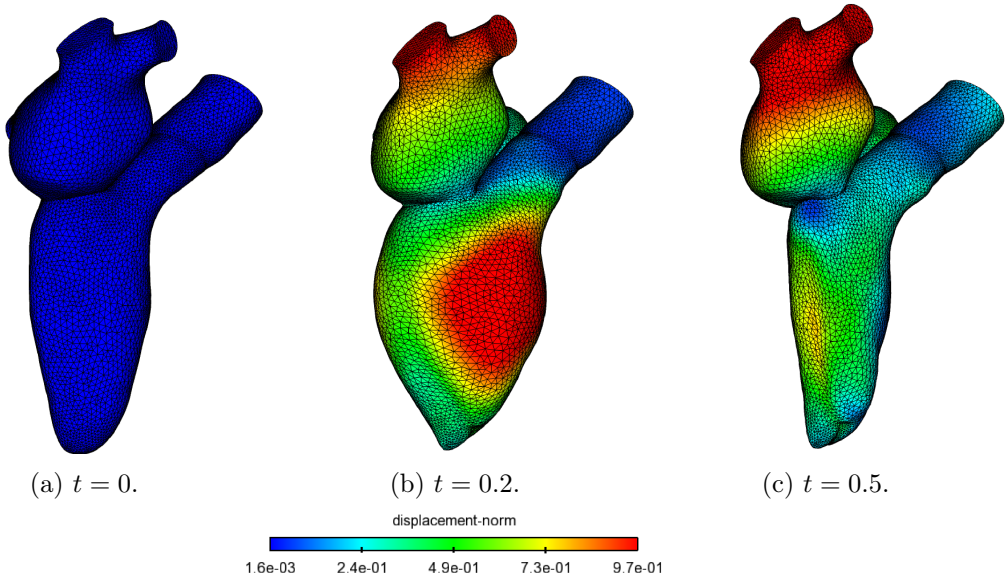

(a) $t = 0.$ (b) $t = 0.2.$ (c) $t = 0.5.$

Figure 3.15 – Snapshots of the displacement magnitude of the computational domain obtained for the realistic model.

In this realistic model, the values of R_{12} and R_{23} are no more arbitrarily prescribed but automatically handled by the physics of the problem, and more specifically by the local values of the velocity and pressure fields near the immersed surfaces. When a valve is closed, it will open if there is a positive pressure jump across it. On the opposite, when a valve is open, it will close if there is a backflow detected through its corresponding open surface. The corresponding physical decision criteria are depicted on Figure 3.16. For the immersed surface Σ_{12}, positive pressure jump and existing backflow mean, respectively, $p^+ - p^- > 0$ on Σ_{12} and $\int_{\Sigma_{12}} \boldsymbol{u} \cdot \boldsymbol{n}^+ < 0$. For the immersed surface Σ_{23}, it means, respectively, $p^- - p^+ > 0$ on Σ_{23} and $\int_{\Sigma_{23}} \boldsymbol{u} \cdot \boldsymbol{n}^- < 0$. A refractory time, typically set to a few time steps, is introduced to prevent the valve from changing its status immediately after a first switch. This arbitrary constraint ensures a full development of the flow physics near the valve.

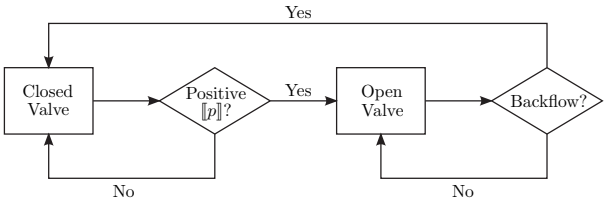

Figure 3.16 – Flow chart representation of the resistive immersed surfaces for the realistic model.

Based on the pressure values previously depicted in Figure 3.14, two short isovolumetric phases (respectively defined by the time intervals $[t = 0.135, t = 0.215]$ and $[t = 0.465, t = 0.533]$) are then expected. The evolution of the volume of the cavity Ω_2, given by the previous mentioned electromechanical simulation, is portrayed in Figure 3.17. As observed in real physiological cases [109], the dilatation of the ventricle lasts longer than its contraction. Two zooms (the blue arrows) show that the incompressibility constraint is not perfectly verified during the iso-

volumetric phases. Therefore, the full pressure correction (3.12) is expected to be mandatory to compute the correct values of the pressures and hence the correct behavior of the resistive immersed valves.

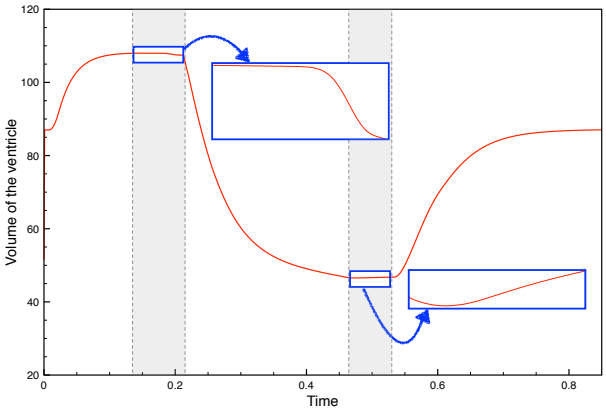

Figure 3.17 – Time history of the volume of the ventricle for the realistic model. The gray areas delimit the expected isovolumetric phases.

In what follows, the ARIS model is applied on this realistic model and the results obtained without pressure correction are compared with the ones obtained by using the corrective term given by (3.10).

To assess the sensitivity of the efficiency of the pressure correction with respect to the parameter R_i and to confirm our previous choice, the same analysis, as the one described in Section 3.2.1, is carried on here. The set of values used for the resistive parameter R_i are still

$$R_i = \{10^i,\, i = 0 \dots 10\}.$$

Eventually, as the structure of the flow dynamics inside the ventricle can be used as a predictor of diseases or malfunction [8, 58], it is crucial to ensure that the new pressure correction does not perturb the velocity field. A comparative study of the velocity and pressure fields obtained during the first isovolumetric phase, with and without the pressure correction, is undertaken in order to highlight the absence of disruption. The first phase is the most pertinent for this comparison as its correct computation is crucial and mandatory to avoid perturbing the physics of the developed flow and, hence, the next time steps of the simulation.

3.2.2.1 Results

On Figure 3.18, the matching of the evolution of the pressures $\overline{P_{\Omega_2}}$ and $P^\star$, obtained with the pressure correction are compared for several values of R_i with respect to the time. The goal is to determine the optimal value of the resistive parameter.

Firstly, positive and negative peak values are observed for $\overline{P_{\Omega_2}}$, respectively, at $t \simeq 0.21$ and at $t \simeq 0.54$ (*i.e.*, respectively, just after the first and the second isovolumetric phases), on all cases. This behavior is similar to what has been observed for the toy model in Section 3.2.1.1. Moreover, even for a case where the pressure correction is not applied (*i.e.*, when $R_i = 0$),

the same pressure peaks are obtained, as depicted on Figure 3.18a. This highlights the fact that these local quickly decaying extrema for $\overline{P_{\Omega_2}}$ are not induced by the introduced pressure correction. A possible explanation would be that the resistance changes, due to valve opening and closing, are explicitly imposed to the fluid. As a result, some time steps are required for the fluid to adapt to these topological changes, inducing pressure oscillations. We refer the reader to the conclusion for some perspectives on how to tackle this behavior.

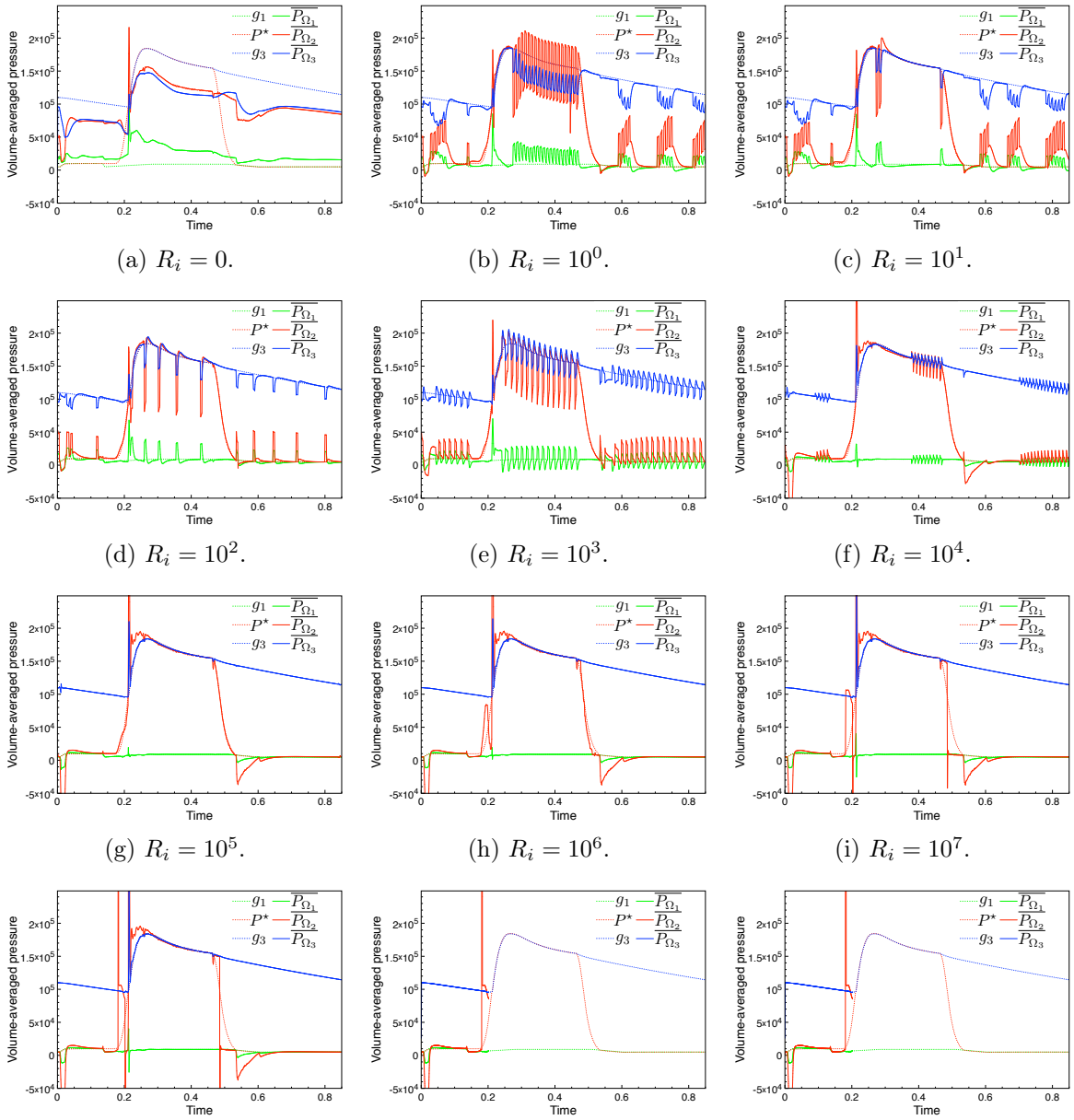

(a) $R_i = 0$. (b) $R_i = 10^0$. (c) $R_i = 10^1$.

(d) $R_i = 10^2$. (e) $R_i = 10^3$. (f) $R_i = 10^4$.

(g) $R_i = 10^5$. (h) $R_i = 10^6$. (i) $R_i = 10^7$.

(j) $R_i = 10^8$. (k) $R_i = 10^9$. (l) $R_i = 10^{10}$.

Figure 3.18 – Time history of the computed pressures, in CGS unit, obtained with pressure correction for different values of R_i for the realistic model.

Figure 3.18a depicts the case where no immersed valve is used (as R_i is set to 0) and where the

matching of the pressures is hence, obviously, impossible to obtain. The computed pressure $\overline{P_{\Omega_2}}$ of Figures 3.18b–3.18f fail to match the reference $P^\star$ outside the isovolumetric phases, due to the bad behavior of the immersed valves which keep fluctuating quickly between their closed and open configurations. This phenomenon is illustrated by the pressures oscillations. Among all the cases, the best pressures matching is obtained for $R_i = 10^5$, as observed on Figure 3.18g. When the resistance is increased beyond this optimal value, results start to worsen, especially for the first isovolumetric phase, as depicted on Figures 3.18h–3.18j. For the case $R_i = 10^6$, portrayed on Figure 3.18h, even if $\overline{P_{\Omega_2}}$ is confined between $\overline{P_{\Omega_1}}$ and $\overline{P_{\Omega_3}}$, it is not monotonous, as it should be in a physiological case. For the two following cases, due to the inaccurate computed physics, and more precisely the wrong intraventricular pressure, the valve status change several times during the isovolumetric phases while they were supposed to keep being closed. Beyond the case of $R_i = 10^8$, where $\overline{P_{\Omega_2}}$ present very strong oscillations for $t \in [0.135, 0.215]$ and for $t \in [0.465, 0.533]$, as represented on Figure 3.18j, the other cases fail to converge and the simulations stops around $t = 0.2$, as portrayed on Figures 3.18k–3.18l. Based on this study, in the following, the value of the resistance R_i is now set to 10^5.

Figures 3.19a–3.19b depict the pressure curves coming from, respectively, the case without and with the use of the corrective term (3.10), both for the optimized value of $R_i = 10^5$. It must be noted that, except for the isovolumetric phases, the computed pressures between both cases are almost perfectly identical. This underlines the fact that the corrective term, only used during the isovolumetric phases, does not have an impact on the other instants of the simulation, as expected.

As portrayed in Figure 3.19a, for the case without correction, $\overline{P_{\Omega_2}}$ is not well-defined when both valves are closed and get arbitrary values. Therefore, this induces wrong behaviors of the immersed valves. On the opposite, when the corrective term is applied, $\overline{P_{\Omega_2}}$ is now correctly defined and the computed pressures match the reference ones, as highlighted in Figure 3.19b.

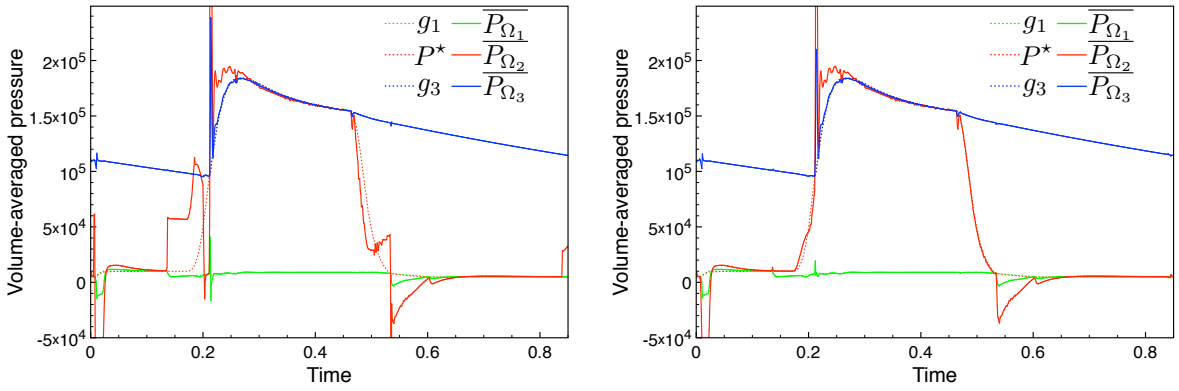

(a) Without correction.

(b) With correction.

Figure 3.19 – Time history of the computed pressures, in CGS unit, for the optimized value of $R_i = 10^5$ for the realistic model.

The time history of the valves status of each immersed surface Σ_{12} and Σ_{23} obtained for the cases without and with pressure correction are depicted, respectively, on Figures 3.20a–3.20b. Major differences are observed during the first isovolumetric phase: non-physiological changes of configuration of each valve are obtained when no pressure correction is applied while the expected

correct behavior, similar to the one used for the toy model on Figure 3.7a, is obtained with the pressure correction. This difference of behavior is crucial to correct as a wrong isovolumetric phase will induce a erroneous computation of the flow characteristics during the rest of the simulation.

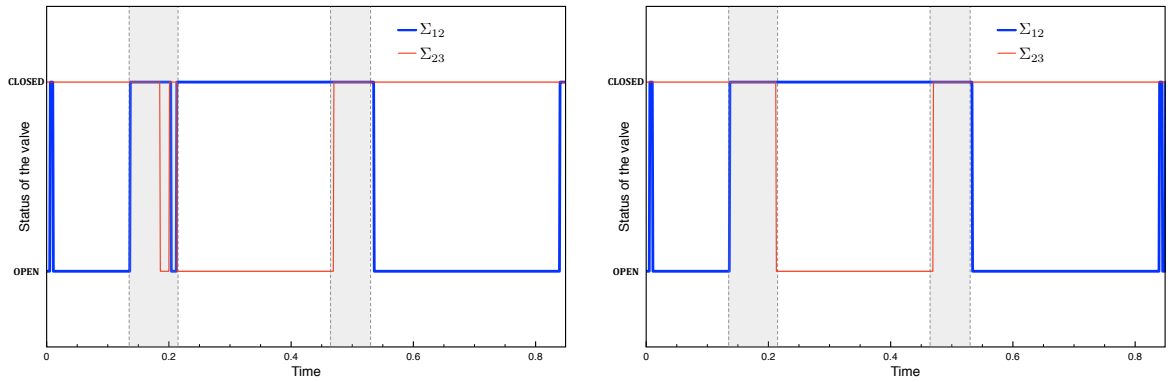

(a) Without correction. (b) With correction.

Figure 3.20 – Time history of the status of the valves obtained for the realistic model. The gray areas delimit the expected isovolumetric phases.

Figures 3.21a–3.21b present the snapshots of the velocity field obtained during the middle of the first isovolumetric phase, at $t = 0.185$, respectively, for the case without and with pressure correction. The same typical features of the velocity field, especially its vorticity, are obtained for the two cases, illustrating the fact that the additional normal stress term (3.8), applied on the immersed surfaces, keeps the velocity field comparable.

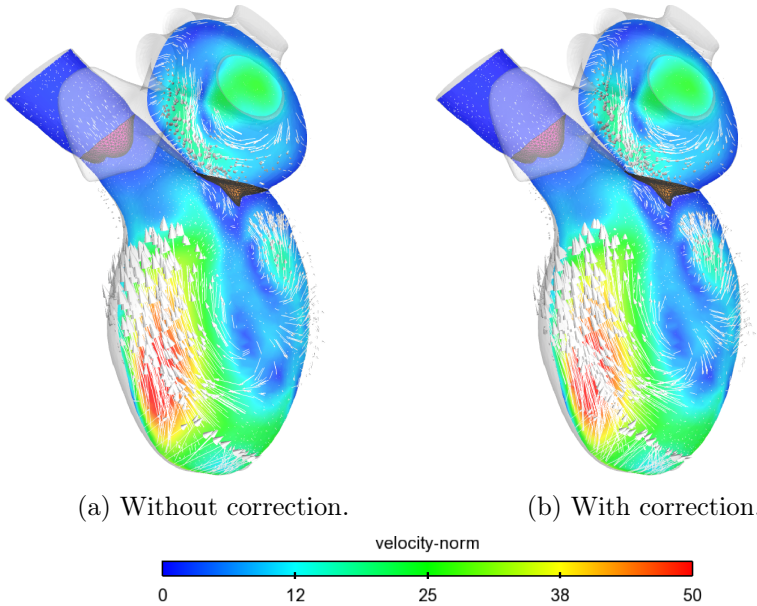

(a) Without correction. (b) With correction.

Figure 3.21 – Snapshots of the velocity field obtained at $t = 0.185$ for the realistic model.

Snapshots of the pressure fields obtained without and with optimized pressure correction are

given in Figures 3.22a–3.22b, respectively. On both figures, observation of the ventricular cavity reveals that even though P_{Ω_2} is not perfectly homogeneous on the scale of the ventricle – as it is assumed in (H2) – the pressure values near the first immersed surface Σ_{12} and near the second immersed surface Σ_{23} are approximately equal. This observation highlights the fact that using the same value P_{Ω_2} for the negative sided-restrictions of the pressure p^- in equations (3.5) and (3.6), respectively, for both immersed surfaces Σ_{12} and Σ_{23}, is coherent.

Based on the reference pressures of Figure 3.14, $\overline{P_{\Omega_2}}$ is expected, at $t = 0.185$, to belong to the interval of values $\left[\overline{P_{\Omega_1}}, \overline{P_{\Omega_3}}\right]$. The intraventricular pressure is correctly computed when pressure correction is applied whereas, when there is no correction, its value is overestimated and even exceed the aortic one, as illustrated on Figure 3.22a. This highlights the benefits brought by the pressure corrective term (3.10) concerning the computation of the correct intermediate values for the pressure during the isovolumetric phases.

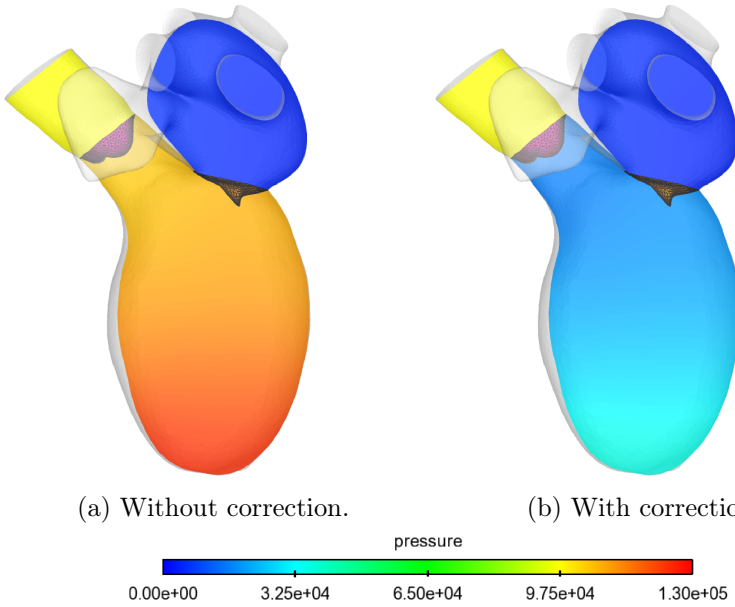

(a) Without correction. (b) With correction.

Figure 3.22 – Snapshots of the pressure field obtained at $t = 0.185$ for the realistic model.

3.3 Conclusions and perspectives

In this chapter, a new reduced model for heart valves has been introduced for the description of the isovolumetric phases within an uncoupling approach.

In Section 3.1.1, the original RIS model [89, 49] has been recalled and its application to heart valves modeling has been presented. The generic problem of a fluid cavity enclosed by two closed RIS valves has been considered by providing an estimate of the internal pressure in Section 3.1.2. A simplified expression estimating the pressure of the cavity has been derived, highlighting that its value depends on several parameters including the exterior pressures, the resistive term of the RIS model and the wall cavity velocities. This analysis proved why realistic isovolumetric phases could not be obtained with the standard RIS model. In Section 3.1.3, the new reduced model, called ARIS, has been presented. An additional normal stress term was introduced in

order to counteract the contributions of the exterior pressures and wall velocities.

In Section 3.2, two numerical examples have been considered to illustrate the benefits of this new approach. First, a toy model with a simplified geometry has been designed to reproduce the main characteristics of more complex heart simulations. Arbitrary pressure values and several different domain motions have been prescribed to test the efficiency of the ARIS model in different configurations. The second numerical example has consisted of a physiological left heart geometry where the pressure values and domain motions were provided by an external electromechanical simulation. In all those cases, the original RIS model failed to properly model the intracavity pressures and the valve behavior during the isovolumetric phases. These experiments highlighted that the intracavity pressure could be computed using the pressure estimate described by (3.4). It also highlighted that the violation of the incompressibility constraint and its correction is a key challenge to compute the correct intraventricular pressure during the isovolumetric phases.

In both numerical examples, an analysis of the influence of the valve resistive parameter R_i showed that a trade-off had to be made between a proper correction of the intracavity pressure and an acceptable impermeability of the valves. Indeed, the introduced corrective term benefits from the fact that the RIS model is penalizing the fluid on the immersed surfaces and is only enforcing Dirichlet boundary conditions in a weak sense. However, as the resistive term keeps increasing, the RIS model converges toward a singular problem equivalent to imposing only Dirichlet boundary conditions. In this setting, the pressure correction was not working anymore.

The optimum value of R_i has been determined in each example and its use in the ARIS model led to strong improvements in the physiological validity of the mathematical models compared to the traditional RIS model. In the realistic model, it was shown that the ARIS model was able to control the left ventricular pressure during the isovolumetric phases resulting in a better physiological behavior of the valves. Moreover, the ARIS model properly corrected the intracavity pressure without alteration of the velocity field and its main features.

The proposed approach therefore offers a good compromise between standard uncoupling and complex FSI models. By expanding the original RIS formulation with an additional reference value, the physiological behavior of the intracavity pressure during the isovolumetric phases is partially recovered without using fully coupled fluid-structure models. Nevertheless, one limitation of applying the ARIS formulation is the potential difficulty to obtain such reference data. In particular, when aiming to produce patient-specific simulations, recovery of the intraventricular pressure by catheterization is an invasive procedure and might not always be possible.

Moreover, it must also be reminded that the simplifications introduced by using this reduced model might affect and disrupt the intraventricular flow. As mentioned in Section 3.2.2.1, some pressure oscillations were observed due to the explicit treatment of the reduced valve model. A first approach to circumvent this issue could be to formulate the valve dynamics as a nonlinear constraints on the fluid velocity. Another interesting extension of this work could be to compare the results coming from the ARIS model with the ones coming from a fully coupled FSI simulation in order to quantify the potential inaccuracies induced by the current simplified approach.

Part II

Image/Model fusion for MR severity quantification

Introduction

The first part of this manuscript discussed the modeling of intracardiac hemodynamics in a generic heart. While such model already provides some useful information regarding hemodynamics, the current trend in the modeling and simulation community is to personalize the models using patient-specific data, geometry and dynamics derived from imaging devices such as CT [84, 110, 79, 75], MRI [111, 112] or echocardiography [113, 112].

The reasons behind this trend is multi-fold. First, by exploiting the patient-specific hemodynamics, relevant clinical information can be obtained [114]. For example, local informations that cannot be directly obtained on the images, such as the pressures, can be obtained from the models. Moreover, if the predictive power of the resulting models are good enough, medical interventions can be simulated in advance to predict their outcomes and provide tailored care to patients. Finally, by building a big database of *in silico* cases based on real patients, the medical community can build a statistical description of the population hemodynamics. Personalizing models, however, brings several additional layers of complexity.

Focusing on intracardiac hemodynamics, several steps are usually required to personalize 3D CFD models based on patient-specific images. The cardiac cavities are first segmented in order to extract the cardiac geometry and dynamics. While this step is nowadays mainly automated, thanks to robust image processing algorithms, the resulting segmented surfaces usually need to go through a serie of operations including mesh cleaning, valve insertion, volumetric mesh generation, surface labeling, inlet and outlet extrusions and refinement of region of interest. Finally, the cardiac dynamics also need to be extracted before being used as boundary condition of the numerical simulations [114]. It has been reported in a recent review of patient-specific cardiac flow simulations that "20-50 hours of human effort are needed for these pre-processing steps" [61] (See also [114]).

Philips Healthcare provides tools to help physicians with the manipulation of the acquired images. More specifically, automatic algorithms were developed to segment and track the cardiac cavity surfaces during the cardiac cycles using echocardiography. Chapter 4 details how such tools can be used. A fully automated pipeline is presented which aims at producing patient-specific numerical simulations while minimizing the required pre-processing time. The proposed pipeline is used in combination with Real Time 3D Echocardiography sequences of 12 volunteers to assess the benefits and limitations. Several synthetic MR are also introduced to investigate the potential variability of the resulting hemodynamics and to propose an assessment of the PISA technique.

Are medical images the holy grail? A focus on the ventricular twist

While it is clear that personalizing the numerical simulations can provide valuable knowledge, the use of medical images is nevertheless not exempt of pitfalls. Echocardiography, for example,

provides information about the LV surface location and the achieved temporal resolution is sufficient to recover the heart dynamics. However, this imaging technique is not sufficient to accurately track specific material point of the heart muscle. As a result, some physiological events such as the ventricular twist may not be properly captured [6].

To understand why this matter might be important, let us describe shortly the physiology of the ventricular twist (based on [115, 116, 6]). The origin of this twist lies in the complex architecture of the heart muscle: the ventricular wall can be decomposed in layers, from the endocardium to the epicardium, in which the myocardial fibers gradually change orientation. The resulting arrangement of muscle fibers leads, during the ventricular systole, to a rotation of the apex in a counter-clockwise direction, while the base rotates clockwise. During diastole, the ventricle recoils back to its initial position. The role of this twist is still not completely understood. Nevertheless, several attempts to explain its importance have been made. One of its possible role would be to increase the ejection fraction of the human heart: as the myocardial fibers only contract by 15 to 20% in the fiber direction, the twisting is believed to help increase the ejection fraction to its physiological range of approximately 50 to 70%.

In the context of electro-mechanical simulations of the myocardium, the inclusion of fiber orientation is of major importance; first, the orientation of the fibers affects the heterogeneous propagation of the electrical waves. As the muscle contraction is triggered by the arrival of the electrical signal, a physiological representation of the electrical propagation is required to avoid a non-physiological propagation of the fiber contraction. For this reason, modeling realistic twisting motion is an important key ingredient to achieve physiological contraction of the heart [117, 118].

In the context of the blood flow simulation, however, the importance of ventricular torsion is still not well understood. In idealized geometries, some studies reported that the impact of ventricular torsion on the flow was small [20, 119]. Such work has nevertheless not yet been carried out with physiological geometries. One particularly important reason is that, depending on the image acquisition process, the LV material points are not tracked and the ventricular twist might not even be recoverable. Often, the absence of ventricular torsion is reported as a limitation of these studies [120, 113, 98]. In some other studies, the uncertainty of the processing pipeline led authors to be cautious about the truthfulness of the boundary condition imposed to the blood flow [99].

MRI tagging [121, 122], as well as speckle tracking echocardiography [123, 124], have been employed to report and quantify more accurately the heart twist. It is, however, difficult to properly recover ventricular twisting from the cardiac images in standard medical exam using echocardiography. S. Nakatani [6] reported several limitations with respect to LV twisting measurement, such as inter-vendor variability of the speckle tracking or the impact of LV motion along the longitudinal direction on the measurement. On top of the difficulties of properly recovering LV torsion from the images, all the geometry reconstruction steps (*e.g.,* the automatic LV wall segmentation) might introduce a loss of information regarding the LV torsion.

The objective of Chapter 5 is to investigate in more detail the influence of properly including LV wall torsion on the intracardiac hemodynamics in the context of physiological geometries of the left ventricle. Starting from LV surface which includes ventricular twisting, we propose a method to generate an alternative version in which the ventricular twist is removed while keeping the surface location as close as possible to the initial data. Comparing the hemodynamics will allow

to quantify the actual influence of the LV torsion.

The need for simplified models in a clinical setting

Significant constributions have been achieved to model 3D intracardiac hemodynamics. Indeed, those models can provide very detailed information about the blood flow, about the influence of personalized dynamics, or about current medical tools. Nevertheless, even if efforts are made to limit the computational complexity, customizing a model and solving the mathematical equations of such complex 3D model still takes a long time, with an order of magnitude of a few hours [61, 114]. This is not feasible in a clinical setting where a clinical exam duration is on the order of a few tens of minutes [125].

The PISA method can help quantify the MR in a very short time-insterval: based on a few simplifying assumptions, this simplified model allows the physician to quantify the MR using a very limited number of measurements. As a result, the PISA method is extremely time-efficient. However, this method suffers from many shortcomings, making the measurement imprecise and difficult to reproduce [38, 30, 29]. It is therefore necessary to find a compromise between complex 3D models, which are precise but computationally too expensive, and the PISA model, very fast but also imprecise due to its extreme simplicity, to improve cardiac exams and, eventually, MR severity quantification. It is in this context that the need for so-called "simplified" model is felt. As echocardiography exams are very fast to implement in a clinical setting, it seems intuitive to use US images to feed information to such models.

Several strategies, different in spirit, can be opposed when it comes to using images in combination with numerical simulations: a first family consists in using the information coming from the medical images to improve the numerical simulations. For example, the Luenberger estimation [126], also called *nudging* in more recent terminology [127, 128, 129], consists of adding a feedback term, based on the observed data, to correct the dynamics predicted from a coarse mathematical model. Another example would be to generate a reduced basis for the intracardiac hemodynamics – based on the images or based on previously computed complex simulations – and to project the model equations onto this new basis. This strategy – called *reduced order modeling* (ROM) – has indeed been used to approximate patient-specific blood flow with some success [130]. Difficulties were nevertheless encountered due to the sensitivity of the method with respect to the transport of the basis from one geometry to another.

Another strategy consists not to use images to improve numerical simulations, but to use models to improve the echocardiographic images. While the difference seems minor, the resulting techniques differ quite a bit. For example, techniques aimed at reconstructing 2D [131] and 3D [132] velocity fields, by combining the measurements from several US probes, have been proposed. As positioning several probes simultaneously is tricky in a clinical setting, an active field of research rather focuses on reconstructing the velocity fields using views from a single probe. 3D Navier-Stokes equations were combined with the image data in an inverse problem to reconstruct the missing velocity components [133]. This approach is nevertheless quite computational demanding as it requires to solve several 3D N-S problems. A much simpler approach has been presented by Assi et al. [134] in which a 2D blood velocity field is reconstructed by considering an optimization problem based on the minimization of a cost function including image terms and physically based constraints.

In Chapter 6, it was chosen to pursue this last direction to reconstruct the blood velocity field. We first describe in detail the theory behind the method to provide some intuition to the reader. Using an optimization problem close to what was presented by Assi et al. [134], we propose a way to reconstruct 2D blood velocity fields. That reconstruction is then extended to 3D velocity fields. To assess the technique, several numerical examples are introduced to quantify how well the blood velocity field is reconstructed. This technique is also applied to pathological blood flow to assess how the reconstruction could be beneficial to MR quantification.

Chapter 4
A pipeline for image-based CFD modeling and application to the evaluation of the PISA method

In this chapter, we propose a strategy to combine patient-specific data with the numerical simulations of blood flow presented in the first part of this manuscript. Using the software *QLab, 3DQAdvanced Plugin (Philips, Andover, MA)*, RT3DE images can be processed to obtain sequences of surfaces that depicts the LV surface and its dynamics. Instead of manually processing the segmented surfaces, a methodology is proposed to minimize the amount of pre-processing work. The basic idea is to morph a generic mesh to produce a personalized geometry, an idea borrowed from the field of bone mechanics [135, 136].

In Section 4.1, a fully automated pipeline is presented. In Section 4.1.1, different types of registration methods are combined in order to produce a personalized geometry: an affine registration is first performed to produce an initial, coarse, overlap of the two geometries. Subsequently, a deformable registration is then used to deform the local ventricular geometry and to produce a patient-specific geometry. Section 4.1.2 describes the transfer of the LV dynamics from the segmented mesh sequence onto the personalized geometry. The full pipeline is summarized in Section 4.1.3.

In Section 4.2, twelve RT3DE sequences from healthy volunteers are used to highlight the benefits and limitations of the proposed pipeline. Several synthetic pathological cases are also introduced to investigate the potential variability of MR hemodynamics and to assess the PISA technique.

4.1 Fully automated patient-specific pipeline

In this section, we present a pipeline which automatically perform all the pre-processing steps required to combine RT3DE sequences with a generic simulation. A reference frame is automatically chosen in the RT3DE sequence to represent the base patient-specific geometry. Using the geometrical domain described in Section 2.1 as the generic mesh, several key differences between the two meshes can be highlighted:

1. The topology, position in space, local geometry and size of the ventricular surfaces are different;
2. The spatial discretization of the generic domain is different from the patient-specific segmentation;
3. The time sampling of the echocardiography is not fine enough for CFD simulation.

Sections 4.1.1 describes how to adapt the generic mesh to the patient-specific ventricular segmentation, taking into account the first difference, while Section 4.1.2 describes the transfer of the patient-specific ventricular dynamics to the deformed generic mesh, taking into account differences 2 and 3.

4.1.1 Generic mesh registration

First, we describes a way to deform a generic mesh to fit the geometries obtained by RT3DE cardiac sequence segmentation. In the following, a schematic representation will be used in order to illustrate the different steps of the proposed method. An example of such schematic representation can be seen on Figure 4.1. The different cavities are simplified to a 2D representation and different colors will be used to represent the generic mesh (in red in the figure) and personalized geometry (in blue in the figure).

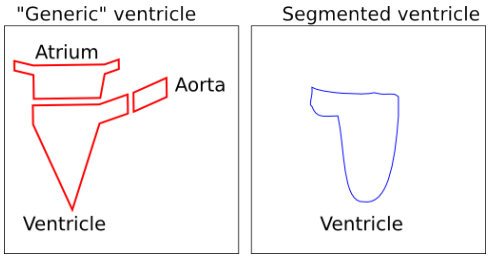

Figure 4.1 – Schematic representation of the generic and segmented meshes.

In their initial state (See Figure 4.2a), the generic mesh and segmented mesh have different local geometries. Moreover, their position in space, their topology and their size are different. As no atrium and aorta exist in the segmented mesh, those two elements will not be used to drive the registration process. Figure 4.2b represents this simplification of topology. It has to be noted that those two elements will be reintroduced later on.

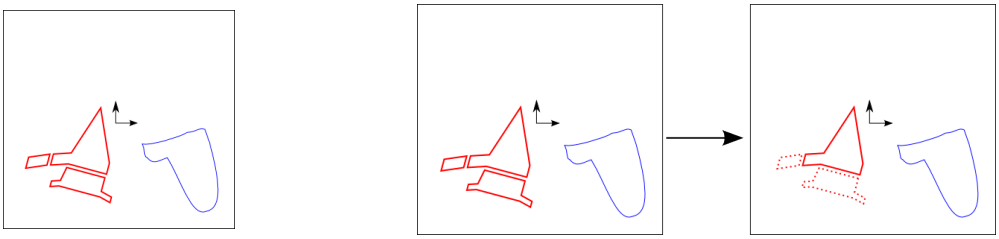

(a) (b)

Figure 4.2 – (a) Initial state and (b) topology simplification step.

Registration is the process of transforming different sets of data in order to align them in a common environment. The objective of a registration algorithm is to find a spatial transformation Φ that maps the position of an object A onto another object B. This amounts to minimize the distance between $\Phi(A)$ and B under some appropriately chosen norm.

As the two LV surfaces exhibit positioning differences as well as local surface differences, a

two-step strategy is proposed to handle this registration process. First, an initial affine transformation Φ_1 will be used to register the main anatomical parts of the generic ventricle to the patient-specific surface. A deformable transformation Φ_2 will then be used to deform this coarsely registered generic surface to fit patient-specific surface. The goal of this two-phase strategy is to use as much *a priori* information as possible in the first phase to simplify the requirements of the deformable registration phase, usually more computationally intensive.

Affine registration

The objective of the affine registration is to coarsely register the two ventricular surfaces. Formally, an affine map is a composition of a linear map and of a translation. While ordinary vector algebra would use matrix multiplication by $\boldsymbol{A}$ to represent the linear map and the addition of a vector $\boldsymbol{b}$ to represent translation, we chose to use the augmented matrix formulation:

$$\begin{bmatrix} \boldsymbol{y} \\ 1 \end{bmatrix} = \left[\begin{array}{ccc|c} & \boldsymbol{A} & & \boldsymbol{b} \\ 0 & \cdots & 0 & 1 \end{array}\right] \begin{bmatrix} \boldsymbol{x} \\ 1 \end{bmatrix} \tag{4.1}$$

By chosing this notation, it is possible to represent both the linear map and translation using a single matrix multiplication. As a result, one can compose several transformations by matrix multiplication. Considering rotation, translation and scaling matrices, one only needs to ensure that the scaling is not degenerate to claim that the composition is invertible. Inverting the full transform therefore either amount to inverting each matrix of the composition or to just invert the final matrix resulting of the composition.

To derive the transform that will coarsely register the generic mesh on the patient-specific data, the following *a-priori* information will be used:

a. The apex position is known for each LV mesh;

b. The aorta outlet position is known for each LV mesh;

c. The base to apex distance is known for each LV mesh.

First, the ventricles are translated to place their respective apex onto a common referential (transformation $\Phi_{1,\mathrm{t}}$ of the generic surface, Figure 4.3).

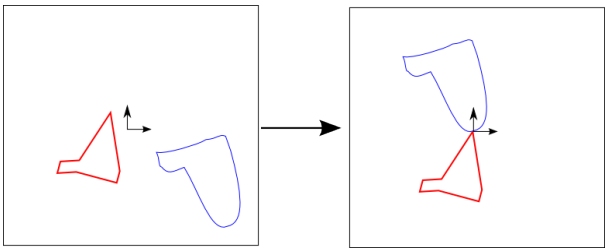

Figure 4.3 – Schematic representation of the translation step

As a second step, the ventricles are reoriented such that the long axis of the ventricles are aligned (transformation $\Phi_{1,\mathrm{la}}$ of the generic surface, Figure 4.4). As the ventricles are mostly elongated

and symmetrical, apart from the aortic tract, the long axis can be approximated as the vector pointing from the apex to the barycenter of the ventricle.

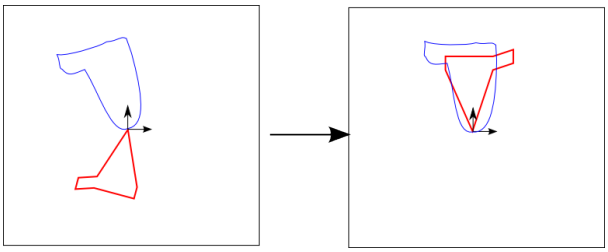

Figure 4.4 – Schematic representation of the long axis alignment step

The ventricles are then rotated about the long axis so that the aorta of both ventricles are aligned (transformation $\Phi_{1,\text{ao}}$ of the generic surface, Figure 4.5). To achieve that objective, the aortic axis of both meshes can be approximated as the normalized vector pointing from the apex in the direction of the aorta, orthogonal to the longitudinal direction.

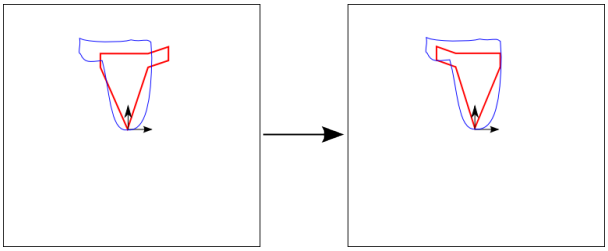

Figure 4.5 – Schematic representation of the aortic axis alignment step

Finally, the ratio of the base to apex distance of both ventricles is used to scale the generic ventricle to match the patient-specific ventricular longitudinal dimensions (transformation $\Phi_{1,\text{s}}$ of the generic surface, Figure 4.6).

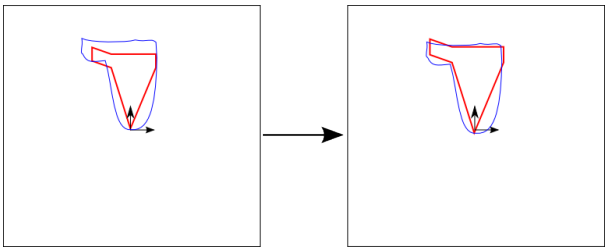

Figure 4.6 – Schematic representation of the scaling step

The total transformation Φ_1 of the generic surface is the composition of all the above transformation:

$$\Phi_1 = \Phi_{1,\text{s}} \circ \Phi_{1,\text{ao}} \circ \Phi_{1,\text{la}} \circ \Phi_{1,t}$$

Deformable registration

As a result of the first registration step, the two ventricle surfaces are considered superimposed with their main anatomical features positioned at approximately the same location. The objective of this second registration step is to obtain a transformation Φ_2 which fits the surface of the generic mesh onto the image segmentation. In order to maintain the original generic mesh integrity, several constraints are imposed: the deformable registration should not change the mesh connectivity, and mesh triangle elements should not be degenerated by the transformation. For those reasons, a special interest was given to the group of diffeomorphisms, a special class of maps which enforces those constraints.

Several registration algorithms have been proposed which ensure that the resulting transformation is a diffeomorphism such as the Diffeomorphic Demons [137] or the Large Deformation Diffeomorphic Metric Mapping (LDDMM) [138, 139, 140]. In this work, the open-source software *Deformetrica*, implementing the LDDMM framework, has been used [140].

In this software, n_{cp} control points $(\boldsymbol{q}_i)_{i=1,\cdots,n_{\text{cp}}}$ are positioned in the ambient $\mathbb{R}^3$ space. These control points are associated with a set of vectors $(\boldsymbol{\mu}_i(t))_{i=1,\cdots,n_{\text{cp}}}$ called *momenta* where $t \in (0,1)$ is a pseudo-time representing the evolution of the transformation. A dense velocity vector field $\boldsymbol{V}$ is defined in the ambient space by radial basis function (RBF) interpolation, namely,

$$\boldsymbol{V}_t(\boldsymbol{x}) = \sum_{i=1}^{n_{\text{cp}}} K(\boldsymbol{x},\boldsymbol{q}_i(t))\boldsymbol{\mu}_i(t), \tag{4.2}$$

where $K(\boldsymbol{x},\boldsymbol{y}) = \exp\left(\frac{\|\boldsymbol{x}-\boldsymbol{y}\|^2}{\sigma^2}\right)$ is a Gaussian kernel of width σ. This velocity vector field is integrated to deform the ambient space and the initial control points by solving

$$\begin{cases} \dfrac{\partial \boldsymbol{x}}{\partial t} = \boldsymbol{V}_t(\boldsymbol{x}), \\ \boldsymbol{x}(0) = \boldsymbol{x}_0. \end{cases} \tag{4.3}$$

It was shown that point trajectories are entirely determined by the initial control point positions $\boldsymbol{q}_i(0)$ and by the time-varying momentas $\boldsymbol{\mu}_i(t)$ [140]. It was also shown that such deformation belongs to the class of diffeomorphisms [141]. The registration algorithm aims to find a set of momenta $\boldsymbol{\mu}_i(t)$ such that a similarity criterion is minimized. As such set may not be unique, the set which minimizes the deformation kinetic energy is chosen.

Using *Deformetrica*, the transformation Φ_2, parameterized by $\left\{(\boldsymbol{q}_i(0))_{i=1,\cdots,n_{\text{cp}}},(\boldsymbol{\mu}_i(t))_{i=1,\cdots,n_{\text{cp}}}\right\}$ is obtained (Figure 4.7).

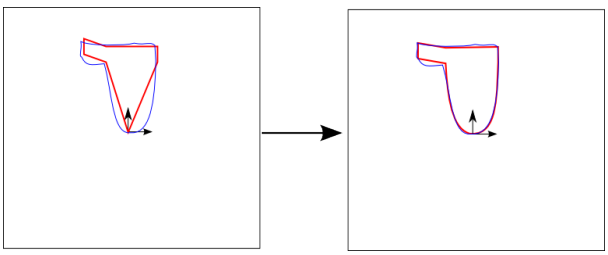

Figure 4.7 – Schematic representation of the non-rigid segmentation step

Final transform

The total deformation of space is obtained by composition of the affine transformation with the deformable transformation: $\Phi = \Phi_2 \circ \Phi_1$. As both Φ_1 and Φ_2 are maps defined on the entire Euclidean space $\mathbb{R}^3$, the composition Φ is too. The map Φ can therefore be applied on the original generic mesh which includes the aorta and the atrium. As a result, the full generic mesh is deformed, so that its ventricular surface fits the patient-specific ventricular surface. Moreover, this method choice ensures that the resulting map Φ is smooth and non-degenerate, thus preserving mesh topology, triangle orientation and global quality of the surface.

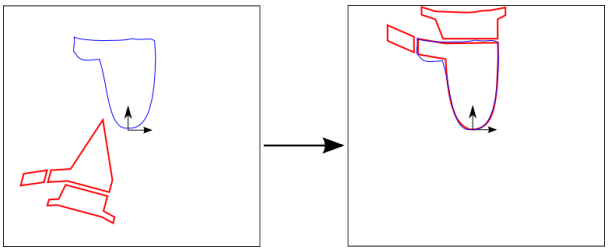

Figure 4.8 – Schematic representation of total registration.

4.1.2 Dynamics transfer

Even though a patient-specific geometry can be obtained using the previously computed map Φ, the LV dynamics from the RT3DE sequence cannot be directly applied as simulation boundary conditions for several reasons. First, the time-resolution of the RT3DE sequence depends on several physical factors and is therefore limited. The CFD simulations usually requires a time resolution ($\approx$ 1000 Hz) that is two orders of magnitude higher than the usual RT3DE time resolution ($\approx$ 30 Hz). As a result, temporal interpolation of the dynamics is required. Moreover, as the deformable registration is a result of minimizing a global energy functional, the two registered ventricular surfaces are not ensured to be exactly matching. This nonconformity of the two surfaces is accentuated by the fact that the resolution of the two surface mesh might also differ. Therefore, a spatial interpolation strategy is also required.

Temporal interpolation

The position of the vertices of the patient-specific ventricular surface is interpolated in time using cubic splines. The appropriate discrete displacement field is then produced by sampling the continuous curves using a time discretization fitting the required simulation time-steps. $\boldsymbol{d}^s_{t_n \to t_{n+1}}(\boldsymbol{x}_i)$ denotes the displacement vector of the i-th vertex of the segmented mesh s at time t_n to its position at time t_{n+1}.

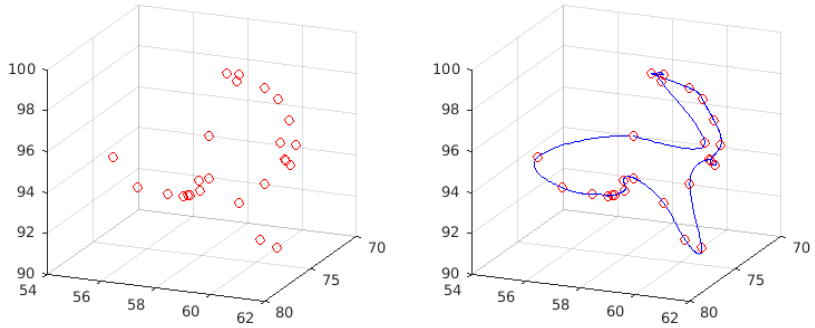

Figure 4.9 – The positions of a vertex at several time instant are depicted on the left image. On the right side, the vertex position with respect to time is interpolated using cubic spline.

Spatial interpolation

The dynamics of the patient-specific ventricle is then transferred onto the deformed generic mesh vertices using the normalized RBF interpolation framework using a Gaussian RBF ϕ parameterized by a smoothing parameter σ:

$$\boldsymbol{d}^g_{t_n \to t_{n+1}}(\boldsymbol{x}) = \frac{\sum_i \boldsymbol{d}^s_{t_n \to t_{n+1}}(\boldsymbol{x}_i)\phi(d_i,\sigma)}{\sum_i \phi(d_i,\sigma)}, \text{ with } d_i = \|\boldsymbol{x} - \boldsymbol{x}_i\| . \tag{4.4}$$

Here, the superscript g indicates that the displacement field is defined on the generic mesh vertices. Note that the RBF's only need to be computed once for each pair of vertices and can be reused for all time steps. The shape of the Gaussian basis function results in a quick decay of the weighting coefficient allowing to prioritize the closest nodes in the interpolation. The mean edge length of the patient-specific ventricular surface is used as the smoothing parameter σ ensuring that each surface vertex is covering a large enough region. Differentiability of the resulting interpolated displacement field is ensured by the choice of Gaussian RBF. The boundary displacement $\boldsymbol{d}^g_{t_n \to t_{n+1}}(\boldsymbol{x})$ is used as the boundary condition of (2.5).

4.1.3 Pipeline summary

The full patient-specific pipeline can be summarized by Figure 4.10: Using the RT3DE images, segmentation and tracking of the left ventricle is performed. A reference frame of the sequence is chosen and a combination of registration techniques are used to personalize a generic mesh. The patient-specific dynamics of the left ventricle is then interpolated, both temporally and spatially, to provide a displacement boundary condition on each node of the ventricle of the personalized mesh. The complete mathematical model described in Section 2.2.4 is then used to generate the hemodynamics using the personalized geometry and dynamics.

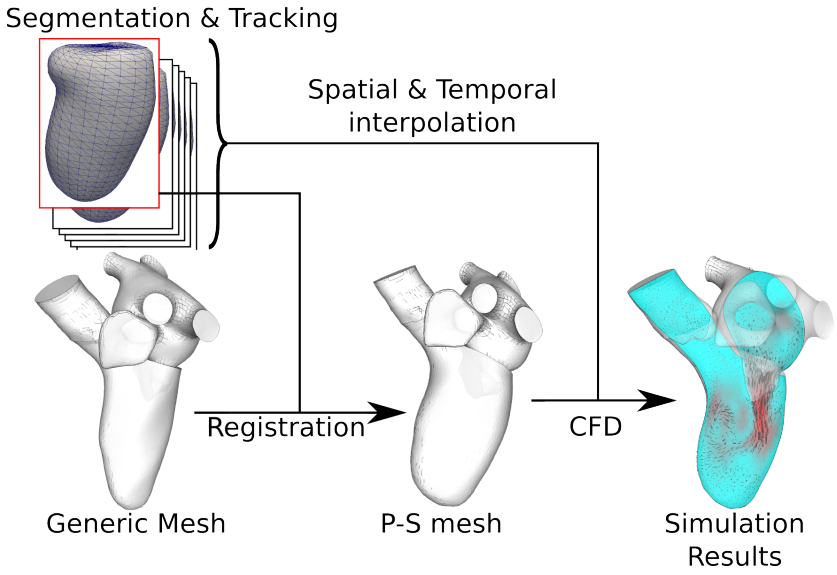

Figure 4.10 – Patient-specific pipeline. The sequence of segmented LV surfaces are combined with a generic mesh to first produce a P-S mesh. Interpolation of the LV dynamics provide the necessary boundary condition for the CFD simulations.

4.2 Application of the pipeline to 12 cases

In this section, the pipeline described in the previous section is applied to a database of 12 cases. The available cases are described in detail and we assess the pipeline capabilities both in term of accuracy and computational complexity. CFD simulations in healthy cases are produced and described to show the advantages of this methodology compared to using synthetic LV displacements. A series of synthetic pathological cases is also produced by applying the mitral regurgitation model described in Chapter 2. An evaluation of the PISA method is finally proposed using those different pathological cases.

4.2.1 Description of the available data

Echocardiographic images of twelve healthy volunteers were acquired using an IE33 ultrasound system (Philips, Andover, MA) equipped with a 1-5 MHz transthoracic matrix array transducer (xMATRIX x5-1). RT3DE images were reconstructed as volumes over one cardiac cycle from acquisitions of sub-volumes over four cardiac cycles. An example of such data is depicted on Figure 4.11. Using the software *QLab, 3DQAdvanced Plugin (Philips, Andover, MA)*, segmentation and tracking of the left ventricle was automatically performed. As a result, sequences of meshed surfaces depicting the left ventricle surface and dynamics were obtained. Each segmented surfaces are described by a triangular surface mesh that is composed of a constant number of 795 vertices and 1584 triangles. Examples of the resulting mesh in end-diastolic and end-systolic phases are respectively depicted on Figure 4.12a and 4.12b.

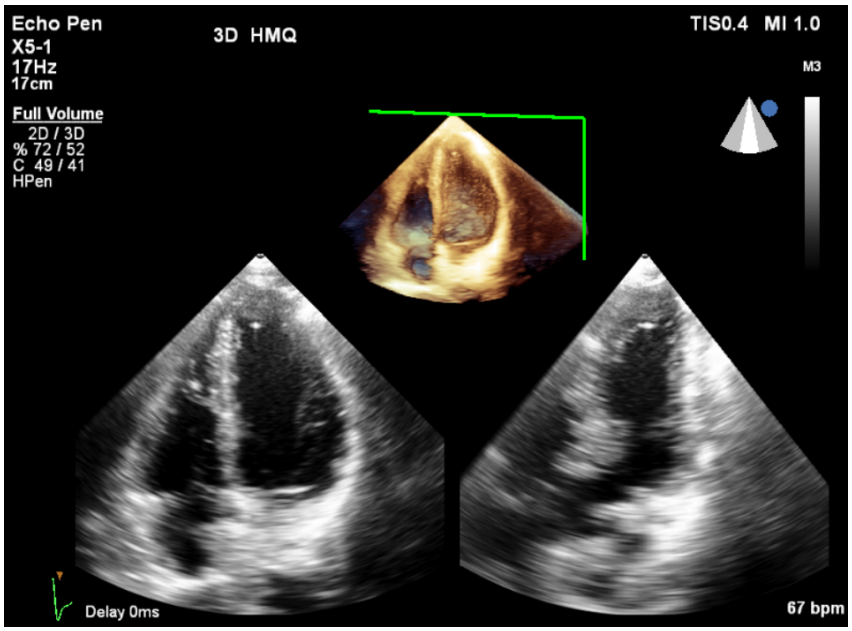

Figure 4.11 – Transthoracic RT3DE. In the figure, the top part depicts the heart tissue in 3D while the two bottom images depict the tissue information on two orthogonal planes.

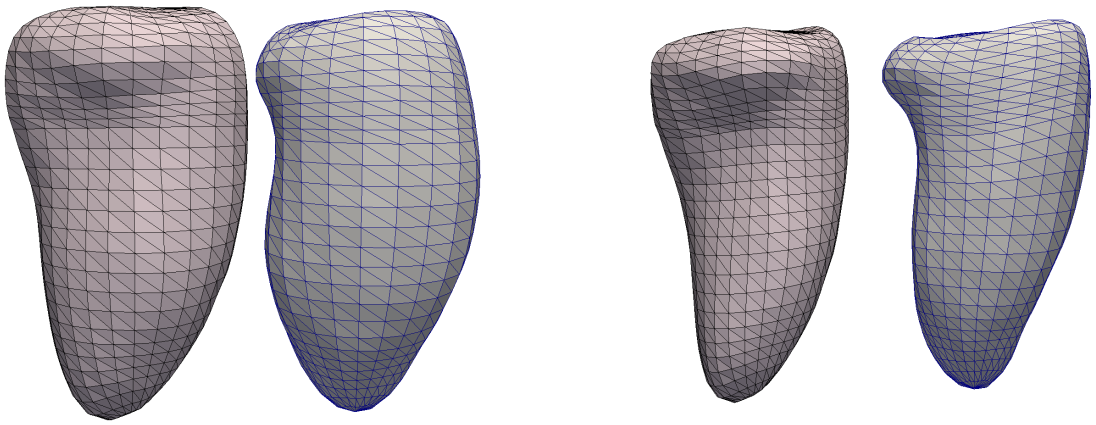

(a) C12_H end-diastolic LV segmentation

(b) C12_H end-systolic LV segmentation

Figure 4.12 – Meshes resulting of the RT3DE image segmentation

Table 4.1 sums up some characteristics about the different sequences. The sequences averaged 25 frames per cardiac cycle, ranging from 15 to 38. Computing the volume curve of each individual segmented sequence using the algorithm described in [142], the end-systolic volume ranged from 27.92 mL to 61.96 mL while the end-diastolic volume ranged from 47.81 mL to 130.27 mL across the database.

Case ID	ESV (mL)	EDV (mL)	Frame rate (frame per beat)
C01_H	50.79	86.20	27
C02_H	61.96	107.51	35
C03_H	51.34	85.30	25
C04_H	31.55	61.84	25
C05_H	60.61	107.40	32
C06_H	27.92	47.81	17
C07_H	55.89	97.76	24
C08_H	77.68	130.27	23
C09_H	57.80	93.02	17
C10_H	58.10	99.57	35
C11_H	58.61	98.91	38
C12_H	61.14	104.51	15

Table 4.1 – Description of the healthy cases

The volume curves of each individual sequences are available in Appendix B. Inspection of the volume curves shows that some major events of the LV volume evolution are properly captured. As an example, case C10_H is depicted on Figure 4.13. Following a systolic decrease of volume, both passive filling (E-wave) and active filling due to atrial contraction (A-wave) can also be seen in the majority of the cases. Small plateau phase between diastole and systole can also be observed even though perfect isovolumic phases are not recovered.

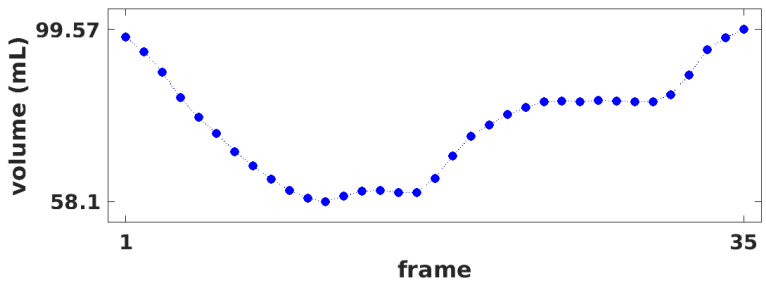

Figure 4.13 – Volume curve for case C10_H. The blue dots represent the acquisition samples.

4.2.2 Healthy cases

In this section, the application of the patient-specific pipeline to the twelve RT3DE sequences is described. The registration step and the transfer of dynamics are assessed both quantitatively and qualitatively. Analysis of the required computational effort is also provided. Finally, the hemodynamics resulting of numerical simulations is described.

4.2.2.1 Registration step results and quantification of the registration error

The results of the two registration steps are shown in front and side views in Figure 4.14 for case C12_H. Similar plots for all the other cases can be found in Appendix C but similar observations were made.

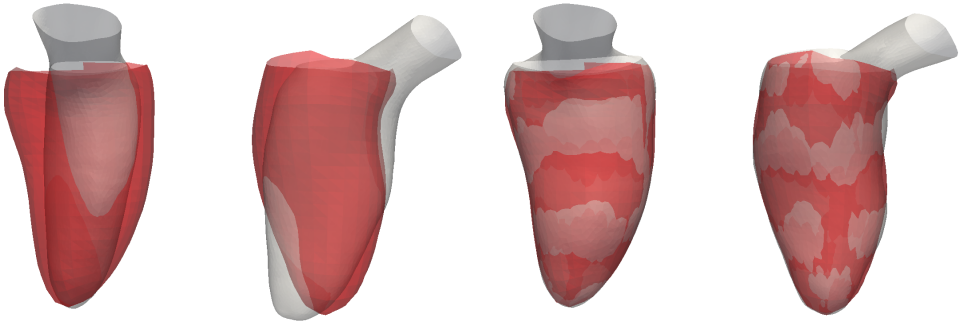

(a) (b) (c) (d)

Figure 4.14 – Generic mesh registration with C12_H as target. Figures a) and b) depict respectively front and side views of the affine registration output. Figures c) and d) depict respectively front and side views of the deformable registration output. The generic mesh is shown as the white surface whereas the target patient LV is shown as the red surface.

Figure 4.14a and 4.14b show respectively the front and side views of the affine registration step. The generic mesh is shown as the white surface while the target patient ventricle is depicted as the red surface. Qualitatively, the affine registration step was successful: the two ventricular surfaces were superimposed in space and the principal axis, *i.e.* the longitudinal and aortic axis of both ventricles were aligned. The mesh scaling allowed to obtain a deformed generic mesh of similar dimensions longitudinally compared to the target patient LV surface. On Figure 4.14c and 4.14d, the output of the deformable registration is presented. Again, qualitatively, one can observe that the resulting deformed generic mesh is well registered to the patient LV surface as revealed by the color visual artifact. An error in the registration is visible at the base of the aortic outflow tract but the overall shape looks satisfying. We now propose to quantitatively assess the final registration accuracy.

Proposed by Aspert et al. [143], a discrete metric based on the Haussdorf distance is used to compute the registration accuracy. Let S denote the source mesh and $S' = \Phi \circ G$ the morphed generic mesh. Using $\|\cdot\|_2$ to denote the standard Euclidean norm, the quantity $d(\boldsymbol{p},S')$, representing the distance between a point $\boldsymbol{p}$, belonging to S, and a surface S' , is computed as:

$$d(\boldsymbol{p},S') = \min_{\boldsymbol{p'}\in S'} \left\|\boldsymbol{p} - \boldsymbol{p'}\right\|_2 . \tag{4.5}$$

Using this point-to-surface distance, and denoting by $|S|$ the area of S, the mean distance $d_{\mathrm{m}}(S,S')$ between two surfaces S and S' is defined as:

$$d_{\mathrm{m}}(S,S') = \frac{1}{|S|} \iint_{\boldsymbol{p}\in S} d(\boldsymbol{p},S')\mathrm{dS}. \tag{4.6}$$

Finally, as this mean distance is not symmetrical, *i.e.* $d_{\mathrm{m}}(S,S') \neq d_{\mathrm{m}}(S',S)$, a symmetrical distance between S and S', denoted $d_{\mathrm{m,s}}(S,S')$, is defined:

$$d_{\mathrm{m,s}}(S,S') = \max\left[d_{\mathrm{m}}(S,S'),d_{\mathrm{m}}(S',S)\right]. \tag{4.7}$$

The metric $d_{\mathrm{m,s}}(S,S')$ was computed for all cases and is reported in Table 4.2 alongside simple statistics. The mean symmetric distance between the patient-specific mesh and the registered generic mesh averaged 1.33 mm (σ =0.08 mm).

Case ID	$d_{\mathrm{m,s}}(S,S')$ (mm)
C01_H	1.3229
C02_H	1.3775
C03_H	1.3079
C04_H	1.1953
C05_H	1.4080
C06_H	1.1588
C07_H	1.3792
C08_H	1.4564
C09_H	1.2877
C10_H	1.3229
C11_H	1.3325
C12_H	1.3583

(a)

Statistics	value (mm)
μ	1.3283
σ	0.0808
min	1.1588
max	1.4564

(b)

Table 4.2 – (a) Symmetric Mean Haussdorf distance for all cases and (b) associated statistics

Direct comparison with the image spatial resolution is difficult as the voxel size of 3D echocardiography are not homogeneous within the image domain. While longitudinal distance between samples is constant, typically 0.5 mm in the RT3DE sequences used, the azimuth and elevation are described by angular shifts, therefore resulting in lower spatial resolution as the voxel distance to the probe increases (as represented schematically, in 2D, on Figure 4.15). In the available RT3DE sequence, the azimutal voxel size was on the order of 2.15 mm and the elevation voxel size was on the order of 3.15 mm in the center of the acquired volumes. The registration distance is therefore small compared to the spatial resolution of the RT3DE images.

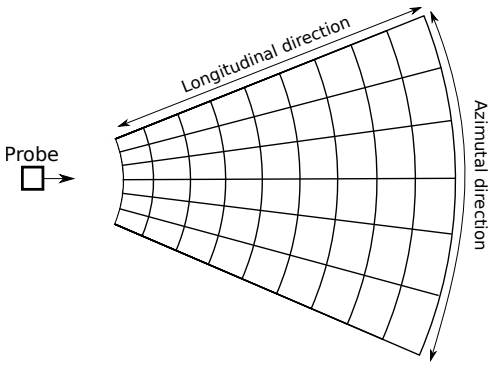

Figure 4.15 – 2D schematic representation of echography inhomogeneous pixel/voxel size. The longitudinal size of the voxels is homogeneous in the entire domain while the azimutal size of the voxel increases as the distance from the probe increases.

Figure 4.16 depicts the left heart surfaces resulting of the registration step for all patients. The variation in shape and size of the left ventricle can be appreciated.

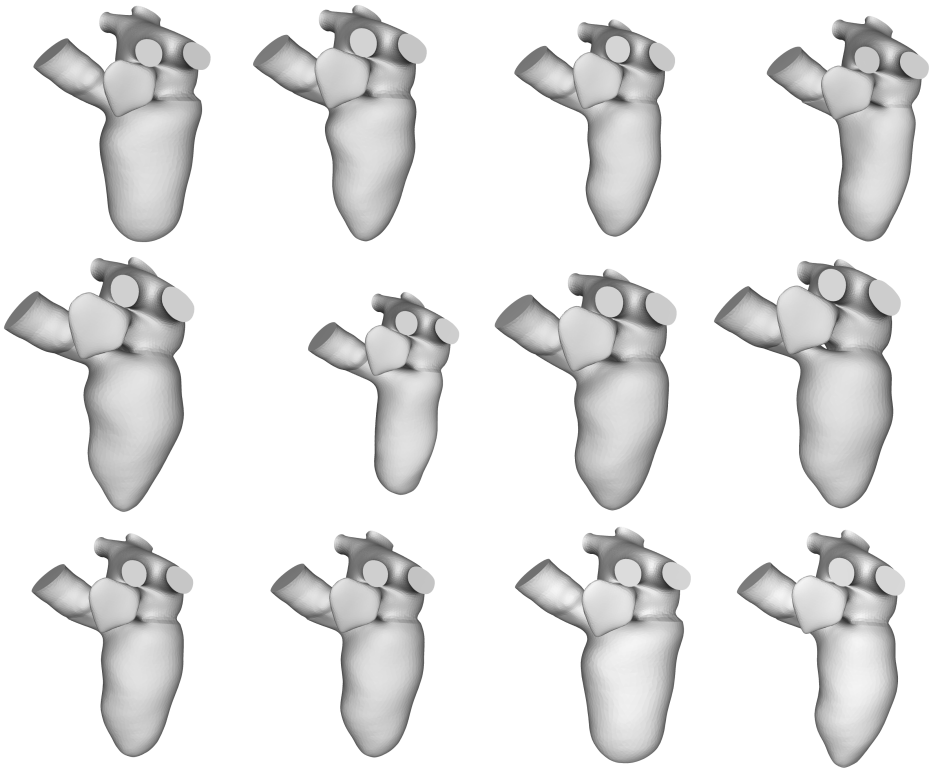

Figure 4.16 – Results from the registration step from cases C_01 to C_12. This figures highlight the strong variability in LV shape and size. One can also appreciate that the same generic atrium was used for all cases.

4.2.2.2 Dynamics transfer

The dynamics transfer step requires the computation of interpolation coefficients provided by radial basis functions. Figure 4.17 provide an example of a RBF's region of influence for case C12_H. The RBF $\phi(d_k, \sigma)$ is computed on the deformed generic mesh with respect to the k^{th} vertex (depicted as a small sphere) of the patient-specific surface (depicted as a wireframe). One can observe that the influence of the RBF is limited to the neighboring region of the vertex and quickly decays when the distance to the vertex increases.

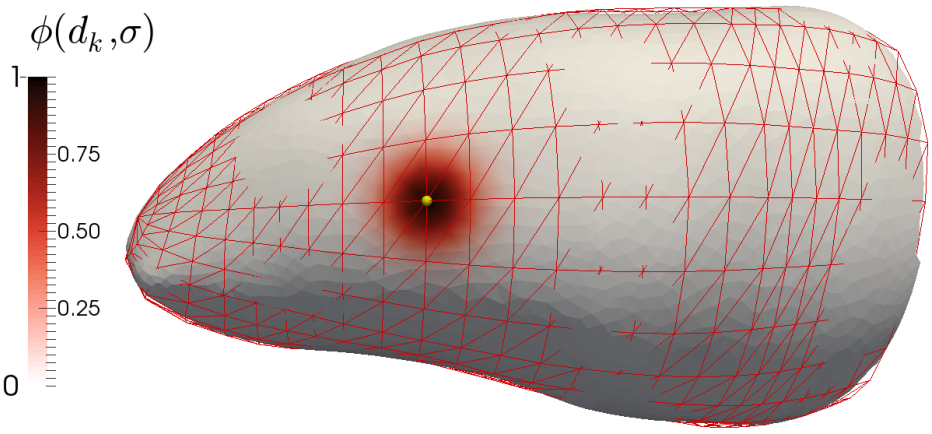

Figure 4.17 – Depiction of the RBF support for the spatial interpolation method.

Temporal interpolation of the segmented ventricular surface allowed to recover a velocity field with a time resolution adapted to the numerical simulations. Using this temporal interpolation and the distance map calculated using the RBFs, the velocity field was interpolated on the deformed generic surface. On Figure 4.18, one can observe the correspondence between the original segmented surface (in red) and the deformed generic surface (in white) under the influence of the velocity field at different time instant of the cardiac cycle. Overlap of the two surfaces is conserved during the full cardiac cycle.

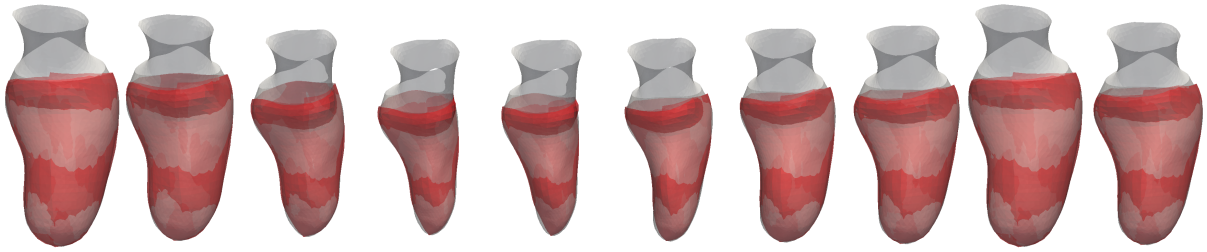

Figure 4.18 – Overlap of deformed generic mesh with the segmented ventricle at different time instants of the cardiac cycle

4.2.2.3 Computational effort

Regarding the computational effort, all the calculations were done on a laptop using a *Intel Core i7-4810MQ* cadenced at 2.8 GHz, 16MB of RAM and a NVIDIA Quadro K4100M graphic card. Table 4.3 reports the computational time required for the pre-processing (*i.e.* automatic segmentation, registration and dynamics transfer) of the image sequences. To provide the best possible estimation, no other task were launched at the same time on the computer. An average time of 55 minutes was dedicated to the automatic registration and dynamics transfer. The deformable registration was the most time-consuming task as it represented around 77 % of the total pre-processing time. The second most time-consuming task was the spatial interpolation of the data, and more specifically the writing of the data files for all the time steps. Writing 1600 individual velocity files (two cardiac cycles) accounted for around 22 % of the total time. The affine registration, time interpolation and distance map generation accounted for less than 1 % of the total computational time. After this pre-processing step, the numerical simulations could be performed instantly without any manual intervention.

Case ID	pre-processing (s)
C01_H	3912
C02_H	3970
C03_H	3271
C04_H	2627
C05_H	2865
C06_H	3631
C07_H	3522
C08_H	2828
C09_H	3457
C10_H	3575
C11_H	3136
C12_H	2812

(a)

Statistics	value (s)
μ	3314
σ	432
min	2627
max	3970

(b)

Table 4.3 – Computation time for all cases and associated statistics

4.2.2.4 CFD simulations

Using the deformed generic meshes as the computational domain and the patient-specific LV dynamics as the boundary conditions $\boldsymbol{d}^n$ applied on the LV surface, the mathematical model described in Section 2.2.4 is used to generate the intracardiac hemodynamics. Table 2.1 (Chapter 2) provides the numerical values of the parameters used for the CFD simulations. The simulations were all carried out for one cardiac cycle.

The major hemodynamical events were similar in all cases and comparable with the synthetic simulation of Chapter 2. Figure 4.19 shows several snapshots of the blood velocity magnitude

of case C12_H as a representative example.

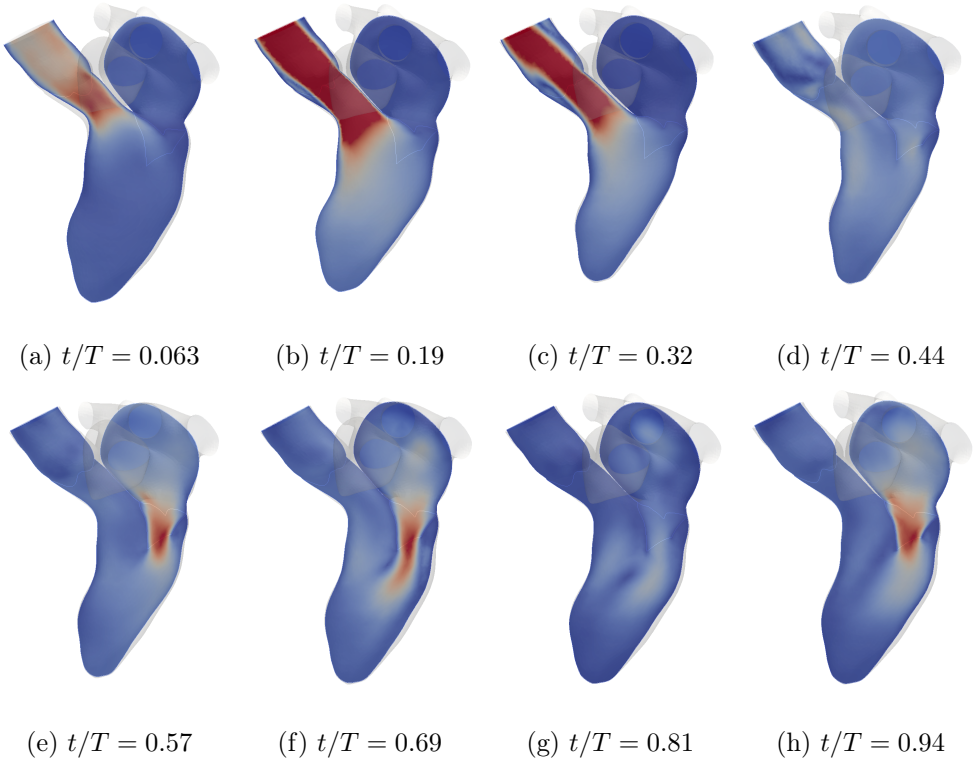

(a) $t/T = 0.063$ (b) $t/T = 0.19$ (c) $t/T = 0.32$ (d) $t/T = 0.44$

(e) $t/T = 0.57$ (f) $t/T = 0.69$ (g) $t/T = 0.81$ (h) $t/T = 0.94$

Figure 4.19 – Blood velocity magnitude of case C12_H

While the global chain of events was similar in all cases, the duration of the different phases was not. For example, the systole of case C08_H had a duration of approximately 30 % of the cardiac cycle while the systole of case C06_H was approximately 50 % of the cardiac cycle (this can be observed on the volume curves depicted in Appendix B).

Moreover, due to the variation in ventricle shape, size, and dynamics, another important difference between those cases is the velocity magnitude resulting of the LV contraction and relaxation. For example, during systole, the blood was ejected of the LV at a velocity of approximately 1.4 m/s in case C12_H, while it was ejected at a velocity of approximately 1.1 m/s in the case C11_H.

Compared to the 3.7 m/s obtained in the healthy fully synthetic simulation described in Chapter 2, the obtained peak systolic velocities were much closer to what is reported in the literature [13]. The same remark can be made for the mitral inflow velocities of the E and A wave: compared to the 2.5 m/s reached by the blood entering the LV in the synthetic simulation, the mitral inflow was ranging from 0.5 to 1 m/s in the personalized simulations.

4.2.3 Synthetic pathological cases and assessment of the PISA method

Using the patient-specific pipeline in combination with the MR modeling methodology described in Section 2.4, several synthetic MR cases were produced by combining a RT3DE sequence, a

generic mesh including a pathological valve and a MR region marking strategy. For example, using the RT3DE sequence of patient C01 with a standard flat MV geometry marked by a circular MR region, a Type 1 MR case referred to as C01_T1 was produced.

Case	MR Type	Comments	Marked area (cm^2)	Case ID
C01	1	Circular hole	0.40	C01_T1
	3	Anterior leaflet restriction	0.23	C01_T3
C02	3	Anterior leaflet restriction	0.22	C02_T3
C04	2	P2 Prolapse	0.28	C04_T2
C05	1	Two small holes	0.66	C05_T1
	2	P2 Prolapse	0.20	C05_T2
C07	1	Wide slit hole	0.77	C07_T1
C09	3	Anterior leaflet restriction	0.20	C09_T3
C10	2	P2 Prolapse	0.30	C10_T2
C11	1	Wide slit hole	0.39	C11_T1
C12	2	P2 Prolapse	0.14	C12_T2

Table 4.4 – Synthetic pathological cases description

A total of 11 MR cases were designed, including four Type 1, four Type 2 and three Type 3 cases, in order to reproduce MR variability. Four cases were designed for T1 MR as it includes a lot of different geometrical subclasses. Moreover, four cases were designed for T2 MR as it is highly prevalent among the different MR types as reported by Andell et al. [23]. Specifics about the designed MR can be found in Table 4.4.

4.2.3.1 CFD simulations

Using the deformed generic meshes as the computational domain and the patient-specific LV dynamics as the boundary conditions $\boldsymbol{d}^n$ applied on the LV surface, the mathematical model described in Chapter 2.1 was used to compute the hemodynamics of all the cases with the model parameters of Table 2.1. Simulations were carried out for one cardiac cycle. The regurgitant volumes and regurgitant fractions computed for each synthetic pathological cases can be found in Table 4.5.

A strong variability in the fraction of blood regurgitated was observed as it ranged from approximately 17 % for case C02_T3 to approximately 82 % for case C07_T1. This reflects the variability of the designed synthetic regurgitant cases. The RF was positively correlated with the area of the hole that was created on the MV surface, as depicted on Figure 4.20. This is coherent with the current philosophy of assessing MR severity using EROA as a surrogate value.

Case ID	RV (mL)	RF (%)
C01_T1	22.07	62.27
C01_T3	7.60	21.46
C02_T3	7.72	16.95
C04_T2	10.91	36.02
C05_T1	29.75	63.58
C05_T2	8.33	17.80
C07_T1	34.28	81.96
C09_T3	7.84	22.26
C10_T2	12.34	29.76
C11_T1	31.77	78.83
C12_T2	11.91	27.46

Table 4.5 – Regurgitant volume and regurgitant fraction resulting of the numerical simulations for all pathological cases.

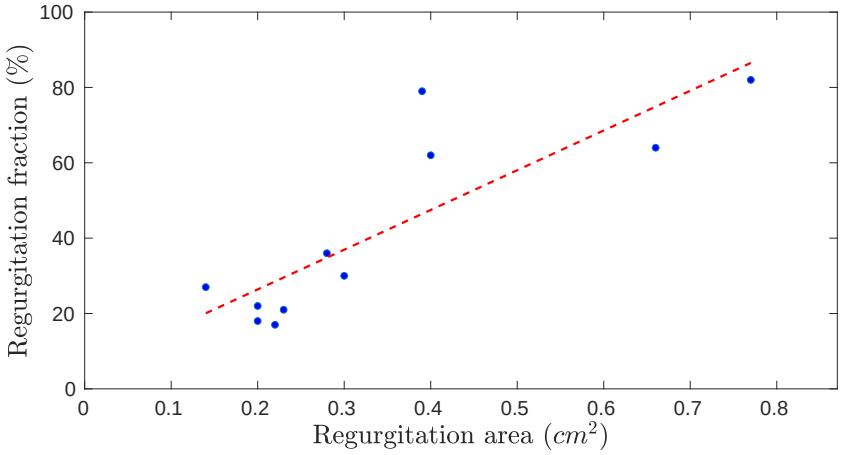

Figure 4.20 – Regurgitant fraction plotted as a function of the regurgitation area for the eleven pathological cases. Linear regression as a red curve highlight the positive correlation between the two quantities.

In all the simulated pathological cases, the major features of the diastolic blood flow was similar to the healthy cases. Due to the variability of the designed MR, both in term of valve surface or in term of region marking, the hemodynamics during systole was, however, quite different from case to case. To highlight some of the differences between all those simulations, the blood flow is investigated at mid-systole for all pathological cases and grouped in several categories.

Case C01_T1 was produced by considering the standard MV geometry with a circular hole. As

a result, while part of the blood pushed by the LV endocardium is ejected towards the aorta as expected during systole, part of the blood is also directed towards the MV hole and creates a jet of blood with high velocities directed towards the posterior-mid atrium wall (Figure 4.21a). The isovelocity surfaces of the converging blood are hemispherically shaped, as depicted on Figure 4.21b.

(a) (b)

Figure 4.21 – (a) Blood flow during systole for case C01_T1 and (b) associated isovelocity surface in the convergence region, at an aliasing velocity of 35 cm/s, represented as a point cloud.

Cases C07_T1 and C11_T1 were produced by considering the standard MV geometry with elongated slit holes. As a result of this geometry, the isovelocity surfaces of the converging blood are not hemispherically shaped anymore, they are elongated hemiellipsoids as can be seen on Figure 4.22 for case C11_T1.

Figure 4.22 – Blood flow during systole for case C11_T1

Case C05_T1 was produced by considering the standard MV geometry and two small holes located at the antero-lateral and postero-medial commissure. Instead of converging towards a single hole, the blood flow splits and part of it passes through one hole while part of it passes through the other. This very specific behavior results in two separate hemispherical isovelocity surfaces (Figure 4.23).

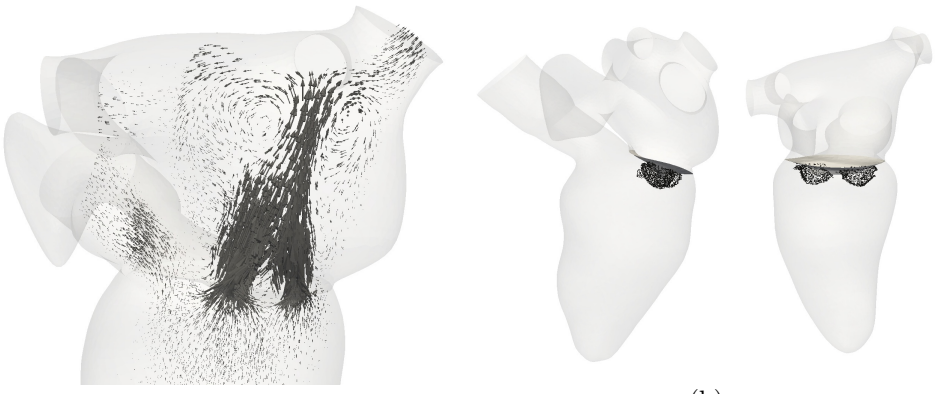

(a) (b)

Figure 4.23 – (a) Blood flow during systole for case C05_T1 and (b) associated isovelocity surface in the convergence region, at an aliasing velocity of 35 cm/s, represented as a point cloud.

Cases C04_T2, C05_T2, C10_T2 and C12_T2 were produced considering the Type 2 MV geometry which included a prolapsed valve with flail posterior leaflets. Contrary to the previously described cases, the resulting MR is highly asymmetric. The blood passes through the MV and the posterior leaflet flail channels the blood flow tangentially with respect to the mitral valve plane. Even though the opening through the MV is rather circular, the isovelocity surfaces are partial hemispheres that are restricted on one side by the presence of the mitral valve (Figure 4.24).

(a) (b)

Figure 4.24 – (a) Blood flow during systole for case C12_T2 and (b) associated isovelocity surface in the convergence region, at an aliasing velocity of 35 cm/s, represented as a point cloud.

Cases C01_T3, C02_T3 and C09_T3 were produced by considering the Type 3 MV geometry which included a restriction of the anterior leaflet. Similarly to the Type 2 cases described above, the valve configuration is asymmetrical. As the anterior MV leaflet is restricted, a channel orients the flow towards the posterior-inferior atrium wall. As a result of the slit orifice, the isovelocity surfaces are elongated hemiellipsoids, similarly to cases C07_T1 and C11_T1 (Figure 4.25).

(a) (b)

Figure 4.25 – (a) Blood flow during systole for case C09_T3 and (b) associated isovelocity surface in the convergence region, at an aliasing velocity of 25 cm/s, represented as a point cloud.

The hemodynamics during systole is therefore highly dependent on the underlying MR pathology, MV geometry and orifice. This variability was partly highlighted by the differences of the isovelocity surfaces in the flow convergence region. Indeed, while the circular orifice resulted in an hemispherical isovelocity surface, elongated orifices resulted in hemisellipsoidal isosurfaces, prolapsed valves resulted in partial hemispherical shapes and collection of small regurgitation orifice resulted in a flow convergence region composed of several small isosurfaces. As the PISA method is based on the assumption that the isovelocity surfaces are hemispheric, questions can be raised about potential inaccuracies of the PISA method.

4.2.3.2 Evaluation of the PISA technique

It is proposed to assess the accuracy and some of the limitations of the PISA method. First, we quickly recall the description of the PISA method presented in Section 1.1.3.

Using Color Doppler echocardiography, the physician choses a frame during systole in which the MR is visible and fully developed. He selects a first landmark $\mathcal{L}_1$ at the MR center and then chooses an aliasing velocity v_{alias}, usually ranging from 20 to 60 cm/s [21, 29, 36, 37]. Under the PISA assumptions, blood is converging towards the regurgitation and the isovalues of this aliasing velocity are hemispherically distributed around the MR center in the convergence region. The physician chooses a second landmark $\mathcal{L}_2$ located on this isovelocity surface and the distance r_{alias} between the two selected landmarks is computed (See Figure 1.10b for an example where $\mathcal{L}_1$ and $\mathcal{L}_2$ are located on an actual Color Doppler image). The physician computes the area of an hemisphere of radius r_{alias} and multiplies it with the velocity v_{alias} to obtain the flow rate at the isovelocity surface level. By dividing this flow rate by the maximal velocity of the regurgitation v_{max}, the physician obtains the EROA:

$$\text{EROA} = \frac{2\pi \cdot \mathrm{r}_{\text{alias}}^2 \cdot \mathrm{v}_{\text{alias}}}{\mathrm{v}_{\text{max}}}. \tag{4.8}$$

Using the velocity time integral, the integral of the velocity magnitude at the valve level with

respect to time during the MR, the total regurgitant volume can also be estimated:

$$R_{\text{vol,PISA}} = \text{VTI} \cdot \text{EROA} = \text{VTI} \cdot \frac{2\pi \cdot \text{r}_{\text{alias}}^2 \cdot \text{v}_{\text{alias}}}{\text{v}_{\text{max}}}. \tag{4.9}$$

To apply this technique in-silico, the numerical simulations were processed as follows. The isosurface tool of the *Ensight*[1] software was used to generate 3D isosurfaces at different aliasing velocities ranging from 20 to 60 cm/s using increments of 10 cm/s. A frame of the sequence was chosen, during systole, in which the isovelocity surfaces were fully developed. The landmark $\mathcal{L}_1$, representing the MR center, was defined as the spatial average of five to ten user-defined landmarks to account for some user variability.

Since the assumption of hemispherical isovelocities is only valid when the hole is round and the valve is flat, as reported in previous studies [39, 53] and as observed in the previous section, there is no unique distance between the MR center and the computed isosurface for the complex MR geometries such as the one presented in this study. Therefore, to imitate the fact that the physician chooses a specific landmark $\mathcal{L}_2$ on the isovelocity surface, the methodology described in the following paragraph is adopted.

For each aliasing velocity, the distances between the MR center all the triangle centers of the discretized 3D isovelocity surface have been used to produce RV estimates using the PISA method. Those different RV estimates were aggregated into weighted histograms where each estimated value was weighted by the area of its associated triangle to account for non-uniform discretization of the surface. Each sample of this histogram can be thought as one possible choice of landmark $\mathcal{L}_2$ by the physician.

The resulting histogram is therefore a probabilistic evaluation of the regurgitant volume for which one assumes a uniform probability of picking any landmark $\mathcal{L}_2$ on the isosurface. Modes in this histogram represents the fact that a specific regurgitant volume has a higher probability of being the one estimated by the physician given the shape of the isovelocity surface.

The RV estimates of all aliasing velocities can also be integrated into one single histogram to provide a single histogram. Both possibilities (either one histogram per aliasing velocity or an aggregated histogram combining all aliasing velocities) was considered. By adding a red vertical line depicting the ground truth RV that needs to be estimated (as reported in Table 4.5) was added to the figures depicting the histograms to provide an indication as how well the PISA method would be at assessing MR in each cases. All the histograms can be found in Appendix C.3 and representative examples are now detailed.

Figure 4.26 depicts the histogram combining all aliasing velocities for case C01_T1. While the RV estimates are a little bit spread, a strong mode is visible, corresponding roughly to the RV that needs to be estimated. This mode is representative of a nearly hemispherical isovelocity surface. As the case C01_T1 regurgitation results of a circular hole on a nearly flat valve, the PISA method therefore provides a good RV estimate.

[1] https://www.ensight.com/ (last accessed 03 Dec 2018)

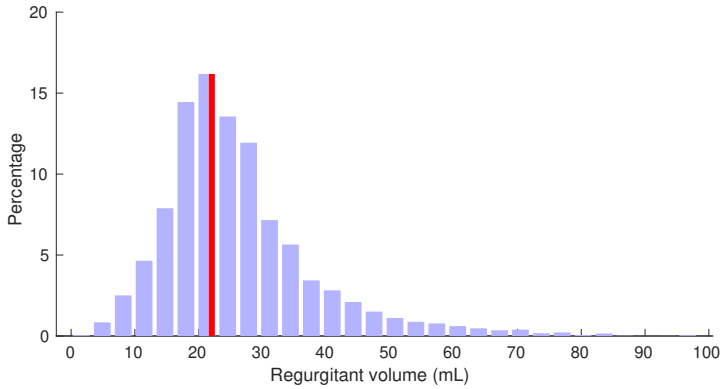

Figure 4.26 – Case C01_T1: Aggregated histogram of all RV estimates at aliasing velocities ranging between 20 to 60 cm/s by increments of 10 cm/s. The ground-truth RV is overlapping the main mode of the histogram.

Figure 4.27 depicts the histogram combining all aliasing velocities for case C07_T1. The histogram is dominated by a main mode but one can observe a strong tail of high RV estimates. This is a result of the hemiellipsoid isovelocity surfaces resulting a the slit hole. In this case, the ground truth RV does not overlap the main mode of the histogram revealing the difficulty for the physician to properly quantify MR using the PISA method.

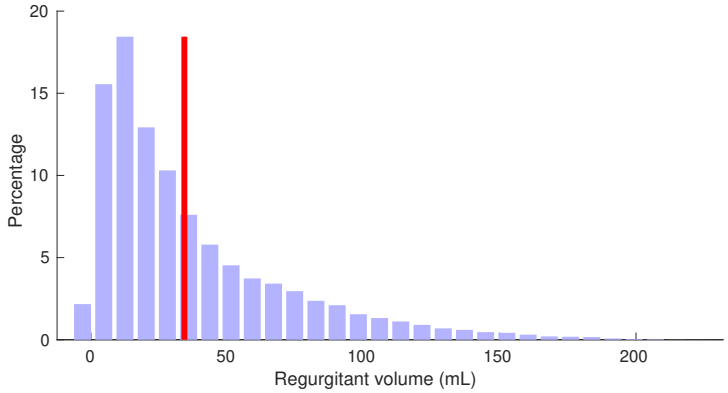

Figure 4.27 – Case 07_T1: Aggregated histogram of all RV estimates at aliasing velocities ranging between 20 to 60 cm/s by increments of 10 cm/s. The ground-truth RV is greater than the main mode of the histogram.

Figure 4.28 depicts the histogram combining all aliasing velocities for case C05_T1. First, one has to note that case C05_T1 is composed of two small regurgitation. Therefore, defining the landmark $\mathcal{L}_1$, the MR center, was difficult and had to be chosen among one of the two holes. For this reason, the resulting histogram is difficult to analyze. The histogram is quite uniform in terms of the representativeness of the estimates and one can barely distinguish two modes that might be the result of including the isosurfaces of both regurgitation at the same time. It is difficult to see a relationship between the actual RV and the provided RV estimates.

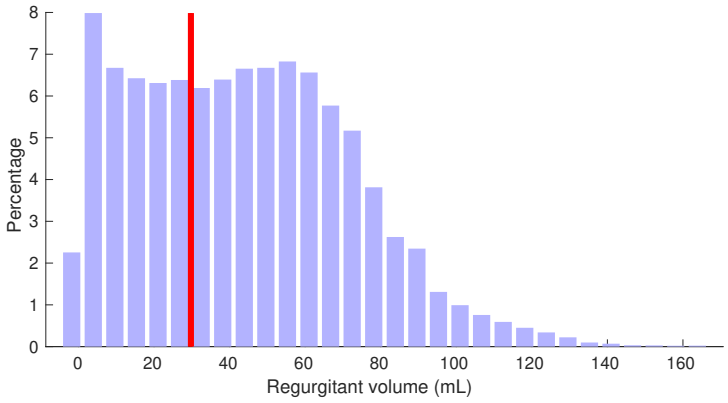

Figure 4.28 – Case C05_T1: Aggregated histogram of all RV estimates at aliasing velocities ranging between 20 to 60 cm/s by increments of 10 cm/s. Two modes are observed in the histogram The ground-truth RV doesn't math any of those modes.

Figure 4.29 depict both the histogram combining all aliasing velocities for case C05_T2 and the histogram specific to one aliasing velocity (40 cm/s). A strong mode, relatively representative of the ground truth RV, is visible on Figure 4.29a. However, one can observe that at specific aliasing velocity, this mode is difficult to observe (Figure 4.29b). Inspection of the individual histograms associated with specific aliasing velocities (Appendix C.3) reveals that at low aliasing velocities, the RV might be overestimated. At higher aliasing velocities, this overestimation is less and less pronounced. This result indicates that in some cases, it might not be sufficient enough to use a single aliasing velocity to estimate the MR severity.

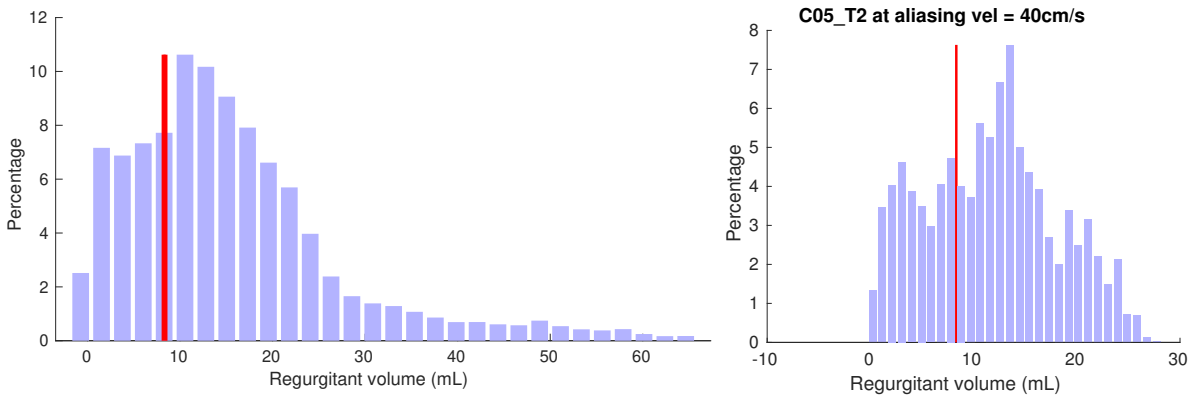

(a) (b)

Figure 4.29 – Case C05_T2: (a) Aggregated histogram of all RV estimates at aliasing velocities ranging between 20 to 60 cm/s by increments of 10 cm/s and (b) specific histogram for an aliasing velocity of 40 cm/s

Finally, Figure 4.30 depicts the histogram combining all aliasing velocities for case C09_T3. Conclusion similar to the Type 1 MR with slit holes can be reached: due to the elongated hole resulting of the anterior leaflet restriction, the histogram contains a main mode with a long tail of high RV estimates. Moreover, the ground truth does not overlap the main mode of the

histogram.

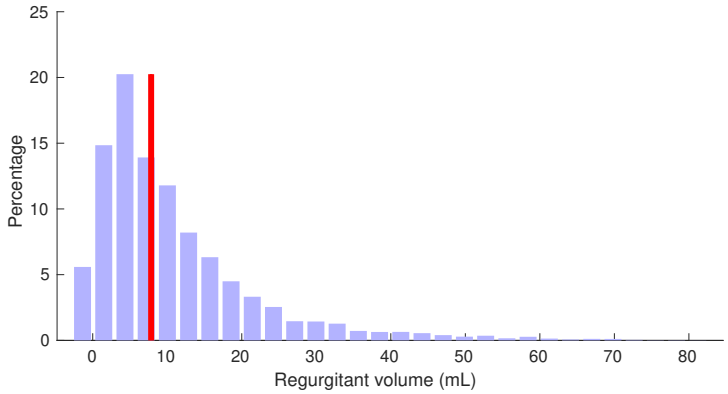

Figure 4.30 – Case C09_T3: Aggregated histogram of all RV estimates at aliasing velocities ranging between 20 to 60 cm/s by increments of 10 cm/s.

Looking at the spread of the RV estimates across the range of aliasing velocities reveals that lower aliasing velocity leads to a lower spread of the potential RV estimates case-wise. As an example, Figure 4.31 depicts the histograms of the case C01_T1 placed side by side as a color-coded image. While the RV estimates range from 5 mL to 50 mL at an aliasing velocity of 20 cm/s, the RV estimates produced using an aliasing velocity of 60 cm/s range from 5 mL to 100 mL. Even though this observation advocates for the use of a small aliasing velocity, one needs to remember that isovelocity surfaces resulting from small aliasing velocities might be disturbed by the aortic outflow. It is therefore important to carefully choose adequate aliasing velocity.

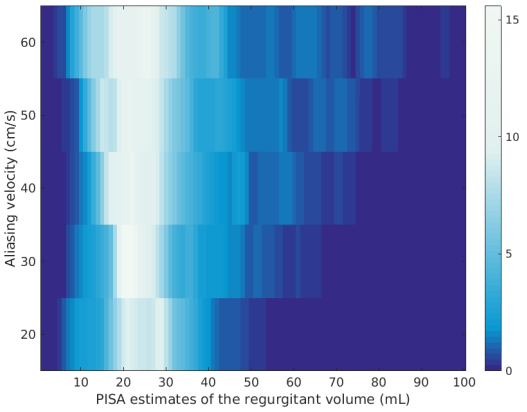

Figure 4.31 – Side by side C01_T1 RV estimates histograms for aliasing velocities ranging from 20 to 60 cm/s. The estimates are more spread in the histograms resulting from high aliasing velocities compared to the histograms resulting from small aliasing velocities.

4.3 Conclusion, discussion and perspectives

In this chapter, a pipeline was designed to automatically prepare personalized numerical simulations using RT3DE image sequences. Using a combination of rigid and deformable registration allowed to morph predefined generic meshes to fit the patient-specific LV geometry. A spatio-temporal interpolation of the US data was used to produce appropriate LV surface dynamics on the vertices of the deformed generic meshes. Using those personalized geometry and dynamics, the blood dynamics inside the heart can then be obtained by numerical simulation.

This pipeline was applied on twelve different RT3DE image sequences. Even though the RT3DE sequences exhibited a strong variability in shape and dynamics of the ventricle, the combination of an affine registration step followed with a deformable registration step allowed to obtain accurate patient-specific ventricular surfaces in all cases. Moreover, as specific constraints on the registration were specified, the resulting meshes were all suited for numerical simulations (*i.e.* no mesh defect were observed in any of the cases). The transfer of the LV dynamics was also successful in providing a smooth velocity field of the ventricular surface.

Regarding the computational effort, the fully automated pre-processing step averaged 55 minutes. This is a huge progress compared to the methodology usually reported in the literature. Indeed, we recall here that recent reviews of patient-specific cardiac flow simulations claimed that the pre-processing step usually accounted for more than 20 hours of human effort [61, 114].

Numerical simulations of the blood flow was performed for all the image sequences. Compared to the fully synthetic simulation of the blood flow described in Chapter 2, the obtained blood velocity was closer to human physiology. Even though this observation advocates for the use of image-based personalized LV dynamics, the shortcomings of directly using the RT3DE images as BC for the LV motion is that one relies on the image quality and segmentation artifacts (*e.g.,* non monotonous volume curves during systole or diastole).

Several limitations limit the simulation of a fully patient-specific blood flow. First, due to the acquisition process, the atrium is not available in the RT3DE sequences. As a result, the same generic atrium was used for all cases. Moreover, due to image quality, there is no clear definition of internal LV structures such as the trabeculae, papillary muscles or chordae. As a result, smooth ventricular geometry, a strong simplification of reality, was used. Indeed, it has been shown in the past that the papillary muscles [79], trabeculae [79] and chordae [144] have an influence on the intracardiac hemodynamics. Finally, as it is difficult to obtain personalized pressure curves for the pulmonary veins inlet and aortic outlet in a clinical setting, population-derived pressure BC was used.

Eleven synthetic pathological cases were designed to model various Type 1, Type 2 and Type 3 MR. Investigation of the hemodynamics in those cases revealed very different systolic blood flow resulting of the underlying pathology and MV geometry. Good agreement between the estimated regurgitant volume using PISA technique and the simulated value was found in the case of a circular hole on a flat mitral valve. However, the PISA method did not offer satisfying estimates for other types of regurgitation. It was also noticed that choosing higher aliasing velocities led to a wider range of potential RV estimates. Those observations highlight the difficulties of properly quantifying MR in a clinical setting.

It was shown that the valve shape has strong impact on the blood flow. Therefore, dynamic changes of the valve geometry either during closing of the valve or during systole might introduce additional variability. While the presented work included dynamic motion of the ventricle walls, the MV dynamics was not considered. This might be an oversimplification of the model in some cases. For example, it is known that the regurgitation and MV dynamics can be highly dynamic in MR caused by mitral prolapse [92]. Additional work should be pursued to further characterize the influence of valve dynamics.

The PISA estimates were obtained using the full velocity field obtained from the numerical simulations. However, US Doppler images only provide the component of the velocity field that is aligned with the US beams. Moreover, additional measurements artifacts such as aliasing can perturb the US images. As such, using unaltered velocities might limit the scope of the findings. Nevertheless, this choice allowed to remove the bias of having to choose a specific probe positioning and using unaltered velocities allowed to draw conclusion in a *best case scenario*.

Chapter 5
Influence of the LV twist on cardiac hemodynamics

This chapter is devoted to the analysis of the impact of the LV wall torsion on the intracardiac hemodynamics.

The issue with respect to LV wall torsion is related to the fact that the intracardiac hemodynamics has been modeled using the ALE formulation (Section 2.2). In the ALE formulation, a Lagrangian information (*i.e.* the displacement of material points) is required on the boundary, whereas the LV surface provided by the image segmentation only gives Eulerian information. In particular, the torsional – or twisting – effects are lost in this data. For this reason, we propose to evaluate the impact of removing the torsional component of a synthetic Lagrangian data, generated with an electro-mechanical model of the heart which included fiber directions, on the intracardiac hemodynamics.

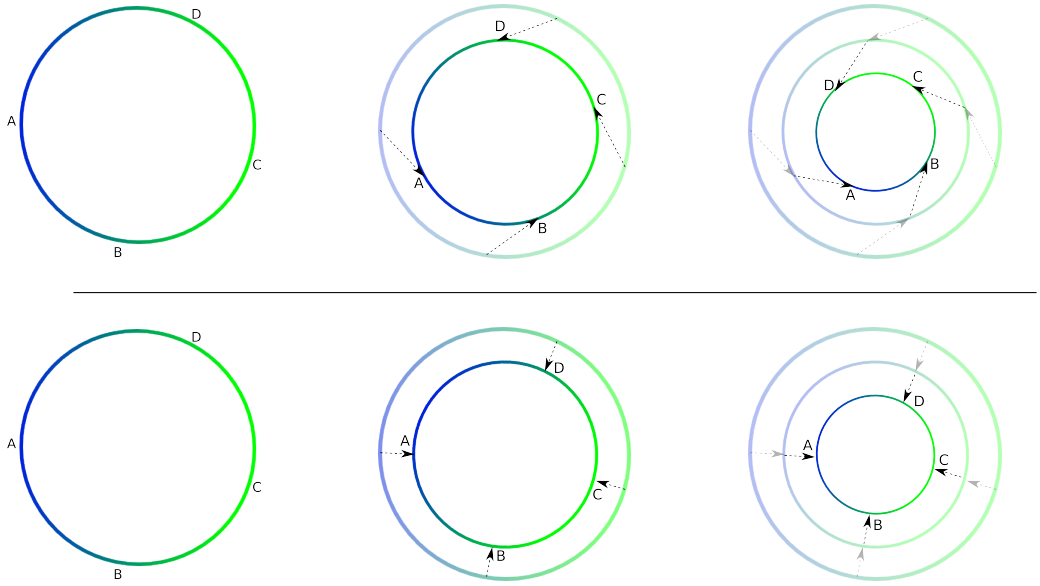

Figure 5.1 – Schematic representation of a ventricular cross section for the physiological case and for a case where twisting was removed . The top row represents the physiological case and the bottom row represents dataset without torsionat three time instants. In the physiological case, a twist rotates the position of material points A,B,C and D. In the case without ventricular twist, however, those material points are only subject to a normal displacement with respect to the surface. In both cases, the surface is similarly located if one disregards the actual position of the material points.

In Section 5.1, the generation of the two set of LV wall dynamics is detailed and a quantitative analysis of the differences between the two sets is provided in Section 5.1.1. In Section 5.1.2, the torsional motion in the two datasets is quantified. Finally, in Section 5.2, the hemodynamics resulting from those two datasets is compared for both a healthy heart (Section 5.2.1) and a pathological heart including MR (Section 5.2.2).

5.1 Datasets generation and analysis

The initial dataset provided by the electro-mechanical simulation consisted of a sequence of 800 surface meshes depicting the position of the endocardium during a cardiac cycle of 0.8 s at a frequency of 1 kHz. In those meshes, each individual vertex is a material point which can be tracked during the full cardiac cycle. As previously described, the model used to generate this dataset included fiber orientation and, as such, includes twisting of the ventricular surface.

Generation of the Reference dataset: The sequence was downsampled to 25 frames per cardiac cycles to mimic the loss of temporal information caused by RT3DE image acquisition: the chosen frame-rate is similar to the data described in Section 4.2 and other similar work which use RT3DE image sequences as the data source [113]. This subsampled version of the initial dataset represented by the set of ventricular surfaces $(\mathcal{C}_k)$ is referred to as the "reference]" case in the rest of this chapter.

Generation of the Torsionless dataset: Using the reference dataset, deformable registration technique is used to remove the torsional displacement of the ventricular surface. More specifically, the software *Deformetrica* [140] is used. The description of the torsion removal is explained as follows:

If one describes a mesh by its vertices $(\boldsymbol{v}_p)_{p=1,\cdots,d}$, one can compute the centers $(\boldsymbol{c}_p)_{p=1,\cdots,d}$ and normals $(\boldsymbol{n}_p)_{p=1,\cdots,d}$ of the mesh edges. Given two meshes $\mathcal{M}$ and $\mathcal{N}$, the distance between the two meshes minimized by *Deformetrica* is given by:

$$d(\mathcal{M},\mathcal{N}) = \sum_p \sum_q K^W(\boldsymbol{c}_p^{\mathcal{M}}, \boldsymbol{c}_q^{\mathcal{N}}) \frac{((\boldsymbol{n}_p^{\mathcal{M}})^T \boldsymbol{n}_q^{\mathcal{N}})^2}{\left\|\boldsymbol{n}_p^{\mathcal{M}}\right\| \left\|\boldsymbol{n}_q^{\mathcal{N}}\right\|},$$

where K^W is a gaussian kernel of width σ^W.

The objective function of the registration algorithm is therefore driven by the distance between edge centers and their respective normal alignment. As there is little to no specific geometrical features on the ventricular surface *giving away* that ventricular torsion occurs (except at the extreme apex), using this registration algorithm enforces the overlap of the ventricular surfaces but cannot enforce tangential motion. As a result, a torsionless version $(\mathcal{T}_k)$ can be produced by propagating the LV wall displacement through iterative registration of the surfaces as described by the following recurrence definition:

Recurrence definition of $(\mathcal{T}_k)$

Set $\mathcal{T}_1 = \mathcal{C}_1$. Then, iteratively $\forall\, k \geq 2$:

1. Compute Φ_k using $\mathcal{T}_{k-1}$ as the source and $\mathcal{C}_k$ as the target of the deformable registration problem
2. Define $\mathcal{T}_k = \Phi_k \circ \mathcal{T}_{k-1}$

Remark: In this definition, the reference frame $\mathcal{C}_1$ was chosen but any frame of the reference case can be used as a reference frame. In our experience, it was better to choose the end systolic time as reference since it allowed to obtain lower geometrical differences with respect to the reference case.

The produced set of ventricular surfaces $(\mathcal{T}_k)$ is referred to as the "torsionless" case in the rest of this chapter.

Final datasets preparation: In order to fit the time-step required by the numerical simulations, the temporal interpolation strategy described in Section 4.1.2 is applied on both $(\mathcal{C}_k)$ and $(\mathcal{T}_k)$ to produce the resulting LV wall boundary condition for the numerical simulations.

5.1.1 Analysis of the geometrical differences

Using the symmetric Haussdorf distance defined in Section 4.2.2.1, the distance between the meshes from the reference case and torsionless case is computed at all time step (Figure 5.2). The global Haussdorf distance averages 0.44 mm on the entire cardiac cycle with a minimum of 0 mm for the reference frame. The median distance is 0.50 mm.

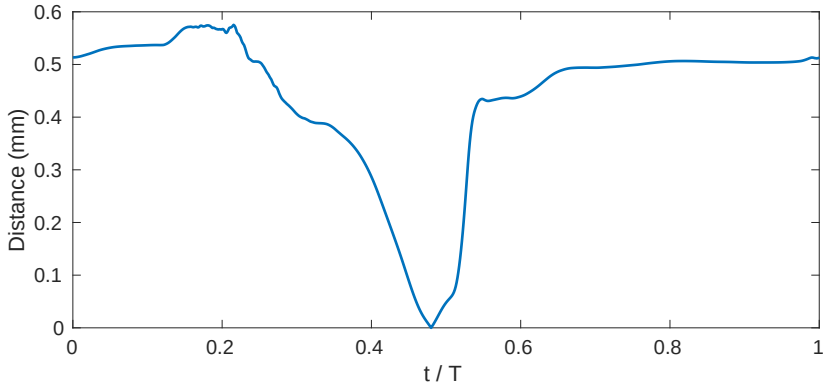

Figure 5.2 – Global Haussdorf distance between the reference and torsionless case. The distance averages 0.44 mm over the cardiac cycles. It is relatively constant except around the reference frame where the distance between the two surfaces drop sharply.

The same measurement was repeated on the different regions of the 17-segment model proposed by the American Heart Association (AHA) [145]. As depicted by the standard deviation computed across the different AHA regions, a non-negligible variability between those regions is observed (See Figure 5.3), especially during the period where the LV undergoes large geometri-

cal changes, as depicted by the peaks occurring during the intervals $t/T = [0.2,0.3]$ (beginning of the systole) and $t/T = [0.5,0.6]$ (beginning of the diastole). Nevertheless, even accounting for that variability, the distance between the meshes of the reference case and torsionless case is relatively small compared to the RT3DE spatial resolution.

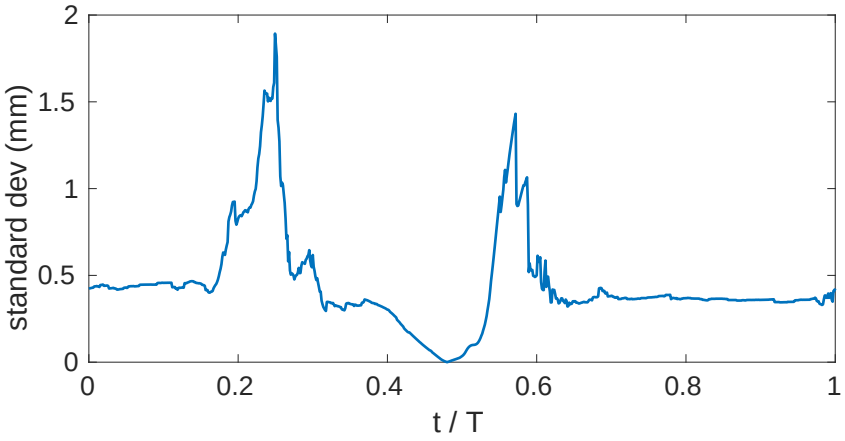

Figure 5.3 – Standard deviation of the Haussdorf distances across AHA regions. Two peaks are observed at $t/T \approx 0.23$ and $t/T \approx 0.57$.

The major difference, qualitatively, between the surfaces is found in the apical region. Figure 5.4 depicts the end-systolic and end-diastolic LV surfaces in both torsionless and reference case, side by side. One can observe that a small recess is visible in the apex of the ventricle in end-systole (Figure 5.4a). As depicted on Figure 5.4b, even though this recess disappears in the reference case, driven by the actual ventricular physiology, one can still see a remnant of this surface feature in the torsionless case. This can be explained by the choice of kernel size for the registration algorithm: choosing a smaller kernel size would allow to get rid of this surface artifact but would increase computational time. Aside from this specific location, the rest of the ventricle surface was smooth and therefore no notable differences were found.

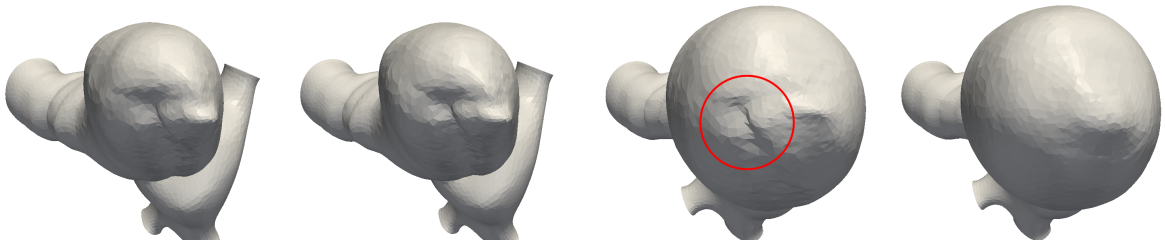

(a) (b)

Figure 5.4 – Ventricular surface of the torsionless (left) and reference (right) cases at end-systole (a) and end diastole (b), as seen from the apex. The remnant recess is highlighted by the red circle.

Due to these small surface differences, the resulting ventricular volumes differ. On Figure 5.5,

both the ventricular volume curves of the reference and torsionless case are depicted. Additionally, the volume difference, in percentage, is reported. Even though a small difference exists between the two volume curves, the torsionless volume difference with respect to the reference case is bounded between $-0.67\,\%$ and $0.32\,\%$ with an average difference of $-0.32\,\%$.

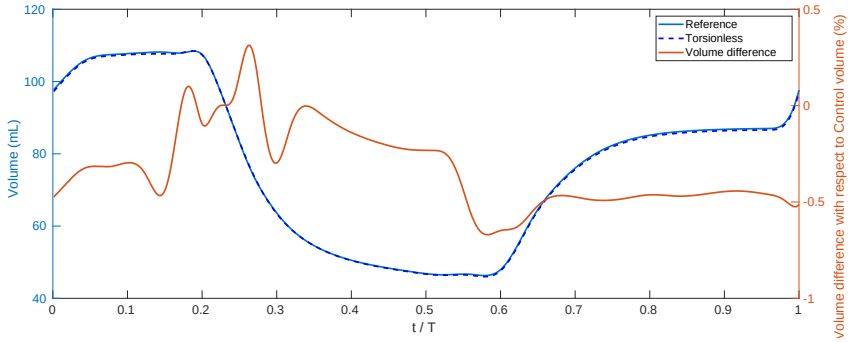

Figure 5.5 – Ventricular volume curves of the reference/torsionless cases and ventricular volume difference between reference and torsionless cases.

5.1.2 Quantification of the torsion removal

Ventricular torsion, in the literature, is defined as the difference between apical and basal rotation. This measurement is sometimes normalized by the end-diastolic longitudinal distance between the apex and the base [115, 6, 122, 124]. This definition of the LV torsion suffers from several important flaws. First, the precise location of the apical and basal slices considered are not standardized, and previous reports have shown that the amount of LV torsion is highly dependent on the measurements site [122]. A second difficulty lies in the fact that contractions of the subendocardium and subepicardium produce rotation in opposite directions, due to the difference in their respective fiber orientations [6]. Finally, the LV is not perfectly symmetric nor is its motion. In a given longitudinal slice of the ventricle, two regions might not rotate by the same amount [122]. For those reasons, a methodology aimed at providing quantitative descriptor of the LV torsion is now described.

By defining:

- $\mathcal{M}_t$ as the time-evolving 2-manifold embedded in $\mathbb{R}^3$ (*i.e.* the surface of the ventricle during the cardiac cycle),
- $\boldsymbol{l_0}$ as the longitudinal unit vector directed from the apex of the ventricle to the base of the ventricle,
- $\boldsymbol{N} : \mathcal{M}_t \times \mathbb{R}^+ \to \mathbb{R}^3$ as the vector field of the exterior normals of the manifold $\mathcal{M}_t$,

one can define the three following vector fields:

$$\boldsymbol{L}: \quad \mathcal{M}_t \times \mathbb{R}^+ \rightarrow \mathbb{R}^3 \tag{5.1}$$

$$(\boldsymbol{x},t) \mapsto \frac{\boldsymbol{l_0}}{\|\boldsymbol{l_0}\|} \tag{5.2}$$

$$\boldsymbol{R}: \quad \mathcal{M}_t \times \mathbb{R}^+ \rightarrow \mathbb{R}^3 \tag{5.3}$$

$$(\boldsymbol{x},t) \mapsto \frac{\boldsymbol{r}(\boldsymbol{x},t)}{\|\boldsymbol{r}(\boldsymbol{x},t)\|} \quad \text{with} \quad \boldsymbol{r}(\boldsymbol{x},t) = \boldsymbol{N}(\boldsymbol{x},t) - \boldsymbol{l_0} \cdot (\boldsymbol{N}(\boldsymbol{x},t) \cdot \boldsymbol{l_0}) \tag{5.4}$$

$$\boldsymbol{T}: \quad \mathcal{M}_t \times \mathbb{R}^+ \rightarrow \mathbb{R}^3 \tag{5.5}$$

$$(\boldsymbol{x},t) \mapsto \frac{\boldsymbol{t}(\boldsymbol{x},t)}{\|\boldsymbol{t}(\boldsymbol{x},t)\|} \quad \text{with} \quad \boldsymbol{t}(\boldsymbol{x},t) = \boldsymbol{L}(\boldsymbol{x},t) \times \boldsymbol{R}(\boldsymbol{x},t) \tag{5.6}$$

Combining those three vector fields, $\mathcal{B}(\boldsymbol{x},t) = \{\boldsymbol{L}(\boldsymbol{x},t), \boldsymbol{R}(\boldsymbol{x},t), \boldsymbol{T}(\boldsymbol{x},t)\}$, a local (in time and in space) orthogonal basis is obtained. Note that, at each point of the manifold, $\boldsymbol{R}$ is representing the radial direction, $\boldsymbol{L}$ is representing the longitudinal direction, and $\boldsymbol{T}$ is representing the tangential direction. Figure 5.6a depicts the basis $\mathcal{B}$ at some randomly selected vertices of the ventricular surface and Figure 5.6b represents the vector field $\boldsymbol{T}$ on the LV vertices from the apex to the base.

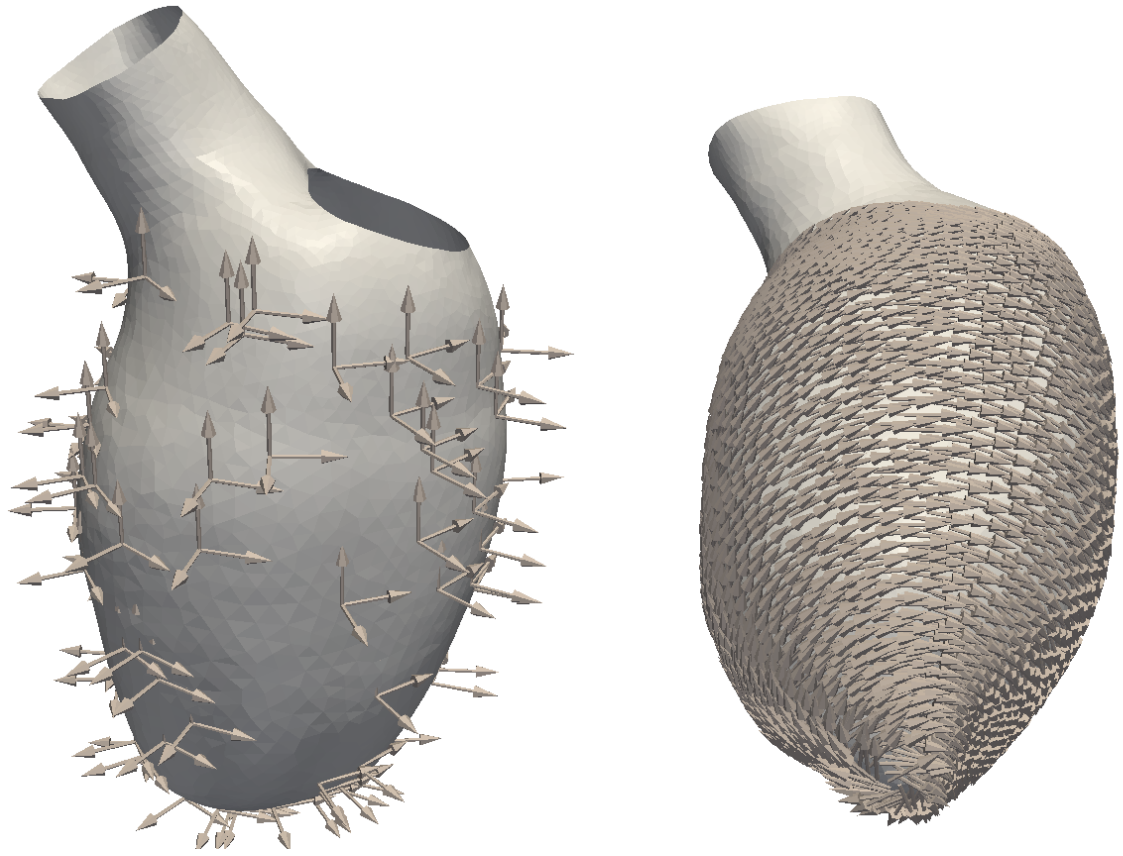

(a) (b)

Figure 5.6 – (a) subset of the basis $\boldsymbol{\mathcal{B}}$ (b) $\boldsymbol{T}$ vector field.

Given a material point $\mathcal{P}$ of the ventricular surface, one can use its initial position $\boldsymbol{x}_0^{\mathcal{P}} \in \mathcal{M}_0$ as well as its velocity $\boldsymbol{v}^{\mathcal{P}}(t) : \mathbb{R}^+ \to \mathbb{R}^3$ to define its position on the ventricular surface at a time τ:

$$\boldsymbol{\Gamma}^{\mathcal{P}}(\tau) = \boldsymbol{x}_0^{\mathcal{P}} + \int_0^{\tau} \boldsymbol{v}^{\mathcal{P}}(t)dt \tag{5.7}$$

Under a simple reparameterization of time, $\boldsymbol{\Gamma}^{\mathcal{P}}$ represents the path of the particle $\mathcal{P}$. Finally, the line integral of the tangential vector field $\boldsymbol{T}$ along the path $\boldsymbol{\Gamma}^{\mathcal{P}}$ can be computed:

$$I_{\boldsymbol{T},\boldsymbol{\Gamma}^{\mathcal{P}}}(\tau) = \int_{t=0}^{\tau} \boldsymbol{T}(\boldsymbol{\Gamma}^{\mathcal{P}}(t),t) \cdot \boldsymbol{v}^{\mathcal{P}}(t)dt \tag{5.8}$$

This line integral can be interpreted physically. As $\boldsymbol{l_0}$ was defined as the unit vector directed from the apex to the base and $\boldsymbol{R}$ to be a unit vector directed outward, the tangential field is oriented clockwise, looking from the apex to the base, as depicted on Figure 5.6b. Therefore, the line integral $I_{\boldsymbol{T},\boldsymbol{\Gamma}^{\mathcal{P}}}$ represents the signed clockwise displacement of the material point $\mathcal{P}$ along the tangential direction defined by $\boldsymbol{T}$.

$I_{\boldsymbol{T},\boldsymbol{\Gamma}^{\mathcal{P}}}$ was computed on all vertices of the reference and torsionless case (Figure 5.7). As it can be seen on Figure 5.7a, in the reference case, the vertices of the apex and the vertices of the base rotate in an opposite direction during systole ($t/T = 0.2$). This phenomenon was already reported in literature [116, 146]. Visual comparison reveals a much smaller tangential displacement of the vertices of the torsionless case (Figure 5.7b) compared to the reference case.

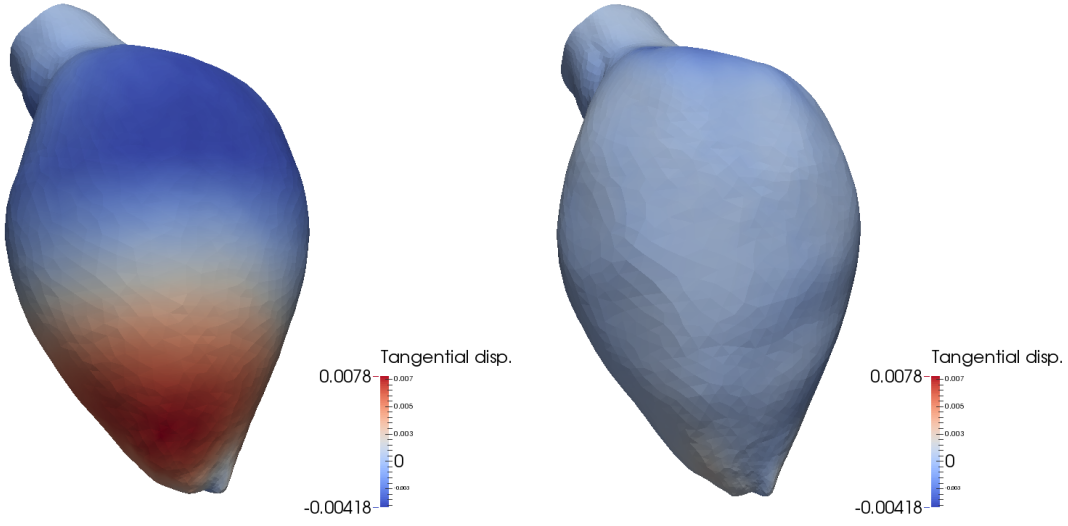

(a) (b)

Figure 5.7 – Total tangential displacement of the (a) **Reference** and (b)**Torsionless** case vertices at the beginning of the systolic phase ($t/T = 0.2$). In the reference case, one can observe a strong tangential displacement at the apex and at the base whereas this tangential displacement is much lower in the torsionless case. The tangential displacement is expressed in meters.

Denoting by $\mathcal{V}$ the set of all vertices of the ventricular surface from apex to base and by $|\mathcal{V}|$ the cardinality of $\mathcal{V}$, the average tangential displacement

$$S_1(t) = \frac{1}{|\mathcal{V}|} \sum_{\mathcal{P} \in \mathcal{V}} I_{\boldsymbol{T}, \boldsymbol{\Gamma}^{\mathcal{P}}}(t), \tag{5.9}$$

and average absolute tangential displacement

$$S_2(t) = \frac{1}{|\mathcal{V}|} \sum_{\mathcal{P} \in \mathcal{V}} |I_{\boldsymbol{T}, \boldsymbol{\Gamma}^{\mathcal{P}}}(t)|, \tag{5.10}$$

are computed in order to first provide global quantities.

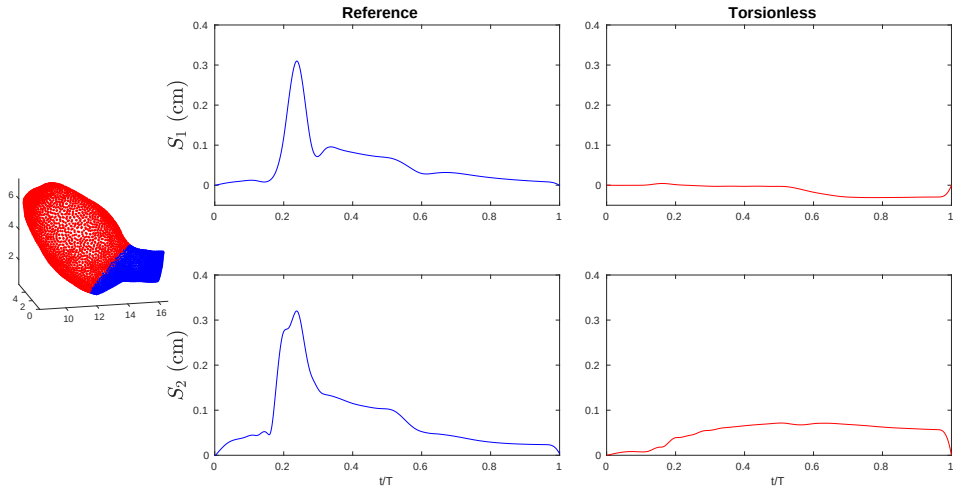

Figure 5.8 – Global quantitative assessment of the tangential displacement. On the left, the vertices of the ventricle are represented as a point cloud. The S_1 and S_2 measurement was applied on all the vertices colored in red. Those measurements are expressed in centimeters.

While the average tangential displacement S_1 provides some information about the main direction of the ventricular torsion, the average absolute tangential displacement S_2 informs about the amplitude of the tangential displacement of the vertices irrespective of whether they move in a clockwise or a counterclockwise direction. The evolution of those two quantities with respect to time is represented on Figure 5.8. On the reference case, it can be seen that the tangential displacement is mainly oriented clockwise, as depicted by the positive value of S_1. Moreover, the majority of the tangential displacement appears to happen during the systole, depicted by the peaks of both S_1 and S_2 at $t/T \approx 0.25$. As revealed by the quantity S_1 and S_2 computed in the torsionless case, the majority of the tangential displacement has been removed, as depicted by the absence of the aforementioned peak. A small residual tangential displacement is nevertheless still present on the torsionless case.

The ventricle is decomposed into layers of equal width across the longitudinal direction in order to provide a more local quantitative analysis, as depicted on Figure 5.9 where each layers was color coded.

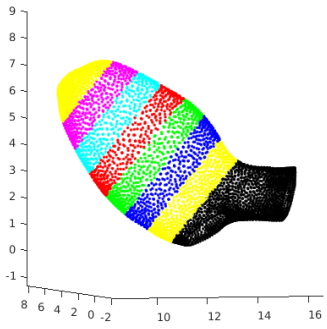

Figure 5.9 – Point cloud of the LV mesh vertices colored with respect to their layer group.

A local average tangential displacement is then computed on each layer by considering only the set $\mathcal{V}_i$ of vertices belonging to the layer i:

$$S_{1,i}(t) = \frac{1}{|\mathcal{V}_i|} \sum_{\mathcal{P} \in \mathcal{V}_i} I_{\boldsymbol{T},\boldsymbol{\Gamma}^{\mathcal{P}}}(t) \tag{5.11}$$

The Figure 5.10 depicts the evolution of the average tangential displacement with respect to time of four of the seven layers distributed across the longitudinal direction. While the original tangential displacement of the reference case is varying greatly across layers, as depicted by the differences between the blue curves, it can be seen that the reduction of the tangential displacement is similar on all layers, as depicted by the nearly flat red curve. As a side note, one can remark that, in the reference case, the apical and basal layers are indeed rotating in opposite direction as reported in the literature [115, 6, 122, 124].

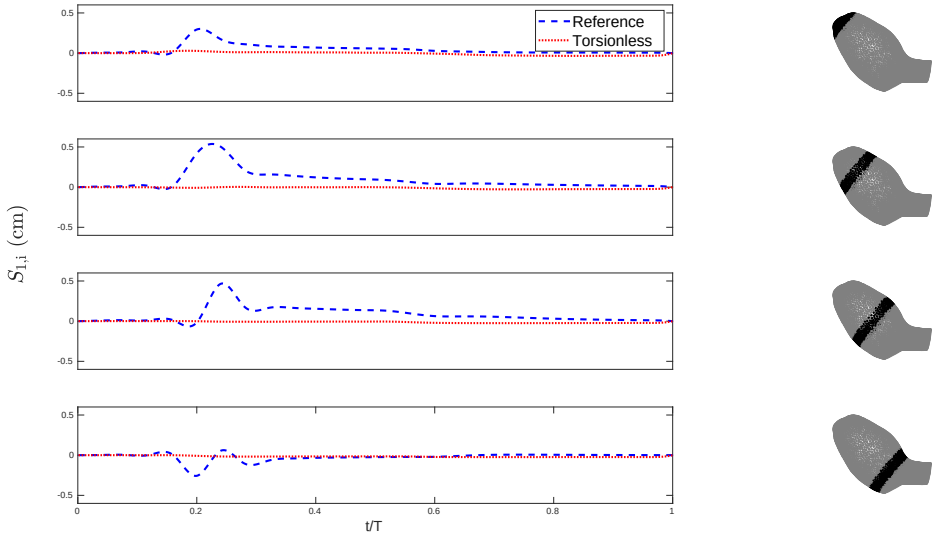

Figure 5.10 – Layerwise average tangential displacement. The black ring corresponds to the layer on which the quantity is calculated.

5.2 Numerical experiments

The intent of this section is to illustrate and discuss the impact of the LV torsion on the hemodynamics. To this purpose, the two datasets generated in Section 5.1 are used as boundary conditions in numerical simulations of an healthy case. Additionally, as one of the deeper motivations is to use ultrasound echocardiography as boundary condition of patient-specific simulations with MR, a synthetic MR is introduced to produce a pathological case. Differences between the resulting hemodynamics, both in the healthy and the pathological situation, are evaluated. The mathematical model described in Section 2.2.4, supplemented by the parameters described in Table 2.1, is used to model the hemodynamics of both numerical experiments of this chapter.

5.2.1 Healthy case

The ventricular surface displacements $\boldsymbol{d}^n$, defined on $\Gamma^n = \partial\Omega^n_{\mathrm{s,v}}$ is provided directly by the two datasets generated in Section 5.1. The reference and torsionless simulations are carried out over a full cardiac cycle, lasting 0.8 s.

The velocity fields for both flows, at ten different time period of the cardiac cycles can be found in Appendix D. As an example, comparison of the flow field during systole (Figure 5.11) and during diastole (Figure 5.12) is presented here.

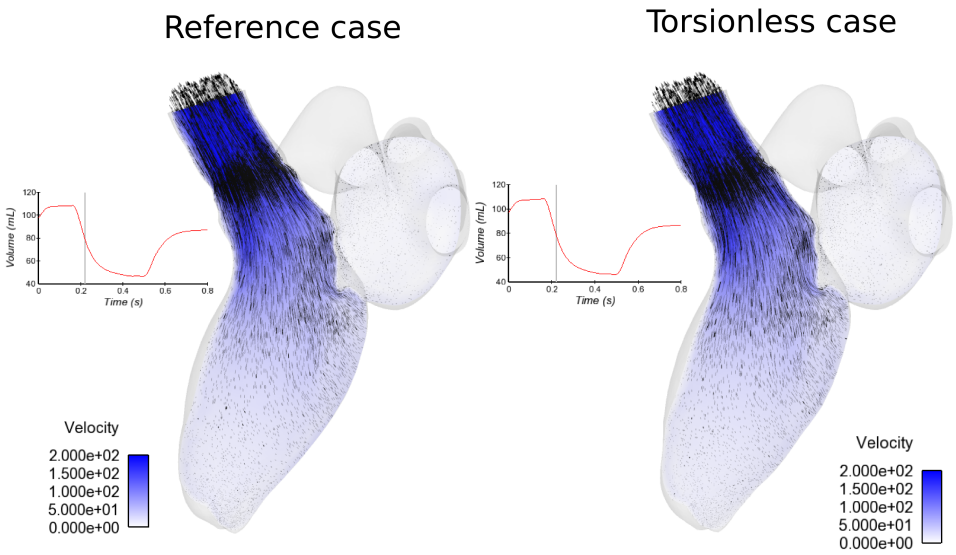

Figure 5.11 – Comparison between reference and torsionless case at $t/T \approx 0.28$ (systole).

Comparing qualitatively the two velocity fields, the removal of the twisting does not seem to have a strong influence on the hemodynamics. In systole, the aortic outflow look similar in both cases both in term of velocity field structure and velocity magnitude.

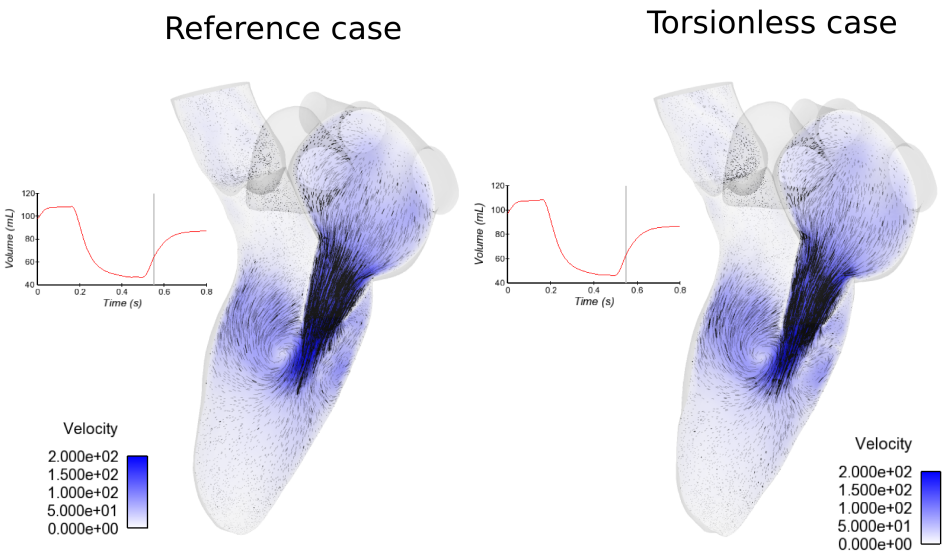

Figure 5.12 – Comparison between reference and torsionless case at $t/T \approx 0.69$ (diastole).

Similarly, in diastole, the location of the ventricular vortex due to mitral inflow is similar and the velocity magnitude is comparable. A similar conclusion can be done for all other time instants depicted in Appendix D even though small differences in the flow structure are visible when the average ventricular velocity magnitude reduces, for example between the E and A wave.

The total kinetic energy for a fluid with velocity v and density ρ) of the left ventricle was computed by:

$$KE = \frac{1}{2} \int_{\Omega} \rho \, \|\boldsymbol{v}\|_2^2 \, d\Omega \tag{5.12}$$

to assess the global energetic difference due to the removal of the twisting.

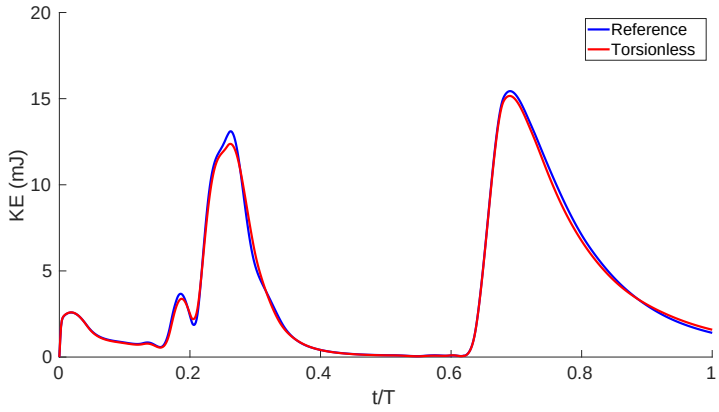

Figure 5.13 – Total ventricular blood kinetic energy for the healthy case.

Figure 5.13 plots the evolution of the total kinetic energy with respect to time for both the reference and torsionless cases. A small difference can be observed between the two curves:

during the peak systole ($t/T = 0.26$), the kinetic energy of the reference case was recorded at 13.11 mJ compared to 12.37 mJ for the torsionless case, a reduction of 5.6 %. During the peak diastole ($t/T = 0.69$), the kinetic energy was recorded at 15.43 mJ for the reference case versus 15.16 mJ for the torsionless case, a reduction of 1.75 %.

5.2.2 Synthetic pathological case

A simple synthetic regurgitation was introduced in the simulation by marking the center of the mitral valve with a ball $\mathcal{B}$ of radius 0.4 cm leading to an regurgitation area of 0.5 cm^2. This configuration corresponds to a severe Type 1 MR characterized by a central MR jet. Similarly to the healthy case, the ventricular surface displacements $\boldsymbol{d}^n$, defined on $\Gamma^n = \partial\Omega^n_{\text{s,v}}$ is provided directly by the two datasets generated in Section 5.1. The reference and torsionless simulations are carried out over a full cardiac cycle, lasting 0.80 s.

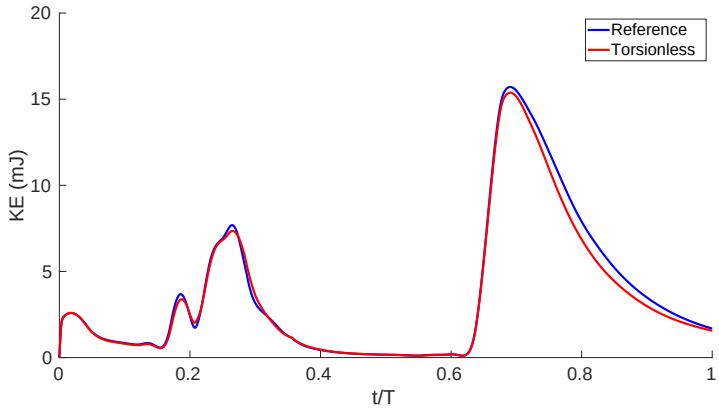

Figure 5.14 – Total ventricular blood kinetic energy for the pathological (MR) case.

Figure 5.14 plots the evolution of the total kinetic energy with respect to time for the reference and torsionless case in this pathological configuration. Modest differences between the two cases are observed: during the peak systole ($t/T = 0.26$), the kinetic energy of the reference case was recorded at 7.7 mJ versus 7.35 mJ for the torsionless case, a reduction of 4.55 %. During the peak diastole ($t/T = 0.69$), the kinetic energy was recorded at 15.71 mJ for the reference case versus 15.38 mJ for the torsionless case, a reduction of 2.1 %.

Remark: The systolic KE was reduced by nearly a factor of two in the pathological case compared to the healthy case. Note that the reported kinetic energy only takes into account the kinetic energy in the LV and therefore doesn't take into account all the energy of the blood jet in the atrium.

As assessing the MR severity, using the PISA method, relies on the surface area of the isovelocity levels, the difference between both cases with respect to to this quantity is assessed. Comparison of the isovelocity surface areas for aliasing velocities ranging from 45 cm/s up to 200 cm/s revealed very little difference, as depicted on Figure 5.15a where the area is plotted with respect to aliasing velocity for both cases. A very high correlation between the isovelocity surface areas for the reference and torsionless case is shown on Figure 5.15b. This is further confirmed by the

parameters obtained by linear regression ($f(x) = 1.02x - 0.05$, $r^2 = 0.9998$).

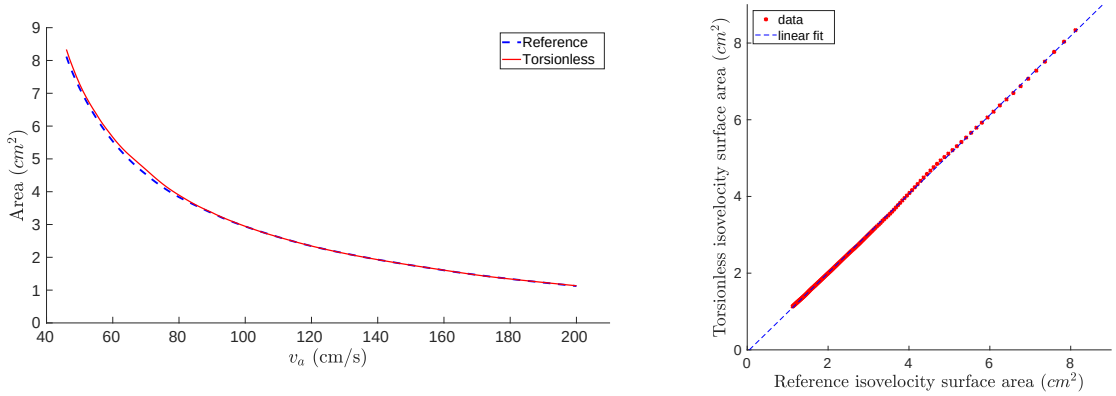

(a) (b)

Figure 5.15 – (a) Isovelocity surface area with respect to to different aliasing velocities and (b) correlation between reference isovelocity surfaces and torsionless isovolocity surfaces.

Figure 5.16 depict the regurgitant flow rate of both the reference case and torsionless case with respect to time. Integration over time of this flow rate yields a regurgitant volume of 37.20 mL for the reference case versus a regurgitant volume of 36.99 mL for the torsionless case, a reduction of 0.56 %.

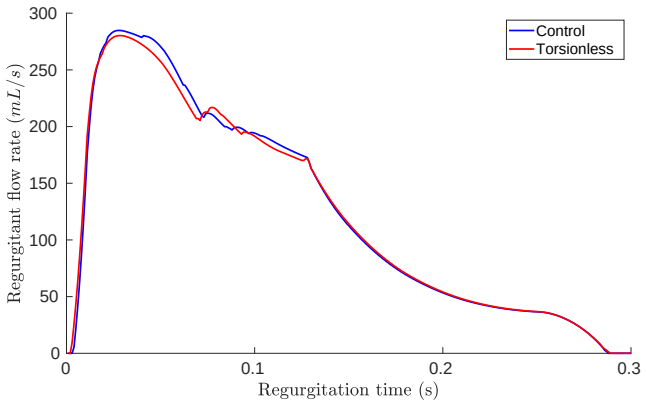

Figure 5.16 – Comparison of the regurgitant flow rate in the reference and torsionless cases.

5.3 Conclusion, discussion and perspectives

In this chapter, the impact of the endocardium twisting on the intracardiac hemodynamics has been evaluated.

In Section 5.1, two ventricular surface displacements were generated. Using an electro-mechanical simulation, which incorporated ventricular twist, a reference case was produced.

A second dataset was generated using deformable registration technique to purposely remove the ventricular twist.

In Section 5.1.1, analysis of both global and local differences between the two datasets, at all time steps, revealed that the geometrical differences were small compared to the RT3DE spatial resolution. Qualitative inspection of the ventricular surface revealed that a geometrical artifact of the registration remained visible at the apical region of the ventricular surface. Nevertheless, it was shown that the variation of volume between the two cases is negligible.

A framework was presented in Section 5.1.2 to quantify the tangential displacement of vertices on the ventricular surface and this framework was used to quantify the removal of the torsion. Tangential displacement of the vertices of the reference and torsionless cases was computed. The tangential displacement of the reference case showed that the base and apex rotated in opposite direction, a reported physiological phenomenon [115, 6, 122, 124]. Quantitative comparison between the two dynamics revealed that the ventricular torsion was strongly reduced both on a global scale and on sub layers defined along the longitudinal direction of the ventricle.

Two sets of ventricular surface dynamics were therefore produced with very similar surface location. The tangential displacement of the vertices was, however, nearly inexistent in the torsionless case. For this reason, the two sets could confidently be used as a way to evaluate the influence of ventricular torsion on the intracardiac hemodynamics.

To achieve this objective, the reference and torsionless datasets were used as boundary conditions of numerical simulations of the intracardiac hemodynamics in both a healthy and a pathological situation (Section 5.2). In the healthy situation (Section 5.2.1), the hemodynamics produced by the torsionless boundary conditions was very similar to the one produced by the reference case. Analysis of the kinetic energy confirmed that the differences between the two cases was indeed very small. Similar conclusions could be reached on a pathological case (Section 5.2.2) including a simple Type 1 mitral regurgitation. Additional analysis was performed on some MR quantities of interest such as isovelocity surface area and RV. The area of the isovelocity surfaces were nearly equal for a high range of aliasing velocity and the regurgitant volume difference between the reference and torsionless case was also very small.

The results obtained in this chapter indicate that absence of ventricular twisting does not impact significantly the blood flow neither in healthy nor in pathological cases. This also indicates that there might not be any need to consider ventricular twisting when performing CFD inside smooth ventricular geometries. This experiment is a novel result which confirms preliminary findings on idealized ventricular geometries [20] and provides an interesting insight into the use of US data to personalize models.

A strong limitation of the analysis is related to the fact that the reported results are only valid in the context of a smooth LV cavity. However, it is already known that including those internal structures modify the intracardiac hemodynamics [147, 79, 148]. It is however not clear if the local changes in the hemodynamics resulting from the presence of those structure have a strong influence on the quantities related to the MR, for example. As such, a natural extension of the analysis would be to evaluate the impact of the twist in the context of a non-smooth LV geometry. Such experiment is nevertheless not easy to set up, as one would need to prevent alteration of the structural integrity of the internal features during the twisting removal step.

Chapter 6
Simplified models for cardiac blood flow estimation

In this chapter, we present a method to reconstruct the intracardiac blood velocity based on Color-Doppler images. The presented approach mainly relies on the method proposed by Assi et al. [134] but further insight is provided by:

- Evaluating the sensitivity of the blood flow reconstruction with respect to the subsambling of the data provided by the synthetic Color-Doppler images;
- Investigating how this well method can reconstruct blood flow in pathological cases which include mitral regurgitation. We try to quantify the benefits of this method with respect to MR severity quantification;
- Extending the 2D method proposed by Assi et al. [134] to the 3D case.

In Section 6.1, some elements of calculus of variations are recalled: several functionals of different complexities and their minimization are considered along numerical examples. In Section 6.2, an optimization problem, similar to the one presented by Assi et al. [134], is introduced to reconstruct 2D fluid velocity fields. Several numerical examples are presented to evaluate the algorithm, its sensitivity to partial data acquisition, and its ability to reconstruct the blood velocity fields. As 3D US probes are increasingly available in a clinical environment, the method is finally generalized to 3D velocity fields reconstruction in Section 6.3 and evaluated on two different numerical examples.

In this chapter, some choices had to be made to satisfy industrial constraints. In particular, the discretization method chosen (finite difference) was imposed.

6.1 Elements of calculus of variations: Theory and examples

In this section, some theoretical background related to functional optimization is recalled. In Section 6.1.1, we present the simplest case: a functional of one function in one variable is considered. In Section 6.1.2 and 6.1.3, extension to more complicated functionals, respectively of one function of n variables and m functions of n variables, is presented.

Presenting these three cases allow to slowly present the building blocks required to solve the optimization problem of Section 6.2 and Section 6.3. The first case aims to establish the link between the stationary point of a functional and the solution of the Euler-Lagrange (E-L) equation. The second case allows to introduce how partial derivatives become involved in the E-L equations. In the provided numerical example, some weighing coefficients are also added in the functional in order to depict the influence of such coefficient on the solution of the E-L equation.

Finally, in the third case, we show how minimizing a functional of several functions result in a system of multiple E-L equations. The numerical example allows to illustrate one way to deal with the discretization of such system.

6.1.1 Functional optimization using the Euler-Lagrange equation

We first consider the optimization problem consisting of finding the stationary points of a functional in a very simple case involving a single function of one variable.

Definition

Let $u \in \mathcal{C}^2$ be a function defined as:

$$\begin{aligned} u(x) :&[a,b] \to \mathbb{R} \\ &x \quad \to u(x) \end{aligned}$$

with boundary conditions $u(a) = A$ and $u(b) = B$.
We also define $F(x,u(x),\frac{d}{dx}u(x)) : [a,b] \times \mathbb{R}^2 \to \mathbb{R} \in \mathcal{C}^1$ and consider the functional $J[u]$:

$$J[u] = \int_a^b F(x,u(x),u'(x)dx \tag{6.1}$$

Proposition 1: The stationary points of the functional $J[u]$ satisfy the E-L equation

$$\frac{dF}{du} - \frac{d}{dx}\frac{dF}{du'} = 0 \quad \text{in} \quad [a,b]. \tag{6.2}$$

For the sake of completeness, we include the proof of Proposition 1 in Appendix E.1.

Numerical example

A function u_d is given on $[a,b] \to [0,1]$ as depicted on Figure 6.1.

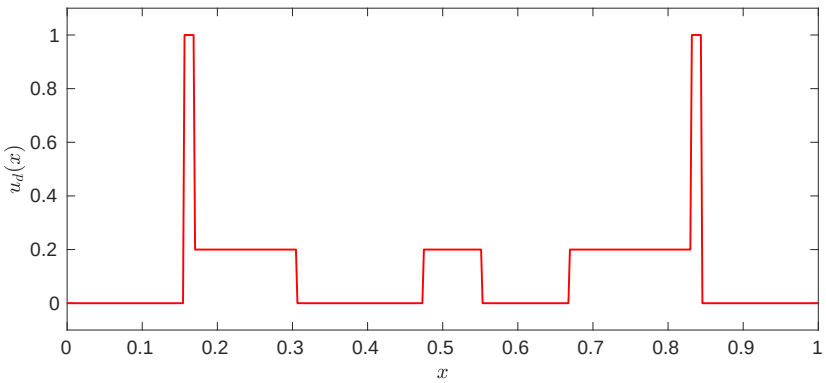

Figure 6.1 – Function $u_d(x) : [a,b] \to [0,1]$ involving sharp variations

We consider the following problem (M1):

Problem (M1)

Given $u_d : [a,b] \subseteq \mathbb{R} \to \mathbb{R}$, find $u(x) : [a,b] \subseteq \mathbb{R} \to \mathbb{R}$ which minimizies:

$$J[u] = \int_a^b \left[\frac{1}{2}(u - u_d)^2 + \frac{1}{2}\left(\frac{du}{dx}\right)^2 \right] dx \tag{6.3}$$

The following boundary conditions $u(a) = u_d(a)$ et $u(b) = u_d(b)$ are given.

This minimization problem intuitively aims to obtain a smooth function u which is close to the given data u_d, to reduce the sharp variations, for example.

The E-L equation associated to problem (M1) can be written:

$$\begin{aligned} \frac{dF}{du} - \frac{d}{dx}\frac{dF}{du'} &= 0 \\ \equiv (u - u_d) - \frac{d}{dx}\left(\frac{du}{dx}\right) &= 0 \\ \equiv u - \frac{d^2u}{dx^2} &= u_d \end{aligned}$$

As $J[u]$ is convex, problem (M1) is equivalent to problem (M1'):

Problème (M1')

Given $u_d : [a,b] \subseteq \mathbb{R} \to \mathbb{R}$, find $u(x) : [a,b] \subseteq \mathbb{R} \to \mathbb{R}$ such that:

$$u - \frac{d^2u}{dx^2} = u_d \quad \text{in } [a,b] \tag{6.4}$$

$$u(a) = u_d(a) \tag{6.5}$$

$$u(b) = u_d(b) \tag{6.6}$$

Problem (M1') is discretized using the finite difference method. The second derivative of f is approximated using the second order central finite difference approximation $\partial_h^2[f](x) = \frac{f(x+h)-2f(x)+f(x-h)}{h^2}$. We define $[\mathbf{f}]$ as the $n \times 1$ vector whose entries consists of the function $f(x)$ uniformly sampled in $[a,b]$ with a discretization step h and D_{xx} as the $n \times n$ tridiagonal matrix discretizing the finite difference operator $\partial_h^2[f](x)$:

$$D_{xx} = \frac{1}{h^2}\begin{bmatrix} -2 & 1 & & 0 \\ 1 & \ddots & \ddots & \\ & \ddots & \ddots & 1 \\ 0 & & 1 & -2 \end{bmatrix},$$

the discretized version of (6.4) is written as a linear system $Ax = b$ with:

$$A = \mathbb{1} - D_{xx}$$
$$x = [\mathbf{u}]$$
$$b = [\mathbf{u_d}]$$

The boundary conditions (6.5)-(6.6) are incorporated in the system by replacing the appropriate entries. By solving the aforementioned linear system, one obtains the solution depicted in Figure 6.2. As intuited in the beginning of this numerical example, one can observe that the function $u(x)$ is indeed a copy of the functon $u_d(x)$ where the sharp variations have been smoothed.

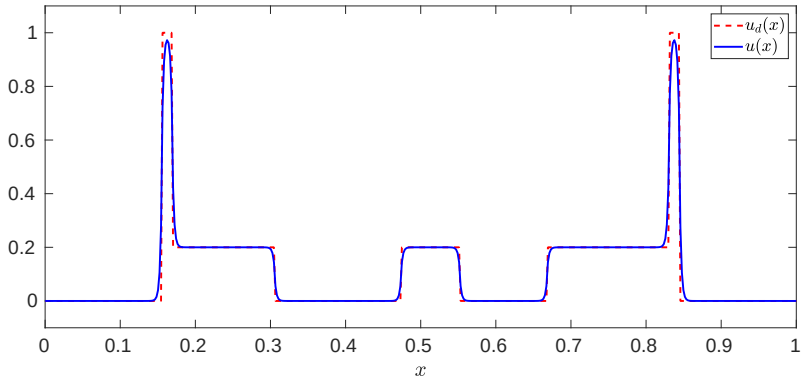

Figure 6.2 – Result of the minimization of $J[u]$ using u_d as the data attachment term.

6.1.2 Generalization for functionals involving a function of several variables

The derivation of Section 6.1.1 is now extended in the case of a function of several variable to highlight how the E-L equation is modified.

Definition

Let $u(x_1,...,x_n) \in \mathcal{C}^2$ be function defined as:

$$u(x_1,...,x_n) : \Omega \subseteq \mathbb{R}^n \rightarrow \mathbb{R}$$
$$(x_1,...,x_n) \rightarrow u(x_1,...,x_n)$$

for which a boundary condition $u|_{\partial\Omega} = u_d$ is given.
We also define $F(x_1,...,x_n,u,\frac{\partial u}{\partial x_1},...,\frac{\partial u}{\partial x_n}) : \Omega \times \mathbb{R}^{n+1} \rightarrow \mathbb{R} \in \mathcal{C}^1$ and consider the functional $J[u]$:

$$J[u] = \int_\Omega F(x_1,...,x_n,u,\frac{\partial u}{\partial x_1},...,\frac{\partial u}{\partial x_n}) d\Omega \tag{6.7}$$

Proposition 2: The stationary points of the functional $J[u]$ satisfy the E-L equation

$$\frac{\partial F}{\partial u} - \sum_i \frac{\partial}{\partial x_i}\frac{\partial F}{\partial u_{x_i}} = 0 \quad \text{in} \quad \Omega. \tag{6.8}$$

For the sake of completeness, we include the proof of Proposition 2 in Appendix E.2.

Numerical example

A function $u_d(x,y) : \Omega \subseteq \mathbb{R}^2 \to \mathbb{R}$, 2D grayscale synthetic phantom of a head, is given as depicted on Figure 6.3:

Figure 6.3 – 2D grayscale synthetic phantom of a head where the large ellipse represents the brain while the smaller internal ellipses represent bran features.

We consider the problem (M2), in which we consider a functional involving one function of two variables:

Problem (M2)

Given $u_d(x,y)$, $\lambda_1 \in \mathbb{R}^{*+}$ and $\lambda_2 \in \mathbb{R}^{*+}$, find $u(x,y) : \Omega \subseteq \mathbb{R}^2 \to \mathbb{R}$ which minimizes:

$$J[u] = \int_\Omega \left[\lambda_1 \frac{1}{2}(u - u_d)^2 + \lambda_2 \frac{1}{2}\|\nabla u\|_2^2\right] d\Omega \tag{6.9}$$

The boundary condition $u|_{\partial\Omega} = u_d|_{\partial\Omega}$ is given.

Similarly to problem (M1), this minimization problem aims to obtain a smooth function $u(x,y)$ close, in a least square sense, to the given data $u_d(x,y)$. This minimization problem can be used to smooth a function $u_d(x,y)$. Weights λ_1 and λ_2 have been introduced, compared to the problem (M1) to give more importance to either the smoothing or to the data attachment term.

The E-L equation for problem (M2) can be written as:

$$\begin{aligned}
&\frac{\partial F}{\partial u} && -\frac{\partial}{\partial x}\frac{\partial F}{\partial u_x} && -\frac{\partial}{\partial y}\frac{\partial F}{\partial u_y} && =0\\
\equiv&\lambda_1(u-u_d) && -\lambda_2\frac{\partial}{\partial x}\left(\frac{\partial u}{\partial x}\right) && -\lambda_2\frac{\partial}{\partial y}\left(\frac{\partial u}{\partial y}\right) && =0\\
\equiv&\lambda_1 u && -\lambda_2\frac{\partial^2 u}{\partial x^2} && -\lambda_2\frac{\partial^2 u}{\partial y^2} && =\lambda_1 u_d
\end{aligned}$$

As $J[u]$ is convex, problem (M2) is equivalent to problem (M2'):

Problème (M2')

Given $u_d(x,y)$, $\lambda_1 \in \mathbb{R}^{*+}$ and $\lambda_2 \in \mathbb{R}^{*+}$, find $u(x,y) : \Omega \subseteq \mathbb{R}^2 \to \mathbb{R}$ such that:

$$\lambda_1 u - \lambda_2\frac{\partial^2 u}{\partial x^2} - \lambda_2\frac{\partial^2 u}{\partial y^2} = \lambda_1 u_d \quad \text{in } \Omega \tag{6.10}$$

$$u|_{\partial\Omega} = u_d|_{\partial\Omega} \tag{6.11}$$

Problem (M2') is discretized using the finite difference method. We define $[\mathbf{f}]$ as the $m \times n$ matrix whose entries consists of the function $f(x,y)$ uniformly sampled in each variable x and y with a discretization step of respectively h and k. We define by $[\text{vec}(\mathbf{f})]$ the $mn \times 1$ vector resulting of the vectorization of the matrix $[\mathbf{f}]$. The first order partial derivatives are approximated using first order central differences $\partial_{x,h}[f](x,y) = \frac{f(x+h,y)-f(x-h,y)}{2h}$ and $\partial_{y,k}[f](x,y) = \frac{f(x,y+k)-f(x,y-k)}{2k}$. Those derivative approximations are discretized as $mn \times mn$ matrices, respectively denoted D_x and D_y. The second order partial differential operator are defined as:

$$\begin{aligned}
D_{xx} &= D_x D_x\\
D_{yy} &= D_y D_y
\end{aligned}$$

(6.10) is written as the linear system $Ax = b$ with:

$$\begin{aligned}
A &= \lambda_1 \mathbb{1} - \lambda_2(Dxx + Dyy)\\
x &= \text{vec}([\mathbf{u}])\\
b &= \lambda_1 \cdot \text{vec}([\mathbf{u_d}])
\end{aligned}$$

The boundary condition (6.11) is then incorporated in the linear system by replacing the appropriate entries. Solving the aforementioned system, the function u obtained is depicted on Figure 6.4. The smoothing effect appears clearly while the main features of u_d are still visible.

(a) (b)

Figure 6.4 – Comparison between a) the original data attachment term u_d and b) the recovered function u using $\lambda_1 = 1$ and $\lambda_2 = 15$.

6.1.3 Generalization for functionals involving multiple functions of several variables

The derivations of sections 6.1.1 and 6.1.2 is extended to the case of minimizing a functional of m functions of n variables.

Definition

Let $u_k \quad \forall k \in [1,m] \in \mathcal{C}^2$ be functions defined as:

$$\begin{aligned} u_k(x_1,...,x_n) : \Omega \subseteq \mathbb{R}^n \quad &\rightarrow \mathbb{R} \\ (x_1,...,x_n) &\rightarrow u_k(x_1,...,x_n) \end{aligned}$$

for which boundary conditions $u_k|_{\partial\Omega} = u_{d,k}$ are given.
We also define the function $F(x_1,...,x_n,u_1,..,u_m,\frac{\partial u_1}{\partial x_1},...,\frac{\partial u_1}{\partial x_n},...,\frac{\partial u_m}{\partial x_1},...,\frac{\partial u_m}{\partial x_n}) : \Omega \times \mathbb{R}^{m*(n+1)} \rightarrow \mathbb{R} \in \mathcal{C}^1$ and consider the functional $J[u_1,...,u_m]$:

$$J[u_1,...,u_m] = \int_\Omega F(x_1,...,x_n,u_1,..,u_m,\frac{\partial u_1}{\partial x_1},...,\frac{\partial u_1}{\partial x_n},...,\frac{\partial u_m}{\partial x_1},...,\frac{\partial u_m}{\partial x_n})d\Omega \tag{6.12}$$

Proposition 3: The stationary points of the functional $J[u]$ satisfy the system of E-L equations

$$\frac{\partial F}{\partial u_k} - \sum_i \frac{\partial}{\partial x_i}\frac{\partial F}{\partial u_{k,x_i}} = 0 \quad \text{in} \quad \Omega \quad \forall k \in [1,m]. \tag{6.13}$$

By adding a small perturbation to each functions u_k while keeping the other fixed, the proof presented in Appendix E.2 can be used to derive each equation of the system 6.13.

Numerical example

The image *Lena* (Figure 6.5) is used as the data attachment term. The red, green and blue channel define respectively $u_{1,d} : \Omega \subseteq \mathbb{R}^2 \to \mathbb{R}$, $u_{2,d} : \Omega \subseteq \mathbb{R}^2 \to \mathbb{R}$ and $u_{3,d} : \Omega \subseteq \mathbb{R}^2 \to \mathbb{R}$.

Figure 6.5 – *Lena*, a traditional image used in the image processing community

We pose the problem (M3), in which we consider a functional involving three functions of two variables:

Problem (M3)

Given functions $u_{1,d}$, $u_{2,d}$, $u_{3,d}$, $\lambda_1 \in \mathbb{R}^{*+}$ and $\lambda_2 \in \mathbb{R}^{*+}$, find the functions $u_{\{1,2,3\}}(x,y) : \Omega \subseteq \mathbb{R}^2 \to \mathbb{R}$ which minimize:

$$J\left[u_1,u_2,u_3\right] = \int_\Omega \left[\sum_{k=1}^{3} \lambda_1 \frac{1}{2}(u_k - u_{k,d})^2 + \lambda_2 \frac{1}{2} \left\|\nabla u_k\right\|_2^2\right] d\Omega. \tag{6.14}$$

The boundary condition $u_{\{1,2,3\}}|_{\partial\Omega} = u_{\{1,2,3\},d}|_{\partial\Omega}$ is prescribed.

This minimization problem aims to obtain smooth functions $u_{\{1,2,3\}}(x,y)$ close, in a least square sense, to the given data $u_{\{1,2,3\},d}(x,y)$. This minimization problem can be used to smooth a function $u_d(x,y)$. Similarly to problem (M2), weights λ_1 and λ_2 can give more importance to either the smoothing or to the data attachment term.

By writing the system of E-L equations associated to $J\left[u_1,u_2,u_3\right]$ and noticing that this functional is convex, the problem (M3) is equivalent to:

Problème (M3')

Given functions $u_{1,d}$, $u_{2,d}$, $u_{3,d}$, $\lambda_1 \in \mathbb{R}^{*+}$ and $\lambda_2 \in \mathbb{R}^{*+}$, find the functions $u_{\{1,2,3\}}(x,y) : \Omega \subseteq \mathbb{R}^2 \to \mathbb{R}$ such that:

$$\lambda_1 u_1 - \lambda_2 \frac{\partial^2 u_1}{\partial x^2} - \lambda_2 \frac{\partial^2 u_1}{\partial y^2} = \lambda_1 u_{1,d} \quad \text{in } \Omega \tag{6.15}$$

$$\lambda_1 u_2 - \lambda_2 \frac{\partial^2 u_2}{\partial x^2} - \lambda_2 \frac{\partial^2 u_2}{\partial y^2} = \lambda_1 u_{2,d} \quad \text{in } \Omega \tag{6.16}$$

$$\lambda_1 u_3 - \lambda_2 \frac{\partial^2 u_3}{\partial x^2} - \lambda_2 \frac{\partial^2 u_3}{\partial y^2} = \lambda_1 u_{3,d} \quad \text{in } \Omega \tag{6.17}$$

$$u_k|_{\partial\Omega} = u_{k,d}|_{\partial\Omega} \quad \forall k \in [1,3] \tag{6.18}$$

Using the finite difference method and the finite differential operators described in Section 6.1.2, problem (M3') can be solved by writing (6.15)-(6.17) as the linear system $Ax = b$ with:

$$A = \begin{bmatrix} \lambda_1 \mathbb{1} - \lambda_2(Dxx + Dyy) & 0 & 0 \\ 0 & \lambda_1 \mathbb{1} - \lambda_2(Dxx + Dyy) & 0 \\ 0 & 0 & \lambda_1 \mathbb{1} - \lambda_2(Dxx + Dyy) \end{bmatrix}$$

$$x = \begin{bmatrix} \text{vec}(\mathbf{u_1}) \\ \text{vec}(\mathbf{u_2}) \\ \text{vec}(\mathbf{u_3}) \end{bmatrix}$$

$$b = \lambda_1 \cdot \begin{bmatrix} \text{vec}(\mathbf{u_{1,d}}) \\ \text{vec}(\mathbf{u_{2,d}}) \\ \text{vec}(\mathbf{u_{3,d}}) \end{bmatrix}$$

The boundary conditions (6.18) are then incorporated in the linear system by replacing the appropriate entries. Solving the aforementioned system the function u_1,u_2 and u_3 are obtained. On Figure 6.6, one can compare the initial data attachment with the image resulting of the minimization process, where the functions u_1, u_2 and u_3 are respectively used as the red, green and blue channel.

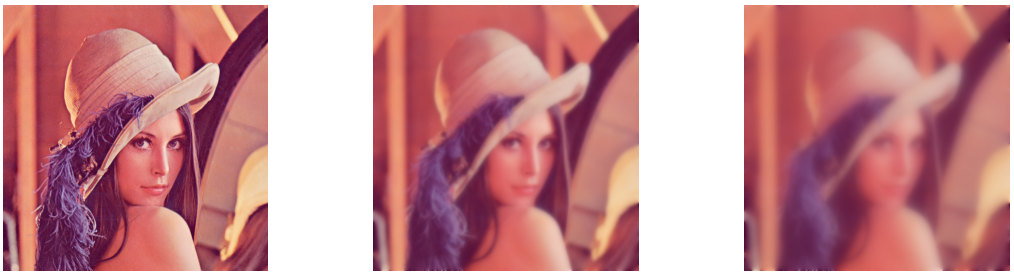

(a) (b) (c)

Figure 6.6 – a) Original data attachment terms $u_{1,d}$, $u_{2,d}$ and $u_{3,d}$, represented as a RGB image, b) u_1, u_2 and u_3 using $\lambda_1 = 1$ and $\lambda_2 = 15$ and c) u_1, u_2 and u_3 using $\lambda_1 = 1$ and $\lambda_2 = 100$

6.2 2D Color Doppler flow reconstruction

In this section, we now consider the problem of reconstructing a 2D blood velocity field based on Color Doppler data. The notation that will be used throughout the section is first exposed. A functional including an image term and physically based constraint is presented. The associated system of E-L equations is then computed and then discretized. Several numerical experiments are used to investigate in more detail the blood flow reconstruction and its sensitivity to partial data acquisition. Moreover a numerical experiment in which the image data involve a pathological MR is used to investigate if blood flow reconstruction could be beneficial to MR quantification.

6.2.1 Notations

Let $\mathbf{p_c}$ denote the position of a 2D ultrasound probe. The probe is oriented to acquire a 2D image on a plane P that can be decribed by $\mathbf{p_c}$ and two orthogonal unit vectors $\mathbf{v_1}$ and $\mathbf{v_2}$. A third vector $\mathbf{v_3} = \mathbf{v_1} \times \mathbf{v_2}$. We change the coordinate system to the Cartesian coordinate system defined as ($\mathbf{p_c}$,$\mathbf{v_1}$,$\mathbf{v_2}$,$\mathbf{v_3}$).

Let $\mathbf{V}$ be a vector field of the blood velocity inside the heart geometrical domain denoted by Ω:

$$\begin{aligned} \mathbf{V} :\Omega \in \mathbb{R}^3 \quad &\rightarrow \mathbb{R}^3 \\ (x_1, x_2, x_3) &\rightarrow \begin{bmatrix} u(x_1, x_2, x_3) \\ v(x_1, x_2, x_3) \\ w(x_1, x_2, x_3) \end{bmatrix}, \quad \text{such that} \quad \boldsymbol{\nabla} \cdot \mathbf{V} = 0 \text{ in } \Omega \end{aligned}$$

Remark 1: Note that, even though a non-standard coordinate system is considered, the divergence operator preserved as it is invariant under translation and rotation.

The plane P intersects the domain Ω as Ω_P and the vector field $\mathbf{V}$ as $\mathbf{V'}$:

$$\begin{aligned} \mathbf{V'} :\Omega_P \in \mathbb{R}^2 &\rightarrow \mathbb{R}^3 \\ (x_1, x_2) \ &\rightarrow \begin{bmatrix} u(x_1,x_2,0) \\ v(x_1,x_2,0) \\ w(x_1,x_2,0) \end{bmatrix} \end{aligned}$$

The vector field $\mathbf{V'}$ out-of plane component is removed to define the 2D vector field $\mathbf{V_P}$:

$$\begin{aligned} \mathbf{V_P} :\Omega_P \in \mathbb{R}^2 &\rightarrow \mathbb{R}^2 \\ (x_1, x_2) \ &\rightarrow \rightarrow \begin{bmatrix} u(x_1,x_2,0) \\ v(x_1,x_2,0) \end{bmatrix} \end{aligned}$$

Let $\mathbf{v_r}(x_1,x_2)$ be the unit vector defined, at any point (x_1,x_2) of P as:

$$\mathbf{v_r}(x_1,x_2) = \frac{[x_1,x_2]^T - \mathbf{p_c}}{\|[x_1,x_2]^T - \mathbf{p_c}\|}$$

The scalar field V_r, resulting of the projection of the vector field $\mathbf{V_P}$ on the unit vectors $\mathbf{v_r}$ is defined:

$$\begin{aligned} V_r :&\Omega_P \in \mathbb{R}^2 \rightarrow \mathbb{R} \\ &(x_1,x_2) \ \rightarrow \mathbf{V_P}(x_1,x_2) \cdot \mathbf{v_r}(x_1,x_2) \end{aligned}$$

Remark 2: The vector field $\mathbf{V_P}$ can be thought as a perfect 2D blood flow representation if Color Doppler was able to quantify the blood velocity in the two components defining the imaging plane.
Remark 3: The scalar field V_r is analogous to the scalar velocity field that would be obtained using Doppler echography as the unit vectors $\mathbf{v_r}$ are the unit vectors aligned along the synthetic US beam directions. For simplicity reason, we choose to not include synthetic aliasing into this scalar field.
Remark 4: The vector field $\mathbf{V_P}$ is not divergence-free. Indeed, the component of $\mathbf{V}$ orthogonal with the plane was removed to generate $\mathbf{V_P}$. However, as noted in previous studies [149, 134], a 2D divergence-free assumption can be reasonably assumed in some cases, such as the apical 3-Chamber view.

Error quantification:

In order to quantify the error and differences between the velocity vector fields, it is proposed to report several quantities.

The quantity $E(\mathbf{V_1},\mathbf{V_2},x_1,x_2)$, velocity error between the vector fields $\mathbf{V_1}$ and $\mathbf{V_2}$ at any point (x_1,x_2) of the domain Ω_P is defined as:

$$E(\mathbf{V_1},\mathbf{V_2},x_1,x_2) = \|\mathbf{V_1}(x_1,x_2) - \mathbf{V_2}(x_1,x_2)\|_2 \,.$$

Moreover, its normalized version $\hat{E}(\mathbf{V_1},\mathbf{V_2},x_1,x_2)$ with respect to V_1 is defined as:

$$\hat{E}(\mathbf{V_1},\mathbf{V_2},x_1,x_2) = \frac{\|\mathbf{V_1}(x_1,x_2) - \mathbf{V_2}(x_1,x_2)\|_2}{\|\mathbf{V_1}(x_1,x_2)\|_2}.$$

The average errors across the entire domain Ω_P are computed as:

$$\begin{aligned} \overline{E}(\mathbf{V_1},\mathbf{V_2}) &= \frac{1}{|\Omega_P|}\int_{\Omega_P} E(\mathbf{V_1},\mathbf{V_2}), \\ \overline{\hat{E}}(\mathbf{V_1},\mathbf{V_2}) &= \frac{1}{|\Omega_P|}\int_{\Omega_P} \hat{E}(\mathbf{V_1},\mathbf{V_2}). \end{aligned}$$

6.2.2 Definition of the functional

Given an observed radial flow velocity V_r, it is aimed to reconstruct the vector field $\mathbf{V_P}$. We frame the reconstruction problem as following:

Problem (R1)

Given an observed radial flow velocity V_r, a boundary data $\mathbf{V_P}|_{\partial\Omega_P}$, and $\lambda_1, \ldots, \lambda_4 \in \mathbb{R}^{+*}$, find the vector field $\mathbf{V_P^\star} : \Omega_P \to \mathbb{R}^2$ which minimizes the functional $J[\mathbf{X}]$:

$$J[\mathbf{X}] = \lambda_1 \int_{\Omega_P} (\mathbf{X} \cdot \mathbf{v_r} - V_r)^2 \tag{6.19}$$

$$+\lambda_2 \int_{\Omega_P} (\boldsymbol{\nabla} \cdot \mathbf{X})^2 \tag{6.20}$$

$$+\lambda_3 \int_{\partial\Omega_P} \|\mathbf{X} - \mathbf{V_P}\|_2^2 \tag{6.21}$$

$$+\lambda_4 \int_{\Omega_P} \|\boldsymbol{\nabla}\mathbf{X}\|_2^2 \tag{6.22}$$

The minimization of the terms of $J[\mathbf{X}]$ can be interpreted as follows:

- (6.19) (associated weight λ_1) aims to match the projection of the vector field $\mathbf{X}$ on the unit vectors $\mathbf{v_r}$ with the observed vector field V_r. This is a data attachment term;
- (6.20) (associated weight λ_2) is associated with the minimization of the divergence of the vector field $\mathbf{X}$. This is a physical constraints to respect the hypothesis of a divergence-free flow;
- (6.21) (associated weight λ_3) corresponds to imposing a boundary condition on the vector field at the boundaries of the ventricle to ensure well-posedness of the minimization problem as reported by Assi et al. [134];
- Finally, (6.22) (associated weight λ_4) aims to minimize the gradient of the recovered vector field. The purpose is to obtain a relatively smooth vector field and penalize sharp variations.

The above formulated functional minimization problem imposes several, possibly incompatible constraints at the same time. The result of the minimization problem is therefore a trade-off between all those constraints parameterized by the weighting factors λ_i. This required tradeoff between the different term also means that the vector field minimizing $J[\mathbf{X}]$ will most probably not be enforcing any of the constraints exactly. A conscious choice therefore has to be made to properly tune the given parameters, for example to minimize a given error norm.

6.2.3 Minimization using variational calculus

In order to solve the reconstruction problem (R1), *i.e.* minimize $J[\mathbf{X}]$, we start by retrieving the system of E-L equations associated to $J[\mathbf{X}]$. Lemmas 1-4 are introduced:

Lemma 1: Let $G_1[\mathbf{X}]$ be defined as

$$G_1[\mathbf{X}] = \int_{\Omega_P} (\mathbf{X} \cdot \mathbf{v_r} - V_r)^2,$$

the stationary points of the functional $G_1[\mathbf{X}]$ satisfy the following system:

$$\cos(\theta)^2 X_1 + \cos(\theta)\sin(\theta) X_2 = \cos(\theta) V_r \quad \text{in } \Omega_P, \tag{6.23}$$
$$\cos(\theta)\sin(\theta) X_1 + \sin(\theta)^2 X_2 = \sin(\theta) V_r \quad \text{in } \Omega_P, \tag{6.24}$$

where θ is the angle between $\mathbf{v_r}$ and $\mathbf{v_1}$.

Lemma 2: Let $G_2[\mathbf{X}]$ be defined as

$$G_2[\mathbf{X}] = \int_{\Omega_P} (\boldsymbol{\nabla} \cdot \mathbf{X})^2,$$

the stationary points of the functional $G_2[\mathbf{X}]$ satisfy the following system:

$$-\left(\frac{\partial^2 X_1}{\partial x_1^2} + \frac{\partial^2 X_2}{\partial x_1 \partial x_2}\right) = 0 \quad \text{in } \Omega_P, \tag{6.25}$$
$$-\left(\frac{\partial^2 X_1}{\partial x_1 \partial x_2} + \frac{\partial^2 X_2}{\partial x_2^2}\right) = 0 \quad \text{in } \Omega_P. \tag{6.26}$$

Lemma 3: Let $G_3[\mathbf{X}]$ be defined as

$$G_3[\mathbf{X}] = \int_{\partial\Omega_P} \|\mathbf{X} - \mathbf{V_P}\|_2^2,$$

the stationary points of the functional $G_3[\mathbf{X}]$ satisfy the following system:

$$X_1 = \mathbf{V_P} \cdot \mathbf{v_1} \quad \text{in } \partial\Omega_P, \tag{6.27}$$
$$X_2 = \mathbf{V_P} \cdot \mathbf{v_2} \quad \text{in } \partial\Omega_P. \tag{6.28}$$

Lemma 4: Let $G_4[\mathbf{X}]$ be defined as

$$G_4[\mathbf{X}] = \int_{\Omega_P} \|\boldsymbol{\nabla}\mathbf{X}\|_2^2,$$

the stationary points of the functional $G_4[\mathbf{X}]$ satisfy the following system:

$$-\frac{\partial^2 X_1}{\partial {x_1}^2} - \frac{\partial^2 X_1}{\partial {x_2}^2} = 0 \quad \text{in } \Omega_P, \tag{6.29}$$
$$-\frac{\partial^2 X_2}{\partial {x_1}^2} - \frac{\partial^2 X_2}{\partial {x_2}^2} = 0 \quad \text{in } \Omega_P. \tag{6.30}$$

The proofs of Lemmas 1-4 are detailed in Appendix E.3.

Theorem: The stationary points of the functional $J[\mathbf{X}]$ satisfy the following system:

$$\begin{aligned}
&\lambda_1 \left[\cos(\theta)^2 X_1 + \cos(\theta)\sin(\theta) X_2\right] \\
&- \lambda_2 \left[\frac{\partial^2 X_1}{\partial x_1^2} + \frac{\partial^2 X_2}{\partial x_1 \partial x_2}\right] \\
&- \lambda_4 \left[\frac{\partial^2 X_1}{\partial {x_1}^2} + \frac{\partial^2 X_1}{\partial {x_2}^2}\right] = \lambda_1 \cos(\theta) V_r \qquad \text{in } \Omega_P \qquad (6.31) \\
&\lambda_1 \left[\cos(\theta)\sin(\theta) X_1 + \sin(\theta)^2 X_2\right] \\
&- \lambda_2 \left[\frac{\partial^2 X_1}{\partial x_1 \partial x_2} + \frac{\partial^2 X_2}{\partial x_2^2}\right] \\
&- \lambda_4 \left[\frac{\partial^2 X_2}{\partial {x_1}^2} + \frac{\partial^2 X_2}{\partial {x_2}^2}\right] = \lambda_1 \sin(\theta) V_r \qquad \text{in } \Omega_P \qquad (6.32) \\
&\lambda_3 X_1 = \lambda_3 (\mathbf{V_P} \cdot \mathbf{v_1}) \qquad \text{in } \partial\Omega_P \qquad (6.33) \\
&\lambda_3 X_2 = \lambda_3 (\mathbf{V_P} \cdot \mathbf{v_2}) \qquad \text{in } \partial\Omega_P \qquad (6.34)
\end{aligned}$$

Proof.
Let $J[\mathbf{X}] = \lambda_1 G_1[\mathbf{X}] + \lambda_2 G_2[\mathbf{X}] + \lambda_3 G_3[\mathbf{X}] + \lambda_4 G_4[\mathbf{X}]$.

The system of E-L equations associated to $J[\mathbf{X}]$ can be derived using Lemmas 1-4: summing (6.23)-(6.24) scaled by λ_1, (6.25)-(6.26) scaled by λ_2, (6.27)-(6.28) scaled by λ_3 and (6.29)-(6.30) scaled by λ_4 completes the proof. □

Remark 5: The systems of E-L equations of Lemmas 1-4 can be rewritten in a more concise way. The reason behind this more complicated notation follows from the chosen discretization method. Indeed, as it was chosen to use the finite difference method to discretize the system, it is easier to see the correspondence between the system and its discretization form, as will be shown in the following discretization section. Nevertheless, for the sake of completeness, we feel the need to point out that:

- (6.23)-(6.24) can be written as: $(\mathbf{X} \cdot \mathbf{v_r})\,\mathbf{v_r} = V_r \mathbf{v_r} \quad \text{in } \Omega_P$;
- (6.25)-(6.26) can be written as: $-\boldsymbol{\nabla}(\boldsymbol{\nabla} \cdot \mathbf{X}) = \mathbf{0} \quad \text{in } \Omega_P$;
- (6.27)-(6.28) can be written as: $\mathbf{X} = \mathbf{V_P} \quad \text{on } \partial\Omega_P$;
- (6.29)-(6.30) can be written as: $-\boldsymbol{\Delta}\mathbf{X} = \mathbf{0} \quad \text{in } \Omega_P$.

Discretization

We define $[\mathbf{f}]$ as the $m \times n$ matrix whose entries consists of the function $f(x_1,x_2)$ uniformly sampled in each variable x_1 and x_2 with a discretization step of respectively h and k. We define by $[\text{vec}(\mathbf{f})]$ the $mn \times 1$ vector resulting of the vectorization of the matrix $[\mathbf{f}]$. We finally define by $[\text{diag}(\text{vec}(\mathbf{f}))]$ the $mn \times mn$ matrix resulting of the matrix procedure transforming the column vector $[\text{vec}(\mathbf{f})]$ into the diagonal of a matrix.

Remark 6: By abuse of notation, $[\text{diag}(\text{vec}(\mathbf{f}))]$ will be simplified as $[\text{diag}(\mathbf{f})]$. Moreover, $[\sin(\mathbf{x})]$, respectively $[\cos(\mathbf{x})]$, are the $m \times n$ matrices consisting of applying the sin, respectively cos, function to each element of the $m \times n$ matrix $[\mathbf{x}]$

The first order partial derivatives are approximated using first order central differences $\partial_{x_1,h}[f](x_1,x_2) = \frac{f(x_1+h,x_2)-f(x_1-h,x_2)}{2h}$ and $\partial_{x_2,k}[f](x_1,x_2) = \frac{f(x_1,x_2+k)-f(x_1,x_2-k)}{2k}$. Those derivative approximations are discretized as $mn \times mn$ matrices, respectively denoted D_x and D_y, and the second order partial differential operator are defined as:

$$\begin{aligned} D_{x_1x_1} &= D_{x_1}D_{x_1}, \\ D_{x_1x_2} &= D_{x_1}D_{x_2}, \\ D_{x_2x_1} &= D_{x_2}D_{x_1}, \\ D_{x_2x_2} &= D_{x_2}D_{x_2}. \end{aligned}$$

Matrices A_1 to A_4 of size $2mn \times 2mn$ are defined as follows:

$$\begin{aligned} A_1 &= \begin{bmatrix} \mathbb{1}_{\Omega_P}\operatorname{diag}(\cos(\boldsymbol{\theta}))^2 & \mathbb{1}_{\Omega_P}\operatorname{diag}(\cos(\boldsymbol{\theta}))\operatorname{diag}(\sin(\boldsymbol{\theta})) \\ \mathbb{1}_{\Omega_P}\operatorname{diag}(\cos(\boldsymbol{\theta}))\operatorname{diag}(\sin(\boldsymbol{\theta})) & \mathbb{1}_{\Omega_P}\operatorname{diag}(\sin(\boldsymbol{\theta}))^2 \end{bmatrix} \\ A_2 &= \begin{bmatrix} -\mathbb{1}_{\Omega_P}D_{x_1x_1} & -\mathbb{1}_{\Omega_P}D_{x_1x_2} \\ -\mathbb{1}_{\Omega_P}D_{x_1x_2} & -\mathbb{1}_{\Omega_P}D_{x_2x_2} \end{bmatrix} \\ A_3 &= \begin{bmatrix} \mathbb{1}_{\partial\Omega_P} & \mathbf{0} \\ \mathbf{0} & \mathbb{1}_{\partial\Omega_P} \end{bmatrix} \\ A_4 &= \begin{bmatrix} -\mathbb{1}_{\Omega_P}(D_{x_1x_1}+D_{x_2x_2}) & 0 \\ 0 & -\mathbb{1}_{\Omega_P}(D_{x_1x_1}+D_{x_2x_2}) \end{bmatrix} \end{aligned}$$

We denote by $\circ$ the Hadamard product, *i.e.* the operation which takes two matrices of the same size and produces a third matrix in which elements i,j is the product of the elements i,j of the original two matrices. Column vectors b_1 to b_4 of size $2mn \times 1$ are defined as follows:

$$\begin{aligned} b_1 &= \begin{bmatrix} \operatorname{vec}(\mathbb{1}_{\Omega_P}) \circ \operatorname{vec}(\cos(\boldsymbol{\theta})) \circ \operatorname{vec}(V_r)) \\ \operatorname{vec}(\mathbb{1}_{\Omega_P}) \circ \operatorname{vec}(\sin(\boldsymbol{\theta})) \circ \operatorname{vec}(V_r)) \end{bmatrix} \\ b_2 &= \begin{bmatrix} \mathbf{0} & \mathbf{0} \end{bmatrix}^T \\ b_3 &= \begin{bmatrix} \operatorname{vec}(\mathbb{1}_{\partial\Omega_P}) \circ \operatorname{vec}(\mathbf{V_P} \cdot \mathbf{v_1}) \\ \operatorname{vec}(\mathbb{1}_{\partial\Omega_P}) \circ \operatorname{vec}(\mathbf{V_P} \cdot \mathbf{v_2}) \end{bmatrix} \\ b_4 &= \begin{bmatrix} \mathbf{0} & \mathbf{0} \end{bmatrix}^T \end{aligned}$$

The full system of E-L equations associated to $J[\mathbf{X}]$ can be discretized to produce problem $(R1')$, equivalent to problem $(R1)$ excluding discretization errors:

Discretized problem (R1')

Given an observed radial flow velocity V_r, a boundary data $\mathbf{V_P}|_{\partial\Omega_P}$, and $\lambda_1,\ldots,\lambda_4 \in \mathbb{R}^{+*}$, find the vector field $\mathbf{V_P^\star} : \Omega_P \to \mathbb{R}^2$, solution of the system $Ax = b$, where A and b are defined as:

$$\begin{aligned} A &= \lambda_1 A_1 + \lambda_2 A_2 + \lambda_3 A_3 + \lambda_4 A_4 \\ b &= \lambda_1 b_1 + \lambda_2 b_2 + \lambda_3 b_3 + \lambda_4 b_4 \end{aligned}$$

6.2.4 Numerical experiments

In this section, we consider three numerical experiments to assess the algorithm capabilities. In Experiment I, the reconstruction of a healthy diastolic blood flow is considered. In Experiment II, the algorithm capabilities in the context of a pathological blood flow including MR is evaluated. Finally, in Experiment III, the sensitivity of the algorithm with respect to partial data sampling is assessed.

6.2.4.1 Experiment I: Physiological blood velocity reconstruction

The blood flow resulting of a numerical simulation of a healthy patient (C12_H, described in Section 4.2), was used as the ground truth for this numerical experiment. It was chosen to investigate the reconstruction of the E-wave, during diastole, at $t/T = 0.75$. The synthetic US probe was placed apically. A rectangular section of a plane similar to the image resulting of a trans-thoracic apical 3-Chamber view was regularly sampled as depicted in Figure 6.7. Note that for computational purpose, some computational points are sampled outside of the heart domain. Numerically, a Dirichlet boundary condition is added to force the velocity to be 0 cm/s.

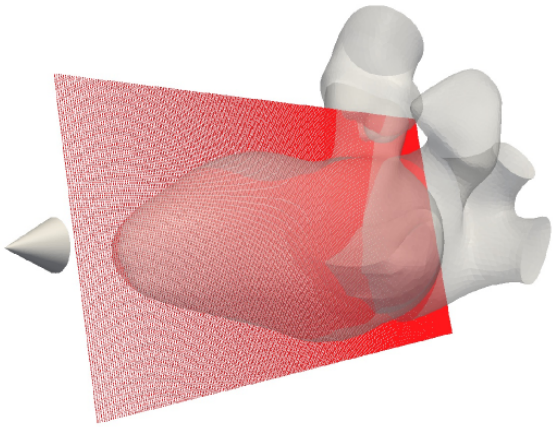

Figure 6.7 – Probe position and acquisition plane for the numerical expermiment I

The velocity field $\mathbf{V}$ resulting from the numerical simulation was interpolated at the sampling points using gaussian radial basis function to produce the resulting velocity field $\mathbf{V}'$ (Figure 6.8a). The out-of-plane component was removed producing the 2D vector field $\mathbf{V_P}$ (Figure 6.8b). Finally, the field V_r was produced by projecting the vector field $\mathbf{V_P}$ on the vectors $\mathbf{v_r}$ (Figure 6.8c) (*i.e.* projecting the velocity on the synthetic ultrasound beams).

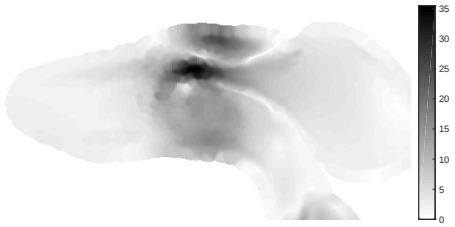

(a) $\mathbf{V}'$ velocity magnitude ($\|\mathbf{V}'\|_2^2$)

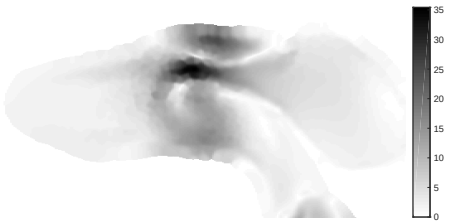

(b) $\mathbf{V_P}$ velocity magnitude ($\|\mathbf{V_P}\|_2^2$)

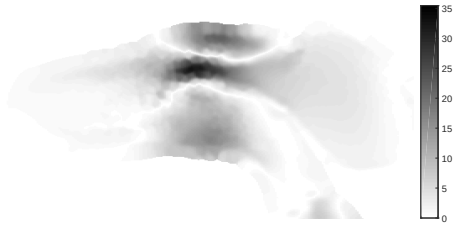

(c) V_r velocity magnitude ($\|V_r\|_2^2$)

Figure 6.8 – Velocity magnitude of (a) real blood velocity, (b) 2D in-plane blood velocity and (c) the synthetic US acquisition produced by projecting the field $\mathbf{V_P}$ onto the US beams.

Figure 6.9 depicts the domains Ω_P and $\partial\Omega_P$.

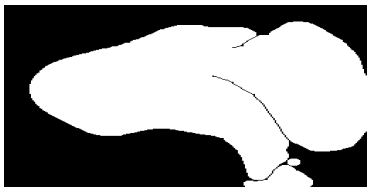

(a) $\mathbb{1}_{\Omega_P}$

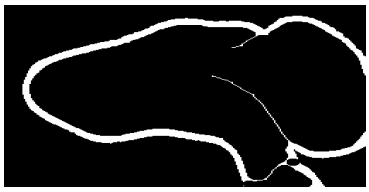

(b) $\mathbb{1}_{\partial\Omega_P}$

Figure 6.9 – Indicator function for the heart domain and the heart boundaries for Experiment I

Solving problem (R1') allows to find the reconstructed field $\mathbf{V}_\mathbf{P}^\star$ given a certain set of parameters $\lambda_1,\ldots,\lambda_4$. The average error between the ground truth and the reconstructed field, $\overline{E}(\mathbf{V_P},\mathbf{V}_\mathbf{P}^\star)$, was used to find the optimal set of parameters $\lambda_1,\ldots,\lambda_4$ by solving the following optimization problem using a gradient descent algorithm with adaptive step size:

$$\min_{\lambda_1,\ldots,\lambda_4} \overline{E}(\mathbf{V_P},\mathbf{V}_\mathbf{P}^\star) \quad \text{s.t} \quad \mathbf{V}_\mathbf{P}^\star \quad \text{solution of problem (R1')}$$

Figure 6.10 depicts the magnitude of the three fields $\mathbf{V_P}$, $\mathbf{V_r}$ and $\mathbf{V}_\mathbf{P}^\star$.

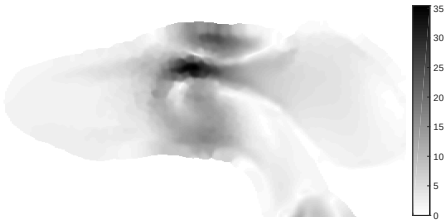

(a) $\mathbf{V_P}$ velocity magnitude ($\|\mathbf{V_P}\|_2^2$)

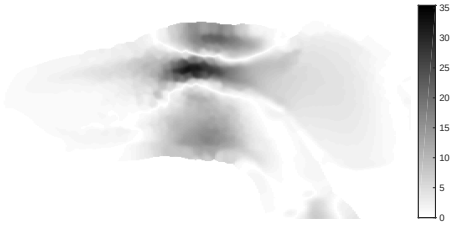

(b) V_r velocity magnitude ($\|V_r\|_2^2$)

(c) $\mathbf{V_P^\star}$ velocity magnitude ($\|\mathbf{V_P^\star}\|_2^2$)

Figure 6.10 – Comparison between the magnitude of (a) the original 2D vector field, (b) the projection of the vector field onto a synthetic ultrasound beam and (c) the reconstructed vector field.

Qualitatively, it can be noted that, in the synthetic US vector field (Figure 6.10b), the velocity magnitude was strongly affected by the loss of the component of the velocity orthogonal to the US beam. This effect is especially visible when considering the intraventricular vortex formed at the tip of the mitral valve, as depicted on Figure 6.11. In the field V_r (Figure 6.11b) the velocity vectors are aligned along the US beams and there is no visible clue of the presence of vortices. On the other hand, looking at the ground truth velocity field $\mathbf{V_P}$ (Figure 6.11a), as well as in the reconstructed field (Figure 6.11c), vortices can be observed on both sides of the mitral inflow by the region of high blood velocities rotating around regions of very low velocity magnitude.

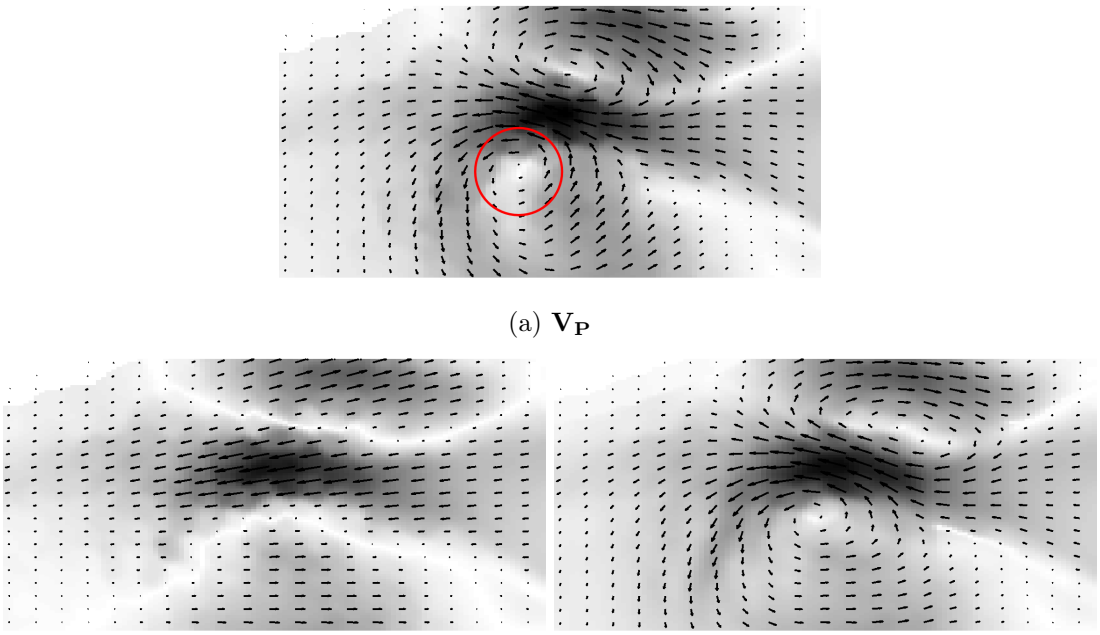

(a) $\mathbf{V_P}$

(b) V_r (c) $\mathbf{V_P^\star}$

Figure 6.11 – Magnitude of $\mathbf{V_P}$,V_r and $\mathbf{V_P^\star}$, overlayed with the respective velocity vectors, at the mitral valve level. On Figure 6.11a, one of the eye of the inflow vortex is highlighted by the red circle

Figure 6.12a depicts the statistics for the velocity error $E(\mathbf{V_P},V_r\mathbf{v_r})$ and $E(\mathbf{V_P},\mathbf{V_P^\star})$, respectively the velocity error of the synthetic US scalar field projected on the beam direction and the velocity error after reconstruction of the velocity vector field. Figure 6.12b depicts the same quantities in their normalized version, *i.e.* $\hat{E}(\mathbf{V_P},V_r\mathbf{v_r})$ and $\hat{E}(\mathbf{V_P},\mathbf{V_P^\star})$.

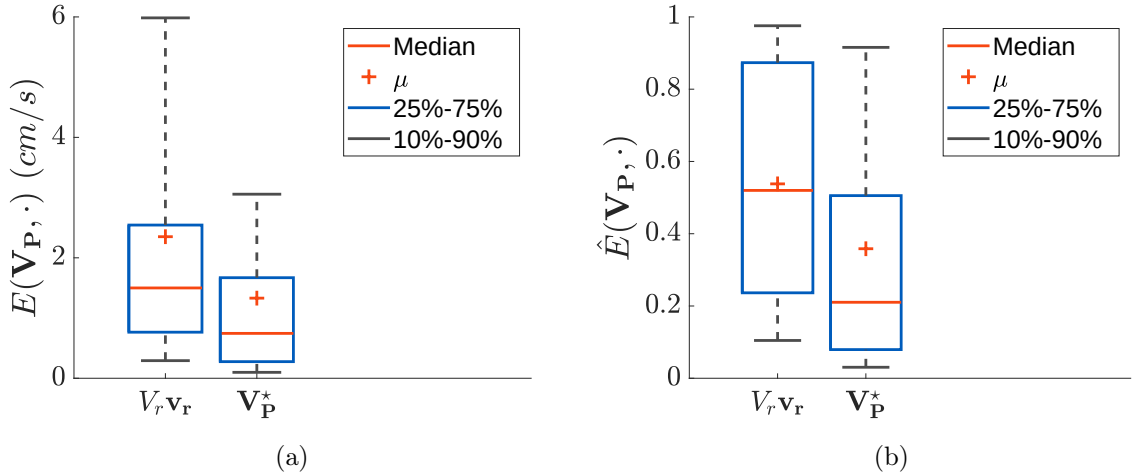

(a) (b)

Figure 6.12 – Box plots depicting the statisticts of (a) the velocity error before and after reconstruction and (b) the normalized velocity error before and after reconstruction.

The average velocity error decreased from 2.35 cm/s (≈ 54 %) to 1.33 cm/s (≈ 36 %) after reconstruction and the median velocity error was reduced from 1.5 cm/s (≈ 52 %) to 0.75 cm/s (≈ 21 %). The first decile (D1) decreased from 0.29 cm/s (≈ 10 %) to 0.1 cm/s (≈ 3 %) and the ninth decile (D9) decreased from 5.99 cm/s (≈ 98 %) to 3.1 cm/s (≈ 92 %). Finally, the first quartile (Q1) decreased from 0.77 cm/s (≈ 24 %) to 0.28 cm/s (≈ 8 %) and the third quartile (Q3) decreased from 2.54 cm/s (≈ 87 %) to 1.67 cm/s (≈ 51 %).

The reconstruction succeeded to recover part of the information that was lost by the synthetic US acquisition as indicated by the reduction in all the error statistics reported. While the average error is still high after reconstruction ($\overline{\hat{E}}(\mathbf{V_P},\mathbf{V_P^\star}) \approx 36\,\%$), it appears that this is mainly due to the presence of some outliers which were not well reconstructed. Indeed, while the normalized error distribution pre-reconstruction $\hat{E}(\mathbf{V_P},V_r\mathbf{v_r})$ is mainly symmetrical with an average error nearly equal to the median error, the post-reconstruction distribution $\hat{E}(\mathbf{V_P},\mathbf{V_P^\star})$ is highly skewed towards the lower errors as indicated by the shift of the median value compared to the mean value and by the big Q3-D9 range compared to the short D1-Q1 range.

6.2.4.2 Experiment II: Pathological blood flow reconstruction

The blood flow resulting of the simulation of a synthetic MR (C11_T1, described in Section 4.2) was used as the input data of this numerical experiment. Similarly to Experiment I, the synthetic US probe was placed apically and a trans-thoracic apical 3-chamber view acquisition plane was regularly sampled. In this case, a time corresponding to the systole was chosen ($t/T = 0.125$). Fields $\mathbf{V}'$,$\mathbf{V_P}$ and V_r are depicted on Figure 6.13. Due to the color scaled imposed by the regurgitation high velocity, it is difficult to visually assess the differences in the flow velocity magnitude. Nevertheless, some inconsistencies are visible qualitatively between the original field $\mathbf{V_P}$ and the synthetic ultrasound V_r. This inconsistency is highligted by the differences between the isovelocity levels of Figure 6.16a and Figure 6.16b.

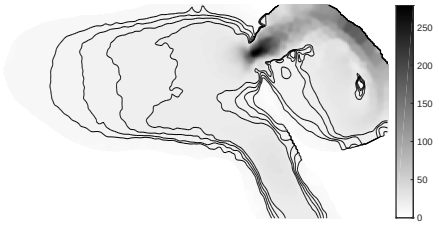

(a) $\mathbf{V}'$ velocity magnitude ($\|\mathbf{V}'\|_2^2$)

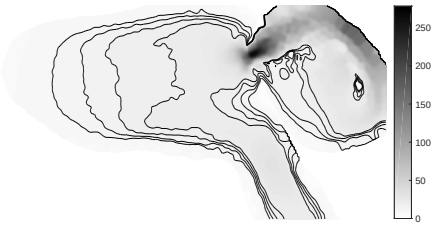

(b) $\mathbf{V_P}$ velocity magnitude ($\|\mathbf{V_P}\|_2^2$)

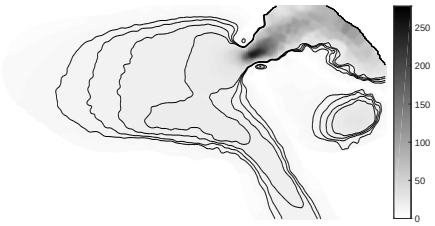

(c) V_r velocity magnitude ($\|V_r\|_2^2$)

Figure 6.13 – Velocity magnitude of the differents vector fields as they are processed from (a) real blood velocity to (c) the synthetic US acquisition. The black lines represent the same contour levels in all figures.

Figure 6.14 depicts the domains Ω_P and $\partial\Omega_P$ used.

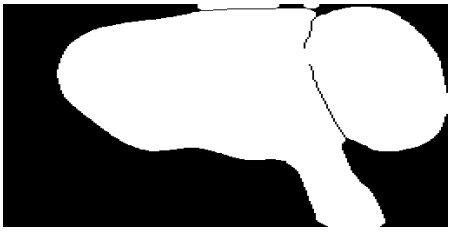

(a) Ω_P

(b) $\partial\Omega_P$

Figure 6.14 – Indicator function for the heart domain and the heart boundaries for Experiment III.

Using the same set of $\lambda_1, \ldots, \lambda_4$ as in Experiment I, the problem (R1') was solved. Figure 6.15 depicts a global comparison of the magnitude of the resulting vector field $\mathbf{V_P^\star}$ with respect to the vector field $\mathbf{V_P}$.

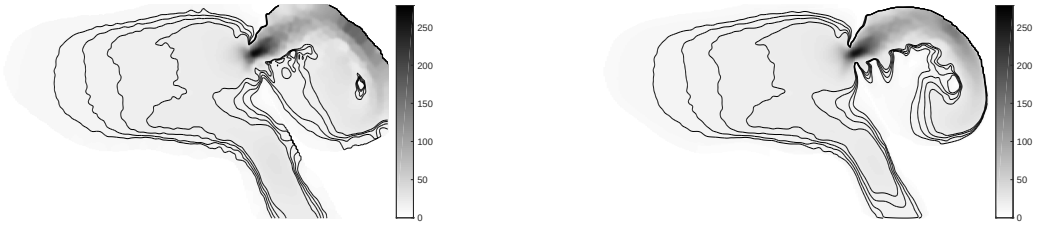

(a) (b)

Figure 6.15 – $\mathbf{V_P}$ velocity magnitude and (b) reconstructed $\mathbf{V_P^\star}$ velocity magnitude ($\|\mathbf{V_P^\star}\|_2^2$). The black lines represent the same contour levels in both figures.

Figure 6.16 proposes a comparison of the velocity fields specifically in the flow convergence region.

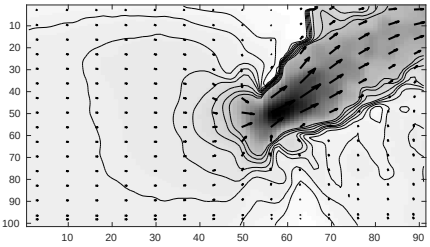

(a) $\mathbf{V_P}$, zoom on the flow convergence area

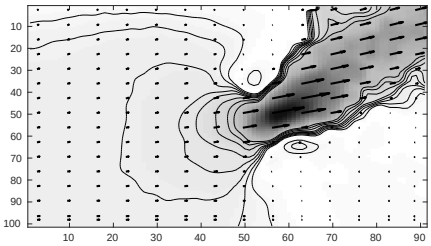

(b) V_r, zoom on the flow convergence area

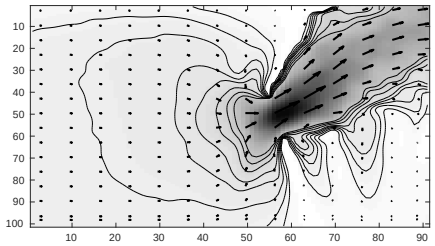

(c) $\mathbf{V_P^\star}$, zoom on the flow convergence area

Figure 6.16 – Magnitude of the vector fields $\mathbf{V_P}$,V_r and $\mathbf{V_P^\star}$ overlayed with the respective 2D velocity vectors.

One can observe the similarities between the isovelocity levels of the original field $\mathbf{V_P}$ and the reconstructed field $\mathbf{V_P^\star}$ in the flow convergence region. It is however noticeable that the reconstruction failed to recover properly the velocities in the atrium (in the right part of Figure 6.16).

Figure 6.17a shows the statistics for the velocity error $E(\mathbf{V_P},V_r\mathbf{v_r})$ and $E(\mathbf{V_P},\mathbf{V_P^\star})$, respectively the velocity error of the synthetic US scalar field projected on the beam direction and the velocity

error after reconstruction of the velocity vector field. Figure 6.17b depicts the same quantities in their normalized version, *i.e.* $\hat{E}(\mathbf{V_P},V_r\mathbf{v_r})$ and $\hat{E}(\mathbf{V_P},\mathbf{V_P^\star})$.

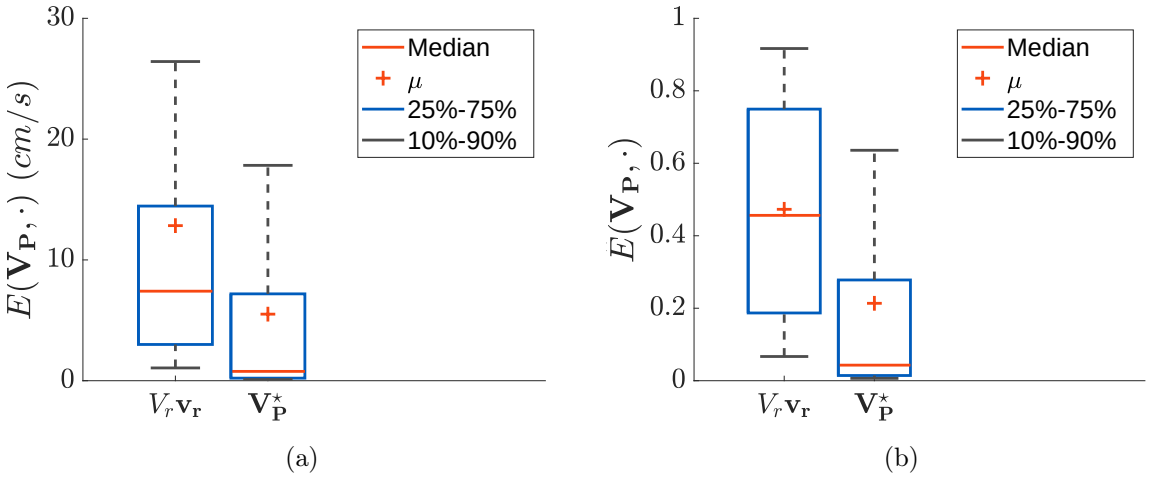

Figure 6.17 – Box plots depicting the statisticts of (a) the velocity error before and after reconstruction and (b) the normalized velocity error before and after reconstruction.

The average velocity error decreased from 12.84 cm/s (≈ 47 %) to 5.51 cm/s (≈ 21 %) after reconstruction and the median velocity error was reduced from 7.41 cm/s (≈ 46 %) to 0.77 cm/s (≈ 4 %). The first decile (D1) decreased from 1.06 cm/s (≈ 7 %) to 0.10 cm/s (≈ 0.6 %) and the ninth decile (D9) decreased from 26.42 cm/s (≈ 92 %) to 17.83 cm/s (≈ 64 %). Finally, the first quartile (Q1) decreased from 3 cm/s (≈ 19 %) to 0.21 cm/s (≈ 1.4 %) and the third quartile (Q3) decreased from 14.46 cm/s (≈ 75 %) to 7.19 cm/s (≈ 28 %).

As indicated by the reduction in all the error statistics, the reconstruction allows to recover part of the lost information. Similarly to Experiment I, while the normalized error distribution pre-reconstruction $\hat{E}(\mathbf{V_P},V_r\mathbf{v_r})$ is mainly symmetrical, with an average error nearly equal to the median error, the post-reconstruction error $\hat{E}(\mathbf{V_P},\mathbf{V_P^\star})$ is skewed towards the lower errors as indicated by the shift of the median value compared to the mean value and by the big Q3-D9 range compared to the short D1-Q1 range.

2D regurgitant flow rate was computed automatically for all three vector fields $\mathbf{V_P}$,V_r and $\mathbf{V_P^\star}$. First, a velocity v_a, between 20 cm/s and 60 cm/s is chosen. The isovelocity contour $\mathcal{C}_{v_a}$ related to this velocity, in the convergence region is considered. Denoting by $\mathbf{n}$ the oriented unit normal to the contour $\mathcal{C}_{v_a}$, the 2D blood flow rate across this isovelocity contour can computed as:

$$Q_{\mathcal{C}_{v_a}} = \int_{\mathcal{C}_{v_a}} \mathbf{v}\cdot\mathbf{n}. \tag{6.35}$$

On Figure 6.18, the thick blue line represents the isovelocity contour $\mathcal{C}_{20}$. The thin blue lines represents the oriented unit normal and the red lines represents the velocity vectors scaled for visualization purpose. Note that contrary to the PISA hypothesis, velocities are not orthogonal to the isovelocity level.

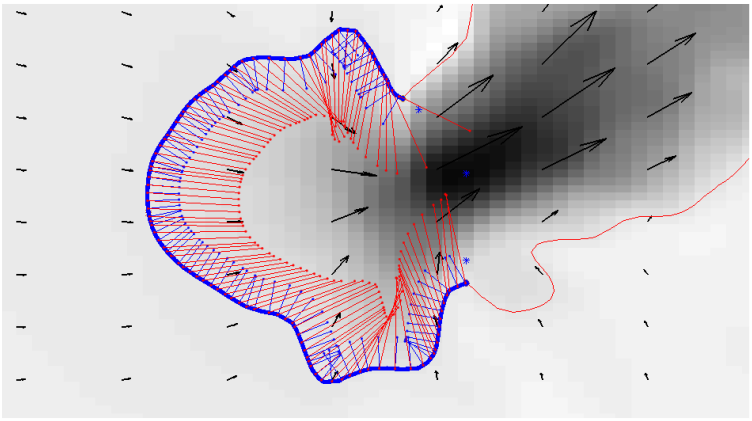

Figure 6.18 – Zoom on the flow convergence area and highlight of the different quantities related to $Q_{\mathcal{C}_{v_a}}$ for $v_a = 20\,\text{cm/s}$. The thin blue lines represents the oriented unit normal and the red lines represents the velocity vectors scaled for visualization purpose.

The scalar values of the field V_r only represents the component of the blood velocity aligned along the synthetic US beam. For this reason, computing $Q_{\mathcal{C}_{v_a}}$ does not make sense. A technique similar to the PISA technique is therefore used. A first landmark $\mathcal{L}_1$, representing the center of the hole, was picked as the center of the line joining the tip of the two mitral leaflet. A landmark $\mathcal{L}_2$ is chosen on the contour $\mathcal{C}_{v_a}$ so that the alignment of the blood velocity and synthetic ultrasound beam is maximized. Based on the PISA hypothesis, the distance between $\mathcal{L}_1$ and $\mathcal{L}_2$ is the radius r_a of a hemi-circular isovelocity level across which the blood flows orthogonally. The 2D regurgitant flow rate is therefore estimated by multiplying the length of the hemi-circle by the velocity v_a:

$$Q_{\text{2D PISA}_{\text{v}_\text{a}}} = \pi r_a v_a. \tag{6.36}$$

Figure 6.19 represents the evolution of the aforementioned quantities for aliasing velocities ranging between 20 and 60 cm/s. It can be observed that the PISA technique ($Q_{V_r,\text{2D PISA}_{\text{v}_\text{a}}}$) is slightly overestimating the flow rate: the relative error compared to the ground truth $Q_{V_P,\mathcal{C}_{v_a}}$ was approximately 22 % across the whole range of aliasing velocities. Using the reconstructed velocity field $V_P^\star$ yielded a flow rate much closer to the ground truth $Q_{V_P,\mathcal{C}_{v_a}}$: the relative error compared to the ground truth averaged approximately 3 % across the range of aliasing velocities.

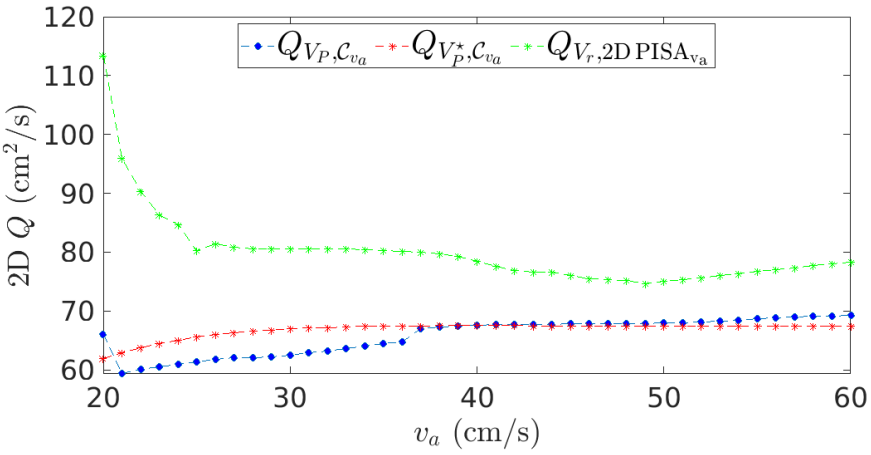

Figure 6.19 – Evolution of the quantities $Q_{V_P,\mathcal{C}_{v_a}}$, $Q_{V_P^\star,\mathcal{C}_{v_a}}$ and $Q_{V_r,\text{2D PISA}_{\text{va}}}$ for aliasing velocities between 20 and 60 cm/s

6.2.4.3 Experiment III: Sensitivity of the reconstruction algorithm to data subsampling

In the two first numerical experiments, the velocity vector field was reconstructed based on a scalar field V_r known in the entire domain Ω_P. This numerical experiment aims to investigate the sensitivity of the algorithm with respect to partial acquisition of the doppler data.

Instead of assuming that the velocity field V_r is known in the complete domain Ω_P, it is instead assumed that the vector field is only known at some specific positions $\Omega_{P,D} \subset \Omega_P$. Problem (R1) was therefore slightly modified to produce problem (R2):

Problem (R2)

Given an observed radial flow velocity $V_r : \Omega_{P,D} \subset \Omega_P \in \mathbb{R}^2 \rightarrow \mathbb{R}^2$, a boundary data $\mathbf{V_P}|_{\partial\Omega_P}$, and $\lambda_1, \ldots, \lambda_4 \in \mathbb{R}^{+*}$, find the vector field $\mathbf{V_P^\star} : \Omega_P \in \mathbb{R}^2 \rightarrow \mathbb{R}^2$ which minimizes $J[\mathbf{X}]$ defined as:

$$J[\mathbf{X}] = \lambda_1 \int_{\Omega_{P,D}} (\mathbf{X} \cdot \mathbf{v_r} - V_r)^2 \tag{6.37}$$

$$+\lambda_2 \int_{\Omega_P} (\boldsymbol{\nabla} \cdot \mathbf{X})^2 \tag{6.38}$$

$$+\lambda_3 \int_{\partial\Omega_P} \|\mathbf{X} - \mathbf{V_P}\|_2^2 \tag{6.39}$$

$$+\lambda_4 \int_{\Omega_P} \|\boldsymbol{\nabla}\mathbf{X}\|_2^2 \tag{6.40}$$

As a result, the matrix A_1 and vector b_1 were modified as:

$$A_1 = \begin{bmatrix} \mathbb{1}_{\Omega_{P,D}} \operatorname{diag}(\cos(\boldsymbol{\theta}))^2 & \mathbb{1}_{\Omega_{P,D}} \operatorname{diag}(\cos(\boldsymbol{\theta})) \operatorname{diag}(\sin(\boldsymbol{\theta})) \\ \mathbb{1}_{\Omega_{P,D}} \operatorname{diag}(\cos(\boldsymbol{\theta})) \operatorname{diag}(\sin(\boldsymbol{\theta})) & \mathbb{1}_{\Omega_{P,D}} \operatorname{diag}(\sin(\boldsymbol{\theta}))^2 \end{bmatrix}$$
$$b_1 = \begin{bmatrix} \operatorname{vec}(\mathbb{1}_{\Omega_{P,D}}) \circ \operatorname{vec}(\cos(\boldsymbol{\theta})) \circ \operatorname{vec}(V_r)) \\ \operatorname{vec}(\mathbb{1}_{\Omega_{P,D}}) \circ \operatorname{vec}(\sin(\boldsymbol{\theta})) \circ \operatorname{vec}(V_r)) \end{bmatrix}$$

The velocity vector field of patient C12_H at $t/T = 0.75$, in a trans-thoracic apical 3-Chamber view setting, was used. The samples of the domain Ω_P were assigned a probability $p \in [0,1]$ of being part of the subset $\Omega_{P,D}$. The probability p was varied from 0 to 1 by increments of 0.01 and problem $(R1')$ was solved for each value of p ten different times to account for the variability of the random sampling. Figure 6.20 depicts examples of the domain $\Omega_{D,P}$ for different values of p.

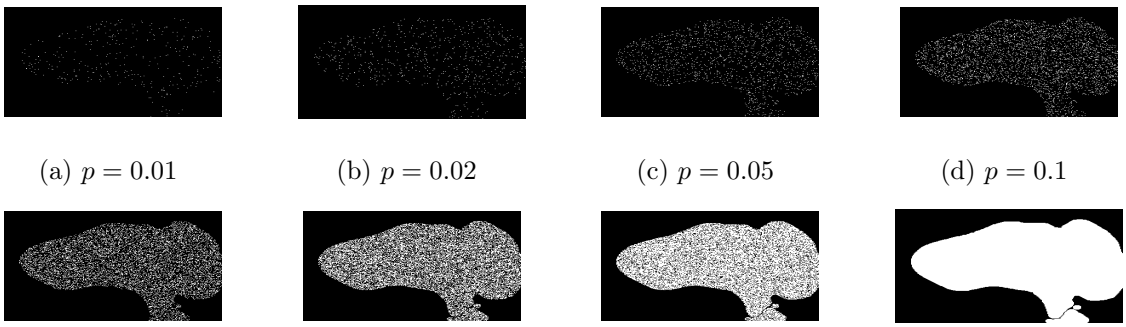

(a) $p = 0.01$ (b) $p = 0.02$ (c) $p = 0.05$ (d) $p = 0.1$

(e) $p = 0.25$ (f) $p = 0.50$ (g) $p = 0.75$ (h) $p = 1$

Figure 6.20 – Domain $\Omega_{P,D}$ for different spatial sampling resulting of different values of p.

Figure 6.21 and Figure 6.22 depicts the reconstructed velocity field magnitude for different values of p. It is interesting to note that even with a very small amount of data, one can reconstruct the velocity field. With 1% of the data, one can already qualitatively locate the vortex ring as well as the regions of high velocities. As the percentage of available pixel increases, the reconstruction appears to get better and better.

(a) $p = 0.01$

(b) $p = 0.02$

(c) $p = 0.05$

(d) $p = 0.1$

Figure 6.21 – Reconstructed field $\mathbf{V}_{\mathbf{P}}^{\star}$ for $p = \{0.01, 0.02, 0.05, 0.1\}$

(a) $p = 0.25$

(b) $p = 0.50$

(c) $p = 0.75$

(d) $p = 1$

Figure 6.22 – Reconstructed field $\mathbf{V}_{\mathbf{P}}^{\star}$ for $p = \{0.25, 0.50, 0.75, 1\}$

Figure 6.23 depicts the evolution of the average velocity error magnitude ($\overline{E}(\mathbf{V_P},\mathbf{V_P^\star})$) with respect to the sampling probability p. Analysis of this figures confirms that the algorithm is able to handle sparsity in the input data. Indeed, one can observe a quick decay of the average error as the sampling probability increase. At $p = 0.2$ (*i.e.* with approximately 20 % of the domain Ω_P sampled), the difference with respect to the error $\overline{E}_{p=1}(\mathbf{V_P},\mathbf{V_P^\star})$ is lower than 5%.

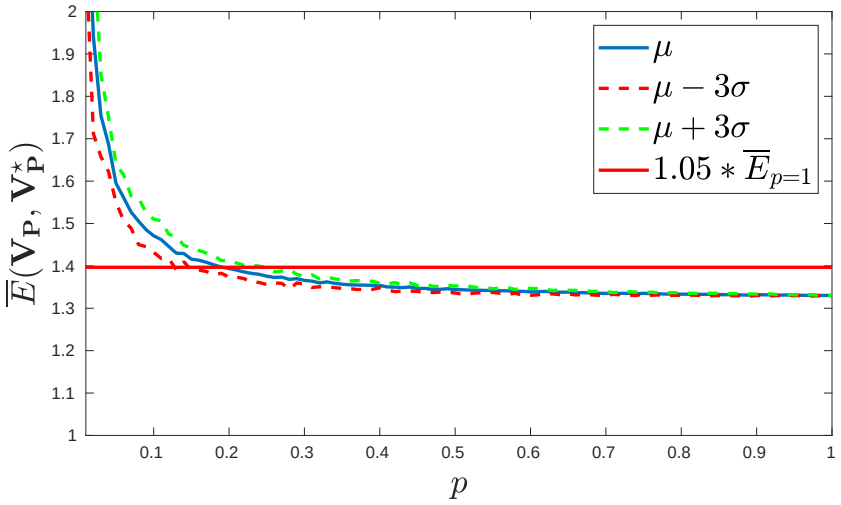

Figure 6.23 – Average reconstruction velocity error for increasing values of the sampling probability p.

Remark 7: In this numerical experiment, the sensitivity analysis of the algorithm with respect to partial sampling of the data was considered. Several other issues can alter the algorithm performances such as aliasing or noise. We propose a specific discussion about those issues in Section 6.4.

6.3 3D Color Doppler flow reconstruction

In this section, the reconstruction of a 3D velocity fields from Color Doppler image is considered. Some notations are first detailed and the functional presented in Section 6.2 is extended to the 3D problem. The associated system of E-L equations is computed and discretized. Some numerical experiments are then presented to assess the flow reconstruction.

6.3.1 Notations

Let $\mathbf{p_c}$ denote the position of the ultrasound probe. We consider the probe to be similarly oriented compared to the previous section. As a result, the probe orientation defines the cartesian coordinate system $(\mathbf{p_c}, \mathbf{v_1}, \mathbf{v_2}, \mathbf{v_3})$.

Let $\mathbf{V}$ be a vector field of the blood velocity inside the heart geometrical domain (denoted Ω):

$$\begin{aligned}\mathbf{V}:\Omega \in \mathbb{R}^3 &\rightarrow \mathbb{R}^3 \\ (x_1,x_2,x_3) &\rightarrow \begin{bmatrix} u(x_1,x_2,x_3) \\ v(x_1,x_2,x_3) \\ w(x_1,x_2,x_3) \end{bmatrix}, \quad \text{such that } \boldsymbol{\nabla}\cdot\mathbf{V}=0 \text{ in } \Omega.\end{aligned}$$

The probe acquires data in a 3D domain P. We define Ω_P as the intersection between the Ω and P. Moreover, the vector field $\mathbf{V}$ is defined as $\mathbf{V_P}$:

$$\begin{aligned}\mathbf{V_P}:\Omega_P \in \mathbb{R}^3 &\rightarrow \mathbb{R}^3 \\ (x_1,x_2,x_3) &\rightarrow \begin{bmatrix} u(x_1,x_2,x_3) \\ v(x_1,x_2,x_3) \\ w(x_1,x_2,x_3) \end{bmatrix}\end{aligned}$$

Let $\mathbf{v_r}(x_1,x_2,x_3)$ be the unit vector defined, at any point (x_1,x_2,x_3) of the 3D domain P as:

$$\mathbf{v_r}(x_1,x_2,x_3) = \frac{[x_1,x_2,x_3]^T - \mathbf{p_c}}{\|[x_1,x_2,x_3]^T - \mathbf{p_c}\|}$$

The scalar field V_r, resulting of the projection of the vector field $\mathbf{V_P}$ on the unit vectors $\mathbf{v_r}$ is defined:

$$\begin{aligned}V_r:\Omega_P \in \mathbb{R}^3 &\rightarrow \mathbb{R} \\ (x_1,x_2,x_3) &\rightarrow \mathbf{V_P}(x_1,x_2,x_3)\cdot\mathbf{v_r}(x_1,x_2,x_3)\end{aligned}$$

Remark 8: The vector field $\mathbf{V_P}$ can be thought as a perfect 3D blood flow representation if Color Doppler was able to quantify the blood velocity.
Remark 9: Similarly to the previous section, the scalar field V_r is analogous to the scalar velocity field that would be obtained using Doppler echography as the unit vectors $\mathbf{v_r}$ are the unit vectors aligned along the US beam directions. This scalar field does not suffer from aliasing.
Remark 10: Contrary to the previous section, the vector field $\mathbf{V_P}$ is divergence-free.

Error quantification:

In order to quantify the error and differences between the velocity vector fields, we ropose to evaluate several quantities.

The quantity $E(\mathbf{V_1},\mathbf{V_2},x_1,x_2,x_3)$, velocity error between the vector fields $\mathbf{V_1}$ and $\mathbf{V_2}$ at any point (x_1,x_2,x_3) of the domain Ω_P is defined as:

$$E(\mathbf{V_1},\mathbf{V_2},x_1,x_2,x_3) = \|\mathbf{V_1}(x_1,x_2,x_3) - \mathbf{V_2}(x_1,x_2,x_3)\|_2 .$$

Moreover, its normalized version $\hat{E}(\mathbf{V_1},\mathbf{V_2},x_1,x_2,x_3)$ with respect to V_1 is defined as:

$$\hat{E}(\mathbf{V_1},\mathbf{V_2},x_1,x_2,x_3) = \frac{\|\mathbf{V_1}(x_1,x_2,x_3) - \mathbf{V_2}(x_1,x_2,x_3)\|_2}{\|\mathbf{V_1}(x_1,x_2,x_3)\|_2}.$$

The average errors across the entire domain Ω_P are computed as:

$$\overline{E}(\mathbf{V_1},\mathbf{V_2}) = \frac{1}{|\Omega_P|}\int_{\Omega_P} E(\mathbf{V_1},\mathbf{V_2}),$$
$$\overline{\hat{E}}(\mathbf{V_1},\mathbf{V_2}) = \frac{1}{|\Omega_P|}\int_{\Omega_P} \hat{E}(\mathbf{V_1},\mathbf{V_2}).$$

6.3.2 Definition of the functional

Given an observed radial flow velocity V_r, it is aimed to reconstruct the vector field $\mathbf{V_P}$. We frame the reconstruction problem as following:

Problem (R3)

Given an observed radial flow velocity V_r, a boundary data $\mathbf{V_P}|_{\partial\Omega_P}$, and $\lambda_1,\dots,\lambda_4 \in \mathbb{R}^{+*}$, find the vector field $\mathbf{V_P^\star} : \Omega_P \to \mathbb{R}^3$ which minimizes the functional $J[\mathbf{X}]$:

$$J[\mathbf{X}] = \lambda_1 \int_{\Omega_P} (\mathbf{X}\cdot\mathbf{v_r} - V_r)^2 \tag{6.41}$$
$$+\lambda_2 \int_{\Omega_P} (\boldsymbol{\nabla}\cdot\mathbf{X})^2 \tag{6.42}$$
$$+\lambda_3 \int_{\partial\Omega_P} \|\mathbf{X}-\mathbf{V_P}\|_2^2 \tag{6.43}$$
$$+\lambda_4 \int_{\Omega_P} \|\boldsymbol{\nabla}\mathbf{X}\|_2^2 \tag{6.44}$$

6.3.3 Minimization using variational calculus

In order to solve the reconstruction problem (R3), *i.e.* minimize $J[\mathbf{X}]$, it is first aimed to find the associated system of E-L equations. To avoid a cumbersome repetition, the Lemmas 5-8, extension of the Lemmas Lemmas 1-4 in 3D, can be found in Appendix E.4.

Theorem: The stationary points of the functional $J[\mathbf{X}]$ satisfy the following system:

$$\begin{aligned}
&\lambda_1\left[(\mathbf{v_r}\cdot\mathbf{v_1})^2X_1+(\mathbf{v_r}\cdot\mathbf{v_1})(\mathbf{v_r}\cdot\mathbf{v_2})X_2+(\mathbf{v_r}\cdot\mathbf{v_1})(\mathbf{v_r}\cdot\mathbf{v_3})X_3\right]\\
&-\lambda_2\left[\frac{\partial^2X_1}{\partial x_1^2}+\frac{\partial^2X_2}{\partial x_1\partial x_2}+\frac{\partial^2X_3}{\partial x_1\partial x_3}\right]\\
&-\lambda_4\left[\frac{\partial^2X_1}{\partial {x_1}^2}+\frac{\partial^2X_1}{\partial {x_2}^2}+\frac{\partial^2X_1}{\partial {x_3}^2}\right]=\lambda_1(\mathbf{v_r}\cdot\mathbf{v_1})V_r \qquad \text{in } \Omega_P \qquad (6.45)\\
&\lambda_1\left[(\mathbf{v_r}\cdot\mathbf{v_2})(\mathbf{v_r}\cdot\mathbf{v_1})X_1+(\mathbf{v_r}\cdot\mathbf{v_2})^2X_2+(\mathbf{v_r}\cdot\mathbf{v_2})(\mathbf{v_r}\cdot\mathbf{v_3})X_3\right]\\
&-\lambda_2\left[\frac{\partial^2X_1}{\partial x_1\partial x_2}+\frac{\partial^2X_2}{\partial x_2^2}+\frac{\partial^2X_3}{\partial x_2\partial x_3}\right]\\
&-\lambda_4\left[\frac{\partial^2X_2}{\partial {x_1}^2}+\frac{\partial^2X_2}{\partial {x_2}^2}+\frac{\partial^2X_2}{\partial {x_3}^2}\right]=\lambda_1(\mathbf{v_r}\cdot\mathbf{v_2})V_r \qquad \text{in } \Omega_P \qquad (6.46)\\
&\lambda_1\left[(\mathbf{v_r}\cdot\mathbf{v_3})(\mathbf{v_r}\cdot\mathbf{v_1})X_1+(\mathbf{v_r}\cdot\mathbf{v_3})(\mathbf{v_r}\cdot\mathbf{v_2})X_2+(\mathbf{v_r}\cdot\mathbf{v_3})^2X_3\right]\\
&-\lambda_2\left[\frac{\partial^2X_1}{\partial x_1\partial x_3}+\frac{\partial^2X_2}{\partial x_2\partial x_3}+\frac{\partial^2X_3}{\partial x_3^2}\right]\\
&-\lambda_4\left[\frac{\partial^2X_3}{\partial {x_1}^2}+\frac{\partial^2X_3}{\partial {x_2}^2}+\frac{\partial^2X_3}{\partial {x_3}^2}\right]=\lambda_1(\mathbf{v_r}\cdot\mathbf{v_3})V_r \qquad \text{in } \Omega_P \qquad (6.47)\\
&\lambda_3X_1=\lambda_3(\mathbf{V_P}\cdot\mathbf{v_1}) \qquad \text{in } \partial\Omega_P \qquad (6.48)\\
&\lambda_3X_2=\lambda_3(\mathbf{V_P}\cdot\mathbf{v_2}) \qquad \text{in } \partial\Omega_P \qquad (6.49)\\
&\lambda_3X_3=\lambda_3(\mathbf{V_P}\cdot\mathbf{v_3}) \qquad \text{in } \partial\Omega_P \qquad (6.50)
\end{aligned}$$

Proof.
Let $J[\mathbf{X}]=\lambda_1G_1[\mathbf{X}]+\lambda_2G_2[\mathbf{X}]+\lambda_3G_3[\mathbf{X}]+\lambda_4G_4[\mathbf{X}]$.

The system of E-L equations associated to $J[\mathbf{X}]$ can be derived using Lemmas 5-8 found in Appendix E.4. Summing (E.10)-(E.12) scaled by λ_1, (E.13)-(E.15) scaled by λ_2, (E.16)-(E.18) scaled by λ_3 and (E.19)-(E.21) scaled by λ_4 completes the proof. □

Discretization

We define $[\mathbf{f}]$ as the $m\times n\times o$ matrix whose entries consists of the function $f(x_1,x_2,x_3)$ uniformly sampled in each variable x_1, x_2 and x_3 with a discretization step of respectively h, k, j. We define by $[\text{vec}(\mathbf{f})]$ the $mno\times 1$ vector resulting of the vectorization of the matrix $[\mathbf{f}]$. We finally define by $[\text{diag}(\text{vec}(\mathbf{f}))]$ the $mno\times mno$ matrix resulting of the matrix procedure transforming the column vector $[\text{vec}(\mathbf{f})]$ into the diagonal of a matrix.

The first order partial derivatives are approximated using first order central differences $\partial_{x_1,h}[f](x_1,x_2,x_3)=\frac{f(x_1+h,x_2,x_3)-f(x_1-h,x_2,x_3)}{2h}$, $\partial_{x_2,k}[f](x_1,x_2,x_3)=\frac{f(x_1,x_2+k,x_3)-f(x_1,x_2-k,x_3)}{2k}$ and $\partial_{x_3,j}[f](x_1,x_2,x_3)=\frac{f(x_1,x_2,x_3+j)-f(x_1,x_2,x_3-j)}{2j}$. Those derivative approximations are discretized as $mno\times mno$ matrices, respectively denoted D_x, D_y and D_z, and the second order partial differential operator are defined as:

$$D_{x_ax_b}=D_{x_a}D_{x_b}\quad\forall\{a,b\}\in\{1,2,3\}^2 \qquad (6.51)$$

Matrices A_1 to A_4 of size $3mno\times 3mno$ are defined as follows:

$$A_1 = \begin{bmatrix} \mathbb{1}_{\Omega_P} \operatorname{diag}(\mathbf{v_r} \cdot \mathbf{v_1})^2 & \mathbb{1}_{\Omega_P} \operatorname{diag}(\mathbf{v_r} \cdot \mathbf{v_1}) \operatorname{diag}(\mathbf{v_r} \cdot \mathbf{v_2}) & \mathbb{1}_{\Omega_P} \operatorname{diag}(\mathbf{v_r} \cdot \mathbf{v_1}) \operatorname{diag}(\mathbf{v_r} \cdot \mathbf{v_3}) \\ \mathbb{1}_{\Omega_P} \operatorname{diag}(\mathbf{v_r} \cdot \mathbf{v_2}) \operatorname{diag}(\mathbf{v_r} \cdot \mathbf{v_1}) & \mathbb{1}_{\Omega_P} \operatorname{diag}(\mathbf{v_r} \cdot \mathbf{v_2})^2 & \mathbb{1}_{\Omega_P} \operatorname{diag}(\mathbf{v_r} \cdot \mathbf{v_2}) \operatorname{diag}(\mathbf{v_r} \cdot \mathbf{v_3}) \\ \mathbb{1}_{\Omega_P} \operatorname{diag}(\mathbf{v_r} \cdot \mathbf{v_1})^2 & \mathbb{1}_{\Omega_P} \operatorname{diag}(\mathbf{v_r} \cdot \mathbf{v_1}) \operatorname{diag}(\mathbf{v_r} \cdot \mathbf{v_2}) & \mathbb{1}_{\Omega_P} \operatorname{diag}(\mathbf{v_r} \cdot \mathbf{v_3}) \operatorname{diag}(\mathbf{v_r} \cdot \mathbf{v_2}) \end{bmatrix}$$

$$A_2 = \begin{bmatrix} -\mathbb{1}_{\Omega_P} D_{x_1x_1} & -\mathbb{1}_{\Omega_P} D_{x_1x_2} & -\mathbb{1}_{\Omega_P} D_{x_1x_3} \\ -\mathbb{1}_{\Omega_P} D_{x_2x_1} & -\mathbb{1}_{\Omega_P} D_{x_2x_2} & -\mathbb{1}_{\Omega_P} D_{x_2x_3} \\ -\mathbb{1}_{\Omega_P} D_{x_3x_1} & -\mathbb{1}_{\Omega_P} D_{x_3x_2} & -\mathbb{1}_{\Omega_P} D_{x_3x_3} \end{bmatrix}$$

$$A_3 = \begin{bmatrix} \mathbb{1}_{\partial\Omega_P} & \mathbf{0} & \mathbf{0} \\ \mathbf{0} & \mathbb{1}_{\partial\Omega_P} & \mathbf{0} \\ \mathbf{0} & \mathbf{0} & \mathbb{1}_{\partial\Omega_P} \end{bmatrix}$$

$$A_4 = \begin{bmatrix} -\mathbb{1}_{\Omega_P} \sum_{i=1}^{3} D_{x_ix_i} & \mathbf{0} & \mathbf{0} \\ \mathbf{0} & -\mathbb{1}_{\Omega_P} \sum_{i=1}^{3} D_{x_ix_i} & \mathbf{0} \\ \mathbf{0} & \mathbf{0} & -\mathbb{1}_{\Omega_P} \sum_{i=1}^{3} D_{x_ix_i} \end{bmatrix}$$

Denoting by $\circ$ the Hadamard product, column vectors b_1 to b_4 of size $3mno \times 1$ are defined as follows:

$$b_1 = \begin{bmatrix} \operatorname{vec}(\mathbb{1}_{\Omega_P}) \circ \operatorname{vec}(\mathbf{v_r} \cdot \mathbf{v_1}) \circ \operatorname{vec}(V_r)) \\ \operatorname{vec}(\mathbb{1}_{\Omega_P}) \circ \operatorname{vec}(\mathbf{v_r} \cdot \mathbf{v_2}) \circ \operatorname{vec}(V_r)) \\ \operatorname{vec}(\mathbb{1}_{\Omega_P}) \circ \operatorname{vec}(\mathbf{v_r} \cdot \mathbf{v_3}) \circ \operatorname{vec}(V_r)) \end{bmatrix}$$

$$b_2 = \begin{bmatrix} \mathbf{0} & \mathbf{0} & \mathbf{0} \end{bmatrix}^T$$

$$b_3 = \begin{bmatrix} \operatorname{vec}(\mathbb{1}_{\partial\Omega_P}) \circ \operatorname{vec}(\mathbf{V_P} \cdot \mathbf{v_1}) \\ \operatorname{vec}(\mathbb{1}_{\partial\Omega_P}) \circ \operatorname{vec}(\mathbf{V_P} \cdot \mathbf{v_2}) \\ \operatorname{vec}(\mathbb{1}_{\partial\Omega_P}) \circ \operatorname{vec}(\mathbf{V_P} \cdot \mathbf{v_3}) \end{bmatrix}$$

$$b_4 = \begin{bmatrix} \mathbf{0} & \mathbf{0} & \mathbf{0} \end{bmatrix}^T$$

The full system of E-L equations associated to $J[\mathbf{X}]$ can be discretized to produce problem $(R3')$, equivalent to problem $(R3)$ excluding discretization errors:

Discretized problem (R3')

Given an observed flow velocity V_r, a boundary condition $\mathbf{V_P}|_{\partial\Omega_P}$, and $\lambda_1, \ldots, \lambda_4 \in \mathbb{R}^{+*}$, find the vector field $\mathbf{V_P^\star} : \Omega_P \to \mathbb{R}^3$, solution of the system $Ax = b$, where A and b are defined as:

$$A = \lambda_1 A_1 + \lambda_2 A_2 + \lambda_3 A_3 + \lambda_4 A_4$$
$$b = \lambda_1 b_1 + \lambda_2 b_2 + \lambda_3 b_3 + \lambda_4 b_4$$

6.3.4 Numerical experiments

In this section, we propose two numerical examples to assess the reconstruction of a 3D blood flow. In Experiment IV, the reconstruction of a diastolic healthy blood flow is considered whereas Experiment V focuses on the reconstruction of a systolic pathological blood flow with MR.

6.3.4.1 Experiment IV: Physiological blood flow reconstruction

We consider the 3D extension of the numerical experiment described in Section 6.2.4.1. The blood flow of patient C12_H, at time $t/T = 0.75$, is used as the ground truth. The synthetic US probe was placed apically and a slab was used as the US acquisition domain. The domain was sampled regularly in each dimensions using discretization steps similar to US sampling in term of order of magnitude (*i.e.* $\approx 0.5\,\text{mm}$ in the longitudinal direction and $\approx 1\,\text{mm}$ in the two orthogonal directions).

Figure 6.24 depicts the boundary $\partial\Omega_P$ on different slices of the acquisition slab in the v_3 direction.

(a) (b) (c) (d)

Figure 6.24 – Slices of $\partial\Omega_P$ across the v_3 direction at approximately (a) 12%, (b) 31%, (c) 47% and (d) 86% of the acquisition slab thickness.

The velocity field $\mathbf{V}$ resulting from the numerical simulation was interpolated at the sampling point using gaussian RBF to produce the velocity field $\mathbf{V_P}$ (Figure 6.25). The scalar field V_r (Figure 6.26) was produced by projecting the velocities of the vector field $\mathbf{V_P}$ on the individual unit vectors $\mathbf{v_r}$ (*i.e.* producing the synthetic ultrasound image).

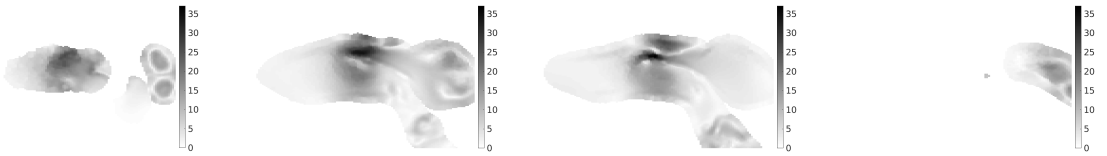

(a) (b) (c) (d)

Figure 6.25 – Vector field $\mathbf{V_P}$ magnitude at approximately (a) 12%, (b) 31%, (c) 47% and (d) 86% of the acquisition slab thickness.

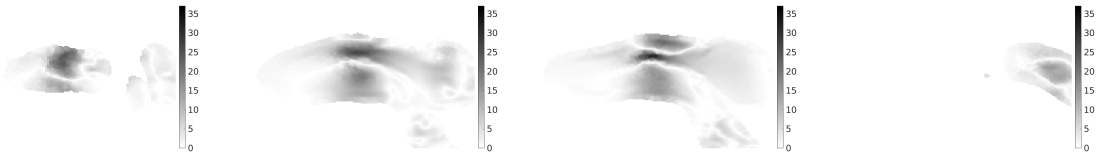

(a) (b) (c) (d)

Figure 6.26 – Scalar field V_r magnitude at approximately (a) 12%, (b) 31%, (c) 47% and (d) 86% of the acquisition slab thickness.

Solving problem (R3') allowed to produce de vector field $\mathbf{V_P^\star}$ (Figure 6.27).

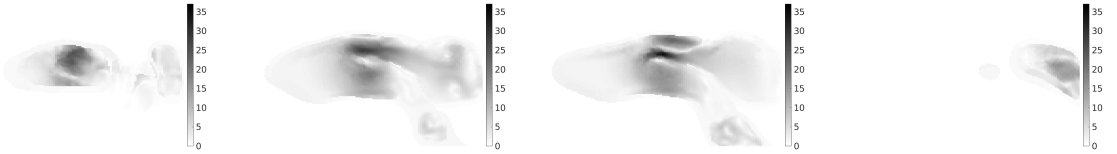

(a) (b) (c) (d)

Figure 6.27 – Vector field $\mathbf{V}_\mathbf{P}^\star$ magnitude at approximately (a) 12%, (b) 31%, (c) 47% and (d) 86% of the acquisition slab thickness.

Figure 6.28a depicts the statistics for the velocity error $E(\mathbf{V_P}, V_r\mathbf{v_r})$ and $E(\mathbf{V_P}, \mathbf{V}_\mathbf{P}^\star)$, respectively the velocity error of the synthetic US scalar field projected on the beam direction and the velocity error after reconstruction of the velocity vector field. Figure 6.28b depicts the same quantities in their normalized version, *i.e.* $\hat{E}(\mathbf{V_P}, V_r\mathbf{v_r})$ and $\hat{E}(\mathbf{V_P}, \mathbf{V}_\mathbf{P}^\star)$.

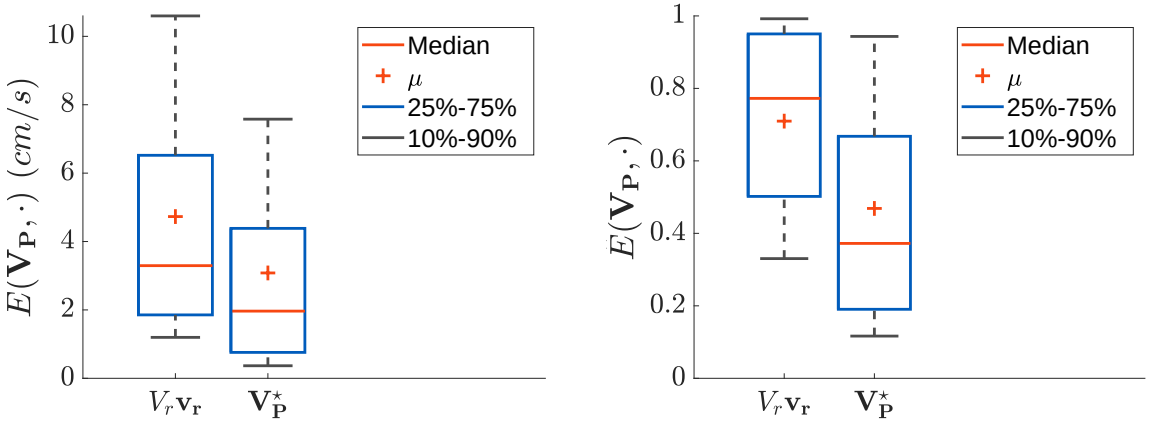

Figure 6.28 – Box plots depicting the statisticts of (a) the velocity error before and after reconstruction and (b) the normalized velocity error before and after reconstruction.

The average velocity error decreased from 4.73 cm/s (≈ 71 %) to 3.08 cm/s (≈ 47 %) after reconstruction and the median velocity error was reduced from 3.29 cm/s (≈ 77 %) to 1.97 cm/s (≈ 37 %). The first decile (D1) decreased from 1.20 cm/s (≈ 33 %) to 0.37 cm/s (≈ 12 %) and the ninth decile (D9) decreased from 10.6 cm/s (≈ 99 %) to 7.58 cm/s (≈ 94 %). Finally, the first quartile (Q1) decreased from 1.85 cm/s (≈ 50 %) to 0.76 cm/s (≈ 19 %) and the third quartile (Q3) decreased from 6.52 cm/s (≈ 95 %) to 4.38 cm/s (≈ 67 %).

After reconstruction of the blood flow, we note a reduction in all the statistics related to the velocity error, highlighting the algorithm ability to recover information lost by the synthetic US acquisition. While the pre-reconstruction normalized error distribution was not as symmetrical as in the 2D cases, the post-reconstruction distribution was skewed towards the lower errors, as depicted by the median normalized error lower than the average normalized error and by the small D1-Q1 range compared to the Q3-D9 range.

6.3.4.2 Experiment V: Pathological blood flow reconstruction

The 3D analog of the numerical experiment described in Section 6.2.4.2 is considered: the blood flow C11_T1, at time $t/T = 0.125$, is used as the ground truth. The synthetic US probe was placed apically and a slab was used as the US acquisition domain. This domain was regularly sampled in each dimensions using discretization steps similar to US sampling in term of order of magnitude (*i.e.* $\approx 0.5\,\text{mm}$ in the longitudinal direction and $\approx 1\,\text{mm}$ in the two orthogonal directions).

Figure 6.29 depicts the boundary $\partial\Omega_P$ on different slices of the acquisition slab in the v_3 direction.

(a) (b) (c) (d) (e)

Figure 6.29 – Slices of $\partial\Omega_P$ across the v_3 direction at approximately (a) 8%, (b) 31%, (c) 47% (d) 63% and (e) 86% of the acquisition slab thickness.

The velocity field $\mathbf{V}$ resulting from the numerical simulation was interpolated at the sampling point using gaussian RBF to produce the velocity field $\mathbf{V_P}$ (Figure 6.30). The scalar field V_r (Figure 6.31) was produced by projecting the velocities of the vector field $\mathbf{V_P}$ on the individual unit vectors $\mathbf{v_r}$ (*i.e.* producing the synthetic ultrasound image).

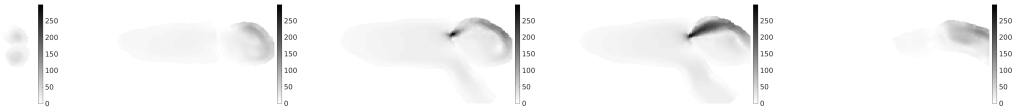

(a) (b) (c) (d) (e)

Figure 6.30 – Vector field $\mathbf{V_P}$ magnitude at approximately (a) 8%, (b) 31%, (c) 47% (d) 63% and (e) 86% of the acquisition slab thickness.

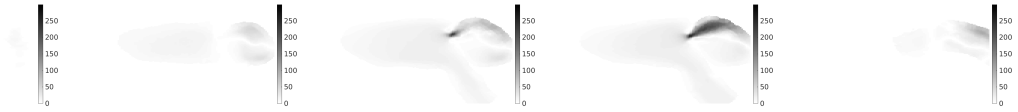

(a) (b) (c) (d) (e)

Figure 6.31 – Scalar field V_r magnitude at approximately (a) 8%, (b) 31%, (c) 47% (d) 63% and (e) 86% of the acquisition slab thickness.

Solving problem (R3') allowed to produce de vector field $\mathbf{V_P^\star}$ (Figure 6.32).

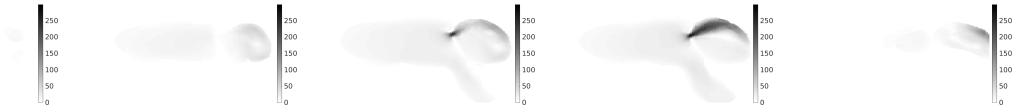

(a) (b) (c) (d) (e)

Figure 6.32 – Vector field $\mathbf{V}_\mathbf{P}^\star$ magnitude at approximately (a) 8%, (b) 31%, (c) 47% (d) 63% and (e) 86% of the acquisition slab thickness.

Figure 6.33a depicts the statistics for the velocity error $E(\mathbf{V_P}, V_r\mathbf{v_r})$ and $E(\mathbf{V_P}, \mathbf{V}_\mathbf{P}^\star)$, respectively the velocity error of the synthetic US scalar field projected on the beam direction and the velocity error after reconstruction of the velocity vector field. Figure 6.33b depicts the same quantities in their normalized version, *i.e.* $\hat{E}(\mathbf{V_P}, V_r\mathbf{v_r})$ and $\hat{E}(\mathbf{V_P}, \mathbf{V}_\mathbf{P}^\star)$.

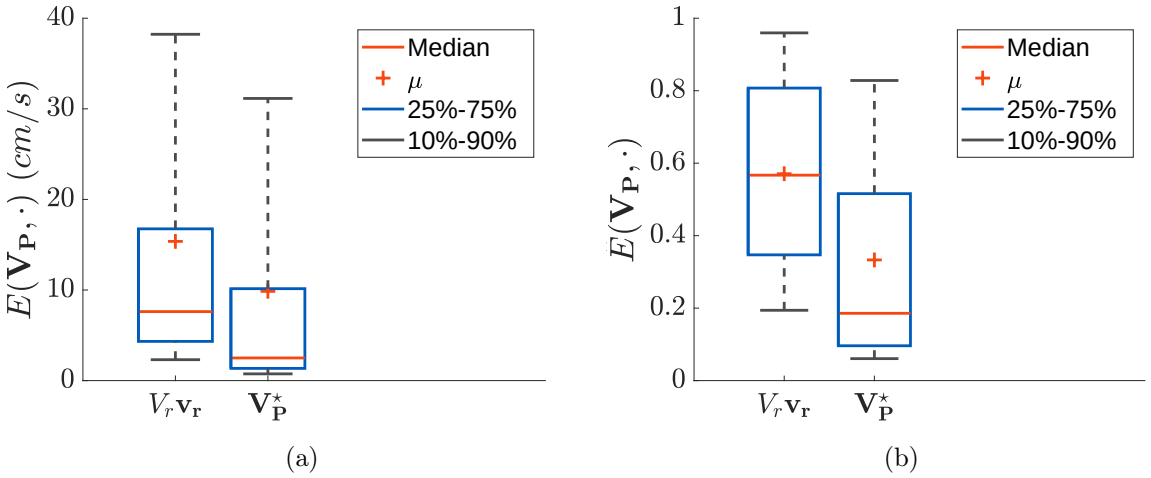

Figure 6.33 – Box plots depicting the statisticts of (a) the velocity error before and after reconstruction and (b) the normalized velocity error before and after reconstruction.

The average velocity error decreased from 15.37 cm/s (≈ 57 %) to 9.86 cm/s (≈ 33 %) after reconstruction and the median velocity error was reduced from 7.60 cm/s (≈ 57 %) to 2.5 cm/s (≈ 19 %). The first decile (D1) decreased from 2.31 cm/s (≈ 19 %) to 0.74 cm/s (≈ 6 %) and the ninth decile (D9) decreased from 38.23 cm/s (≈ 96 %) to 31.15 cm/s (≈ 83 %). Finally, the first quartile (Q1) decreased from 4.33 cm/s (≈ 35 %) to 1.35 cm/s (≈ 10 %) and the third quartile (Q3) decreased from 16.75 cm/s (≈ 81 %) to 10.15 cm/s (≈ 52 %).

6.4 Conclusion, discussion and perspectives

In this chapter, the reconstruction of the intracardiac blood velocity based on Color-Doppler images han been considered.

In Section 6.1, some elements of calculus of variations were recalled. Section 6.2 was dedicated to the reconstruction of 2D fluid velocity fields. An optimization problem, similar to the work of Assi et al. [134], was introduced. Three numerical experiments were designed to assess the

velocity field reconstruction in different setting including healthy blood flow reconstruction (Experiment I and Experiment III) and pathological MR blood flow reconstruction (Experiment II) using the numerical simulations presented in Chapter 4. Finally, in Section 6.3, this optimization problem was extended to the reconstruction of a 3D velocity vector field. Two numerical experiments were conducted to assess the velocity field reconstruction conditions similar to the 2D cases including healthy blood flow reconstruction (Experiment IV) and pathological MR blood flow reconstruction (Experiment V).

Reconstruction results and computational effort

Experiments I and II were designed to assess the quality of the velocity field reconstruction in a 2D setting. In both cases, it was shown that the reconstruction algorithm lowered the velocity error. More importantly, while the error distribution was relatively symmetric around the average error, the error distribution for the reconstructed velocity field was highly skewed towards lower errors in both experiments. This results indicates a global success of the reconstruction with some outliers for which the correction was not as successful. Very similar results were obtained for the 3D Experiments IV and V.

Regarding the computational effort, the linear systems were solved on a laptop using a *Intel Core i7-4810MQ* cadenced at 2.8 GHz, 16MB of RAM. The 2D cases were solved in less than one second and the 3D cases were solved within 30 seconds, making this algorithm suitable for integration in a clinical setting. Some improvements on the computational complexity could easily be obtained. First, the linear system can be restricted only to the discretization points located inside the heart with no degradation of the resulting reconstruction. A second improvement can be to solve the reconstruction problem in a reduced region of interest. In that setting, careful evaluation would be required to assess how this decision would impact the reconstruction error.

The reconstruction algorithm relies on the proper choice of parameters $\lambda_1, \ldots, \lambda_4$. In the 2D setting, those parameters could be optimally chosen by solving an optimisation problem and resulted in order of magnitude that were quite different from one parameter to the other ($\lambda_1 > \lambda_2 \approx \lambda_3 > \lambda_4$). The same analysis was nevertheless not reproduced in the 3D case. Nevertheless, in our experience, the best results in 3D were obtained with similar order of magnitude between the weighting coefficients. It would be interesting to understand why this particular result is obtained.

Sensitivity analysis

In Experiment I and II, the synthetic US data was considered known in the entire domain. As this is likely not the case in a clinical setting, Experiment III was designed to assess the sensitivity of the reconstruction to partial data sampling. Instead of imposing the data attachment term everywhere in the domain, the data was purposefully subsampled at different sampling rates and the optimization functional was modified to reflect that change. The results of this experiment highlight the fact that only a small amount of data is required to obtain nearly as good results as when the entire velocity field is known. Indeed, the reconstruction error quickly decayed as the sampling rate increased. This results underlines the robustness of the algorithm to partial data sampling. In this analysis, the partial sampling strategy considered that all the data samples

were independent throughout the domain. An interesting extension could be to investigate the robustness of the algorithm to different partial sampling strategies, for example by considering patches of samples scattered in the domain.

The sensitivity analysis presented above was restricted to the sensitivity of the algorithm to partial data sampling. Several other issues could affect the algorithm performances. Sensitivity analysis with respect to to the presence of aliasing, for example, seems a very important next step of the presented work. Indeed, aliasing of the data occurs when the velocities are too high compared to the US system settings and physical limitations. In particular, aliasing if very often observed in the case of MR because of the high velocities at the regurgitation level. As the algorithm reconstructs a blood velocity field mainly based on the Color-Doppler information, aliasing could be a big issue.

Finally, a sensitivity analysis of the algorithm with respect to to noise could also allow to test the algorithm reconstruction in non-optimal conditions. Nevertheless, one should be careful when designing the experiment. Indeed, instead of evaluating the sensitivity of the algorithm to white or Gaussian noise, for example, one should consider to incorporate noises which are more related with the US technique. In particular, the two major noises in Color-Doppler images are clutter noise and speckle noise. Briefly, clutter noise is due to slow moving tissue limiting the maximum penetration depth of the US signal, biasing the flow velocity estimation, and speckle noise is due to constructive and destructive summation of ultrasound echoes that might cause local noise in the data [150]. We quickly note that some robustness to noise is intrinsically included in the algorithm thanks to the contribution of the regularization term.

MR severity quantification

The Experiment II aimed to reconstruct a velocity field which included a MR. To assess how the reconstruction could be beneficial for MR severity assessment, the regurgitant volume computed on the reconstructed velocity field was compared both to a 2D PISA-like measurement and to the regurgitant volume computed on the ground truth velocity field for a large range of aliasing velocities. It was shown that while the PISA-like measurement overestimated the regurgitant volume, the regurgitant volume computed using the reconstructed velocity field was much closer to the ground truth value. Further work is required to confirm that this observations also holds with respect to the 3D velocity field reconstruction. Nevertheless, this first result in 2D hints that reconstruction of the blood velocity field could be beneficial to better assess MR severity.

Some other perspectives regarding the reconstruction functional

Considering the functional used in the reconstruction algorithm, the following two propositions are thought to be interesting research directions:

1. Color-Doppler images are usually recorded as image sequences. A first extension could be to incorporate the temporal coherence of the blood velocity field into the optimization problem.

2. The four different terms of the functional used in this chapter are weighted by scalar coefficients $\lambda_1, \ldots, \lambda_4$. A second extension could be to modify those coefficients locally in order to incorporate finer information with respect to the CD images. For example the

influence of the data attachment term could be locally lowered in regions were aliasing is detected and the relative influence of the wall BC could be scaled by taking into account the intensity of the US tissue images.

Chapter 7
Thesis conclusion and perspectives

The research work presented in this thesis was motivated by the observation that modern echocardiography techniques allow the obtention of useful data, both in term of cardiac motion and in term of hemodynamical quantities. MR is a prevalent disease for which clinical decisions might strongly impact the patients survival, the current quantification tools, such as the PISA technique, present several limitations. Therefore, a general objective was to investigate how such data could be combined with numerical simulations the the intracardiac hemodynamics to assess MR severity. Therefore, we expressed the hypothesis that combining numerical simulations with echocardiography data could improve our current understanding of cardiac hemodynamics, improve our understanding of the limitations of the current MR quantification techniques and help to build new tools to provide better quantification of its severity.

Before describing the contributions presented in this thesis, we first quickly recall the objectives described in Chapter 1:

A. Develop physiological simulations of the heart hemodynamics starting from [49], including the following objectives:
    1. Improve the geometrical aspects of the model in the context of MR modeling (*e.g.,* include the left atrium and improve the mitral valve geometry.)
    2. Propose an improvement of the current model to allow the simulation of mitral regurgitation.
    3. Derive a methodology to include US image data into the model, in particular cardiac motion and/or hemodynamic boundary conditions (BC).

B. In order to propose a better MR quantification:
    1. Evaluate the current quantification tools and propose new hemodynamic features to quantify MR.
    2. Develop a simplified mathematical model of the blood flow, based on US images and biophysical principles, which accounts for the constraints of the clinical setting.
    3. Evaluate the simplified model with respect to the complex 3D model and other potentially available data.

C. Improve current understanding of cardiac hemodynamics

Thesis contributions

We now recall the contributions presented in this thesis.

Chapter 2 describes a mathematical model of the left heart hemodynamics which can simulate both a healthy and a pathological blood flow. First, a geometrical domain of the left-heart is carefully constructed. A mathematical model of the 3D intracardiac hemodynamics is then presented. Modeling choices were made to keep the computational complexity reasonable. A versatile model of the MR was obtained by modifying a simplified MV model. Numerical simulations, both in healthy and pathological cases, provided physiological results of the intracardiac hemodynamics. Nevertheless, several limitations were observed, such as the difficulty of the model to represent isovolumetric phases or the strong dependence of the hemodynamics quantities to the LV wall synthetic data.

In Chapter 3, a new approach was proposed to circumvent the difficulty of modeling the isovolumetric phases when uncoupling the fluid and solid problems. By considering the mathematical model of Chapter 2, an analysis of the intraventricular pressure is provided to highlight the reasons which makes it difficult to model the isovolumetric phases. By enhancing the valve model with an external pressure data, the isovolumetric phases could be obtained both in a toy example and a realistic physiological heart.

In Chapter 4, we described a novel methodology aimed at combining the segmentations of the LV wall coming from RT3DE images with the numerical simulations presented in Chapter 2. This methodology was designed to be fully automatic and application to twelve cases showed that it reduced the pre-processing time to approximately one hour, 5 % of what is usually reported. This pipeline was used to generate a dataset of intracardiac hemodynamics both in healthy and pathological situations using the MR model introduced in Part 2. The hemodynamics of the different pathological cases were assessed qualitatively and quantitatively to improve our understanding of the limitations related to the PISA technique, which is the current medical tool to quantify MR. In particular, it was shown that the mitral valve shape has a strong influence on the regurgitation hemodynamics. Moreover, we showed several situations where the standard PISA techniques was not able to accurately quantify the MR severity.

In Chapter 5, we investigated in detail how a misrepresentation of the LV wall torsion in the model boundary condition might affect the intracardiac hemodynamics. Using a LV surface dynamics which included ventricular twisting, we produced a LV surface dynamics where twisting was removed. By comparing the intracardiac hemodynamics using both LV dynamics as boundary conditions, it has been concluded that the ventricular twisting does not influence significantly the hemodynamics in the context of smooth LV geometries (*i.e.* not including internal features such as trabeculae, papillary muscles or chordae). This experiment was also conducted in a pathological case. These results helped reinforce the confidence in hemodynamical results and interpretations made in Chapter 4. Nevertheless, it is important to remember that a strong limitation of this study is that the analysis was conducted in the context of a smooth LV surface, *i.e.* the impact of trabeculae, papillary muscles or chordae were not taken into account.

As the mathematical models presented in the rest of the manuscript are too computationally demanding to evaluate MR severity in a clinical setting, Chapter 6 introduces a 2D velocity reconstruction method which maily relies on the work of Assi et al [134]. While the original method was aimed at reconstructing a 2D blood flow using 2D US data, we extended this reconstruction algorithm to allow the reconstruction of 3D blood velocity fields. By the means of variational calculus, we show how those 2D and 3D reconstruction problems can be solved numerically. Several examples were proposed, using blood velocity fields extracted from the intracardiac hemodynamics library generated in Chapter 4 as ground truth. It is shown that

the reconstruction algorithm is robust to partial data sampling and that reconstruction of the intracardiac blood velocity could be beneficial for MR severity assessment.

Global perspectives

Here, we discuss global perspectives with respect to the work presented in this manuscript.

In this thesis, techniques were developed to model the intracardiac hemodynamics in healthy and pathological cases. Those developments allowed to improve our understanding of the hemodynamical phenomena and to assess the limitations of the current MR quantification tools

In term of perspectives, with respect to the mathematical modeling of the cardiac hemodynamics, several paths can be pursued. In particular, FSI can be used to study the interaction between the blood and the MV in the context of MR. Indeed, this type of model could help understand how the structure of the blood flow in the convergence region evolve with respect to time. This is, however, challenging for several reasons: one need to be able to handle large deformations of the valve leaflets, to detect the contact between them and to handle topology changes. Moreover, recreating the different types of MR might not be as straightforward as what was presented in this document.

In term of patient-specific simulations, the image/model fusion pipeline was used to generate a dataset of intracardiac hemodynamics based on twelve RT3DE sequences. This capability can be used to systematically assess the new quantification tools proposed. For example, this philosophy motivated the use of the cardiac hemodynamics generated in Chapter 4 to assess the reconstruction algorithm in Chapter 6. In particular, one of the advantage of using such synthetic data to validate new algorithms is that all the relevant quantities of interest might be obtained, unlike *in vitro* and *in vivo* data. From an industrial perspective, a natural next step with respect to the blood flow reconstruction would be to also try to recover the intracardiac pressure gradients. To achieve this goal, synthetic cardiac hemodynamics will also be very valuable.

Finally, even though *in silico* data provide a controlled environment to assess the quality of algorithms, transfer to the clinical context is, however, not straightforward. A preliminary study has been initiated in that regard, with respect to to the transfer of the reconstruction algorithm presented in Chapter 6 to the clinical setting. With the help of the Laboratoire de Biomécanique Appliquée of the Aix-Marseille University[1], RT3DE images of the left ventricle were acquired using a double activation pulsed duplicator which simulates the left human heart from the pulmonary valve to the systemic capillaries [151]. Depicted in Figure 7.1, this mock simulation system includes anatomical shapes of the LV, the LA, the aorta, the mitral and aortic valves as well as compliances and resistance for pulmonary and systemic circulation simulation. Using two piston pumps[2], the system reproduces a pulsatile flow. The RT3DE images were acquired in different configurations by varying the flow parameter and by manually creating valve defects. By using an electromagnetic flowmeter[3] (internal diameter 30mm, accuracy +/- 2mL/min) upstream of the mitral valve, the regurgitation volume could be recorded in the

[1]Laboratoire de Biomécanique Appliquée, Aix-Marseille Université, IFSTTAR, LBA UMR_T24, Marseille, France

[2]Vivitro Labs Inc, Victoria, Canada

[3]Probe 95, Carolina Medical Electronics, East Bend, NC

pathological cases. The next step of this preliminary study is therefore to assess how well the reconstruction algorithm performs by comparing the regurgitant volume estimated *via* the algorithm to the regurgitant volume recorded by the flow meter.

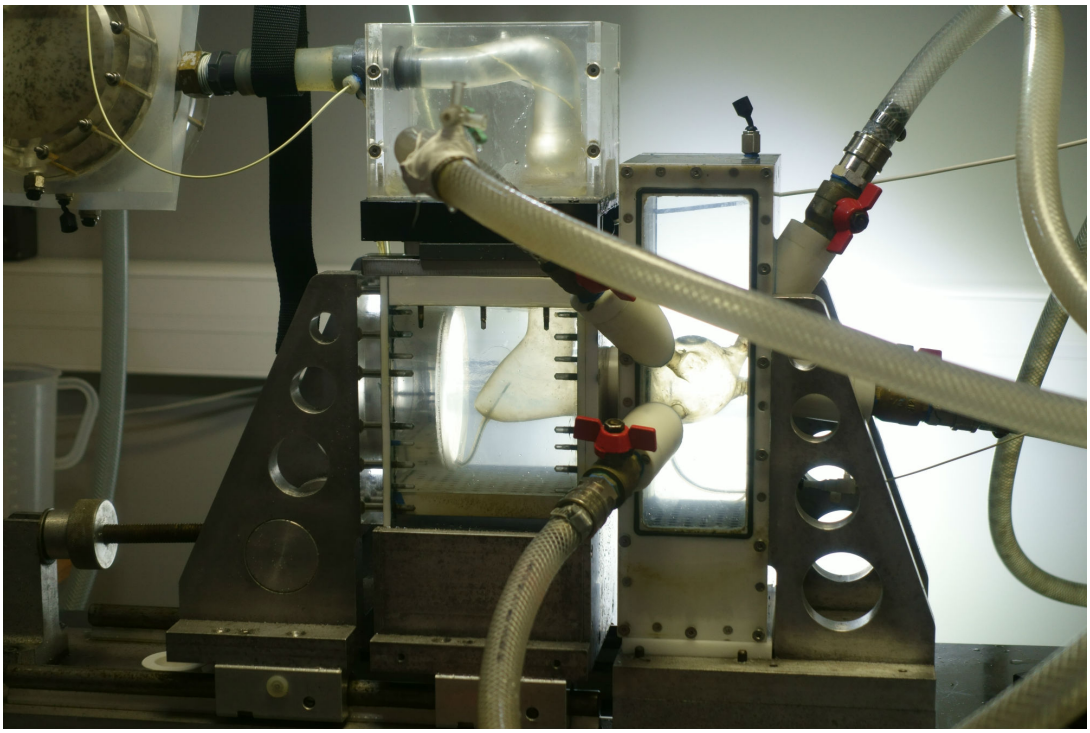

Figure 7.1 – Mock circulatory system developed at the Laboratoire de Biomécanique Appliquée, Aix-Marseille University

Part III

Appendices

Appendix A
Mitral valve geometrical modeling

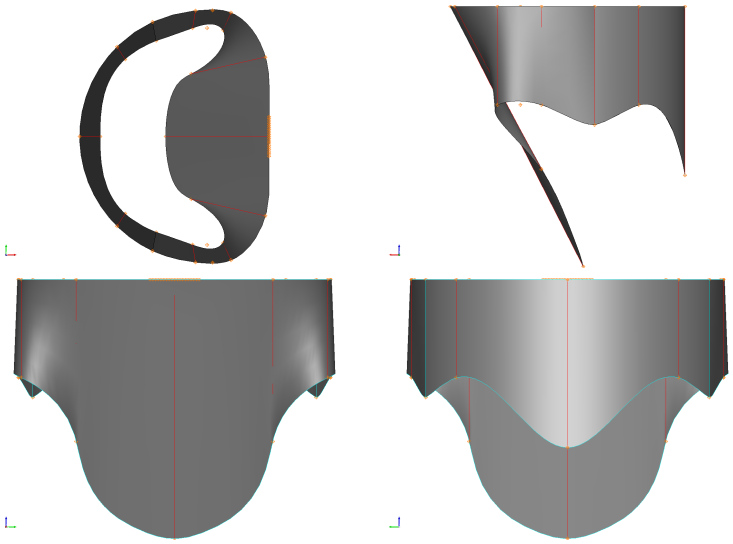

Figure A.1 – Open configuration of the mitral valve, based on the dimensions reported in Table A.1

Quantity	Value	Reference
AL width	3.375cm	[15]
AL height	2.22cm	[15, 14, 18]
PL-P1 width	1.275cm	[15]
PL-P1 height	0.98cm	[15, 14, 18]
PL-P2 width	2.9cm	[15]
PL-P2 height	1.28cm	[15, 14, 18]
PL-P3 width	1.275cm	[15]
PL-P3 height	0.98cm	[15, 14, 18]
Commisural width	1.0cm	[15]
Commisural height	0.75cm	[15, 14, 18]
Mitral annulus perimeter (diastole)	10.82cm	[16, 17]
Mitral annulus area (diastole)	8.44cm^2	[16]
closed AL/Mitral plane angle	7°	[152]
open AL/Mitral plane angle	63.5°	[152, 153]
Aortic plane/Mitral plane angle	130°	[18]
Inter-commisural distance	3.5cm	[18, 17]

Table A.1 – Reference dimensions and values for the different quantities related to the mitral valve geometry design

Appendix B
Patient-specific data

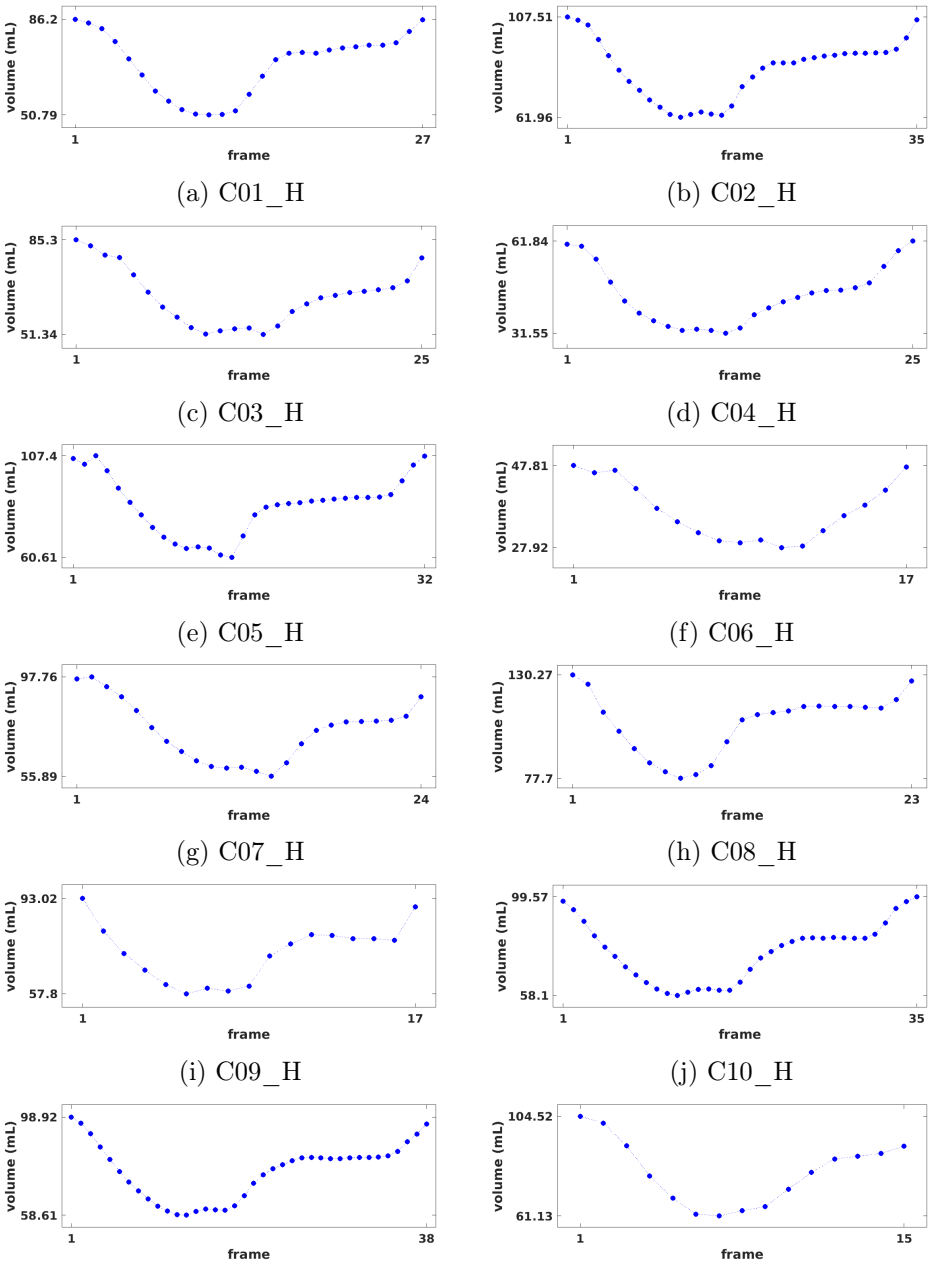

(a) C01_H (b) C02_H

(c) C03_H (d) C04_H

(e) C05_H (f) C06_H

(g) C07_H (h) C08_H

(i) C09_H (j) C10_H

(k) C11_H (l) C12_H

Figure B.1 – Volume curves of the LV meshes

Appendix C
Patient-Specific pipeline

C.1 Registration output

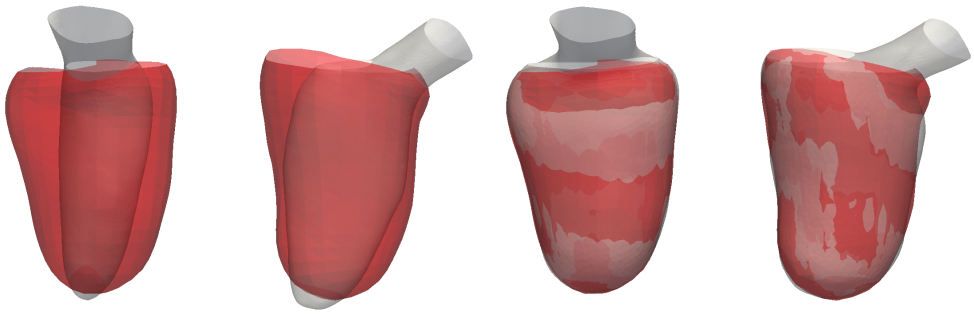

(a) (b) (c) (d)

Figure C.1 – C01_H registration a) and b) respectively front and side view of the affine registration output. c) and d) respectively front and side view of the non rigid registration output.

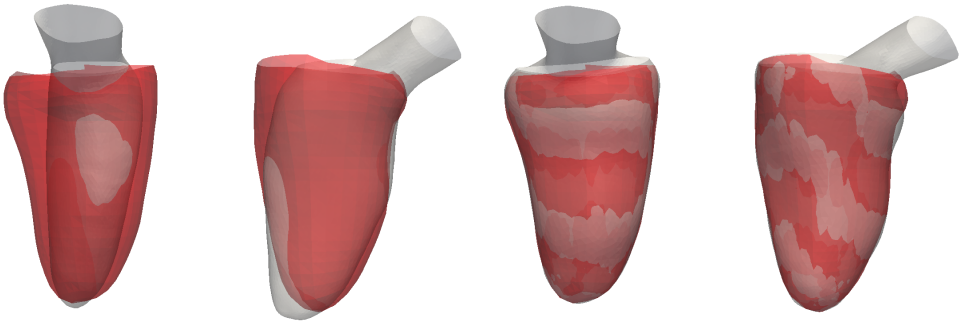

(a) (b) (c) (d)

Figure C.2 – C02_H registration a) and b) respectively front and side view of the affine registration output. c) and d) respectively front and side view of the deformable registration output.

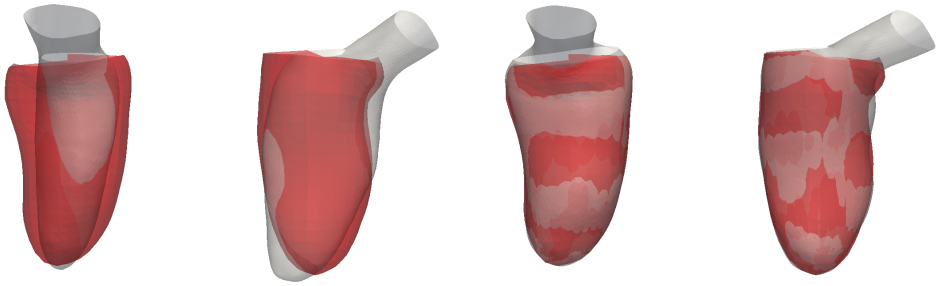

(a) (b) (c) (d)

Figure C.3 – C03_H registration a) and b) respectively front and side view of the affine registration output. c) and d) respectively front and side view of the deformable registration output.

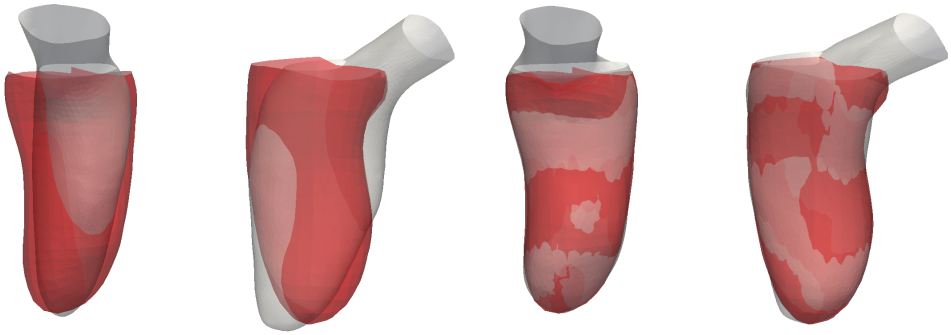

(a) (b) (c) (d)

Figure C.4 – C04_H registration a) and b) respectively front and side view of the affine registration output. c) and d) respectively front and side view of the deformable registration output.

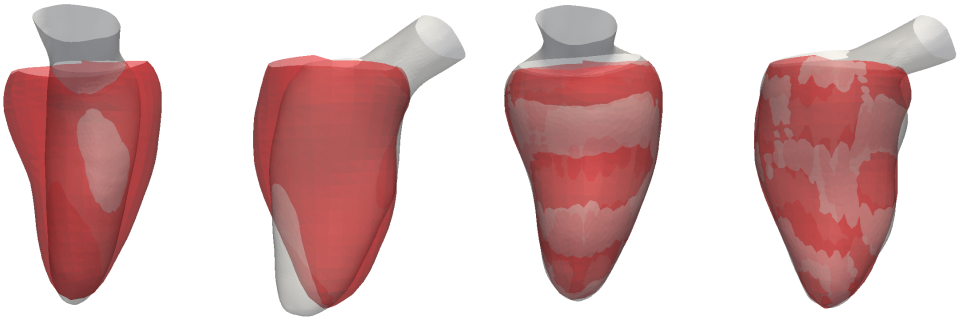

(a) (b) (c) (d)

Figure C.5 – C05_H registration a) and b) respectively front and side view of the affine registration output. c) and d) respectively front and side view of the deformable registration output.

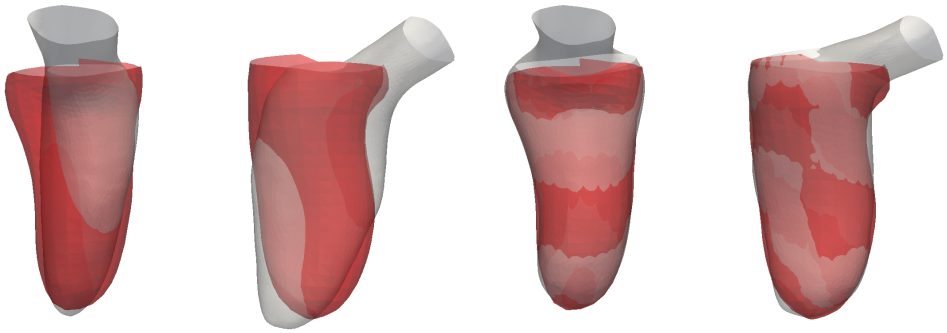

(a) (b) (c) (d)

Figure C.6 – C06_H registration a) and b) respectively front and side view of the affine registration output. c) and d) respectively front and side view of the deformable registration output.

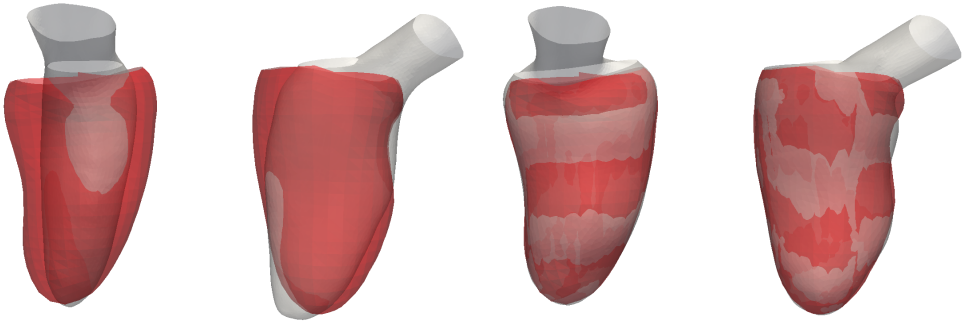

(a) (b) (c) (d)

Figure C.7 – C07_H registration a) and b) respectively front and side view of the affine registration output. c) and d) respectively front and side view of the deformable registration output.

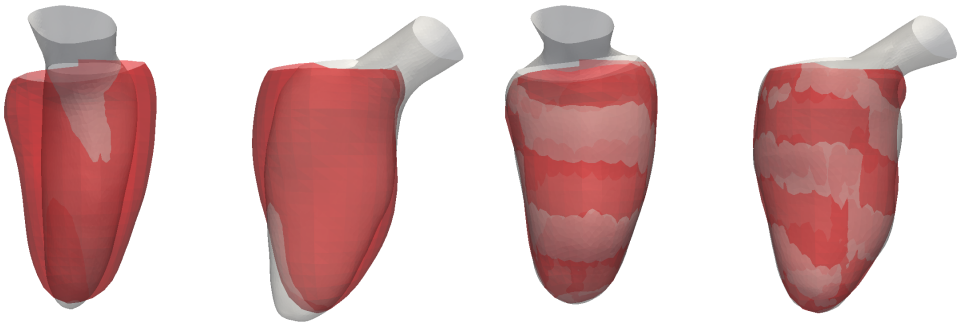

(a) (b) (c) (d)

Figure C.8 – C08_H registration a) and b) respectively front and side view of the affine registration output. c) and d) respectively front and side view of the deformable registration output.

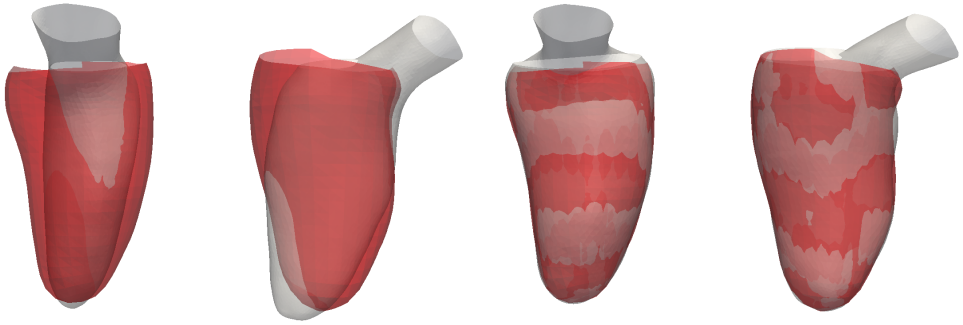

(a) (b) (c) (d)

Figure C.9 – C09_H registration a) and b) respectively front and side view of the affine registration output. c) and d) respectively front and side view of the deformable registration output.

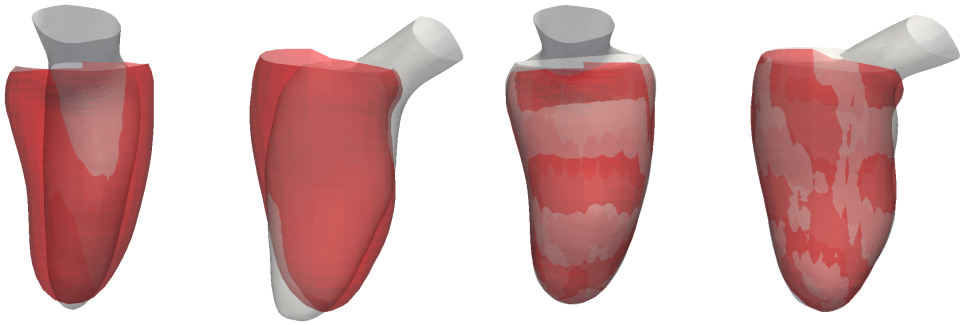

(a) (b) (c) (d)

Figure C.10 – C10_H registration a) and b) respectively front and side view of the affine registration output. c) and d) respectively front and side view of the deformable registration output.

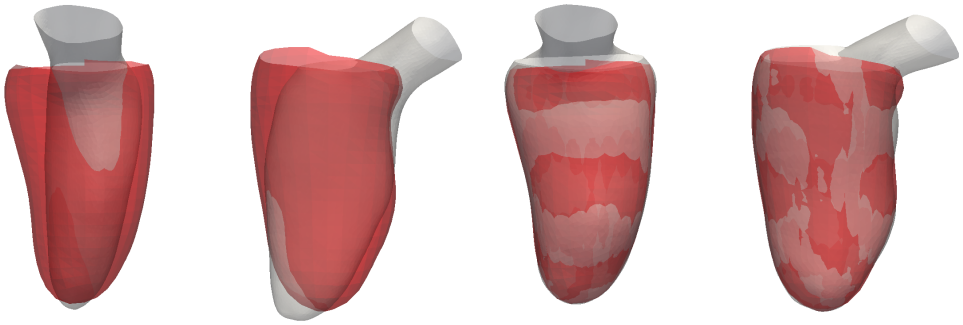

(a) (b) (c) (d)

Figure C.11 – C11_H registration a) and b) respectively front and side view of the affine registration output. c) and d) respectively front and side view of the deformable registration output.

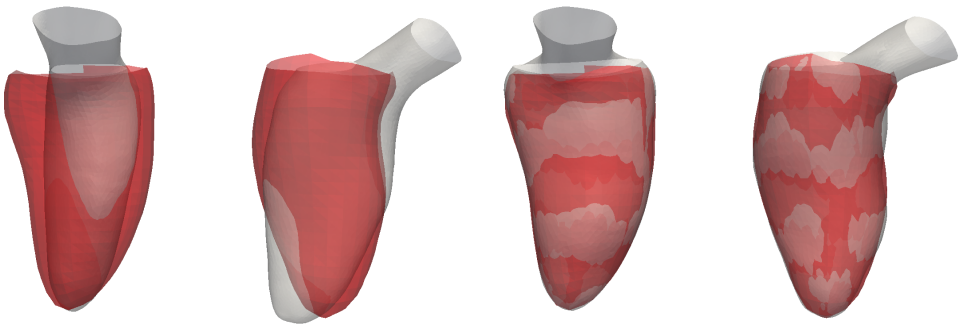

(a) (b) (c) (d)

Figure C.12 – C12_H registration a) and b) respectively front and side view of the affine registration output. c) and d) respectively front and side view of the deformable registration output.

C.2 Blood flow snapshots for all healthy cases

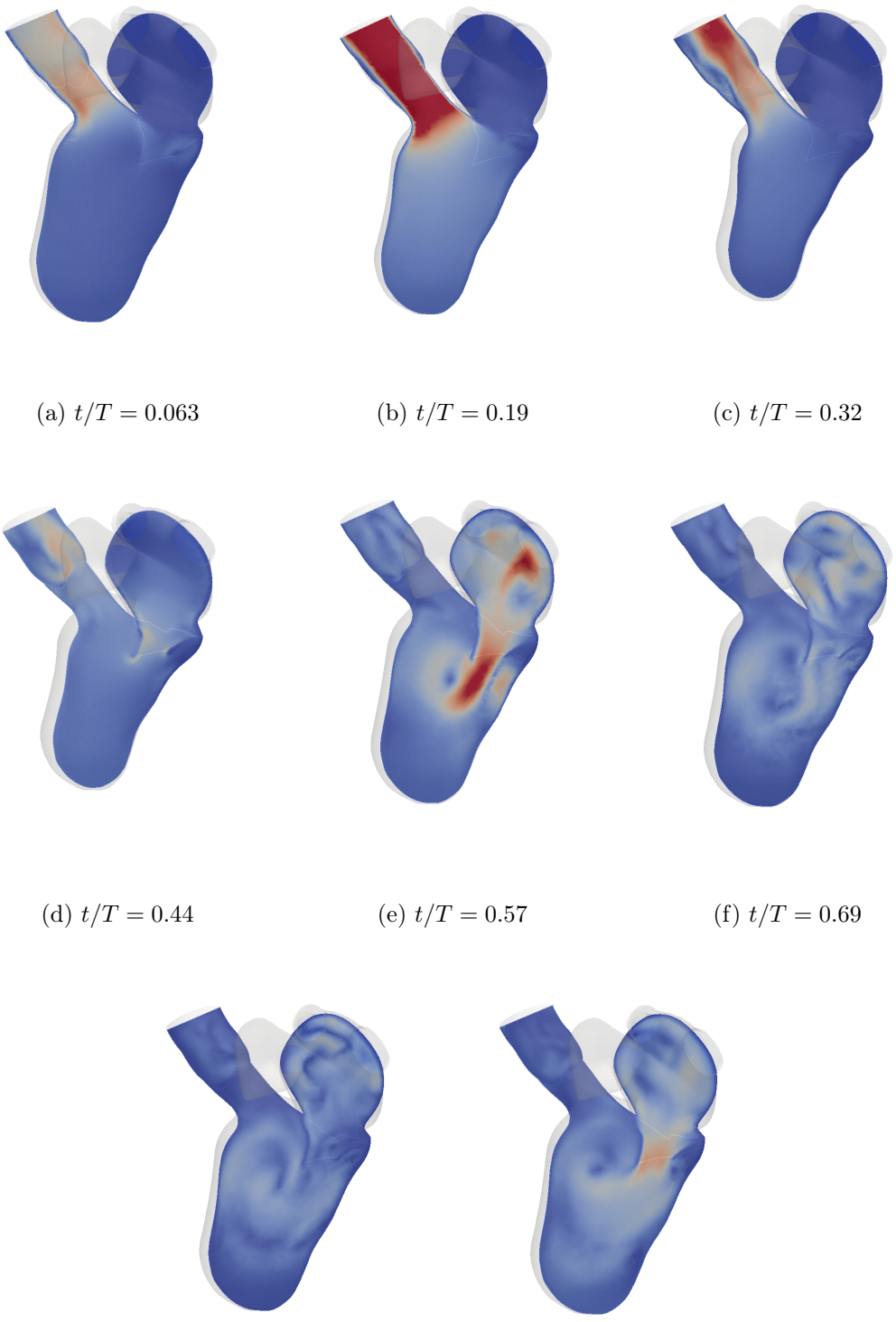

(a) $t/T = 0.063$ (b) $t/T = 0.19$ (c) $t/T = 0.32$

(d) $t/T = 0.44$ (e) $t/T = 0.57$ (f) $t/T = 0.69$

(g) $t/T = 0.81$ (h) $t/T = 0.94$

Figure C.13 – Blood velocity magnitude for case C01_H

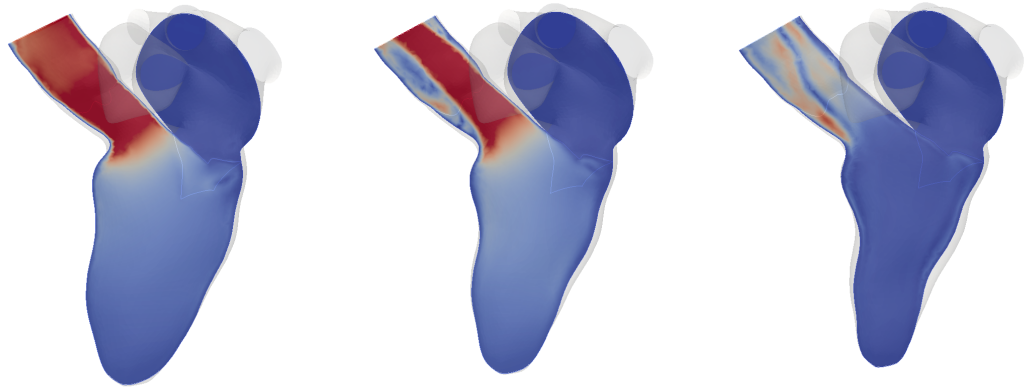

(a) $t/T = 0.063$ (b) $t/T = 0.19$ (c) $t/T = 0.32$

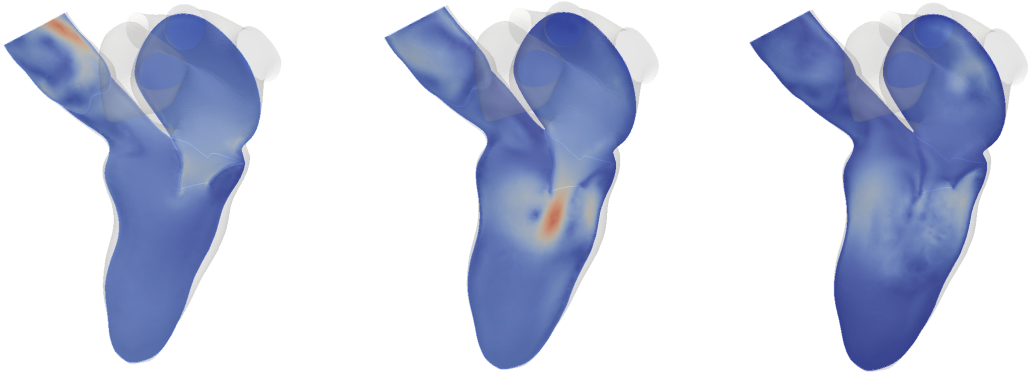

(d) $t/T = 0.44$ (e) $t/T = 0.57$ (f) $t/T = 0.69$

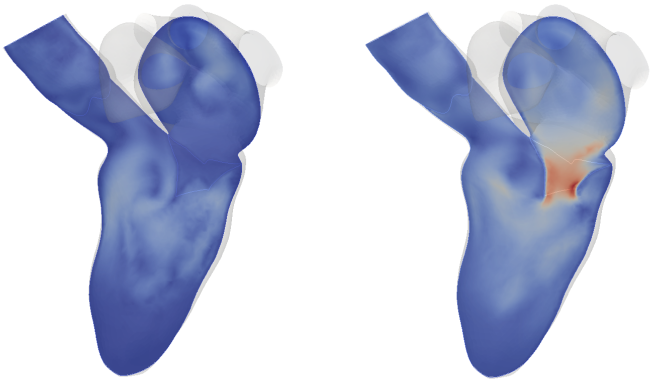

(g) $t/T = 0.81$ (h) $t/T = 0.94$

Figure C.14 – Blood velocity magnitude for case C02_H

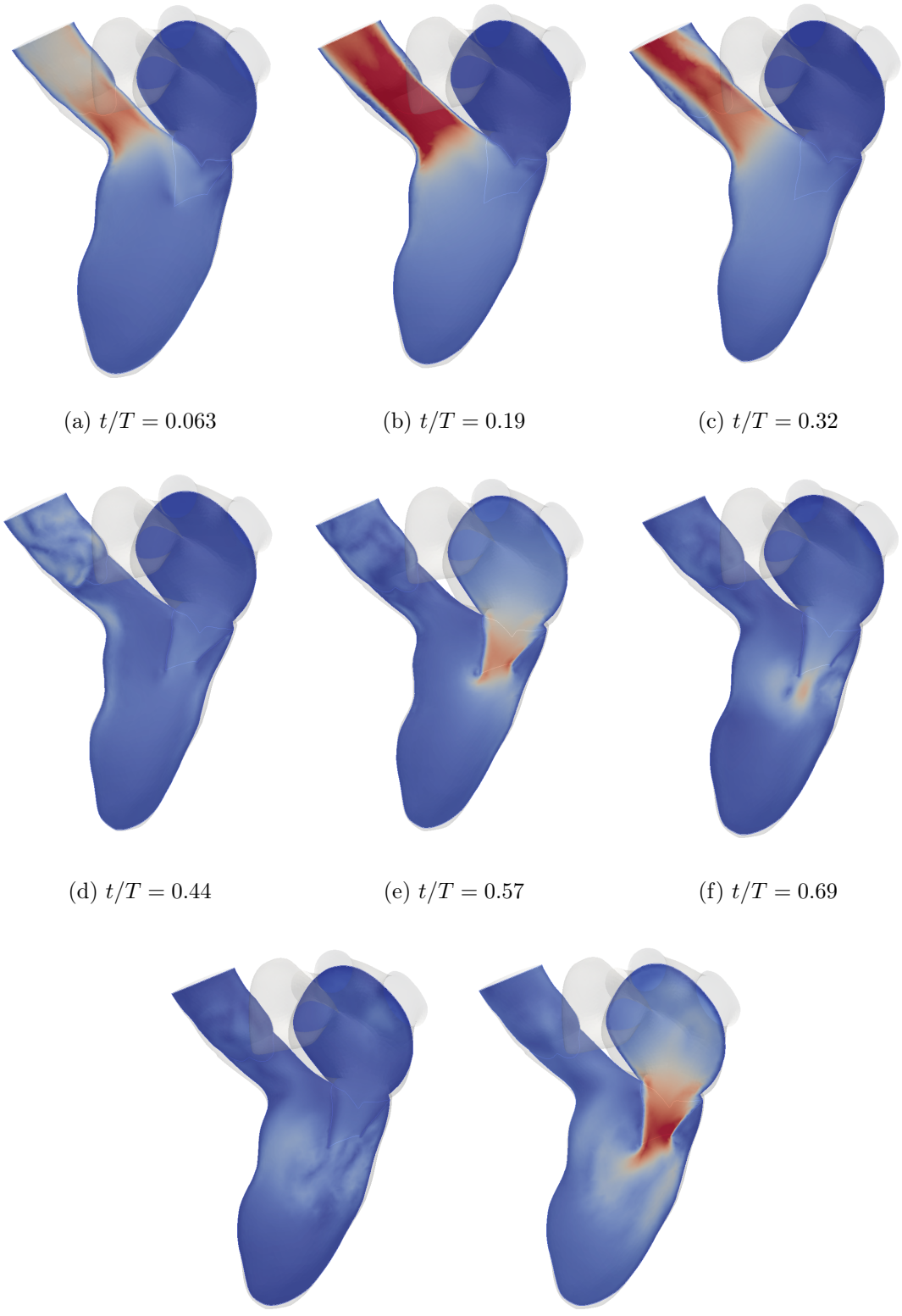

(a) $t/T = 0.063$ (b) $t/T = 0.19$ (c) $t/T = 0.32$

(d) $t/T = 0.44$ (e) $t/T = 0.57$ (f) $t/T = 0.69$

(g) $t/T = 0.81$ (h) $t/T = 0.94$

Figure C.15 – Blood velocity magnitude for case C03_H

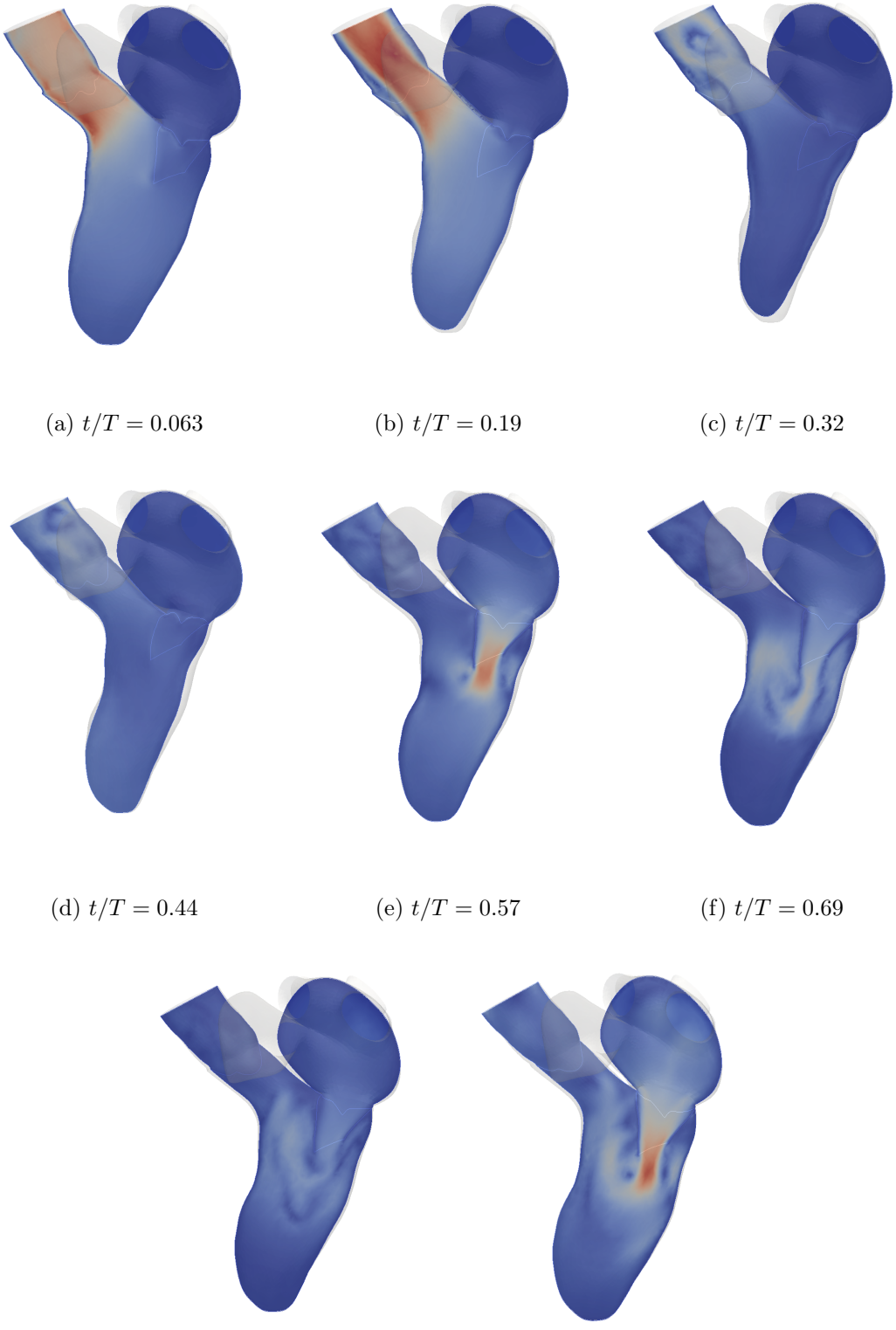

(a) $t/T = 0.063$ (b) $t/T = 0.19$ (c) $t/T = 0.32$

(d) $t/T = 0.44$ (e) $t/T = 0.57$ (f) $t/T = 0.69$

(g) $t/T = 0.81$ (h) $t/T = 0.94$

Figure C.16 – Blood velocity magnitude for case C04_H

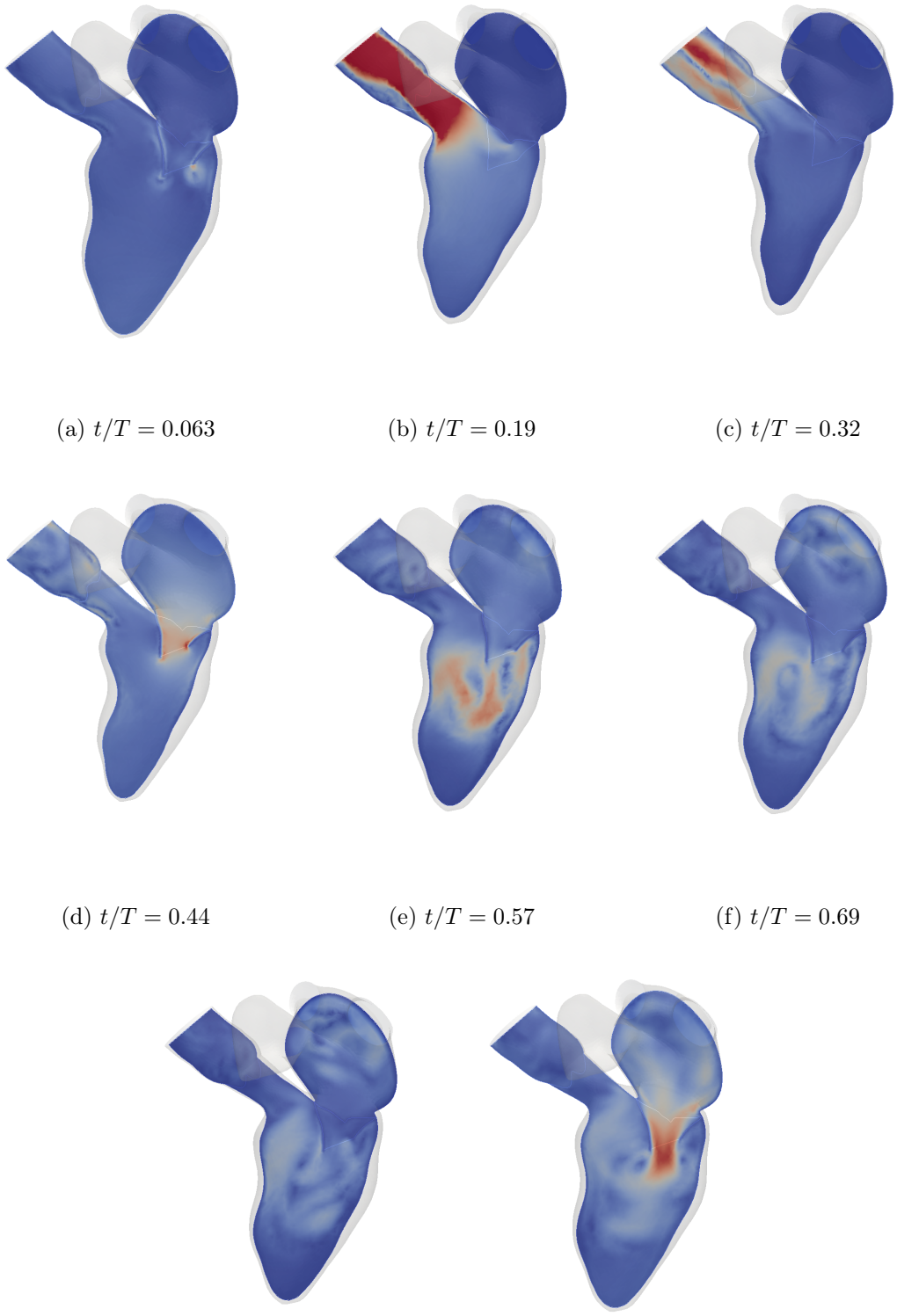

(a) $t/T = 0.063$ (b) $t/T = 0.19$ (c) $t/T = 0.32$

(d) $t/T = 0.44$ (e) $t/T = 0.57$ (f) $t/T = 0.69$

(g) $t/T = 0.81$ (h) $t/T = 0.94$

Figure C.17 – Blood velocity magnitude for case C05_H

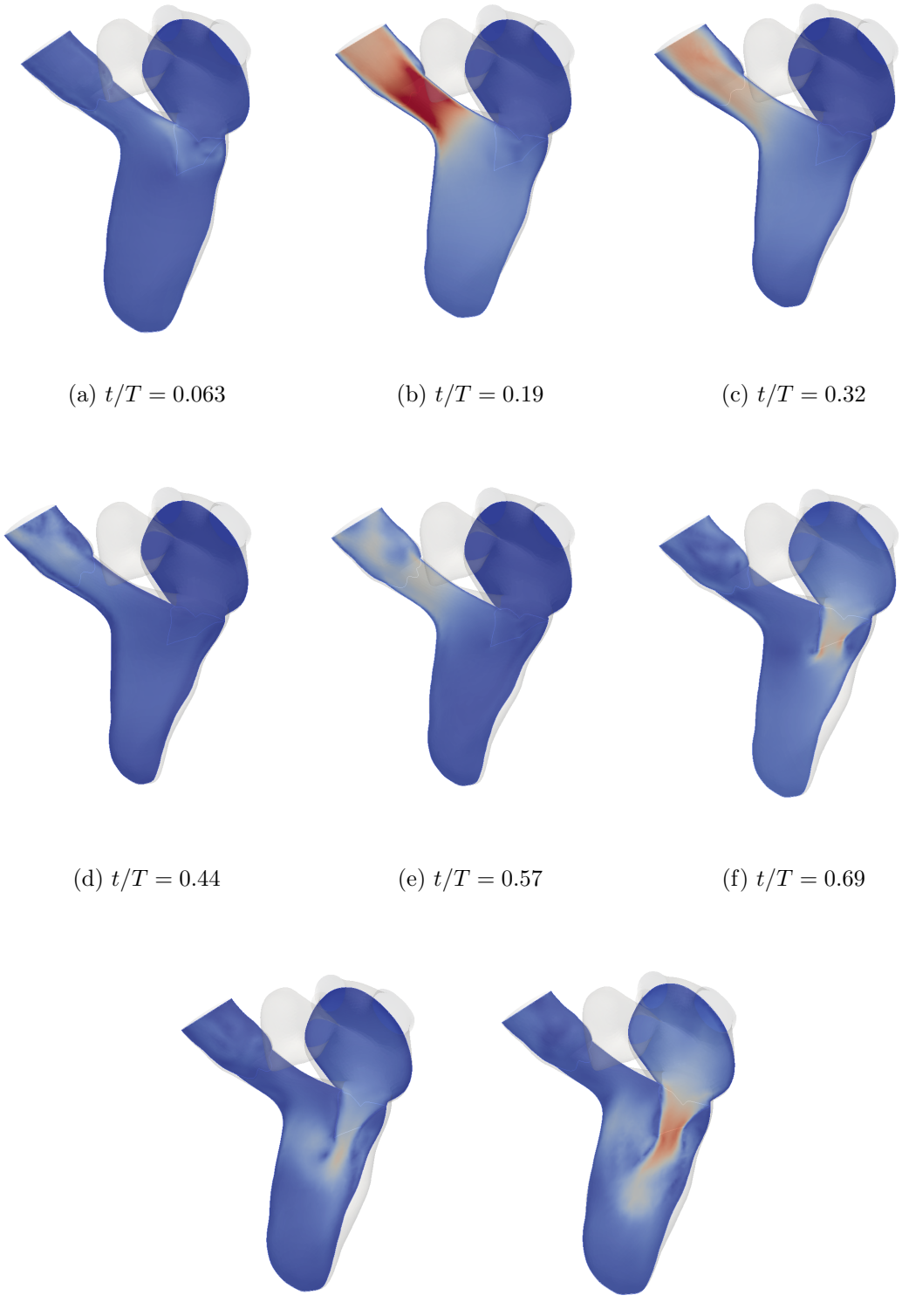

(a) $t/T = 0.063$ (b) $t/T = 0.19$ (c) $t/T = 0.32$

(d) $t/T = 0.44$ (e) $t/T = 0.57$ (f) $t/T = 0.69$

(g) $t/T = 0.81$ (h) $t/T = 0.94$

Figure C.18 – Blood velocity magnitude for case C06_H

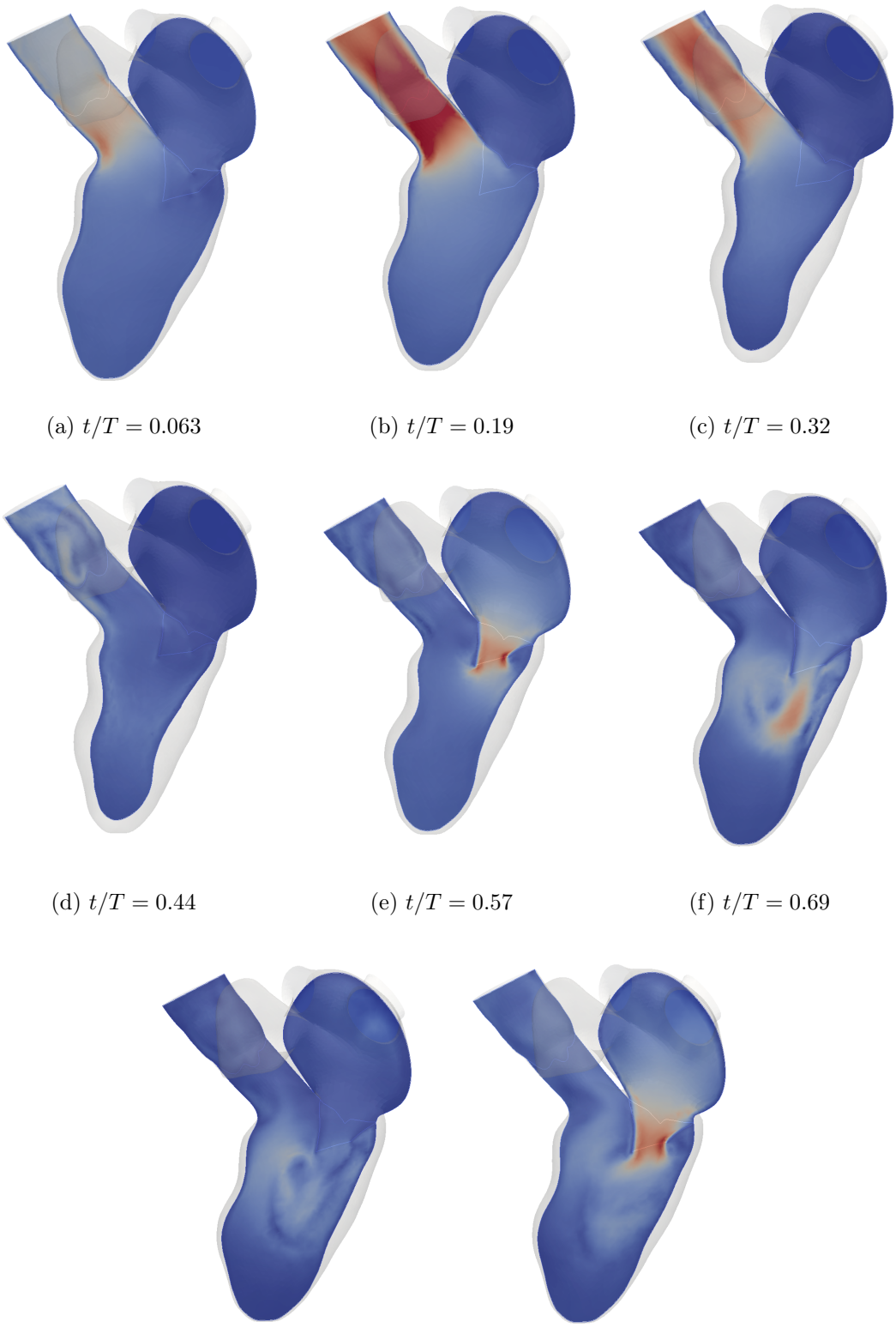

(a) $t/T = 0.063$ (b) $t/T = 0.19$ (c) $t/T = 0.32$

(d) $t/T = 0.44$ (e) $t/T = 0.57$ (f) $t/T = 0.69$

(g) $t/T = 0.81$ (h) $t/T = 0.94$

Figure C.19 – Blood velocity magnitude for case C07_H

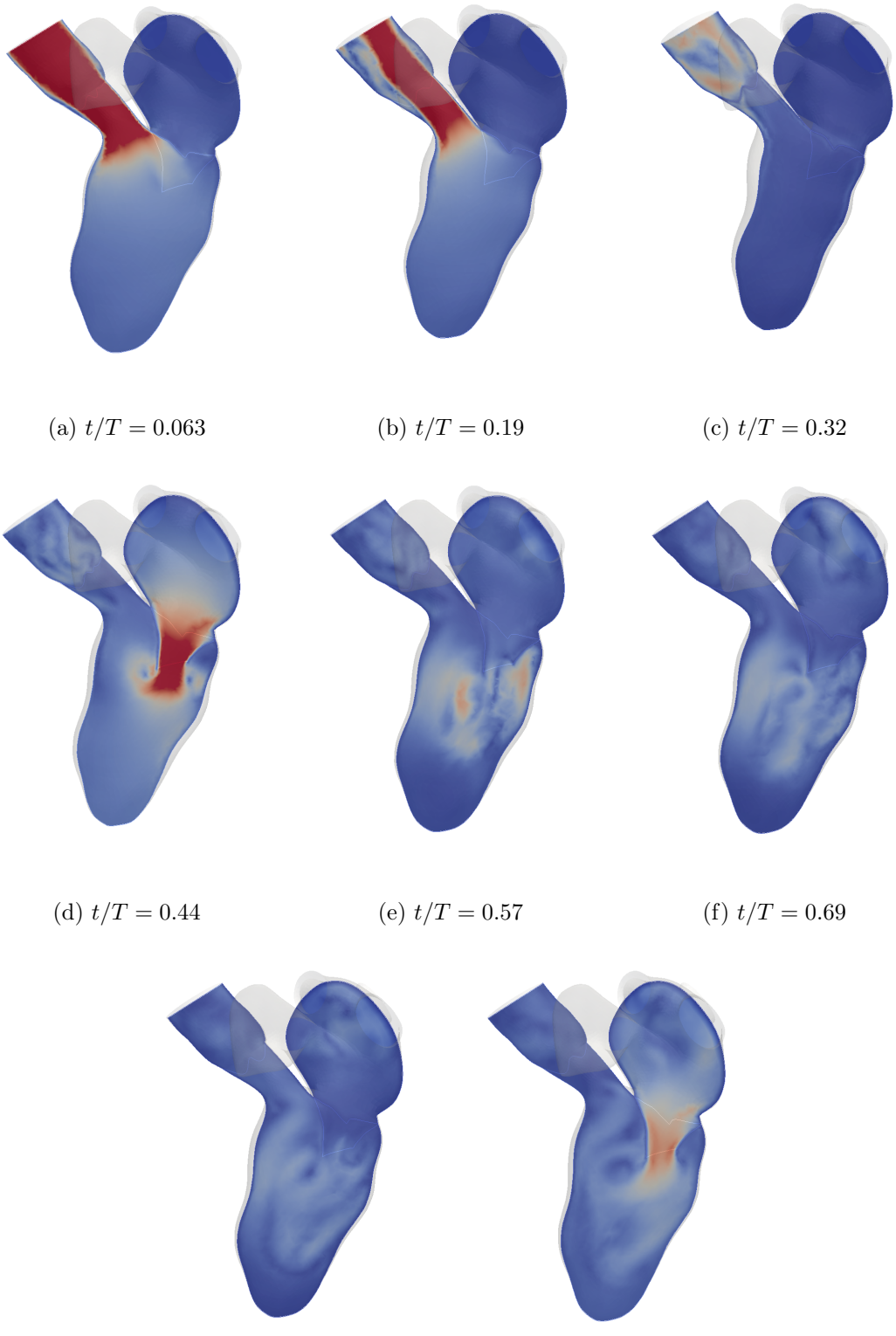

(a) $t/T = 0.063$ (b) $t/T = 0.19$ (c) $t/T = 0.32$

(d) $t/T = 0.44$ (e) $t/T = 0.57$ (f) $t/T = 0.69$

(g) $t/T = 0.81$ (h) $t/T = 0.94$

Figure C.20 – Blood velocity magnitude for case C08_H

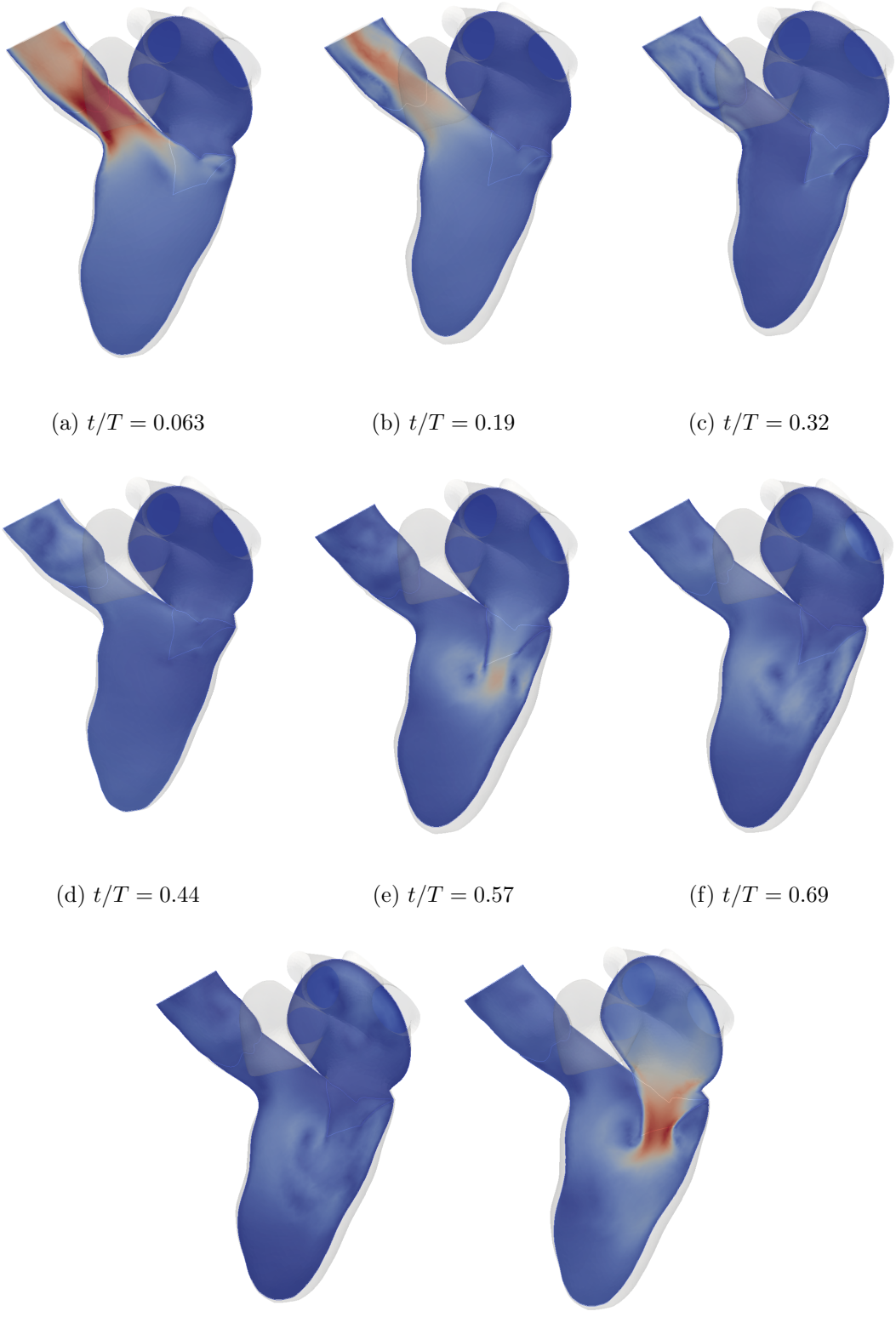

(a) $t/T = 0.063$ (b) $t/T = 0.19$ (c) $t/T = 0.32$

(d) $t/T = 0.44$ (e) $t/T = 0.57$ (f) $t/T = 0.69$

(g) $t/T = 0.81$ (h) $t/T = 0.94$

Figure C.21 – Blood velocity magnitude for case C09_H

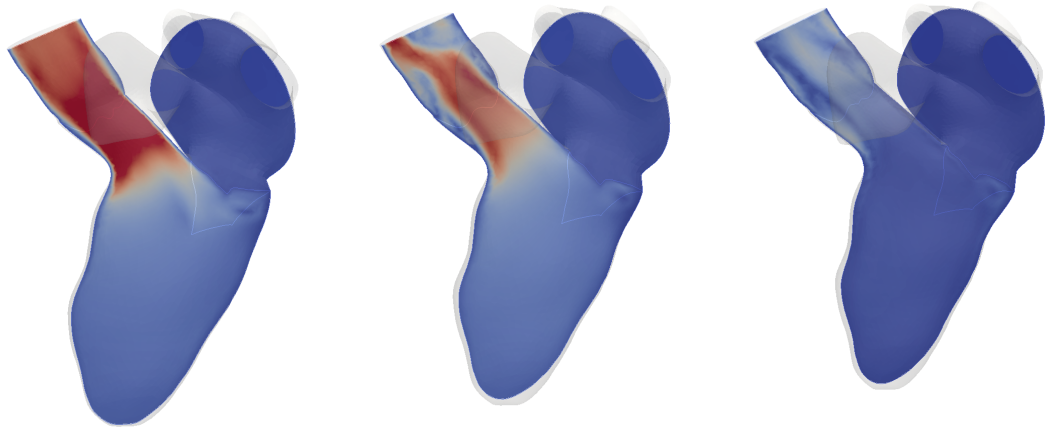

(a) $t/T = 0.063$ (b) $t/T = 0.19$ (c) $t/T = 0.32$

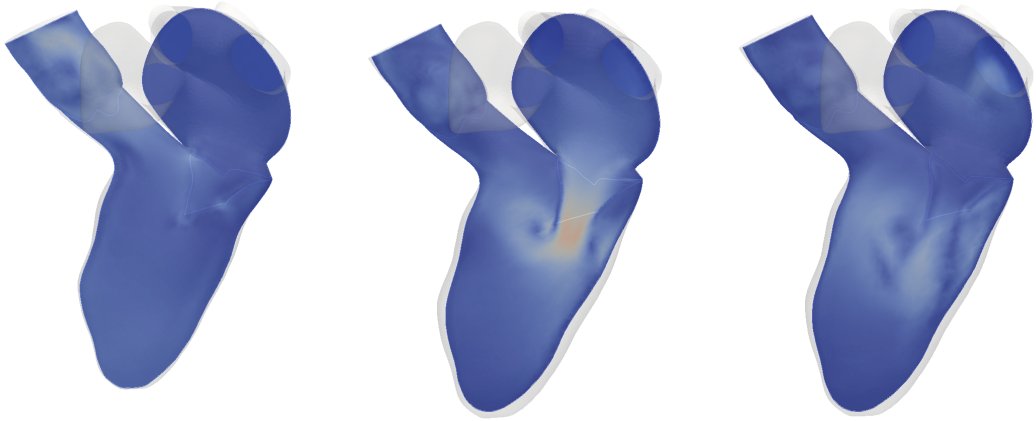

(d) $t/T = 0.44$ (e) $t/T = 0.57$ (f) $t/T = 0.69$

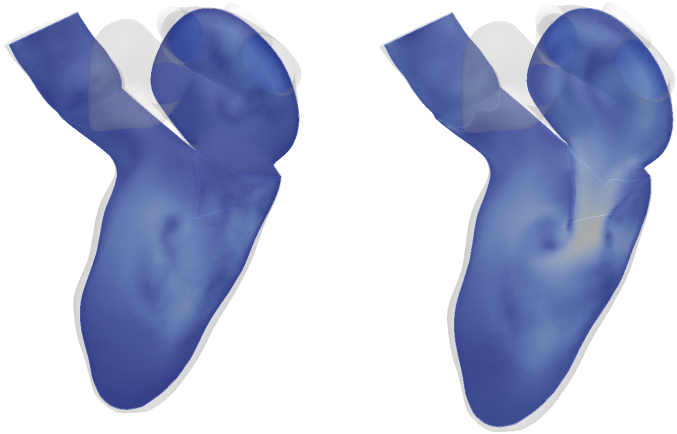

(g) $t/T = 0.81$ (h) $t/T = 0.94$

Figure C.22 – Blood velocity magnitude for case C10_H

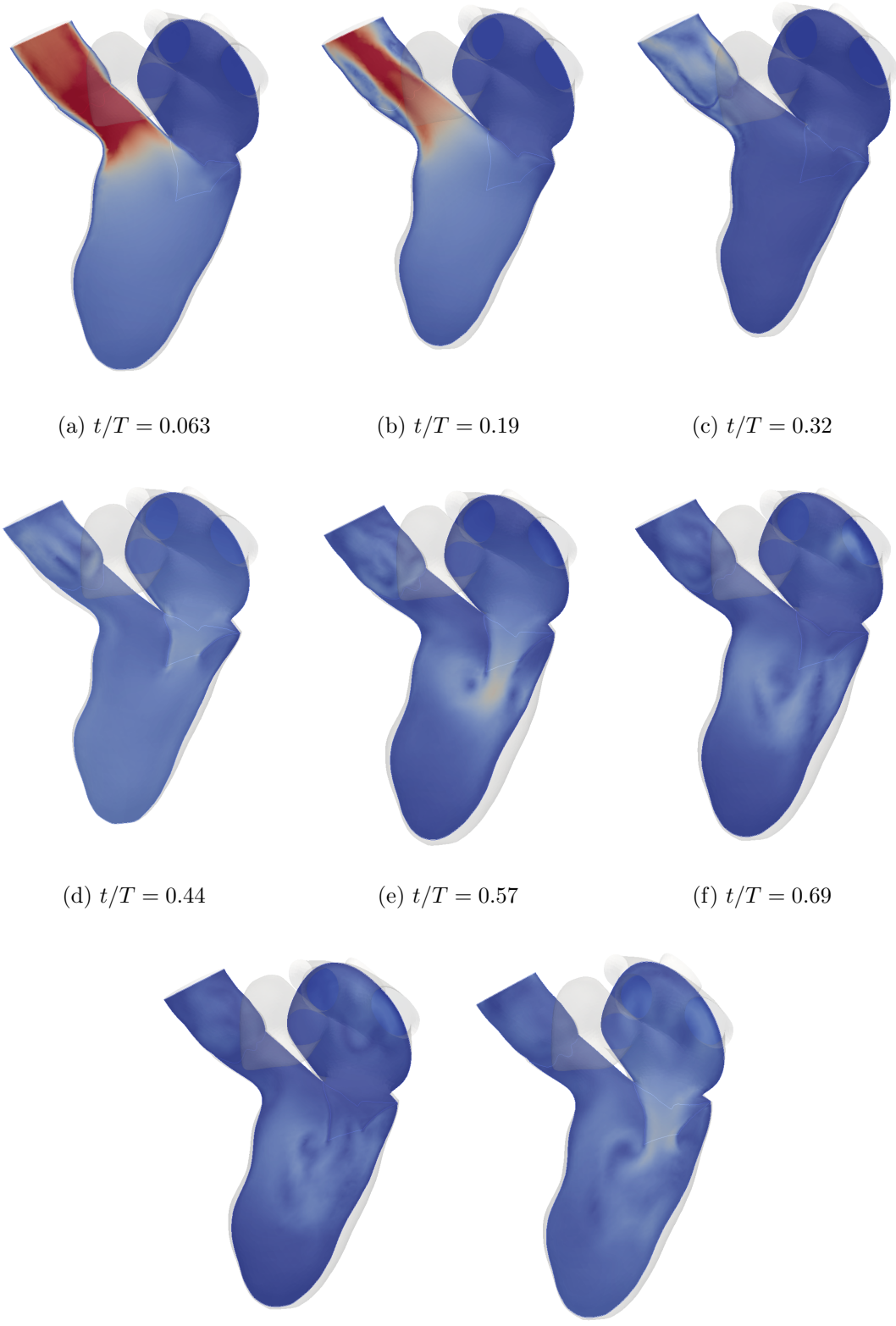

(a) $t/T = 0.063$ (b) $t/T = 0.19$ (c) $t/T = 0.32$

(d) $t/T = 0.44$ (e) $t/T = 0.57$ (f) $t/T = 0.69$

(g) $t/T = 0.81$ (h) $t/T = 0.94$

Figure C.23 – Blood velocity magnitude for case C11_H

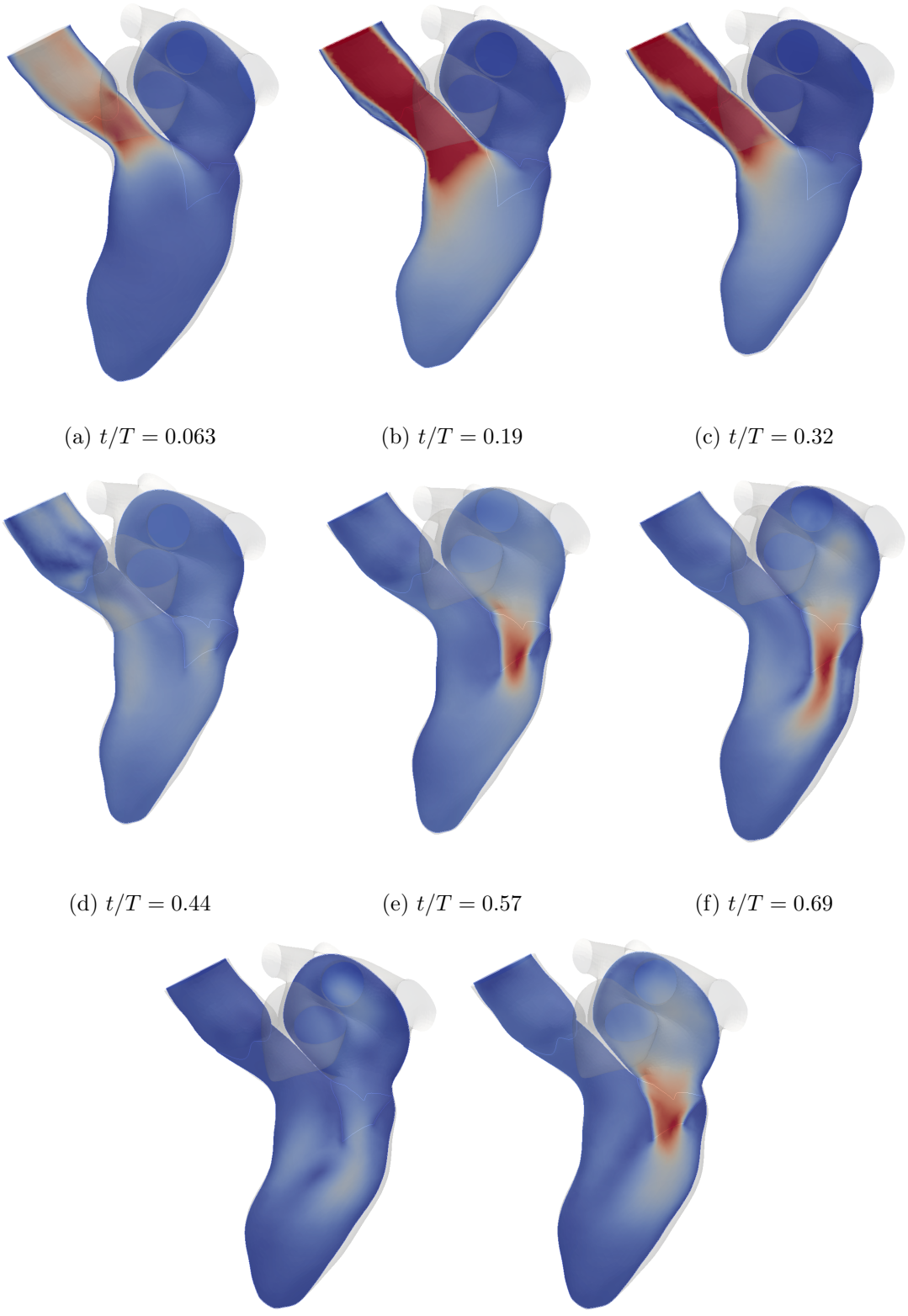

(a) $t/T = 0.063$ (b) $t/T = 0.19$ (c) $t/T = 0.32$

(d) $t/T = 0.44$ (e) $t/T = 0.57$ (f) $t/T = 0.69$

(g) $t/T = 0.81$ (h) $t/T = 0.94$

Figure C.24 – Blood velocity magnitude for case C12_H

C.3 In-silico PISA histograms

C.3.1 Type 1

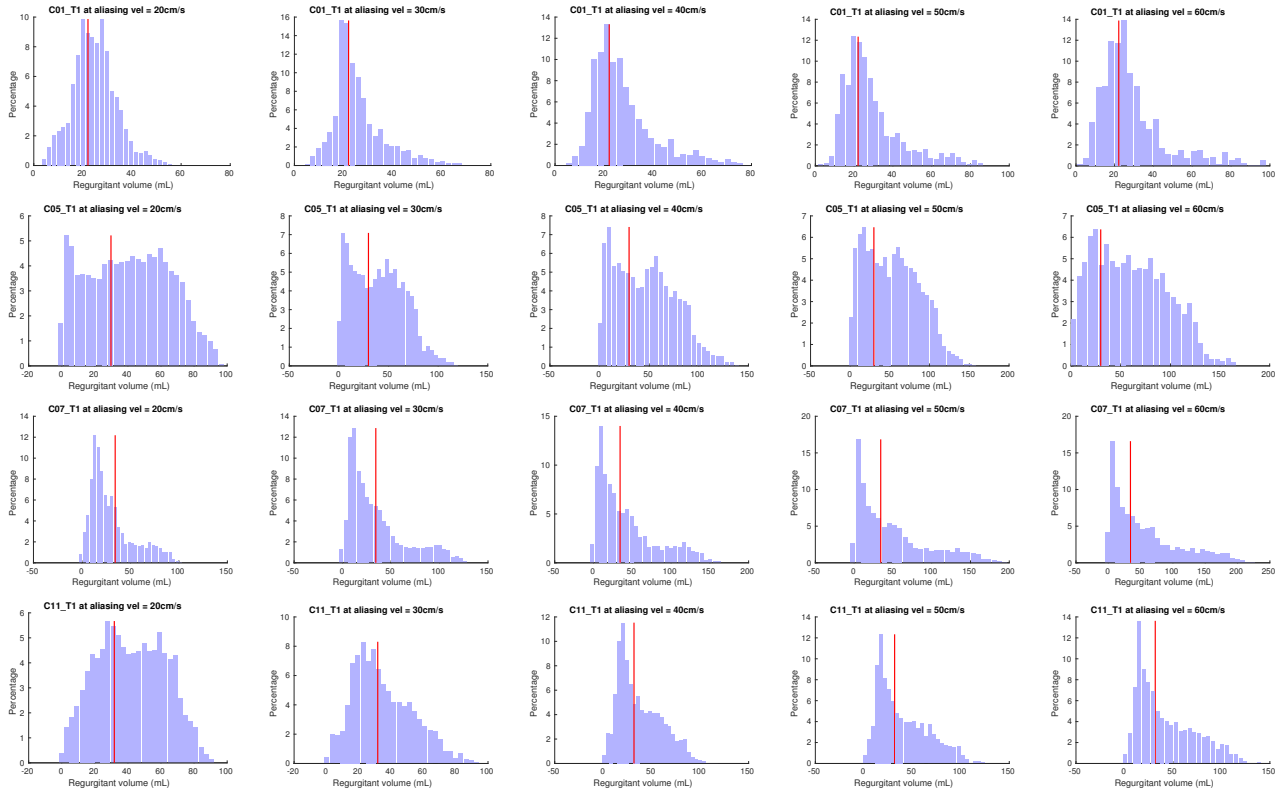

Figure C.25 – PISA Estimates histogram for Type 1 cases

C.3.2 Type 2

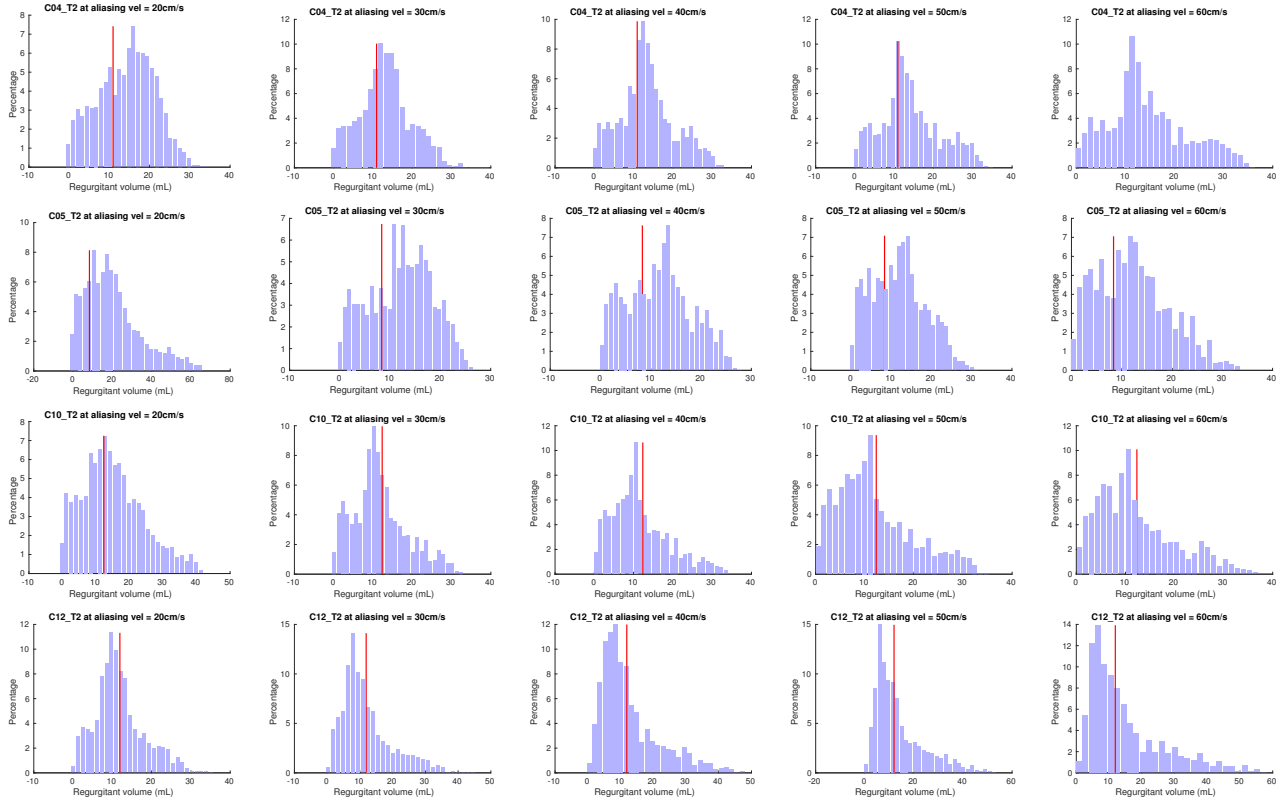

Figure C.26 – PISA Estimates histogram for Type 2 cases

C.3.3 Type 3

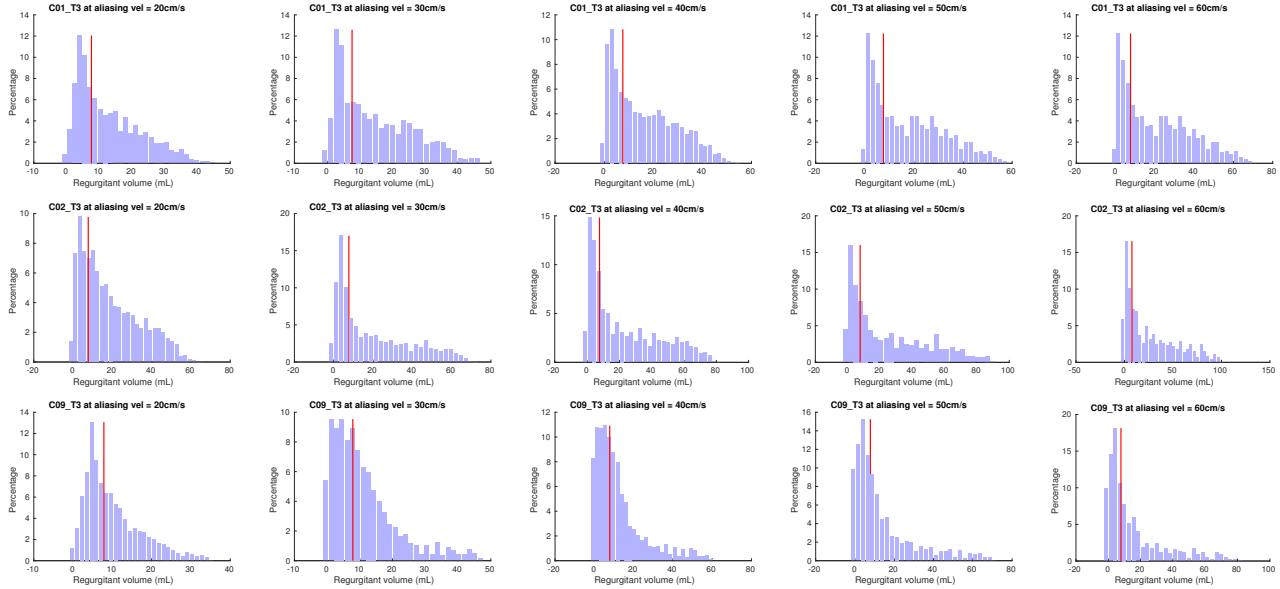

Figure C.27 – PISA Estimates histogram for Type 3 cases

Appendix D
Twisting analysis

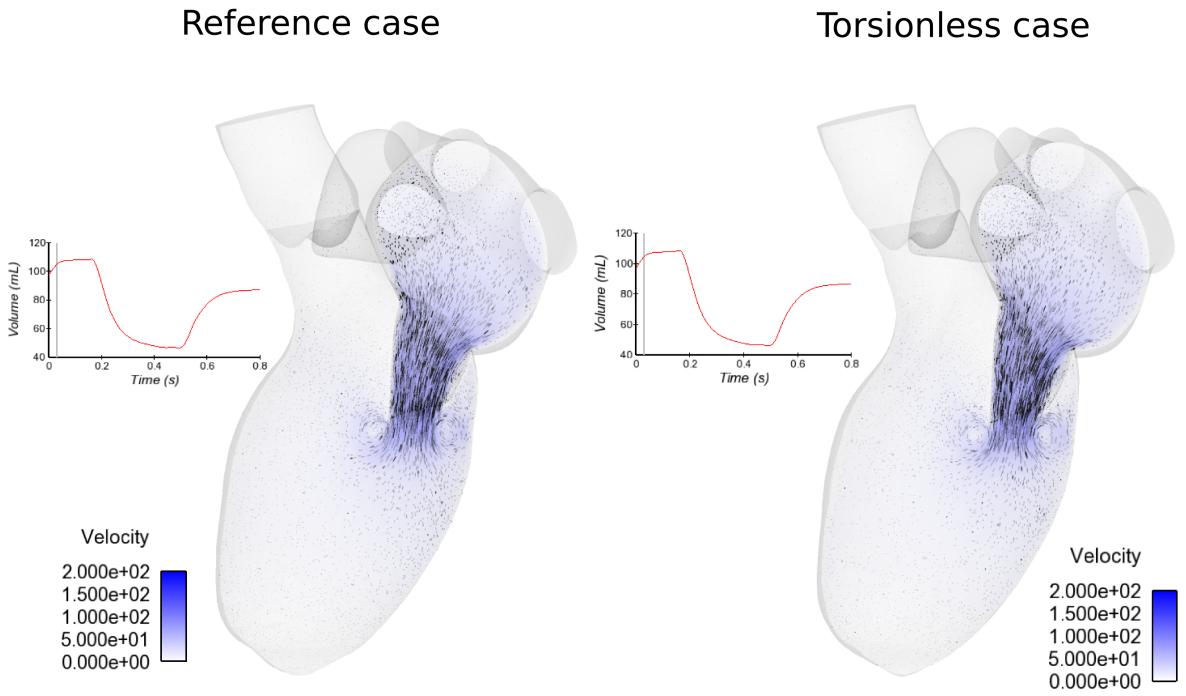

Figure D.1 – Comparison of the velocity fields between the reference case and the torsionless case at $t/T = 0.04$

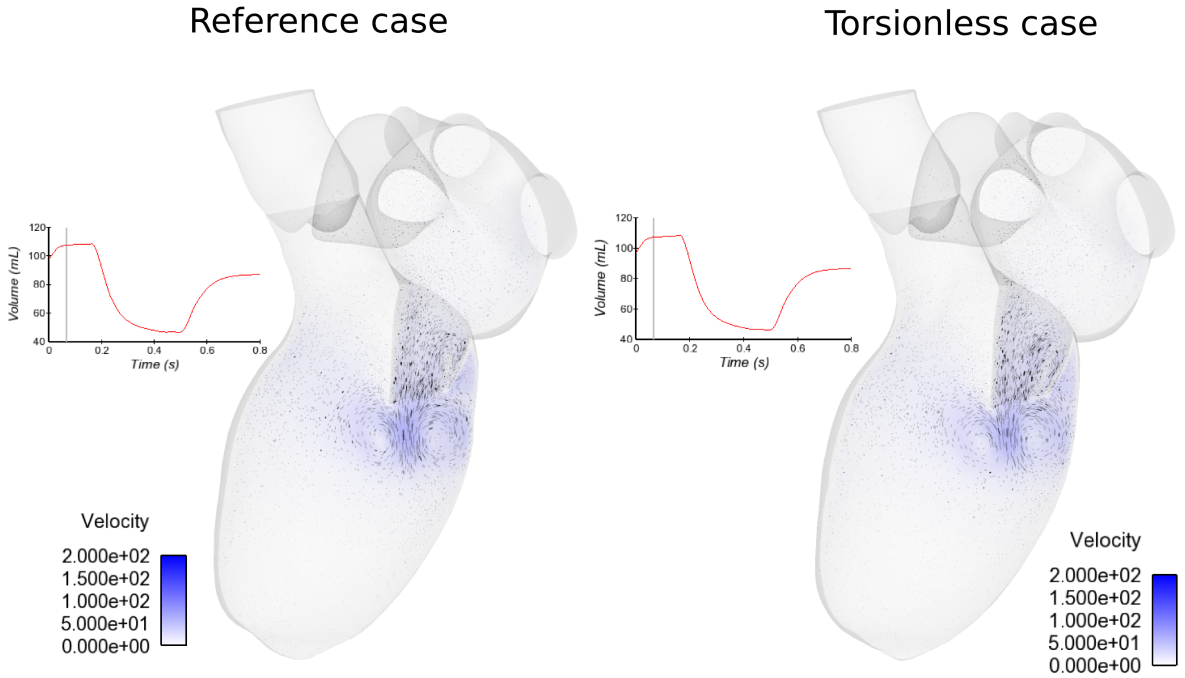

Figure D.2 – Comparison of the velocity fields between the reference case and the torsionless case at $t/T = 0.08$

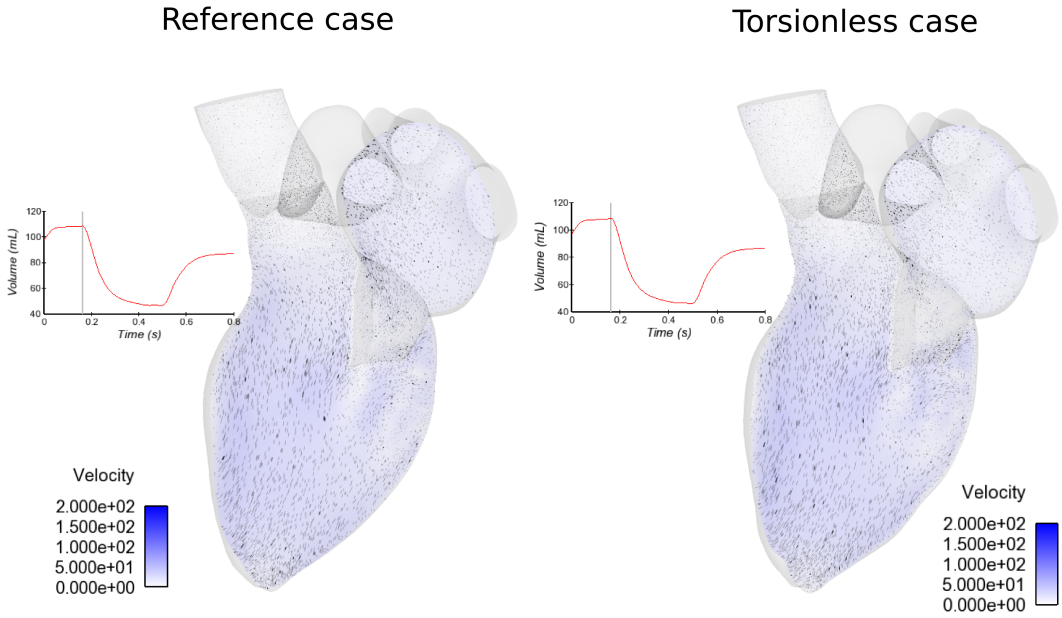

Figure D.3 – Comparison of the velocity fields between the reference case and the torsionless case at $t/T = 0.2$

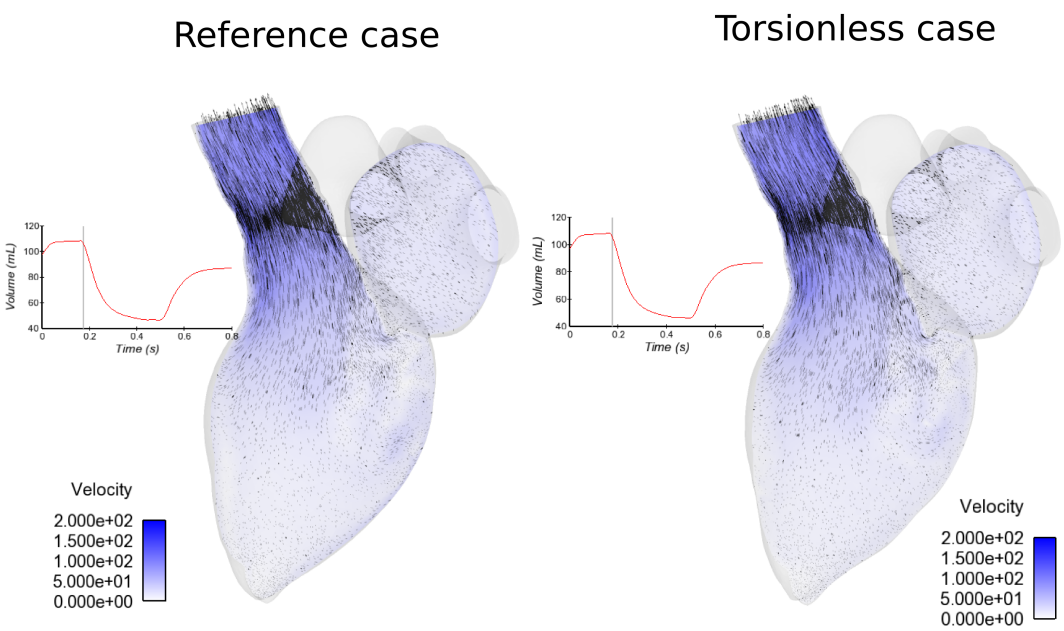

Figure D.4 – Comparison of the velocity fields between the reference case and the torsionless case at $t/T = 0.22$

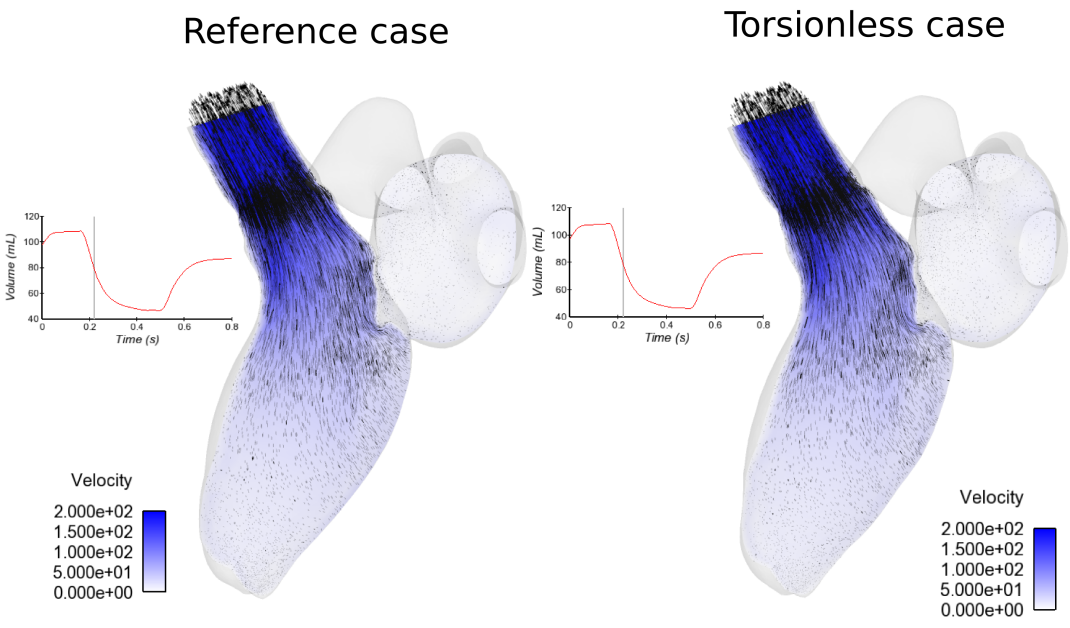

Figure D.5 – Comparison of the velocity fields between the reference case and the torsionless case at $t/T = 0.28$

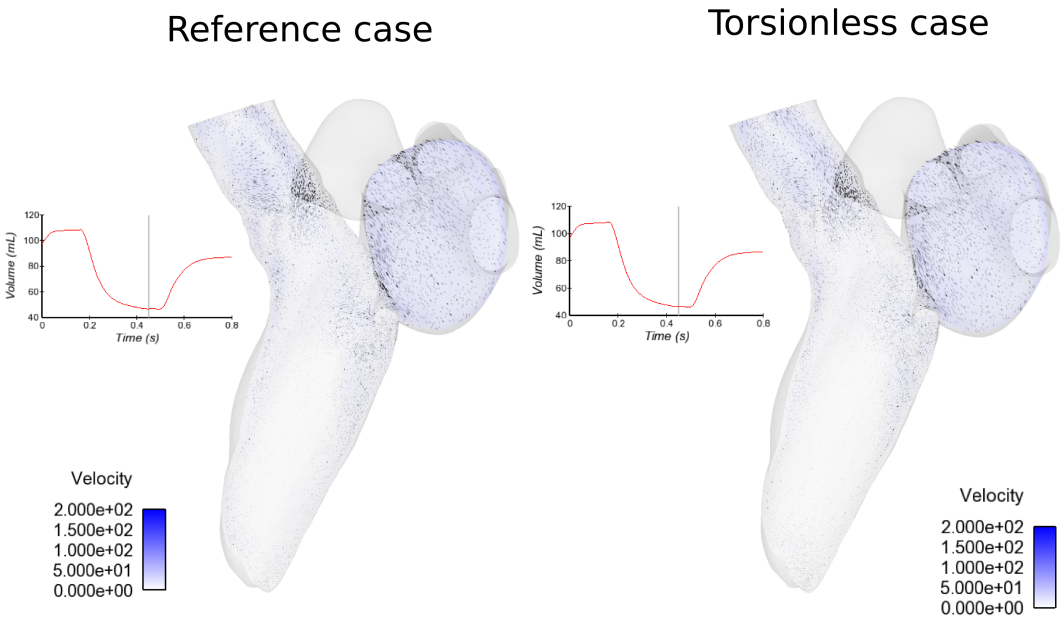

Figure D.6 – Comparison of the velocity fields between the reference case and the torsionless case at $t/T = 0.56$

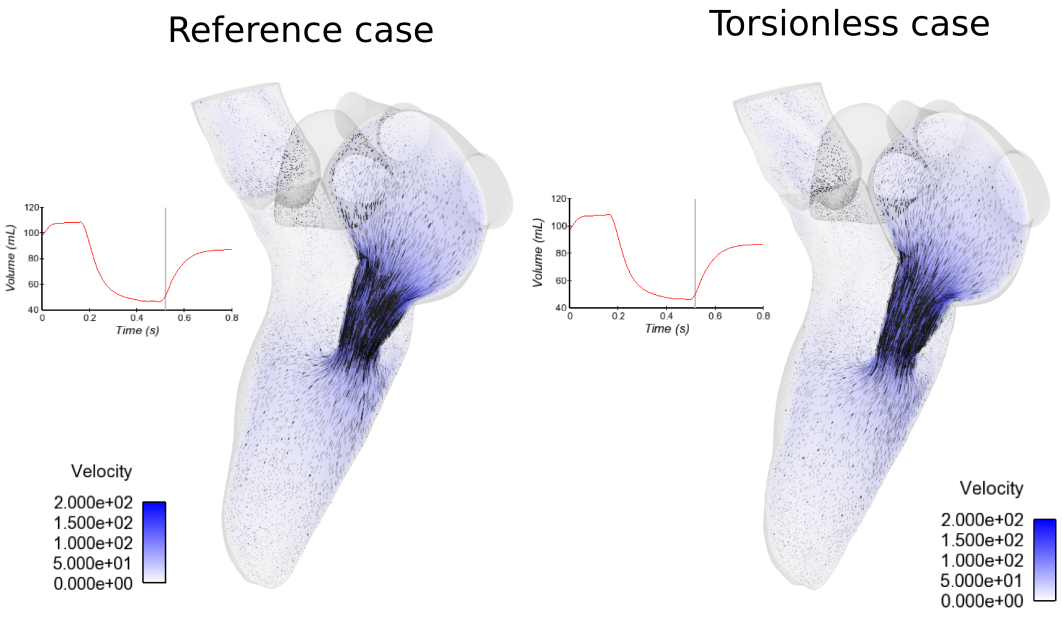

Figure D.7 – Comparison of the velocity fields between the reference case and the torsionless case at $t/T = 0.65$

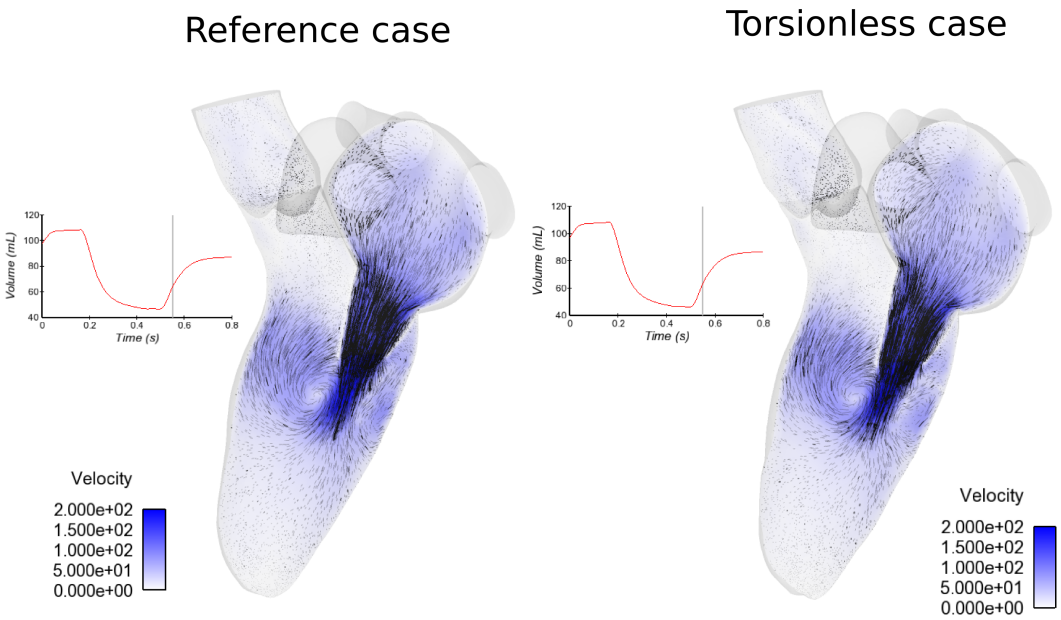

Figure D.8 – Comparison of the velocity fields between the reference case and the torsionless case at $t/T = 0.69$

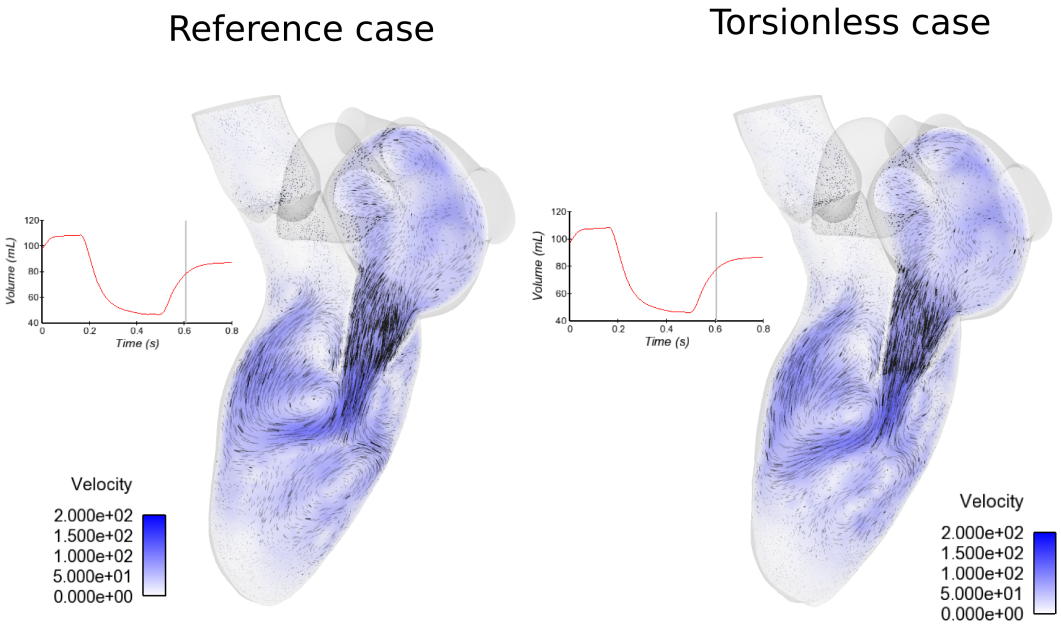

Figure D.9 – Comparison of the velocity fields between the reference case and the torsionless case at $t/T = 0.76$

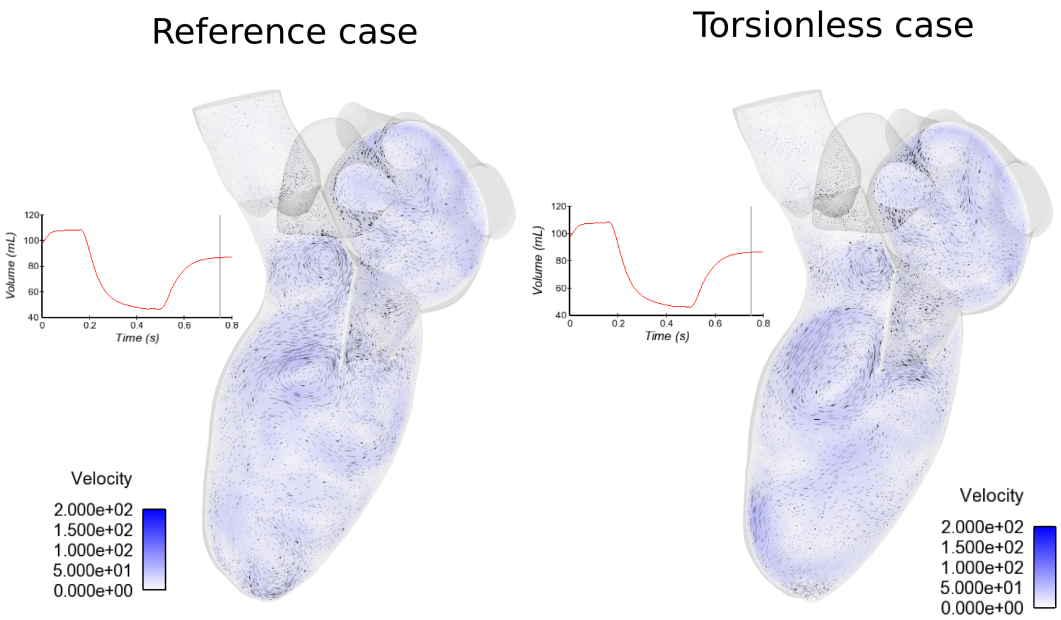

Figure D.10 – Comparison of the velocity fields between the reference case and the torsionless case at $t/T = 0.94$

Appendix E
Appendix 5

E.1 Proof of Proposition 1

We first recall Proposition 1.

Proposition: The stationary points of the functional $J[u]$ satisfy the Euler-Lagrange equation

$$\frac{dF}{du} - \frac{d}{dx}\frac{dF}{du'} = 0.$$

Proof. The proof is obtained by the means of variational calculus

Assume that u minimizes $J[u]$ and let $g_\varepsilon(x) = u(x) + \varepsilon\eta(x)$ be a small perturbation of u that preserves the boundary values and differentiability (ε is small, $\eta|_{\partial\Omega} = 0$ and $\eta(x) \in \mathcal{C}^1$).

The functional J, at g_ε, can be written as:

$$J[g_\varepsilon] = \int_a^b F(x, g_\varepsilon(x), \frac{d}{dx} g_\varepsilon(x))dx$$

The following notations are introduced:

$$\begin{aligned} f'(x) &= \frac{d}{dx} f(x) \\ F_\varepsilon &= F(x, g_\varepsilon(x), g'_\varepsilon(x)) \\ J_\varepsilon &= \int_a^b F_\varepsilon \end{aligned}$$

As u minimizes $J[u]$, J_ε is minimized for $\varepsilon = 0$. This implies:

$$\frac{dJ_\varepsilon}{d\varepsilon}\Big|_{\varepsilon=0} = 0. \tag{E.1}$$

To compute (E.1), the total derivative $\frac{dJ_\varepsilon}{d\varepsilon}$ is first computed:

$$\begin{aligned} \frac{dJ_\varepsilon}{d\varepsilon} &= \frac{d}{d_\varepsilon} \int_a^b F_\varepsilon dx \\ &= \int_a^b \frac{dF_\varepsilon}{d_\varepsilon} dx \\ &= \int_a^b \left[\frac{dF_\varepsilon}{dx}\frac{dx}{d\varepsilon} + \frac{dF_\varepsilon}{dg_\varepsilon}\frac{dg_\varepsilon}{d\varepsilon} + \frac{dF_\varepsilon}{dg'_\varepsilon}\frac{dg'_\varepsilon}{d\varepsilon} \right] dx. \end{aligned}$$

As the following equalities hold:

$$\begin{aligned}\frac{dx}{d\varepsilon} &= 0,\\ \frac{dg_\varepsilon}{d\varepsilon} &= \eta(x),\\ \frac{dg'_\varepsilon}{d\varepsilon} &= \frac{d}{dx}\eta(x) = \eta'(x),\end{aligned}$$

the total derivative can be rewritten as:

$$\frac{dJ_\varepsilon}{d\varepsilon} = \int_a^b \left[\eta(x)\frac{dF_\varepsilon}{dg_\varepsilon} + \eta'(x)\frac{dF_\varepsilon}{dg'_\varepsilon}\right] dx.$$

Evaluating $\frac{dJ_\varepsilon}{d\varepsilon}$ for $\varepsilon = 0$ gives

$$\begin{aligned}\frac{dJ_\varepsilon}{d\varepsilon}\Big|_{\varepsilon=0} &= \int_a^b \left[\eta(x)\frac{dF_\varepsilon}{dg_\varepsilon}\Big|_{\varepsilon=0} + \eta'(x)\frac{dF_\varepsilon}{dg'_\varepsilon}\Big|_{\varepsilon=0}\right] dx\\ &= \int_a^b \left[\eta(x)\frac{dF}{du} + \eta'(x)\frac{dF}{du'}\right] dx.\end{aligned}$$

Integrating by parts, one obtains:

$$\begin{aligned}\frac{dJ_\varepsilon}{d\varepsilon}\Big|_{\varepsilon=0} &= \int_a^b \left[\eta(x)\frac{dF}{du} - \eta(x)\frac{d}{dx}\frac{dF}{du'}\right] dx\\ &= \int_a^b \eta(x)\left[\frac{dF}{du} - \frac{d}{dx}\frac{dF}{du'}\right] dx.\end{aligned}$$

We can therefore conclude that

$$\int_a^b \eta(x)\left[\frac{dF}{du} - \frac{d}{dx}\frac{dF}{du'}\right] dx = 0 \quad \forall \eta(x).$$

Using the fundamental lemma of calculus of variations, this implies

$$\frac{dF}{du} - \frac{d}{dx}\frac{dF}{du'} = 0.$$

This concludes the proof. □

E.2 Proof of Proposition 2

We first recall Proposition 2

Proposition: The stationary points of the functional $J[u]$ satisfy the Euler-Lagrange equation

$$\frac{\partial F}{\partial u} - \sum_i \frac{\partial}{\partial x_i}\frac{\partial F}{\partial u_{x_i}} = 0.$$

Proof. The proof is obtained by the means of variational calculus.

Assume that u minimizes $J[u]$ and let $g_\varepsilon(x_1,...,x_n) = u(x_1,...,x_n) + \varepsilon\eta(x_1,...,x_n)$ be a small perturbation that preserves the boundary values and differentiability (ε is small, $\eta|_{\partial\Omega} = 0$ and $\eta(x_1,...,x_n) \in \mathcal{C}^1$).

The functional J, at g_ε, can be written as:

$$J[g_\varepsilon] = \int_\Omega F(x_1,...,x_n,g_\varepsilon,\frac{\partial g_\varepsilon}{\partial x_1},...,\frac{\partial g_\varepsilon}{\partial x_n})d\Omega$$

The following notation is introduced:

$$\begin{aligned} f_{x_i} &= \frac{\partial}{\partial x_i} f(x) \\ F_\varepsilon &= F(x_1,...,x_n,g_\varepsilon, g_{\varepsilon,x_1},...,g_{\varepsilon,x_n}) \\ J_\varepsilon &= \int_\Omega F_\varepsilon d\Omega \end{aligned}$$

As u minimizes $J[u]$, J_ε is minimized for $\varepsilon = 0$. This implies:

$$\frac{dJ_\varepsilon}{d\varepsilon}\Big|_{\varepsilon=0} = 0. \tag{E.2}$$

To compute (E.2), the total derivative $\frac{dJ_\varepsilon}{d\varepsilon}$ is first computed:

$$\begin{aligned} \frac{dJ_\varepsilon}{d\varepsilon} &= \frac{d}{d_\varepsilon}\int_\Omega F_\varepsilon \Omega \\ &= \int_\Omega \frac{dF_\varepsilon}{d_\varepsilon} d\Omega \\ &= \int_\Omega \left[\sum_i \frac{\partial F_\varepsilon}{\partial x_i}\frac{\partial x_i}{\partial \varepsilon}\right] + \left[\frac{\partial F_\varepsilon}{\partial g_\varepsilon}\frac{\partial g_\varepsilon}{\partial \varepsilon}\right] + \left[\sum_i \frac{\partial F_\varepsilon}{\partial g_{\varepsilon,x_i}}\frac{\partial g_{\varepsilon,x_i}}{\partial \varepsilon}\right] d\Omega. \end{aligned}$$

Ahe following equalities hold:

$$\begin{aligned} \frac{\partial x_i}{\partial \varepsilon} &= 0 \quad \forall i \in [1,n], \\ \frac{\partial g_\varepsilon}{\partial \varepsilon} &= \eta, \\ \frac{\partial g_{\varepsilon,x_i}}{\partial \varepsilon} &= \frac{\partial \eta}{\partial x_i}, \end{aligned}$$

the total derivative can be rewritten as:

$$\frac{dJ_\varepsilon}{d\varepsilon} = \int_\Omega \eta\frac{\partial F_\varepsilon}{\partial g_\varepsilon} + \left[\sum_i \frac{\partial \eta}{\partial x_i}\frac{\partial F_\varepsilon}{\partial g_{\varepsilon,x_i}}\right] d\Omega.$$

Evaluating $\frac{dJ_\varepsilon}{d\varepsilon}$ for $\varepsilon = 0$ gives

$$\begin{aligned}\frac{dJ_\varepsilon}{d\varepsilon}\Big|_{\varepsilon=0} &= \int_\Omega \eta \frac{\partial F_\varepsilon}{\partial g_\varepsilon}\Big|_{\varepsilon=0} + \left[\sum_i \frac{\partial \eta}{\partial x_i}\frac{\partial F_\varepsilon}{\partial g_{\varepsilon,x_i}}\Big|_{\varepsilon=0}\right] d\Omega \\ &= \int_\Omega \eta \frac{\partial F}{\partial u} + \left[\sum_i \frac{\partial \eta}{\partial x_i}\frac{\partial F}{\partial u_{x_i}}\right] d\Omega.\end{aligned}$$

Integrating by parts, one obtains:

$$\begin{aligned}\frac{dJ_\varepsilon}{d\varepsilon}\Big|_{\varepsilon=0} &= \int_\Omega \left[\eta \frac{\partial F}{\partial u} - \sum_i \eta \frac{\partial}{\partial x_i}\frac{\partial F}{\partial u_{x_i}}\right] d\Omega \\ &= \int_\Omega \eta \left[\frac{\partial F}{\partial u} - \sum_i \frac{\partial}{\partial x_i}\frac{\partial F}{\partial u_{x_i}}\right] d\Omega\end{aligned}$$

We can therefore conclude that

$$\int_\Omega \eta \left[\frac{\partial F}{\partial u} - \sum_i \frac{\partial}{\partial x_i}\frac{\partial F}{\partial u_{x_i}}\right] d\Omega = 0 \quad \forall \eta(x_1, \cdots, x_n).$$

Using the fundamental lemma of variational calculus, this implies:

$$\frac{\partial F}{\partial u} - \sum_i \frac{\partial}{\partial x_i}\frac{\partial F}{\partial u_{x_i}} = 0$$

This concludes the proof. □

E.3 Proof of Lemma 1-4

Proof of Lemma 1.
Defining $F = (\mathbf{X} \cdot \mathbf{v_r} - V_r)^2$, one can write the E-L equations associated to $G_1[\mathbf{X}]$:

$$\begin{aligned}\frac{\partial F}{\partial X_1} - \frac{\partial}{\partial x_1}\frac{\partial F}{\partial X_{1x_1}} - \frac{\partial}{\partial x_2}\frac{\partial F}{\partial X_{1x_2}} = 0 \quad \text{in } \Omega_P \\ \frac{\partial F}{\partial X_2} - \frac{\partial}{\partial x_1}\frac{\partial F}{\partial X_{2x_1}} - \frac{\partial}{\partial x_2}\frac{\partial F}{\partial X_{2x_2}} = 0 \quad \text{in } \Omega_P\end{aligned}$$

By expanding $\mathbf{X}$ in its two components, one can rewrite F:

$$F = \left(X_1 \left(\mathbf{v_r} \cdot \mathbf{v_1}\right) + X_2 \left(\mathbf{v_r} \cdot \mathbf{v_2}\right) - V_r\right)^2$$

First, one can notice that:

$$\frac{\partial F}{\partial X_{1x_1}} = 0, \quad \frac{\partial F}{\partial X_{1x_2}} = 0, \quad \frac{\partial F}{\partial X_{2x_1}} = 0, \quad \frac{\partial F}{\partial X_{2x_2}} = 0.$$

The remaining terms of the E-L system can be calculated as follows:

Calculation of $\frac{\partial F}{\partial X_1}$

$$\begin{aligned}\frac{\partial F}{\partial X_1} &= \frac{\partial}{\partial X_1}\left(X_1\left(\mathbf{v_r}\cdot\mathbf{v_1}\right)+X_2\left(\mathbf{v_r}\cdot\mathbf{v_2}\right)-V_r\right)^2\\ &= 2\left(\mathbf{v_r}\cdot\mathbf{v_1}\right)\left(X_1\left(\mathbf{v_r}\cdot\mathbf{v_1}\right)+X_2\left(\mathbf{v_r}\cdot\mathbf{v_2}\right)-V_r\right)\\ &= 2\left(X_1\left(\mathbf{v_r}\cdot\mathbf{v_1}\right)^2+X_2\left(\mathbf{v_r}\cdot\mathbf{v_1}\right)\left(\mathbf{v_r}\cdot\mathbf{v_2}\right)-V_r\left(\mathbf{v_r}\cdot\mathbf{v_1}\right)\right)\end{aligned}$$

Calculation of $\frac{\partial F}{\partial X_2}$

$$\begin{aligned}\frac{\partial F}{\partial X_2} &= \frac{\partial}{\partial X_2}\left(X_1\left(\mathbf{v_r}\cdot\mathbf{v_1}\right)+X_2\left(\mathbf{v_r}\cdot\mathbf{v_2}\right)-V_r\right)^2\\ &= 2\left(\mathbf{v_r}\cdot\mathbf{v_2}\right)\left(X_1\left(\mathbf{v_r}\cdot\mathbf{v_1}\right)+X_2\left(\mathbf{v_r}\cdot\mathbf{v_2}\right)-V_r\right)\\ &= 2\left(X_1\left(\mathbf{v_r}\cdot\mathbf{v_1}\right)\left(\mathbf{v_r}\cdot\mathbf{v_2}\right)+X_2\left(\mathbf{v_r}\cdot\mathbf{v_2}\right)^2-V_r\left(\mathbf{v_r}\cdot\mathbf{v_2}\right)\right)\end{aligned}$$

The E-L system can therefore be written as:

$$\begin{aligned}X_1\left(\mathbf{v_r}\cdot\mathbf{v_1}\right)^2+X_2\left(\mathbf{v_r}\cdot\mathbf{v_1}\right)\left(\mathbf{v_r}\cdot\mathbf{v_2}\right)-V_r\left(\mathbf{v_r}\cdot\mathbf{v_1}\right)=0 \quad \text{in } \Omega_P\\ X_1\left(\mathbf{v_r}\cdot\mathbf{v_1}\right)\left(\mathbf{v_r}\cdot\mathbf{v_2}\right)+X_2\left(\mathbf{v_r}\cdot\mathbf{v_2}\right)^2-V_r\left(\mathbf{v_r}\cdot\mathbf{v_2}\right)=0 \quad \text{in } \Omega_P\end{aligned}$$

Let θ be the angle $\mathbf{v_r}$ and $\mathbf{v_1}$, and θ_2 be the angle between $\mathbf{v_r}$ and $\mathbf{v_2}$, one has:

$$\begin{aligned}\mathbf{v_r}\cdot\mathbf{v_1} &= \|\mathbf{v_r}\|\,\|\mathbf{v_1}\|\cos(\theta)=\cos(\theta)\\ \mathbf{v_r}\cdot\mathbf{v_2} &= \|\mathbf{v_r}\|\,\|\mathbf{v_2}\|\cos(\theta_2)=\cos(\theta_2)=\cos(\pi/2-\theta)=\sin(\theta)\end{aligned}$$

As a result, the E-L system associated to $G_1[\mathbf{X}]$ can be rewritten as:

$$\begin{aligned}\cos(\theta)^2X_1+\cos(\theta)\sin(\theta)X_2=\cos(\theta)V_r \quad \text{in } \Omega_P\\ \cos(\theta)\sin(\theta)X_1+\sin(\theta)^2X_2=\sin(\theta)V_r \quad \text{in } \Omega_P\end{aligned}$$

This completes the proof. □

Proof of Lemma 2.
Defining $F=(\boldsymbol{\nabla}\cdot\mathbf{X})^2$ and expanding the divergence operator, one has:

$$F=\left(\frac{\partial X_1}{\partial x_1}+\frac{\partial X_2}{\partial x_2}\right)^2 \tag{E.3}$$

By noticing that:

$$\frac{\partial F}{\partial X_1}=0,\quad \frac{\partial F}{\partial X_2}=0,\quad \frac{\partial F}{\partial X_{1x_2}}=0,\quad \frac{\partial F}{\partial X_{2x_1}}=0,$$

we can write the E-L system of equations associated to $G_2[\mathbf{X}]$ as:

$$-\frac{\partial}{\partial x_1}\frac{\partial F}{\partial X_{1x_1}} = 0 \quad \text{in } \Omega_P$$
$$-\frac{\partial}{\partial x_2}\frac{\partial F}{\partial X_{2x_2}} = 0 \quad \text{in } \Omega_P$$

The two terms of the E-L system can be calculated as follows:

Calculation of $\frac{\partial}{\partial x_1}\frac{\partial F}{\partial X_{1x_1}}$

$$\begin{aligned}\frac{\partial}{\partial x_1}\frac{\partial F}{\partial X_{1x_1}} &= \frac{\partial}{\partial x_1}\frac{\partial}{\partial X_{1x_1}}\left(\frac{\partial X_1}{\partial x_1}+\frac{\partial X_2}{\partial x_2}\right)^2 \\ &= \frac{\partial}{\partial x_1}2\left(\frac{\partial X_1}{\partial x_1}+\frac{\partial X_2}{\partial x_2}\right) \\ &= 2\left(\frac{\partial^2 X_1}{\partial x_1^2}+\frac{\partial^2 X_2}{\partial x_1 \partial x_2}\right)\end{aligned}$$

Calculation of $\frac{\partial}{\partial x_2}\frac{\partial F}{\partial X_{2x_2}}$

$$\begin{aligned}\frac{\partial}{\partial x_2}\frac{\partial F}{\partial X_{2x_2}} &= \frac{\partial}{\partial x_2}\frac{\partial}{\partial X_{2x_2}}\left(\frac{\partial X_1}{\partial x_1}+\frac{\partial X_2}{\partial x_2}\right)^2 \\ &= \frac{\partial}{\partial x_2}2\left(\frac{\partial X_1}{\partial x_1}+\frac{\partial X_2}{\partial x_2}\right) \\ &= 2\left(\frac{\partial^2 X_1}{\partial x_1 \partial x_2}+\frac{\partial^2 X_2}{\partial^2 x_2}\right)\end{aligned}$$

As a result, the E-L equations associated to $G_2[\mathbf{X}]$ can be written as:

$$-\left(\frac{\partial^2 X_1}{\partial x_1^2}+\frac{\partial^2 X_2}{\partial x_1 \partial x_2}\right) = 0 \quad \text{in } \Omega_P$$
$$-\left(\frac{\partial^2 X_1}{\partial x_1 \partial x_2}+\frac{\partial^2 X_2}{\partial x_2^2}\right) = 0 \quad \text{in } \Omega_P$$

This completes the proof. □

Proof of Lemma 3.
Defining $F = \|\mathbf{X} - \mathbf{V_P}\|_2^2$ and expanding $\mathbf{X}$ and $\mathbf{V_P}$, we have:

$$\begin{aligned}F(...) &= \left(\sqrt{(X_1 - \mathbf{V_P}\cdot\mathbf{v_1})^2 + (X_2 - \mathbf{V_P}\cdot\mathbf{v_2})^2}\right)^2 \\ &= (X_1 - \mathbf{V_P}\cdot\mathbf{v_1})^2 + (X_2 - \mathbf{V_P}\cdot\mathbf{v_2})^2\end{aligned}$$

By noting that:

$$\frac{\partial F}{\partial X_{1_{x_1}}} = 0, \quad \frac{\partial F}{\partial X_{1_{x_2}}} = 0, \quad \frac{\partial F}{\partial X_{2_{x_1}}} = 0, \quad \frac{\partial F}{\partial X_{2_{x_2}}} = 0,$$

we can rewrite the E-L system of equations associated to $G_3[\mathbf{X}]$ as:

$$\begin{aligned} \frac{\partial F}{\partial X_1} &= 0 \quad \text{in } \partial\Omega_P \\ \frac{\partial F}{\partial X_2} &= 0 \quad \text{in } \partial\Omega_P \end{aligned}$$

The E-L terms can be computed as:

Calculation of $\frac{\partial F}{\partial X_1}$

$$\begin{aligned} \frac{\partial F}{\partial X_1} &= \frac{\partial}{\partial X_1}\left((X_1 - \mathbf{V_P}\cdot\mathbf{v_1})^2 + (X_2 - \mathbf{V_P}\cdot\mathbf{v_2})^2\right) \\ &= \frac{\partial}{\partial X_1}(X_1 - \mathbf{V_P}\cdot\mathbf{v_1})^2 \\ &= 2\,(X_1 - \mathbf{V_P}\cdot\mathbf{v_1}) \end{aligned}$$

Calculation of $\frac{\partial F}{\partial X_2}$

$$\begin{aligned} \frac{\partial F}{\partial X_2} &= \frac{\partial}{\partial X_2}\left((X_1 - \mathbf{V_P}\cdot\mathbf{v_1})^2 + (X_2 - \mathbf{V_P}\cdot\mathbf{v_2})^2\right) \\ &= \frac{\partial}{\partial X_2}(X_2 - \mathbf{V_P}\cdot\mathbf{v_2})^2 \\ &= 2\,(X_2 - \mathbf{V_P}\cdot\mathbf{v_2}) \end{aligned}$$

As a result, the E-L system of equations associated to $G_3[\mathbf{X}]$ is written:

$$X_1 = \mathbf{V_P}\cdot\mathbf{v_1} \quad \text{in } \partial\Omega_P \tag{E.4}$$
$$X_2 = \mathbf{V_P}\cdot\mathbf{v_2} \quad \text{in } \partial\Omega_P \tag{E.5}$$

This completes the proof. □

Proof of Lemma 4.
Defining $F = \|\nabla\mathbf{X}\|_2^2$, we can write F as:

$$F(...) = \|\nabla\mathbf{X}\|_2^2 \tag{E.6}$$
$$= \frac{\partial {X_1}^2}{\partial x_1} + \frac{\partial {X_1}^2}{\partial x_2} + \frac{\partial {X_2}^2}{\partial x_1} + \frac{\partial {X_2}^2}{\partial x_2} \tag{E.7}$$

By noticing first:

$$\frac{\partial F}{\partial X_1} = 0, \quad \frac{\partial F}{\partial X_2} = 0,$$

we can write the E-L system of equations associated to $G_4[\mathbf{X}]$ as:

$$\begin{aligned} -\frac{\partial}{\partial x_1}\frac{\partial F}{\partial X_{1x_1}} - \frac{\partial}{\partial x_2}\frac{\partial F}{\partial X_{1x_2}} = 0 \quad \text{in } \Omega_P \\ -\frac{\partial}{\partial x_1}\frac{\partial F}{\partial X_{2x_1}} - \frac{\partial}{\partial x_2}\frac{\partial F}{\partial X_{2x_2}} = 0 \quad \text{in } \Omega_P \end{aligned}$$

The terms are calculated as follows:

Calculation of $\frac{\partial}{\partial x_1}\frac{\partial F}{\partial X_{1x_1}}$

$$\begin{aligned} \frac{\partial F}{\partial X_{1x_1}} &= \frac{\partial}{\partial x_1}\frac{\partial}{\partial X_{1x_1}}\left(\frac{\partial {X_1}^2}{\partial x_1} + \frac{\partial {X_1}^2}{\partial x_2} + \frac{\partial {X_2}^2}{\partial x_1} + \frac{\partial {X_2}^2}{\partial x_2}\right) \\ &= \frac{\partial}{\partial x_1}\left(2\frac{\partial X_1}{\partial x_1}\right) \\ &= 2\frac{\partial^2 X_1}{\partial {x_1}^2} \end{aligned}$$

Using the same reasoning, one obtains:

$$\begin{aligned} \frac{\partial}{\partial x_2}\frac{\partial F}{\partial X_{1x_2}} &= 2\frac{\partial^2 X_1}{\partial {x_2}^2} \\ \frac{\partial}{\partial x_1}\frac{\partial F}{\partial X_{2x_1}} &= 2\frac{\partial^2 X_2}{\partial {x_1}^2} \\ \frac{\partial}{\partial x_2}\frac{\partial F}{\partial X_{2x_2}} &= 2\frac{\partial^2 X_2}{\partial {x_2}^2} \end{aligned}$$

As a result, the E-L system of equations associated to $G_4[\mathbf{X}]$ can be written as:

$$-\frac{\partial^2 X_1}{\partial {x_1}^2} - \frac{\partial^2 X_1}{\partial {x_2}^2} = 0 \quad \text{in } \Omega_P \tag{E.8}$$

$$-\frac{\partial^2 X_2}{\partial {x_1}^2} - \frac{\partial^2 X_2}{\partial {x_2}^2} = 0 \quad \text{in } \Omega_P \tag{E.9}$$

This completes the proof. □

E.4 Lemmas used to derive the system of E-L equations for the 3D reconstruction problem

Lemma 5: Defining $G_1[\mathbf{X}]$ as

$$G_1[\mathbf{X}] = \int_{\Omega_P} (\mathbf{X} \cdot \mathbf{v_r} - V_r)^2,$$

the stationary points of the functional $G_1[\mathbf{X}]$ satisfy the following system:

$$(\mathbf{v_r} \cdot \mathbf{v_1})^2 X_1 + (\mathbf{v_r} \cdot \mathbf{v_1})(\mathbf{v_r} \cdot \mathbf{v_2}) X_2 + (\mathbf{v_r} \cdot \mathbf{v_1})(\mathbf{v_r} \cdot \mathbf{v_3}) X_3 = (\mathbf{v_r} \cdot \mathbf{v_1}) V_r \quad \text{in } \Omega_P, \tag{E.10}$$

$$(\mathbf{v_r} \cdot \mathbf{v_2})(\mathbf{v_r} \cdot \mathbf{v_1}) X_1 + (\mathbf{v_r} \cdot \mathbf{v_2})^2 X_2 + (\mathbf{v_r} \cdot \mathbf{v_2})(\mathbf{v_r} \cdot \mathbf{v_3}) X_3 = (\mathbf{v_r} \cdot \mathbf{v_2}) V_r \quad \text{in } \Omega_P, \tag{E.11}$$

$$(\mathbf{v_r} \cdot \mathbf{v_3})(\mathbf{v_r} \cdot \mathbf{v_1}) X_1 + (\mathbf{v_r} \cdot \mathbf{v_3})(\mathbf{v_r} \cdot \mathbf{v_2}) X_2 + (\mathbf{v_r} \cdot \mathbf{v_3})^2 X_3 = (\mathbf{v_r} \cdot \mathbf{v_3}) V_r \quad \text{in } \Omega_P. \tag{E.12}$$

Lemma 6: Defining $G_2[\mathbf{X}]$ as

$$G_2[\mathbf{X}] = \int_{\Omega_P} (\boldsymbol{\nabla} \cdot \mathbf{X})^2,$$

the stationary points of the functional $G_2[\mathbf{X}]$ satisfy the following system:

$$-\left(\frac{\partial^2 X_1}{\partial x_1^2} + \frac{\partial^2 X_2}{\partial x_1 \partial x_2} + \frac{\partial^2 X_3}{\partial x_1 \partial x_3} \right) = 0 \quad \text{in } \Omega_P, \tag{E.13}$$

$$-\left(\frac{\partial^2 X_1}{\partial x_1 \partial x_2} + \frac{\partial^2 X_2}{\partial x_2^2} + \frac{\partial^2 X_3}{\partial x_2 \partial x_3} \right) = 0 \quad \text{in } \Omega_P, \tag{E.14}$$

$$-\left(\frac{\partial^2 X_1}{\partial x_1 \partial x_3} + \frac{\partial^2 X_2}{\partial x_2 \partial x_3} + \frac{\partial^2 X_3}{\partial x_3^2} \right) = 0 \quad \text{in } \Omega_P. \tag{E.15}$$

Lemma 7: Defining $G_3[\mathbf{X}]$ as

$$G_3[\mathbf{X}] = \int_{\partial\Omega_P} \|\mathbf{X} - \mathbf{V_P}\|_2^2,$$

the stationary points of the functional $G_3[\mathbf{X}]$ satisfy the following system:

$$X_1 = \mathbf{V_P} \cdot \mathbf{v_1} \quad \text{in } \partial\Omega_P, \tag{E.16}$$

$$X_2 = \mathbf{V_P} \cdot \mathbf{v_2} \quad \text{in } \partial\Omega_P, \tag{E.17}$$

$$X_3 = \mathbf{V_P} \cdot \mathbf{v_3} \quad \text{in } \partial\Omega_P. \tag{E.18}$$

Lemma 8: Defining $G_4[\mathbf{X}]$ as

$$G_4[\mathbf{X}] = \int_{\Omega_P} \|\boldsymbol{\nabla}\mathbf{X}\|_2^2,$$

the stationary points of the functional $G_4[\mathbf{X}]$ satisfy the following system:

$$-\frac{\partial^2 X_1}{\partial {x_1}^2} - \frac{\partial^2 X_1}{\partial {x_2}^2} - \frac{\partial^2 X_1}{\partial {x_3}^2} = 0 \quad \text{in } \Omega_P, \tag{E.19}$$

$$-\frac{\partial^2 X_2}{\partial {x_1}^2} - \frac{\partial^2 X_2}{\partial {x_2}^2} - \frac{\partial^2 X_2}{\partial {x_3}^2} = 0 \quad \text{in } \Omega_P, \tag{E.20}$$

$$-\frac{\partial^2 X_3}{\partial {x_1}^2} - \frac{\partial^2 X_3}{\partial {x_2}^2} - \frac{\partial^2 X_3}{\partial {x_3}^2} = 0 \quad \text{in } \Omega_P. \tag{E.21}$$

The proofs of Lemmas 5-8 follow directly from the proofs of Lemmas 1-4 detailed in Appendix E.3.

Bibliography

[1] H. Gray, *Anatomy of the human body*. 1918.

[2] S. Y. Ho, "Anatomy and myoarchitecture of the left ventricular wall in normal and in disease," *European Journal of Echocardiography*, vol. 10, no. 8, pp. 3–7, 2009.

[3] C. G. Caro, T. J. Pedley, and R. C. Schroter, *The mechanics of the circulation*. Cambridge University Press, 2012.

[4] M. E. Silverman and J. Hurst, "The mitral complex," *American Heart Journal*, vol. 76, no. 3, pp. 399–418, 1968.

[5] "Wikipedia webpage for wiggers diagram." https://en.wikipedia.org/wiki/File:Wiggers_Diagram.svg. Last accessed: 29 Oct. 2018.

[6] S. Nakatani, "Left Ventricular Rotation and Twist: Why Should We Learn?," *Journal of cardiovascular ultrasound*, vol. 19, no. 1, pp. 1–6, 2011.

[7] N. Wilson, S. J. Goldberg, D. F. Dickinson, and O. Scott, "Normal intracardiac and great artery blood velocity measurements by pulsed Doppler echocardiography.," *British heart journal*, vol. 53, no. 4, pp. 451–8, 1985.

[8] F. Domenichini, G. Querzoli, A. Cenedese, and G. Pedrizzetti, "Combined experimental and numerical analysis of the flow structure into the left ventricle," *Journal of Biomechanics*, vol. 40, no. 9, pp. 1988–1994, 2007.

[9] R. Faludi, M. Szulik, J. D'hooge, P. Herijgers, F. Rademakers, G. Pedrizzetti, and J. U. Voigt, "Left ventricular flow patterns in healthy subjects and patients with prosthetic mitral valves: An in vivo study using echocardiographic particle image velocimetry," *Journal of Thoracic and Cardiovascular Surgery*, vol. 139, no. 6, pp. 1501–1510, 2010.

[10] O. Rodevand, R. Bjornerheim, T. Edvardsen, O. a. Smiseth, and H. Ihlen, "Diastolic Flow Pattern in the Normal Left Ventricle," *Journal of the American Society of Echocardiography*, vol. 12, no. 6, pp. 500–507, 1999.

[11] G. R. Hong, G. Pedrizzetti, G. Tonti, P. Li, Z. Wei, J. K. Kim, A. Baweja, S. Liu, N. Chung, H. Houle, J. Narula, and M. A. Vannan, "Characterization and quantification of vortex flow in the human left ventricle by contrast echocardiography using vector particle image velocimetry," *JACC. Cardiovascular imaging*, vol. 1, no. 6, pp. 705–717, 2008.

[12] P. J. Kilner, G. Z. Yang, a. J. Wilkes, R. H. Mohiaddin, D. N. Firmin, and M. H. Yacoub, "Asymmetric redirection of flow through the heart.," *Nature*, vol. 404, no. 6779, pp. 759–761, 2000.

[13] H. G. Bogren and M. H. Buonocore, "4D magnetic resonance velocity mapping of blood flow patterns in the aorta in young vs. elderly normal subjects," *Journal of Magnetic Resonance Imaging*, vol. 10, pp. 861–869, nov 1999.

[14] I. E. RUSTED, C. H. SCHEIFLEY, and J. E. EDWARDS, "Studies of the mitral valve. I. Anatomic features of the normal mitral valve and associated structures.," *Circulation*, vol. 6, pp. 825–31, dec 1952.

[15] N. Ranganathan, J. H. Lam, E. D. Wigle, and M. D. Silver, "Morphology of the human mitral valve. II. The value leaflets.," *Circulation*, vol. 41, no. 3, pp. 459–467, 1970.

[16] P. Blanke, D. Dvir, A. Cheung, R. A. Levine, C. Thompson, J. G. Webb, and J. Leipsic, "Mitral Annular Evaluation With CT in the Context of Transcatheter Mitral Valve Replacement," *JACC: Cardiovascular Imaging*, vol. 8, pp. 612–615, may 2015.

[17] C. Naoum, J. Leipsic, A. Cheung, J. Ye, N. Bilbey, G. Mak, A. Berger, D. Dvir, C. Arepalli, J. Grewal, D. Muller, D. Murphy, C. Hague, N. Piazza, J. Webb, and P. Blanke, "Mitral Annular Dimensions and Geometry in Patients With Functional Mitral Regurgitation and Mitral Valve Prolapse," *JACC: Card. Imag.*, vol. 9, no. 3, pp. 269–280, 2016.

[18] P. Thériault-Lauzier, M. Dorfmeister, D. Mylotte, M. Spaziano, P. Blanke, G. Martucci, R. Lange, J. Leipsic, L. Bilodeau, N. Piazza, and A. Andalib, "Quantitative multi-slice computed tomography assessment of the mitral valvular complex for transcatheter mitral valve interventions part 2: geometrical measurements in patients with functional mitral regurgitation," *EuroIntervention*, vol. 12, pp. e1021–e1030, oct 2016.

[19] G. Pedrizzetti, F. Domenichini, and G. Tonti, "On the left ventricular vortex reversal after mitral valve replacement," *Ann Biomed Eng*, vol. 38, no. 3, pp. 769–773, 2010.

[20] F. Domenichini and G. Pedrizzetti, "Intraventricular vortex flow changes in the infarcted left ventricle: Numerical results in an idealised 3D shape," *Computer Methods in Biomechanics and Biomedical Engineering*, vol. 14, no. 1, pp. 95–101, 2011.

[21] a. S. Lambert, "Proximal Isovelocity Surface Area Should Be Routinely Measured in Evaluating Mitral Regurgitation: A Core Review," *Anesthesia & Analgesia*, vol. 105, pp. 940–943, oct 2007.

[22] V. T. Nkomo, J. M. Gardin, T. N. Skelton, J. S. Gottdiener, C. G. Scott, and M. Enriquez-Sarano, "Burden of valvular heart diseases: a population-based study," *Lancet*, vol. 368, no. 9540, pp. 1005–1011, 2006.

[23] P. Andell, X. Li, A. Martinsson, C. Andersson, M. Stagmo, B. Zöller, K. Sundquist, and J. G. Smith, "Epidemiology of valvular heart disease in a Swedish nationwide hospital-based register study," *Heart*, vol. 103, pp. 1696–1703, nov 2017.

[24] H. Baumgartner, V. Falk, J. J. Bax, M. De Bonis, C. Hamm, P. J. Holm, B. Iung, P. Lancellotti, E. Lansac, D. R. Muñoz, R. Rosenhek, J. Sjögren, P. Tornos Mas, A. Vahanian, T. Walther, O. Wendler, S. Windecker, and J. L. Zamorano, "2017 ESC/EACTS Guidelines for the management of valvular heart disease," *European Heart Journal*, no. October, pp. 2739–2786, 2017.

[25] A. Carpentier, "Cardiac valve surgery: The 'French correction'," *The Journal of thoracic and cardiovascular surgery*, vol. 86, pp. 323–337, 1983.

[26] J. G. Castillo, J. Solís, Á. González-Pinto, and D. H. Adams, "Surgical Echocardiography of the Mitral Valve," *Revista Española de Cardiología (English Edition)*, vol. 64, pp. 1169–1181, dec 2011.

[27] R. a. Nishimura, C. M. Otto, R. O. Bonow, B. a. Carabello, J. P. Erwin, R. a. Guyton, P. T. O'Gara, C. E. Ruiz, N. J. Skubas, P. Sorajja, T. M. Sundt, and J. D. Thomas, "2014 AHA/ACC Guideline for the Management of Patients With Valvular Heart Disease: Executive Summary," *Circulation*, vol. 129, pp. 2440–2492, jun 2014.

[28] R. A. Nishimura, C. M. Otto, R. O. Bonow, B. A. Carabello, J. P. Erwin, L. A. Fleisher, H. Jneid, M. J. Mack, C. J. McLeod, P. T. O'Gara, V. H. Rigolin, T. M. Sundt, and A. Thompson, "2017 AHA/ACC Focused Update of the 2014 AHA/ACC Guideline for the Management of Patients With Valvular Heart Disease," *Journal of the American College of Cardiology*, vol. 70, pp. 252–289, jul 2017.

[29] P. a. Grayburn, "How to measure severity of mitral regurgitation.," *Postgraduate medical journal*, vol. 84, no. 994, pp. 395–402, 2008.

[30] W. ZOGHBI, "Recommendations for evaluation of the severity of native valvular regurgitation with two-dimensional and doppler echocardiography," *Journal of the American Society of Echocardiography*, vol. 16, pp. 777–802, jul 2003.

[31] P. Thavendiranathan, D. Phelan, P. Collier, J. D. Thomas, S. D. Flamm, and T. H. Marwick, "Quantitative assessment of mitral regurgitation: how best to do it.," *JACC. Cardiovascular imaging*, vol. 5, pp. 1161–75, nov 2012.

[32] X. Zhou, M. A. Vannan, and P. Lancellotti, "Quantitative Three-Dimensional Color Flow Echocardiography of Chronic Mitral Regurgitation: New Methods, New Perspectives, New Challenges," *Journal of the American Society of Echocardiography*, vol. 29, no. 10, pp. 935–937, 2016.

[33] E. S. of Cardiology, "Valvular heart disease," in *Forthcoming ESC TEXTBOOK OF CARDIOVASCULAR MEDICINE 3e*, ch. 35, OXFORD university press, 2017.

[34] D. G. Mitchell, "Color Doppler imaging: principles, limitations, and artifacts.," *Radiology*, vol. 177, pp. 1–10, oct 1990.

[35] D. H. Evans, J. A. Jensen, and M. B. Nielsen, "Ultrasonic colour Doppler imaging," *Interface Focus*, vol. 1, pp. 490–502, aug 2011.

[36] S. Biner, A. Rafique, F. Rafii, K. Tolstrup, O. Noorani, T. Shiota, S. Gurudevan, and R. J. Siegel, "Reproducibility of Proximal Isovelocity Surface Area, Vena Contracta, and Regurgitant Jet Area for Assessment of Mitral Regurgitation Severity," *JACC: Cardiovascular Imaging*, vol. 3, no. 3, pp. 235–243, 2010.

[37] S. Chandra, I. S. Salgo, L. Sugeng, L. Weinert, S. H. Settlemier, V. Mor-Avi, and R. M. Lang, "A three-dimensional insight into the complexity of flow convergence in mitral regurgitation: adjunctive benefit of anatomic regurgitant orifice area.," *American journal of physiology. Heart and circulatory physiology*, vol. 301, no. 3, pp. H1015–H1024, 2011.

[38] I. A. Simpson, T. Shiota, M. Gharib, and D. J. Sahn, "Current status of flow convergence for clinical applications: Is it a leaning tower of "PISA"?," *Journal of the American College of Cardiology*, vol. 27, pp. 504–509, feb 1996.

[39] A. Quaini, S. Canic, G. Guidoboni, R. Glowinski, S. R. Igo, C. J. Hartley, W. a. Zoghbi, and S. H. Little, "A Three-Dimensional Computational Fluid Dynamics Model of Regurgitant Mitral Valve Flow: Validation Against In Vitro Standards and 3D Color Doppler

Methods," *Cardiovascular Engineering and Technology*, vol. 2, no. 2, pp. 77–89, 2011.

[40] P. Thavendiranathan, S. Liu, S. Datta, S. Rajagopalan, T. Ryan, S. R. Igo, M. S. Jackson, S. H. Little, N. De Michelis, and M. a. Vannan, "Quantification of chronic functional mitral regurgitation by automated 3-dimensional peak and integrated proximal isovelocity surface area and stroke volume techniques using real-time 3-dimensional volume color doppler echocardiography: In vitro and clini," *Circulation: Cardiovascular Imaging*, vol. 6, no. 1, pp. 125–133, 2013.

[41] S. H. Little, S. R. Igo, B. Pirat, M. McCulloch, C. J. Hartley, Y. Nosé, and W. A. Zoghbi, "In Vitro Validation of Real-Time Three-Dimensional Color Doppler Echocardiography for Direct Measurement of Proximal Isovelocity Surface Area in Mitral Regurgitation," *The American Journal of Cardiology*, vol. 99, pp. 1440–1447, may 2007.

[42] C.-H. H. Yap, K. Thiele, Q. Wei, A. Santhanakrishnan, R. Khiabani, M. M. Cardinale, I. S. Salgo, and A. P. Yoganathan, "Novel method of measuring valvular regurgitation using three-dimensional nonlinear curve fitting of doppler signals within the flow convergence zone," *IEEE Transactions on Ultrasonics, Ferroelectrics, and Frequency Control*, vol. 60, no. 7, pp. 1295–1311, 2013.

[43] M. Jamil, O. Ahmad, K. K. Poh, and C. H. Yap, "Feasibility of Ultrasound-Based Computational Fluid Dynamics as a Mitral Valve Regurgitation Quantification Technique: Comparison with 2-D and 3-D Proximal Isovelocity Surface Area-Based Methods," *Ultrasound in Medicine & Biology*, pp. 1–17, apr 2017.

[44] F. Zürcher, N. Brugger, S. E. Jahren, S. F. de Marchi, and C. Seiler, "Quantification of Multiple Mitral Regurgitant Jets: An In Vitro Validation Study Comparing Two- and Three-Dimensional Proximal Isovelocity Surface Area Methods," *Journal of the American Society of Echocardiography*, vol. 30, pp. 511–521, may 2017.

[45] P. J. Cawley, C. Hamilton-Craig, D. S. Owens, E. V. Krieger, W. E. Strugnell, L. Mitsumori, C. L. D'Jang, R. G. Schwaegler, K. Q. Nguyen, B. Nguyen, J. H. Maki, and C. M. Otto, "Prospective comparison of valve regurgitation quantitation by cardiac magnetic resonance imaging and transthoracic echocardiography," *Circulation: Cardiovascular Imaging*, vol. 6, no. 1, pp. 48–57, 2013.

[46] E. V. Krieger, J. Lee, K. R. Branch, and C. Hamilton-Craig, "Quantitation of mitral regurgitation with cardiac magnetic resonance imaging: a systematic review," *Heart*, vol. 102, pp. 1864–1870, dec 2016.

[47] A. W. Harris, E. V. Krieger, M. K. Ms, P. J. Cawley, D. S. O. Ms, C. H.-c. Mbbs, J. Maki, and C. M. Otto, "Cardiac Magnetic Resonance Imaging Versus Transthoracic Echocardiography for Prediction of Outcomes in Chronic Aortic or Mitral Regurgitation," *The American Journal of Cardiology*, vol. 119, no. 7, pp. 1074–1081, 2017.

[48] L. Gorodisky, Y. Agmon, M. Porat, S. Abadi, and J. Lessick, "Assessment of mitral regurgitation by 3-dimensional proximal flow convergence using magnetic resonance imaging: comparison with echo-Doppler," *The International Journal of Cardiovascular Imaging*, vol. 34, pp. 793–802, dec 2017.

[49] M. Astorino, J. Hamers, S. C. Shadden, and J.-F. J.-F. Gerbeau, "A robust and efficient valve model based on resistive immersed surfaces," *International Journal for Numerical*

Methods in Biomedical Engineering, vol. 28, pp. 937–959, sep 2012.

[50] A. This, L. Boilevin-Kayl, M. A. Fernández, and J.-F. Gerbeau, "Augmented Resistive Immersed Surfaces valve model for the simulation of cardiac hemodynamics with isovolumetric phases." 2018.

[51] A. This, H. G. Morales, O. Bonnefous, M. A. Fernández, and J.-F. Gerbeau, "Synthetic Mitral Valve Regurgitation modeling using 3D echocardiography : Assessment of the PISA technique.".

[52] A. This, L. Boilevin-Kayl, H. G. Morales, O. Bonnefous, P. Allain, M. A. Fernández, and J.-F. Gerbeau, "One Mesh to Rule Them All: Registration-Based Personalized Cardiac Flow Simulations," in *International Conference on Functional Imaging and Modeling of the Heart*, pp. 441–449, Springer, Cham, 2017.

[53] A. This, H. G. Morales, and O. Bonnefous, "PROXIMAL ISOVELOCITY SURFACE FOR DIFFERENT MITRAL VALVE HOLE GEOMETRIES," in *Proceedings of the VII European Congress on Computational Methods in Applied Sciences and Engineering (ECCOMAS Congress 2016)*, vol. 94, (Athens), pp. 155–163, Institute of Structural Analysis and Antiseismic Research School of Civil Engineering National Technical University of Athens (NTUA) Greece, 2016.

[54] L. Boilevin-Kayl, A. This, M. A. Fernández, and J.-f. Gerbeau, "An efficient valve model based on resistive immersed surfaces enhanced with physiological data," in *5th International Conference on Computational & Mathematical Biomedical Engineering*, 2017.

[55] È. Lluch, R. Doste, S. Giffard-Roisin, A. This, M. Sermesant, O. Camara, M. De Craene, and H. Morales, "Smoothed particle hydrodynamics for electrophysiological modeling: An alternative to finite element methods," in *International Conference on Functional Imaging and Modeling of the Heart*, pp. 333–343, 2017.

[56] N. A. Trayanova, "Whole-Heart Modeling: Applications to Cardiac Electrophysiology and Electromechanics," *Circulation Research*, vol. 108, pp. 113–128, jan 2011.

[57] A. Quarteroni, T. Lassila, S. Rossi, and R. Ruiz-Baier, "Integrated Heart – coupling multiscale and multiphysics models for the simulation of the cardiac function," *Computer Methods in Applied Mechanics and Engineering (in press)*, 2016.

[58] C. Chnafa, S. Mendez, and F. Nicoud, "Image-Based Simulations Show Important Flow Fluctuations in a Normal Left Ventricle: What Could be the Implications?," *Annals of biomedical engineering*, vol. 44, 2016.

[59] M. Fedele, E. Faggiano, L. Dedè, and A. Quarteroni, "A patient-specific aortic valve model based on moving resistive immersed implicit surfaces," *Biomech. Model. Mechanobiol.*, vol. 16, no. 5, pp. 1779–1803, 2017.

[60] A. Tagliabue, L. Dedè, and A. Quarteroni, "Fluid dynamics of an idealized left ventricle: the extended Nitsche's method for the treatment of heart valves as mixed time varying boundary conditions," *International Journal for Numerical Methods in Fluids*, vol. 85, pp. 135–164, sep 2017.

[61] R. Mittal, J. H. Seo, V. Vedula, Y. J. Choi, H. Liu, H. H. Huang, S. Jain, L. Younes, T. Abraham, and R. T. George, "Computational modeling of cardiac hemodynamics: Cur-

rent status and future outlook," *Journal of Computational Physics*, vol. 305, pp. 1065–1082, 2016.

[62] L. Formaggia, J. F. Gerbeau, F. Nobile, and A. Quarteroni, "On the coupling of 3D and 1D Navier-Stokes equations for flow problems in compliant vessels," *Comp. Meth. Appl. Mech. Engrg.*, vol. 191, pp. 561–582, 2001.

[63] I. Vignon-Clementel, *A coupled multidomain method for computational modeling of blood flow*. PhD thesis, Stanford University, 2005.

[64] Y. Shi, P. Lawford, and R. Hose, "Review of Zero-D and 1-D Models of Blood Flow in the Cardiovascular System," *BioMedical Engineering Online*, vol. 10, no. 1, p. 33, 2011.

[65] B. Su, L. Zhong, X.-K. K. Wang, J.-M. M. Zhang, R. S. Tan, J. C. Allen, S. K. Tan, S. Kim, H. L. Leo, R. San Tan, J. C. Allen, S. K. Tan, S. Kim, and H. L. Leo, "Numerical simulation of patient-specific left ventricular model with both mitral and aortic valves by FSI approach," *Computer Methods and Programs in Biomedicine*, vol. 113, no. 2, pp. 474–482, 2014.

[66] H. Gao, L. Feng, N. Qi, C. Berry, B. E. Griffith, and X. Luo, "A coupled mitral valve—left ventricle model with fluid–structure interaction," *Medical Engineering & Physics*, vol. 47, pp. 128–136, sep 2017.

[67] K. S. Kunzelman, D. R. Einstein, and R. P. Cochran, "Fluid-structure interaction models of the mitral valve: function in normal and pathological states.," *Philosophical transactions of the Royal Society of London. Series B, Biological sciences*, vol. 362, no. 1484, pp. 1393–1406, 2007.

[68] T. Pham, F. Kong, C. Martin, Q. Wang, C. Primiano, R. McKay, J. Elefteriades, and W. Sun, "Finite Element Analysis of Patient-Specific Mitral Valve with Mitral Regurgitation," *Cardiovascular Engineering and Technology*, vol. 8, pp. 3–16, mar 2017.

[69] D. R. Einstein, F. D. Pin, X. Jiao, A. P. Kuprat, P. James, K. S. Kunzelman, R. P. Cochran, J. M. Guccione, B. Mark, F. Del Pin, X. Jiao, A. P. Kuprat, J. P. Carson, K. S. Kunzelman, R. P. Cochran, J. M. Guccione, and M. B. Ratcliffe, "Fluid-structure interactions of the mitral valve and left heart: Comprehensive strategies, past, present and future," *International Journal for Numerical Methods in Biomedical Engineering*, vol. 26, pp. 348–380, mar 2010.

[70] L. Rodriguez, J. Anconina, F. A. Flachskampf, a. E. Weyman, R. A. Levine, and J. D. Thomas, "Impact of finite orifice size on proximal flow convergence. Implications for Doppler quantification of valvular regurgitation.," *Circulation research*, vol. 70, no. 5, pp. 923–930, 1992.

[71] A. Quaini, S. Canic, R. Glowinski, S. Igo, C. J. Hartley, W. Zoghbi, and S. Little, "Validation of a 3D computational fluid-structure interaction model simulating flow through an elastic aperture," *Journal of Biomechanics*, vol. 45, no. 2, pp. 310–318, 2012.

[72] Y. Wang, A. Quaini, S. Čanić, M. Vukicevic, and S. H. Little, "3D Experimental and Computational Analysis of Eccentric Mitral Regurgitant Jets in a Mock Imaging Heart Chamber," *Cardiovascular Engineering and Technology*, vol. 8, no. 4, pp. 419–438, 2017.

[73] C. Phillips, "A simple lumped parameter model of the cardiovascular system," *Zhurnal*

Eksperimental'noi i Teoreticheskoi Fiziki, 2011.

[74] T. Lassila, C. Malossi, M. Stevanella, E. Votta, A. Redaelli, and S. Deparis, "Simulation of left ventricle fluid dynamics with mitral regurgitation from magnetic resonance images with fictitious elastic structure regularization," *arXiv preprint*, pp. 1–12, jul 2017.

[75] M. Fedele, E. Faggiano, L. Dedè, and A. Quarteroni, "A patient-specific aortic valve model based on moving resistive immersed implicit surfaces," *Biomechanics and Modeling in Mechanobiology*, vol. 16, pp. 1779–1803, oct 2017.

[76] S. S. Khalafvand, E. Y. K. Ng, and L. Zhong, "CFD simulation of flow through heart: a perspective review.," *Computer methods in biomechanics and biomedical engineering*, vol. 14, no. 1, pp. 113–132, 2011.

[77] M. Astorino, *Fluid-Structure Interaction in the Cardiovascular System . Numerical Analysis and Simulation.* PhD thesis, Universite Pierre et Marie Curie - Paris VI, 2013.

[78] A. Bavo, A. Pouch, J. Degroote, J. Vierendeels, J. Gorman, R. Gorman, and P. Segers, "Patient-specific CFD models for intraventricular flow analysis from 3D ultrasound imaging: Comparison of three clinical cases," *Journal of Biomechanics*, vol. 50, pp. 144–150, jan 2016.

[79] J. Lantz, L. Henriksson, A. Persson, M. Karlsson, and T. Ebbers, "Patient-Specific Simulation of Cardiac Blood Flow From High-Resolution Computed Tomography," *Journal of Biomechanical Engineering*, vol. 138, no. 12, p. 121004, 2016.

[80] B. Baillargeon, I. Costa, J. R. Leach, L. C. Lee, M. Genet, A. Toutain, J. F. Wenk, M. K. Rausch, N. Rebelo, G. Acevedo-Bolton, E. Kuhl, J. L. Navia, and J. M. Guccione, "Human Cardiac Function Simulator for the Optimal Design of a Novel Annuloplasty Ring with a Sub-valvular Element for Correction of Ischemic Mitral Regurgitation," *Cardiovascular Engineering and Technology*, vol. 6, pp. 105–116, jun 2015.

[81] G. B. Thurston, "Viscoelastic properties of blood and blood analogs," in *Advances in Hemodynamics and Hemorheology, Volume 1*, vol. 1, pp. 1–30, JAI Press, 1996.

[82] M. A. Fogel, "Ventricular function and blood flow in congenital heart disease," *John Wiley \& Sons*, 2008.

[83] M. E. H. van Dongen, F.N. van de Vosse and M. van Dongen, F.N. van de Vosse, *Cardiovascular Fluid Mechanics*, vol. 53. Vienna: Springer Vienna, 1998.

[84] C. Chnafa, S. Mendez, and F. Nicoud, "Image-based large-eddy simulation in a realistic left heart," *Comput Fluids*, vol. 94, pp. 173–187, 2014.

[85] J. Donea, A. Huerta, J.-P. Ponthot, and A. Rodríguez-Ferran, "Arbitrary Lagrangian-Eulerian Methods," in *Encyclopedia of Computational Mechanics*, pp. 1–25, Chichester, UK: John Wiley & Sons, Ltd, nov 2004.

[86] M. Landajuela, M. Vidrascu, D. Chapelle, and M. A. Fernández, "Coupling schemes for the FSI forward prediction challenge: Comparative study and validation," *International Journal for Numerical Methods in Biomedical Engineering*, 2016.

[87] K. Stein, T. Tezduyar, and R. Benney, "Mesh Moving Techniques for Fluid-Structure Interactions With Large Displacements," *Journal of Applied Mechanics*, vol. 70, no. 1,

p. 58, 2003.

[88] M. Esmaily Moghadam, Y. Bazilevs, T.-Y. Hsia, I. E. Vignon-Clementel, and A. L. Marsden, "A comparison of outlet boundary treatments for prevention of backflow divergence with relevance to blood flow simulations," *Computational Mechanics*, vol. 48, pp. 277–291, sep 2011.

[89] M. A. Fernández, J.-F. J.-F. Gerbeau, and V. Martin, "Numerical simulation of blood flows through a porous interface," *ESAIM: Mathematical Modelling and Numerical Analysis*, vol. 42, pp. 961–990, nov 2008.

[90] T. Tezduyar, "Stabilized finite element formulations for incompressible flow computations," in *Advances in applied mechanics, Vol. 28*, vol. 28 of *Adv. Appl. Mech.*, pp. 1–44, Boston, MA: Academic Press, 1992.

[91] D. Chapelle, P. Le Tallec, P. Moireau, and M. Sorine, "Energy-Preserving Muscle Tissue Model: Formulation and Compatible Discretizations," *International Journal for Multiscale Computational Engineering*, vol. 10, no. 2, pp. 189–211, 2012.

[92] E. Schwammenthal, C. Chen, F. Benning, M. Block, G. Breithardt, and R. A. Levine, "Dynamics of mitral regurgitant flow and orifice area. Physiologic application of the proximal flow convergence method: clinical data and experimental testing," *Circulation*, vol. 90, pp. 307–322, jul 1994.

[93] P. Ponikowski, A. A. Voors, S. D. Anker, H. Bueno, J. G. F. Cleland, A. J. S. Coats, V. Falk, J. R. González-Juanatey, V.-P. Harjola, E. A. Jankowska, M. Jessup, C. Linde, P. Nihoyannopoulos, J. T. Parissis, B. Pieske, J. P. Riley, G. M. C. Rosano, L. M. Ruilope, F. Ruschitzka, F. H. Rutten, and P. van der Meer, "2016 ESC Guidelines for the diagnosis and treatment of acute and chronic heart failure," *European Heart Journal*, vol. 37, pp. 2129–2200, jul 2016.

[94] O. Pierrakos and P. P. Vlachos, "The effect of vortex formation on left ventricular filling and mitral valve efficiency.," *Journal of biomechanical engineering*, vol. 128, no. 4, pp. 527–539, 2006.

[95] N. Al-Wakeel, J. F. Fernandes, A. Amiri, H. Siniawski, L. Goubergrits, F. Berger, and T. Kuehne, "Hemodynamic and energetic aspects of the left ventricle in patients with mitral regurgitation before and after mitral valve surgery," *Journal of Magnetic Resonance Imaging*, vol. 42, no. 6, pp. 1705–1712, 2015.

[96] G. Pedrizzetti and F. Domenichini, "Nature optimizes the swirling flow in the human left ventricle," *Physical Review Letters*, vol. 95, no. 10, pp. 1–4, 2005.

[97] K. Nakashima, K. Itatani, T. Kitamura, N. Oka, T. Horai, S. Miyazaki, M. Nie, and K. Miyaji, "Energy dynamics of the intraventricular vortex after mitral valve surgery," 2017.

[98] S. S. Khalafvand, E. Y.-k. Ng, L. Zhong, and T.-k. Hung, "Three-dimensional diastolic blood flow in the left ventricle," *Journal of Biomechanics*, vol. 50, pp. 71–76, 2017.

[99] C. Chnafa, "Using image-based large-eddy simulations to investigate the intracardiac ow and its turbulent nature," *Thesis*, 2014.

[100] S. F. Nagueh, C. P. Appleton, T. C. Gillebert, P. N. Marino, J. K. Oh, O. A. Smiseth, A. D. Waggoner, F. A. Flachskampf, P. A. Pellikka, and A. Evangelisa, "Recommendations for the Evaluation of Left Ventricular Diastolic Function by Echocardiography," *European Journal of Echocardiography*, vol. 10, pp. 165–193, aug 2008.

[101] M. Fedele, E. Faggiano, L. Dedè, and A. Quarteroni, "A patient-specific aortic valve model based on moving resistive immersed implicit surfaces," *Biomechanics and Modeling in Mechanobiology*, vol. 16, pp. 1779–1803, oct 2017.

[102] A. Caiazzo, M. A. Fernández, J.-F. Gerbeau, and V. Martin, "Projection Schemes for Fluid Flows through a Porous Interface," *SIAM Jour. on Sc. Comp.*, vol. 33, no. 2, pp. 541–564, 2011.

[103] H. Fukuta and W. C. L., "The Cardiac Cycle and the Physiological Basis of Left Ventricular Contraction, Ejection, Relaxation, and Filling," *Heart Failure Clin.*, vol. 4, no. 1, pp. 1–11, 2008.

[104] M. Landajuela, M. Vidrascu, D. Chapelle, and M. A. Fernández, "Coupling schemes for the FSI forward prediction challenge: Comparative study and validation," *International Journal for Numerical Methods in Biomedical Engineering*, vol. 33, p. e2813, apr 2017.

[105] I. E. RUSTED, C. H. SCHEIFLEY, and J. E. EDWARDS, "Studies of the Mitral Valve. I. Anatomic Features of the Normal Mitral Valve and Associated Structures," *Circulation*, vol. 6, pp. 825–831, dec 1952.

[106] L. A. Du Plessis and P. Marchand, "The Anatomy of the Mitral Valve and its Associated Structures," *Thorax*, vol. 19, pp. 221–227, may 1964.

[107] E. Votta, E. Caiani, F. Veronesi, M. Soncini, F. M. Montevecchi, and A. Redaelli, "Mitral valve finite-element modelling from ultrasound data: a pilot study for a new approach to understand mitral function and clinical scenarios.," *Philosophical transactions of the Royal Society. Series A, Mathematical, Physical, and Engineering Sciences*, vol. 366, no. 1879, pp. 3411–3434, 2008.

[108] J. Hart, "Normal resting pulse rate ranges," *Journal of Nursing Education and Practice*, vol. 5, jun 2015.

[109] J. Wikstrand, G. Berglund, L. Wilhelmsen, and I. Wallentin, "Value of systolic and diastolic time intervals. Studies in normotensive and hypertensive 50-year-old men and in patients after myocardial infarction," *Br. Heart J.*, vol. 40, no. 3, pp. 256–267, 1978.

[110] V. Mihalef, R. I. Ionasec, P. Sharma, B. Georgescu, I. Voigt, M. Suehling, and D. Comaniciu, "Patient-specific modelling of whole heart anatomy, dynamics and haemodynamics from four-dimensional cardiac CT images," *Interface Focus*, vol. 1, pp. 286–296, jun 2011.

[111] E. Votta, T. B. Le, M. Stevanella, L. Fusini, E. G. Caiani, A. Redaelli, and F. Sotiropoulos, "Toward patient-specific simulations of cardiac valves: State-of-the-art and future directions," *Journal of Biomechanics*, vol. 46, no. 2, pp. 217–228, 2013.

[112] A. D. Vecchi, A. Gomez, K. Pushparajah, T. Schaeffter, J. M. Simpson, R. Razavi, G. P. Penney, N. P. Smith, and D. A. Nordsletten, "A novel methodology for personalized simulations of ventricular hemodynamics from noninvasive imaging data," *Computerized Medical Imaging and Graphics*, vol. 51, pp. 20–31, 2016.

[113] A. M. Bavo, A. M. Pouch, J. Degroote, J. Vierendeels, J. H. Gorman, R. C. Gorman, and P. Segers, "Patient-specific CFD simulation of intraventricular haemodynamics based on 3D ultrasound imaging," *BioMedical Engineering OnLine*, vol. 15, p. 107, dec 2016.

[114] S. N. Doost, D. Ghista, B. Su, L. Zhong, and Y. S. Morsi, "Heart blood flow simulation: a perspective review.," *Biomedical engineering online*, vol. 15, no. 1, p. 101, 2016.

[115] P. P. Sengupta, A. J. Tajik, K. Chandrasekaran, and B. K. Khandheria, "Twist Mechanics of the Left Ventricle. Principles and Application," 2008.

[116] I. K. Rüssel, M. J. Götte, J. G. Bronzwaer, P. Knaapen, W. J. Paulus, and A. C. van Rossum, "Left Ventricular Torsion. An Expanding Role in the Analysis of Myocardial Dysfunction," *JACC: Cardiovascular Imaging*, vol. 2, no. 5, pp. 648–655, 2009.

[117] P. Bovendeerd, T. Arts, J. Huyghe, D. van Campen, and R. Reneman, "Dependence of local left ventricular wall mechanics on myocardial fiber orientation: A model study," *Journal of Biomechanics*, vol. 25, pp. 1129–1140, oct 1992.

[118] J. D. Bayer, R. C. Blake, G. Plank, and N. A. Trayanova, "A Novel Rule-Based Algorithm for Assigning Myocardial Fiber Orientation to Computational Heart Models," *Annals of Biomedical Engineering*, vol. 40, pp. 2243–2254, oct 2012.

[119] V. Vasudevan, A. Jia, J. Low, S. P. Annamalai, S. Sampath, K. K. Poh, T. Totman, M. Mazlan, G. Croft, A. M. Richards, D. P. V. Kleijn, C.-l. Chin, and C. H. Yap, "Flow dynamics and energy efficiency of flow in the left ventricle during myocardial infarction," *Biomechanics and Modeling in Mechanobiology*, 2017.

[120] T. Schenkel, M. Malve, M. Reik, M. Markl, B. Jung, and H. Oertel, "MRI-Based CFD analysis of flow in a human left ventricle: Methodology and application to a healthy heart," *Annals of Biomedical Engineering*, vol. 37, no. 3, pp. 503–515, 2009.

[121] M. B. Buchalter, J. L. Weiss, W. J. Rogers, E. A. Zerhouni, M. L. Weisfeldt, R. Beyar, and E. P. Shapiro, "Noninvasive quantification of left ventricular rotational deformation in normal humans using magnetic resonance imaging myocardial tagging," *Circulation*, vol. 81, no. 4, pp. 1236–1244, 1990.

[122] J. T. Kowallick, P. Lamata, S. T. Hussain, S. Kutty, M. Steinmetz, J. M. Sohns, M. Fasshauer, W. Staab, C. Unterberg-Buchwald, B. Bigalke, J. Lotz, G. Hasenfuß, and A. Schuster, "Quantification of Left Ventricular Torsion and Diastolic Recoil Using Cardiovascular Magnetic Resonance Myocardial Feature Tracking," *PLoS ONE*, vol. 9, p. e109164, oct 2014.

[123] Y. Notomi, P. Lysyansky, R. M. Setser, T. Shiota, Z. B. Popović, M. G. Martin-Miklovic, J. A. Weaver, S. J. Oryszak, N. L. Greenberg, R. D. White, and J. D. Thomas, "Measurement of ventricular torsion by two-dimensional ultrasound speckle tracking imaging," *Journal of the American College of Cardiology*, vol. 45, no. 12, pp. 2034–2041, 2005.

[124] E. J. Stöhr, R. E. Shave, A. L. Baggish, and R. B. Weiner, "Left ventricular twist mechanics in the context of normal physiology and cardiovascular disease: a review of studies using speckle tracking echocardiography," *American Journal of Physiology - Heart and Circulatory Physiology*, vol. 311, no. 3, pp. H633–H644, 2016.

[125] B. J. Kimura and A. N. DeMaria, "Time requirements of the standard echocardiogram:

implications regarding limited studies," *Journal of the American Society of Echocardiography*, vol. 16, pp. 1015–1018, oct 2003.

[126] D. Luenberger, "An introduction to observers," *IEEE Transactions on Automatic Control*, vol. 16, pp. 596–602, dec 1971.

[127] D. Auroux and J. Blum, "A nudging-based data assimilation method: the Back and Forth Nudging (BFN) algorithm," *Nonlinear Processes in Geophysics*, vol. 15, pp. 305–319, mar 2008.

[128] P. Moireau, C. Bertoglio, N. Xiao, C. a. Figueroa, C. a. Taylor, D. Chapelle, and J.-f. Gerbeau, "Sequential identification of boundary support parameters in a fluid-structure vascular model using patient image data," *Biomechanics and Modeling in Mechanobiology*, vol. 12, pp. 475–496, 2013.

[129] C. Foias, C. F. Mondaini, and E. S. Titi, "A Discrete Data Assimilation Scheme for the Solutions of the Two-Dimensional Navier–Stokes Equations and Their Statistics," *SIAM Journal on Applied Dynamical Systems*, vol. 15, no. 4, pp. 2109–2142, 2016.

[130] K. McLeod, A. Caiazzo, M. A. Fernández, T. Mansi, I. E. Vignon-Clementel, M. Sermesant, X. Pennec, Y. Boudjemline, and J.-f. Gerbeau, "Atlas-Based Reduced Models of Blood Flows for Fast Patient-Specific Simulations," in *International Workshop on Statistical Atlases and Computational Models of the Heart* (Springer, ed.), pp. 95–104, 2010.

[131] M. Arigovindan, M. Suhling, C. Jansen, P. Hunziker, and M. Unser, "Full Motion and Flow Field Recovery From Echo Doppler Data," *IEEE Transactions on Medical Imaging*, vol. 26, pp. 31–45, jan 2007.

[132] A. Gomez, A. De Vecchi, M. Jantsch, W. Shi, K. Pushparajah, J. M. Simpson, N. P. Smith, D. Rueckert, T. Schaeffter, and G. P. Penney, "4D Blood Flow Reconstruction over the Entire Ventricle from Wall Motion and Blood Velocity Derived from Ultrasound Data," *IEEE Transactions on Medical Imaging*, vol. 34, no. 11, pp. 2298–2308, 2015.

[133] J. Jang, C. Y. Ahn, J. I. Choi, and J. K. Seo, "Inverse Problem for Color Doppler Ultrasound-Assisted Intracardiac Blood Flow Imaging," *Computational and Mathematical Methods in Medicine*, vol. 2016, 2016.

[134] K. C. Assi, E. Gay, C. Chnafa, S. Mendez, F. Nicoud, J. F. Abascal, P. Lantelme, F. Tournoux, and D. Garcia, "Intraventricular vector flow mapping - A Doppler-based regularized problem with automatic model selection," *Physics in Medicine and Biology*, vol. 62, no. 17, pp. 7131–7147, 2017.

[135] B. Couteau, Y. Payan, and S. Lavallée, "The mesh-matching algorithm: an automatic 3D mesh generator for finite element structures," *Journal of Biomechanics*, vol. 33, pp. 1005–1009, aug 2000.

[136] M. Bucki, C. Lobos, and Y. Payan, "A fast and robust patient specific Finite Element mesh registration technique: Application to 60 clinical cases," *Medical Image Analysis*, vol. 14, no. 3, pp. 303–317, 2010.

[137] T. Vercauteren, X. Pennec, A. Perchant, and N. Ayache, "Non-parametric Diffeomorphic Image Registration with the Demons Algorithm," in *Medical Image Computing and Computer-Assisted Intervention – MICCAI 2007*, vol. 45, pp. 319–326, Berlin, Heidelberg:

Springer Berlin Heidelberg, mar 2009.

[138] J. Ashburner, "A fast diffeomorphic image registration algorithm," *NeuroImage*, vol. 38, pp. 95–113, oct 2007.

[139] M. Hernandez, M. N. Bossa, and S. Olmos, "Registration of Anatomical Images Using Paths of Diffeomorphisms Parameterized with Stationary Vector Field Flows," *International Journal of Computer Vision*, vol. 85, pp. 291–306, dec 2009.

[140] S. Durrleman, M. Prastawa, N. Charon, J. R. Korenberg, S. Joshi, G. Gerig, and A. Trouvé, "Morphometry of anatomical shape complexes with dense deformations and sparse parameters," *NeuroImage*, vol. 101, pp. 35–49, nov 2014.

[141] M. I. Miller, A. Trouvé, and L. Younes, "Geodesic Shooting for Computational Anatomy," *Journal of Mathematical Imaging and Vision*, vol. 24, pp. 209–228, mar 2006.

[142] Cha Zhang and Tsuhan Chen, "Efficient feature extraction for 2D/3D objects in mesh representation," in *Proceedings 2001 International Conference on Image Processing (Cat. No.01CH37205)*, vol. 2, pp. 935–938, IEEE, 2001.

[143] N. Aspert, D. Santa-Cruz, and T. Ebrahimi, "MESH: measuring errors between surfaces using the Hausdorff distance," in *Proceedings. IEEE International Conference on Multimedia and Expo*, vol. 1, pp. 705–708, IEEE, 2002.

[144] V. Meschini, M. D. de Tullio, and R. Verzicco, "Effects of mitral chordae tendineae on the flow in the left heart ventricle," *The European Physical Journal E*, vol. 41, p. 27, feb 2018.

[145] M. D. Cerqueira, N. J. Weissman, V. Dilsizian, A. K. Jacobs, S. Kaul, W. K. Laskey, D. J. Pennell, J. A. Rumberger, T. Ryan, and M. S. Verani, "Standardized myocardial segmentation and nomenclature for tomographic imaging of the heart: A statement for healthcare professionals from the Cardiac Imaging Committee of the Council on Clinical Cardiology of the American Heart Association," *Journal of the American Society of Echocardiography*, vol. 15, pp. 463–467, may 2002.

[146] R. B. Weiner and A. L. Baggish, "Left ventricular torsion: feeling the heat," *Experimental Physiology*, vol. 96, pp. 71–72, feb 2011.

[147] S. Kulp, M. Gao, S. Zhang, Z. Qian, S. Voros, D. Metaxas, and L. Axel, "Using high resolution cardiac CT data to model and visualize patient-specific interactions between trabeculae and blood flow," *Lecture Notes in Computer Science (including subseries Lecture Notes in Artificial Intelligence and Lecture Notes in Bioinformatics)*, vol. 6891 LNCS, no. PART 1, pp. 468–475, 2011.

[148] F. Sacco, B. Paun, O. Lehmkuhl, T. L. Iles, P. A. Iaizzo, G. Houzeaux, M. Vázquez, C. Butakoff, and J. Aguado-Sierra, "Left ventricular trabeculations decrease the wall shear stress and increase the intra-ventricular pressure drop in CFD simulations," *Frontiers in Physiology*, vol. 9, no. April, 2018.

[149] D. Garcia, J. C. Juan, D. Tanné., R. Yotti, C. Cortina, É. Bertrand, J. C. Antoranz, E. Pérez-David, R. Rieu, F. Fernández-Avilés, and J. Bermejo, "Two-dimensional intraventricular flow mapping by digital processing conventional color-doppler echocardiography images," *IEEE Transactions on Medical Imaging*, vol. 29, no. 10, pp. 1701–1713, 2010.

[150] K.-T. Chang, C.-Z. Zhan, and A.-Y. Wu, "Joint-decision adaptive clutter filter and motion-tracking adaptive persistence for color doppler processing in ultrasonic systems," in *Signal Processing Systems (SIPS), 2010 IEEE Workshop on*, pp. 249–253, IEEE, 2010.

[151] D. Tanné, E. Bertrand, L. Kadem, P. Pibarot, and R. Rieu, "Assessment of left heart and pulmonary circulation flow dynamics by a new pulsed mock circulatory system," *Experiments in Fluids*, vol. 48, pp. 837–850, may 2010.

[152] Y. Otsuji, D. Gilon, L. Jiang, S. He, M. Leavitt, M. J. Roy, M. J. Birmingham, and R. A. Levine, "Restricted diastolic opening of the mitral leaflets in patients with left ventricular dysfunction: Evidence for increased valve tethering," *Journal of the American College of Cardiology*, vol. 32, no. 2, pp. 398–404, 1998.

[153] T. Watanabe, H. Arai, E. Nagaoka, K. Oi, T. Hachimaru, H. Kuroki, T. Fujiwara, and T. Mizuno, "Influence of procedural differences on mitral valve configuration after surgical repair for functional mitral regurgitation: in which direction should the papillary muscle be relocated?," *Journal of Cardiothoracic Surgery*, vol. 9, p. 185, dec 2014.